Alma Mater Studiorum - Università di Bologna

DOTTORATO DI RICERCA IN

INGEGNERIA BIOMEDICA, ELETTRICA E DEI SISTEMI

Ciclo 33

Settore Concorsuale: 09/E2 - INGEGNERIA DELL'ENERGIA ELETTRICA

Settore Scientifico Disciplinare: ING-IND/33 - SISTEMI ELETTRICI PER L'ENERGIA

PROTECTION SYSTEMS AND STABILITY OF DISTRIBUTION NETWORKS AND MICROGRIDS WITH DISTRIBUTED ENERGY RESOURCES

Presentata da: Juan Diego Rios Penaloza

Coordinatore Dottorato

Prof. Michele Monaci

Supervisore

Prof. Carlo Alberto Nucci

Co-supervisore

Prof. Alberto Borghetti

Esame finale anno 2021

ACKNOWLEDGMENT

First of all, I would like to express my infinite gratitude to the members of the LISEP laboratory of the University of Bologna, my tutor Prof. Carlo Alberto Nucci, my co-tutor Prof. Alberto Borghetti, Prof. Fabio Napolitano, Eng. Fabio Tossani and my colleagues of the PhD program. The thesis presented here is the result of a collective work that would not have been possible otherwise. In many cases the teachings, especially those coming from my tutors, went beyond the scientific field.

I would like to thank Prof. João Peças Lopes, Prof. Carlos Moreira and Eng. Justino Rodrigues from the INESC TEC Institute in Portugal, who have welcomed me during my period abroad and have allowed me to expand my knowledge, professional vision and experience.

With much affection, I want to thank all the people that contributed in many ways to my maturement as a person and as a professional and who allowed me to maintain my intentions during the tough path that the doctorate represents. I will be forever grateful for all the support to my mother Tere, my father Juan, my brother Oscar, my aunt Isa and my life companion Alexandra. Likewise, I want to thank the rest of my family and my friends, in Bolivia and in Italy, who have always been an unforgettable motivation for me.

I dedicate this work to my grandparents René and Maruja.

TABLE OF CONTENTS

LIST OF FIGURES

LIST OF TABLES

ABSTRACT

The large-scale integration of Distributed Energy Resources (DERs) in distribution networks has several technical implications and consequences, which increase in complexity when energy sources are of renewable type (RES, or Renewable Energy Sources). Apart from the case of hydro, RESs are characterized by intermittent/unpredictable availability and are connected to the grid through converters, often close to the final users, which means that they are more prone to cause instability issues, inverse power flow occurrence and potential mis-operation of protection schemes. The above-mentioned effects on existing protection schemes and on system stability are the objects of this thesis.

A protection system against earth faults in radial distribution networks with unearthed and compensated neutral is proposed and assessed. The faulty feeder identification algorithm is based on the angle between the zero-sequence voltage and current phasors, estimated at the dominant transient frequency inferred from the transient response of the network within the first milliseconds after the fault. Critical scenarios in which transient-based protection systems are prone to mis-operate are analyzed. A sensitivity analysis explores the influence of some characteristics inherent to the protection system and to the fault. The performances of the protection system algorithm are assessed in radial distribution networks with both unearthed and compensated neutrals through a Monte Carlo method that considers the fault resistance, incidence angle and fault location variations. The power system is simulated within the EMTP-RV environment, while the protection algorithm is developed in Matlab.

Since the large deployment of distributed resources constitute a strong drive for meshing networks, the protection system is extended to such systems by implementing a communication network that communicates the relays installed at both ends of each line. The relays implement the proposed algorithm to determine the directionality of the fault, and the faulty section is then identified by implementing a directional comparison scheme. By using a specifically developed co-simulation tool that interfaces EMTP-RV with Matlab, the influence of the communication latency is also assessed. The robustness of the protection system in front of harmonic injection due to the presence of power converter-interfaced distributed resources is also analyzed. Finally, the performances of the protection system are evaluated for different network configurations in which a Monte Carlo method is applied to analyze the effects of fault resistance, incidence angle and fault location variations. Results of a real-time simulation obtained in the Opal-RT environment further support the applicability of the algorithm.

Another important aspect of the large deployment of distributed resources are the diffusion of Microgrids (MGs) which are characterized by faster dynamics than conventional grid-connected distributions systems. This is in part due to the lack of inertia of inverter-interfaced resources. In this context, load dynamics considerably affect the transient stability performance of MGs, especially during islanding transition and in standalone mode.

The transient stability of a medium voltage MG is analyzed in two different cases, namely an islanding transition and a fault when the MG is standalone: i) in the first case, the influence of the load composition is analyzed. The MG consists of a photovoltaic power plant, two battery energy storage systems, a synchronous generator and different classes and types of load. The system is implemented in the EMTP-RV simulation environment; ii) in the second case, a fault is considered in an inertia-less standalone MG. The exclusion of any rotating generator is expected to heighten the load influence on the dynamics of the system. Modern controllable loads are included, namely an electric vehicle charging station and variable speed heat pumps. The system is implemented in Simulink and real-time simulations are carried out in the Opal-RT environment.

In both cases, a sensitivity analysis is carried out in a simple system to assess individually the impact of some parameters of conventional loads and of some control parameters of controllable loads on the minimum values reached by the frequency and voltage during the transient. The analysis is then extended to a more complex network, in order to verify the results obtained in the sensitivity analysis and appraise the interaction between all the analyzed components.

LIST OF ACRONYMS

ADN	Active Distribution Network
AMI	Advanced Metering Infrastructure
BESS	Battery Energy Storage System
CAMC	Central Autonomous Management Controller
CB	Circuit Breaker
CHP	Combined Heat and Power
CP	Constant Parameter
CC-VSC	Current-Controlled Voltage Sourced Converter
CT	Current Transformer
DFT	Discrete Fourier Transform
DER	Distributed Energy Resource
DG	Distributed Generation
DMS	Distribution Management System
DSO	Distribution System Operator
DLL	Dynamic Link Library
EV	Electric Vehicle
EV-CS	Electric Vehicle – Charging Station
ESS	Energy Storage System
FFT	Fast Fourier Transform
FCL	Fault Current Limiter
FD	Frequency Dependent
HP	Heat Pump
IM	Induction Motor
IG	Induction Generator
IGBT	Insulated-Gate Bipolar Transistor
LPF	Low-Pass Filter

LV	Low Voltage
MPPT	Maximum Power Point Tracking
MV	Medium Voltage
MG	Microgrid
MGCC	Microgrid Central Controller
MMG	Multi-Microgrid
OLTC	On-Load Tap Changer
PLL	Phase-Locked Loop
PV	Photovoltaic
PHIL	Power-Hardware-In-The-Loop
PQM	Power Reference Maintenance
PI	Proportional Integral
PSTT	Protection Scheme Tripping Time
PWM	Pulse-Width Modulation
RES	Renewable Energy Source
RTI	Runtime Infrastructure
SoC	State of Charge
SG	Synchronous Generator
TRD	Total Rated Current Distortion
TSO	Transmission System Operator
TVI	Transient Virtual Impedance
VI	Virtual Inertia
VSM	Virtual Synchronous Machine
VC-VSC	Voltage-Controlled Voltage-Sourced Converter
VSI	Voltage Source Inverter
VSC	Voltage-Sourced Converter
ZPM	Zero Power Mode

CHAPTER 1
INTRODUCTION

1.1 Background

According to the *International Renewable Energy Agency*, in order to comply to long-term climate policies, the share of renewable energy in the power sector in the world is expected to increase to 85% by 2050, mostly due to growth in solar and wind power generation [1]. While this is an hypothetical although somewhat realistic scenario, in Europe the expansion of the amount of renewable energy is already bonding for 2030, being 32% the target established by the Clean Energy Package (March, 2019) [2]. In Italy, the number of power-generating units connected to the grid has increased from 3.000 units in 2000 to more than 800.000 units in 2018. More than 99% of them are distributed within the Medium Voltage (MV) and Low Voltage (LV) levels, which in terms of power constitutes around 25% of the total power consumption [3].

One of the main issues of the large deployment of renewable energy resources is due to their unpredictable and intermittent nature, while the balance between generation and consumption must be met at every instant. Therefore, the trend for which renewable resources are being widely installed must entail an equally relevant deployment of Energy Storage Systems (ESSs), not only aiming at ensuring the security and flexibility of the power system, but also to contain the overgeneration of renewable sources that cannot be dispatched and the derived energy curtailment. In Italy, as well as in many parts of Europe and the globe, this is indeed a reality. Excluding traditional pumped hydro storage, by the

end of 2020 more than 36.000 storage units are already installed in Italy, for a total capacity and power of around 267 MWh and 170 MW, respectively. A great portion of the installed ESSs are residential, and practically all of them are combined with PhotoVoltaic (PV) units [4]. For 2023 a necessity of almost 1000 MW of installed ESSs of any kind is expected, while for 2030 such value increases to 1000 GW, in which 40% would correspond to distributed ESSs [5].

The large deployment of Distributed Energy Resources (DERs) above-mentioned has a significant impact on the operation of electrical power systems and constitutes a challenge in many aspects, from the development of business models and the market design to the power system operation itself. Not only the distributed nature of these resources rises complications, but most types of DERs (e.g., PV units, batteries, fuel cells, most wind turbines, etc.) are electronically interfaced to the grid, through power converters that behave completely different to traditional power plants. In consequence, the traditional way of dealing with the main issues regarding the secure operation of distribution networks is evolving, in terms of protection strategies, and frequency and voltage control. These are the two subjects that are dealt with in this thesis. Other relevant issues include the increase of power losses at the distribution level in some scenarios, deterioration of the power quality e.g., due to harmonic distortion, the voltage rise effect, network congestion and dispatchment, and are deliberately not addressed.

In particular, concerning protection methods, relevant strategies must take into consideration that one of the solutions to overcome some of the above-mentioned issues raised by the growing installation of DERs is that open ring configurations, typically used in urban power distribution systems at LV and MV levels, are being replaced by loop and, more in general, meshed network configurations. This results in tangible advantages in terms of hosting capacity, power quality, operation flexibility, voltage control and reduction of power losses and of maintenance efforts. Adversely, other than the presence of DERs, the meshing of distribution networks also alters the protection system logic, prejudicing its sensitivity and selectivity by altering the short circuit currents and their unidirectionality. For this reason, various international standards contemplate a fast disconnection of DERs when a fault occurs in order to ensure the correct operation of currently installed protection systems. However, this practice is inconvenient since it disconnects an amount of generation, that is becoming larger as more DER units are installed, precisely when the system is more vulnerable and propense to instability. Moreover, the intentional islanding operation of portions of the network gets compromised, thus preventing the possible benefits of islanding in terms of supply continuity.

If the network is provided with a fast and reliable protection system that allows DERs to remain connected to the grid, a number of advantages can be derived. In this context, MicroGrids (MGs) constitute an important concept that facilitates the integration of DERs while increasing the reliability of power supply and the resilience of the power system. Moreover, the concept of Multi-Microgrids (MMGs) introduces the possibility of managing several MGs together with DER units connected

directly to the MV network, thus under such paradigm, portions of MV network might operate in the future as autonomous systems, e.g., during maintenance or fault clearances and system restoration.

Within this context, the control strategies of MGs and of the DERs connected to it, must guarantee the reliable operation of the system, i.e., guarantee the power balance while achieving an optimal economic dispatch and ensuring stability, even under harmful conditions, such as faults and transitions between grid-connected and standalone modes of operation.

The problem of maintaining the stability in MGs is mainly caused by the low-inertia level of the system, leading to large and fast frequency and voltage variations when power imbalances and electrical faults occur. Indeed, as already mentioned, most types of DERs are connected to the grid through power converters that do not inherently contribute to the system inertia. Typical models used in conventional power systems might be therefore no longer representative and accurate enough for the study of MGs [6]. In low-inertia MGs, the influence of the dynamic response of loads might be of great significance for the stability of the system. Indeed, as the frequency and voltage change during a transient, the load consumptions will also vary, thus influencing the DERs response and the overall MG dynamics. Therefore, the importance of appropriate load modelling for the analysis of the MG transient response is worth of discussion. Also, the impact of the load composition is worth of analysis, particularly in those conditions in which the system is prone to instability, e.g., when a fault occurs in a standalone MG or during their islanding transition.

1.2 Aim of the thesis

This thesis deals with two of the above-mentioned technical issues relevant to the integration of DERs in distribution networks and MGs: protection against faults and stability in islanded conditions.

Regarding the first protection against faults, the main objective is the development of a transient-based algorithm for the protection of distribution networks against electrical faults. The milestones are the following:

- Develop a protection system against earth faults: since single phase-to-earth faults constitute the great majority of electrical faults in distribution networks, the algorithm development is focused on this type of faults.
- Assess the protection system performance for distribution networks with different topologies: unearthed and compensated neutral grounding methods are very diffused in MV networks around the world, particularly in Europe and in Italy, for their advantages in terms of small single phase-to-ground currents and the possibility of keeping the system in operation. Therefore, the proposed protection algorithm is assessed in these two types of network.

The protection algorithm is assessed in typical distribution networks operated radially. Moreover, due to the above-mentioned trend to mesh distribution networks, the algorithm is extended and assessed also for these configurations.

The analysis of different network topologies on the protection performance aims at assessing the robustness of the proposed algorithm and at individuating the conditions in which it could mis-operate and to implement proper countermeasures.

- Address the impact of DER units on the protection algorithm in terms of the protection performance.
- Illustrate the applicability of the protection system: demonstrate that the algorithm can perform all the required processing in operational times through real-time simulations.

Regarding the MG stability in islanded conditions, the main objective of the thesis is to assess the influence of load modelling and load composition on the transient stability of MV-MGs. The milestones are the following:

- Assess the influence of load modelling on the outcome of transient stability simulations: the studied scenario is the islanding transition of a MV-MG initiated by the opening of the Circuit Breaker (CB) after a fault occurs in the main power system. The most common approaches of modelling conventional loads are considered, and two different types of MGs: with and without synchronous-based energy resources.
- Assess the influence of the load composition on the transient stability of the MG: based on the conclusions attained in the previous point a proper load modelling is chosen. The studied scenarios are two: the islanding transition of the MG and the disturbance caused by a fault in a standalone MG. The stability is appraised in terms of minimum values of frequency and voltage reached.

  Controllable loads are an important feature of MGs, for which their influence is also addressed, and their relevance in the participation in the frequency and voltage control is discussed.

  The influence of the load composition is assessed in two steps: a sensitivity analysis is carried out in a simplified system to evaluate the impact of several parameters inherent to each load and to the control strategies of both DERs and controllable loads; to verify the results obtained in the sensitivity analysis and to include the interaction between all the considered types of loads and DERs, the analysis is extended to a realistic distribution network in which multiple classes of loads with different load components are included.
- Validate the obtained results through real-time simulations.

1.3 Structure of the thesis

Besides the Introduction, the thesis is composed by 5 more chapters organized in the following manner:

Chapter 2 briefly summarizes the typical disturbances that can occur in a power system. Thereafter, it presents a literature review of the ground fault protection methods implemented in distribution systems in which steady state and transient-based are the most diffused.

Chapter 3 presents an algorithm proposed for the protection of distribution networks against single phase-to-earth faults. First, the algorithm is tested in radial networks with both unearthed and compensated neutrals. The influence of some parameters inherent to both the fault, e.g., the fault resistance, and to the protection system, e.g., the sampling frequency is then illustrated. The performance of the algorithm in scenarios in which it is recognized that traditional protection schemes might mis-operate is addressed too. The investigation relevant to radial networks is concluded with a Monte Carlo analysis that validates the effectiveness of the protection system. Then, the algorithm is assessed in meshed distribution networks with the neutral unearthed. Since a communication network is needed in this case, a review of the requirements for its implementation in smart grids is accomplished. Moreover, a co-simulation environment that interfaces Matlab and EMTP-RV is developed and introduced. For this case too, the influence of several parameters is illustrated and a Monte Carlo analysis for different networks with diverse characteristics is carried out. Finally, the protection system applicability is validated through the performance analysis of real-time simulations.

Chapter 4 briefly introduces the control architectures of Active Distribution Networks (ADNs) as well as the notion of Distribution Management System (DMS) and its role in modern distribution networks involving DERs and MGs. It presents an overview of the state of the art regarding the control strategies of DERs in distribution networks and MGs, along with a general schematization of the operational strategies implemented in the power converters of distributed resources.

Chapter 5 is dedicated to the study of the influence of load dynamics on the stability of MGs. First, the influence of load modelling is assessed, from which the necessity of representing the dynamics of rotating loads is derived. Second, the influence of the load composition of a MG is studied in two scenarios: during islanding transition and when a fault occurs in an islanded system. The composition of the MG is thoroughly described, from the loads to the distributed resources, i.e., the general schematization performed in the previous chapter is addressed in detail for each component of the MG. An overall view of the MG behavior during these transients for diverse load compositions is obtained through the identification of relevant load parameters affecting the MG stability, assessed in terms of minimum frequency and voltage reached during the transient events analyzed. Finally, the results obtained through Power-Hardware-In-The-Loop (PHIL) simulations are presented and discussed.

Chapter 6 summarizes and discusses the main results of the thesis, providing an outlook of possible paths for future work.

Moreover, Appendix A presents an overview of general concepts relative to typical components of traditional distribution networks and MGs. It illustrates the dynamic models used to represent the components that constitute a distribution network, namely lines, transformers, loads, power converters and DERs. Focus is given to the components and models employed in the thesis, but an outline of other technologies not implemented here, but that relate to modern distribution networks, is also provided. Finally, Appendix B presents the main space-vector transformations used in this thesis, namely the Clarke and Park transformations.

CHAPTER 2

PROTECTION STRATEGIES IN DISTRIBUTION NETWORKS

A brief review of the system disturbances is presented, with particular attention to single phase-to-ground faults, which are the object of analysis of the next chapter.

A literature review of the relevant protection algorithms implemented in distribution networks is presented too, in which steady state and transient-based are the most diffused.

2.1 System disturbances

A fault in the power system is any failure that interferes with the normal flow of power. The fault analysis is important for many reasons: i) to determine the rating of interrupting devices such as CBs; ii) to adjust the protection system settings; iii) to plan the expansion of the network; iv) to assess network reconfiguration actions during operation, among others. For the sake of fault analysis, the symmetrical components method is normally applied. The symmetrical networks for each type of fault are reported in the following, with particular attention to the single line-to-ground faults which are the main object of the contributions given in this thesis.

Short circuits are caused by any accidental contact between two points that are in normal conditions at different voltage and constitute the most common type of faults in power systems. Besides short circuits, the opening of one or two phases leads also to a faulty condition. This type of faults, known as

longitudinal or series faults, may occur e.g., as a result of snapped line conductors, failure at cable joints, incorrect operation of CBs, etc.

Short circuits may be solid or welded, in which the fault impedance is very low. They may involve an arc, which may or may not extinguish itself. In this case the fault impedance depends on such arc. Finally, they may involve a high impedance path, e.g., a tree or a cement structure. Short circuits can be classified into three-phase faults, which may or may not involve the ground, single line-to-ground faults, line-to-line faults and double line-to-ground faults. Only three-phase faults are balanced (symmetrical) type of faults, whether all the others lead to an imbalance between the phases, i.e., are unbalanced (unsymmetrical) type of faults.

The different types of short circuits are summarized in the following, and their sequence networks are illustrated. For such a purpose it is considered that the pre-fault positive-, negative- and zero-sequence voltages[1] at the point of fault are equal to $v^{(+-0)}$; the relative equivalent impedances are $z^{(+-0)}$; and the fault impedance is z_F.

2.1.1 Three-phase faults

Three-phase faults usually result in the largest fault currents, although they represent merely a 5% of the faults [7], being the rarest. If the system is balanced before the fault occurs, it remains symmetrical also after the fault.

The circuital representation and the sequence network are shown in Figure 2.1. If the three-phase fault does not involve the ground, then the zero-sequence network is absent.

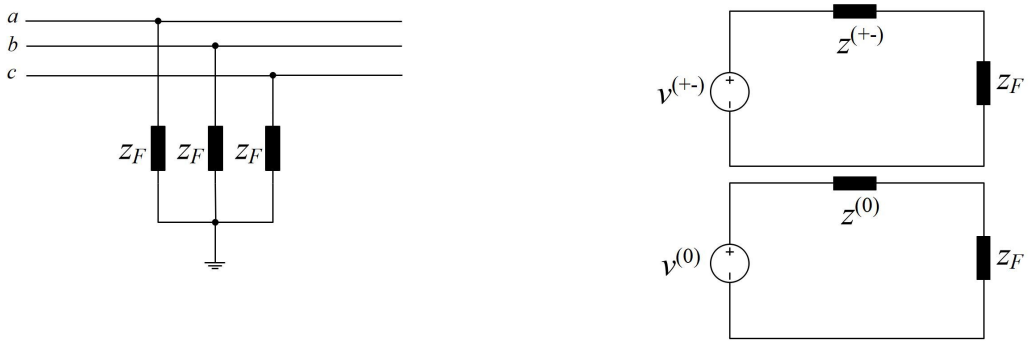

(a) (b)

Figure 2.1 – Three-phase fault. (a) Circuital representation and (b) sequence network.

[1] Normally, only the positive-sequence pre-fault voltage is considered. However, for a more general formulation, also the negative and zero-sequence voltages are represented in the sequence networks, which rise due to current or voltage unbalances between phases.

2.1.2 Single line-to-ground faults

They constitute about 70 – 80 % of transmission line faults [7] and the majority in industrial and commercial power systems [8]. They occur e.g., due to lightning or when a phase conductor comes in contact with a grounded element, such as a tree or a building structure, or insulation break.

The circuital representation and the sequence network are shown in Figure 2.2.

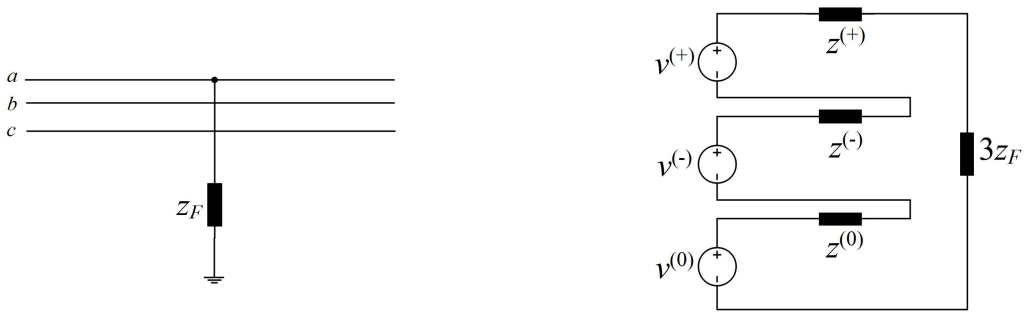

(a) (b)

Figure 2.2 – Single line-to-ground fault. (a) Circuital representation and (b) sequence network.

As known, the magnitude of the current under fault conditions depends on the fault impedance but also on the return path impedance, i.e., on the grounding method.

Typical grounding methods for MV networks can be summarized as: i) isolated neutral; ii) solid grounding, which can be uni- or multi-grounded; iii) grounded through an impedance, which can be a low or high impedance, or through a Petersen coil in which case it is called resonant or compensated grounding.

With respect to other grounding methods (except for the high impedance one which has similar characteristics as the isolated neutral), the advantages of isolated and compensated neutral can be found in the possibility of maintaining the service uninterrupted even with a permanent ground fault; the increased possibility of a self-extinction of the fault; the low equipment thermal stress because of the very low values of fault current. On the contrary, the main drawbacks are the high insulation level required because of the overvoltages that the system may experience during the fault, and the relatively low protection sensitivity.

2.1.3 Line-to-line fault

Usually, this type of fault results in the lowest fault current. The circuital representation and the sequence network are shown in Figure 2.3. The zero-sequence network remains inactive.

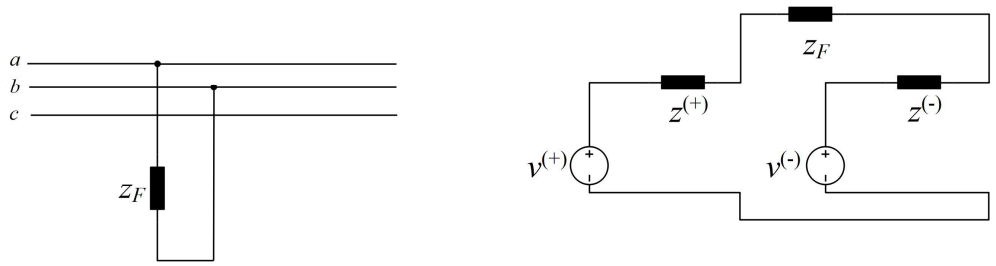

(a) (b)

Figure 2.3 – Line-to-line fault. (a) Circuital representation and (b) sequence network.

2.1.4 Double line-to-ground fault

This type of fault is quite frequently, resulting in some cases as an evolution of the single phase-to-ground fault, as will be described below.

The circuital representation and the sequence network are shown in Figure 2.4.

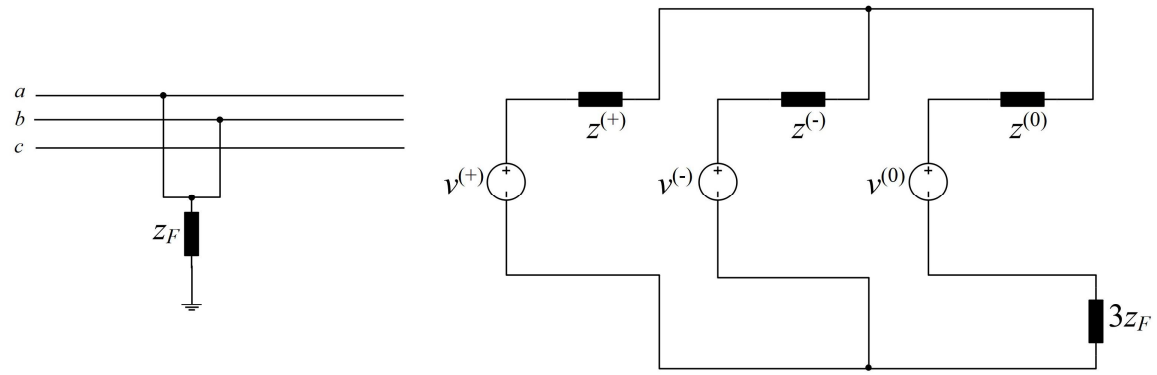

(a) (b)

Figure 2.4 – Double line-to-ground fault. (a) Circuital representation and (b) sequence network.

2.1.5 Cross country faults

When a single line-to-ground occurs in a network with isolated or compensated neutral, temporary overvoltages arise in the healthy phases due to the Ferranti effect provoked by the predominantly capacitive current flowing through the lines. The study presented in [9] shows that values up to 3.5 pu can be registered in the healthy phases of an isolated neutral network. Such value depends on several factors such as the extension of the lines and the presence of underground cables, and could be minor in compensated neutral networks depending on the level of compensation [10]. These overvoltages could lead to the evolution of the fault into double line-to-ground faults or cross-country faults, i.e., two single line-to-ground faults involving different phases. Cross-country faults occur due to insulation failure at weak points of the healthy phases and may occur at different locations of the same feeder or even at different feeders.

2.2 Protection of Distribution Networks

The five basic characteristics of any electrical protection system are [11]:

- Reliability, which is the "*measure of the degree of certainty that the relay, or relay system, will perform correctly*". It has two facets: dependability, defined as "*the degree of certainty that a relay or relay system will operate correctly*"; and security, which "*relates to the degree of certainty that a relay or relay system will not operate incorrectly*" [12].
- Selectivity, which describes "*the interrelated performance of relays and breakers, and other protective devices*", and refers to the maximum continuity of service with minimum system disconnection.
- Speed, which refers to the fault duration related to equipment damage and system instability. Generally, a faster operation increases the probability of incorrect operation of the protection.
- Simplicity, which refers to the minimum protective equipment and the relative circuitry employed.
- Economics, which refer to the maximum protection performance at the minimal total cost.

All these aspects of the protection system are important and will be addressed when the performance of the proposed protection system is assessed, with particular interest in the first three. Other important characteristics such as availability and redundancy will be disregarded during the analysis but are acknowledged.

2.2.1 Steady state-based algorithms

Most ground-fault protection algorithms use the voltage and current at the utility frequency.

a) Voltage detection method

Earth faults in isolated or compensated neutral lead to the rising of the zero-sequence voltage. Such characteristic could constitute a fault indicator. However, the main drawback of this method is its non-selectivity. Indeed, the zero-sequence voltage reaches nearly the same value in the entire network since the voltage drops in the lines and transformers are very small. Moreover, the voltage change might not be significative when dealing with high-resistance faults.

The voltage detection can be used as starting function of other protection algorithms that are selective, such as directional comparison schemes.

b) Wattmetric and varmetric methods

Traditionally, compensated systems are protected against single phase-to-ground faults by implementing the zero-sequence wattmetric method, while unearthed systems implement the varmetric method [13]. The wattmetric and varmetric methods assess the next quantities, respectively,

$$W = \Re\left[\overline{v}_0 \cdot \overline{i}_0^*\right] \tag{2.1}$$

$$Q = \Im\left[\overline{v}_0 \cdot \overline{i}_0^*\right] \tag{2.2}$$

The operational characteristics are shown in Figure 2.5. A combination of both methods yields the directional element (ANSI 67N) [14].

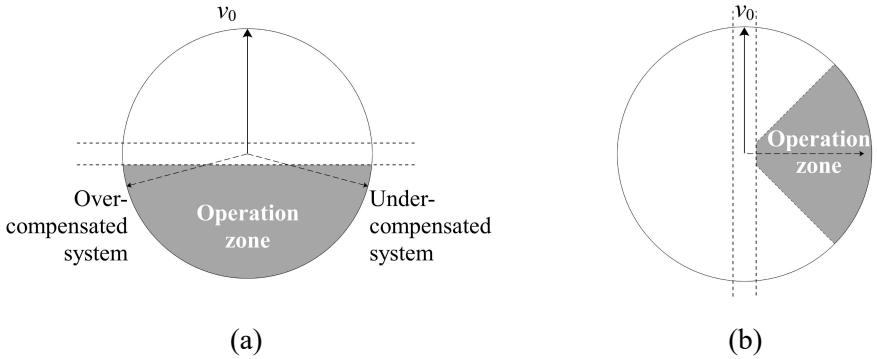

(a) (b)

Figure 2.5 – Typical (a) wattmetric and (b) varmetric operating characteristic in compensated and unearthed networks respectively (Adapted from [13]).

The main issue regarding these methods is the low sensitivity due to the intrinsic low values of fault current, specially at the utility frequency[1]. It is also sensitive to the Current Transformer (CT) accuracy.

c) Impedance and admittance methods

Neutral admittance protection is based on the assessment of the ratio between the zero-sequence current and the zero-sequence voltage or vice versa, i.e., the assessment of the zero-sequence admittance or impedance.

In order to deal with the negative effects that the asymmetry of the network and the fault resistance have on the proper operation of protection algorithms based on the neutral admittance, the incremental admittance method is implemented [15]. It consists of the assessment of the ratio between the zero-sequence current and voltage changes with respect to the pre-fault condition.

While the incremental admittance method is recommended for compensated networks, the impedance method is recommended for unearthed ones [13]. Some typical characteristics of such protection methods are reported in Figure 2.6.

[1] As will be further illustrated, during transients and for a wide range of fault resistances, the current reaches significantly higher values than in steady state.

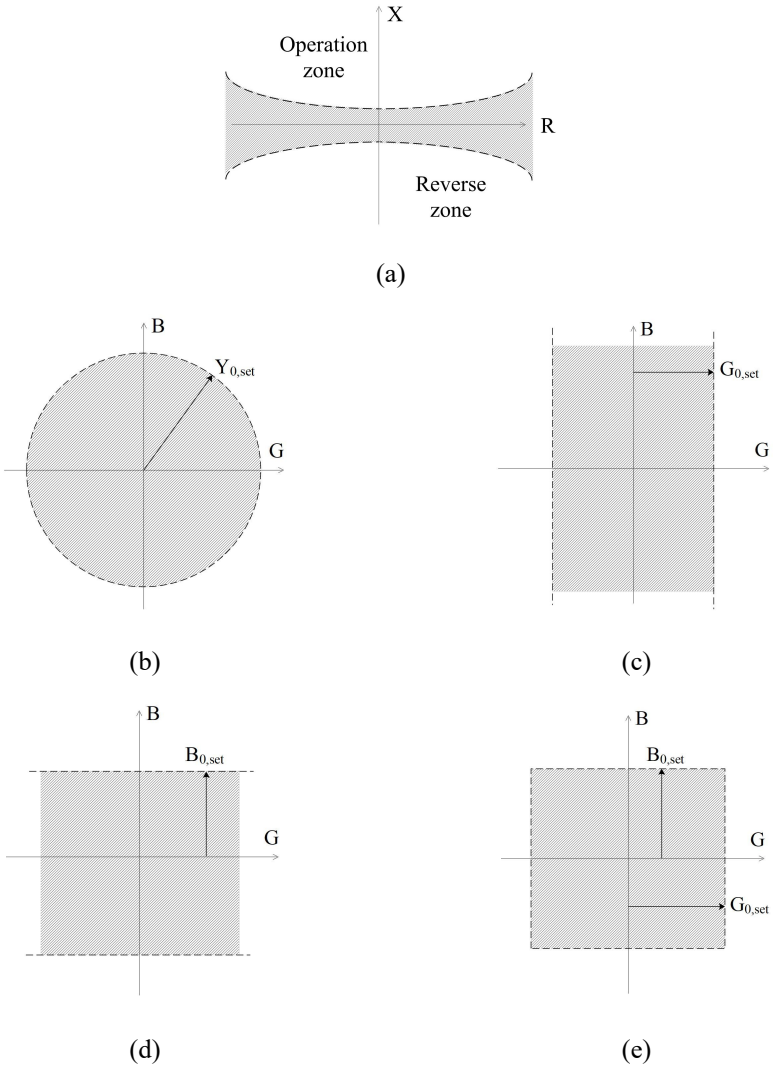

Figure 2.6 – (a) Neutral impedance-based operating characteristic and neutral admittance-based operating characteristic for: (b) over-admittance; (c) over-conductance; (d) over-susceptance and; (e) combination of the latter two (Adapted from [13], [15]).

2.2.2 Transient-based algorithms

With the developments of modern electronics, transient signals can be easily recorded and processed with relatively high sampling frequencies, allowing transient-based protective methods to be considered a promising and efficient solution, particularly for unearthed and compensated networks since they are more sensitive than steady state-based algorithms and they are not significantly affected either by the level of compensation of the neutral or by the fault characteristics [16]–[18]. Furthermore, transient-based algorithms allow, in general, for a prompt operation. This is an important aspect especially in unearthed MV networks as an earth fault may lead to considerable overvoltages in the sound phase conductors. The overvoltages may cause a subsequent line-to-line fault or an earth fault in a different phase, as described in Section 2.1.5. In [19], e.g., an average time of 160 ms was observed before the earth fault evolves in both unearthed and compensated networks. Another requirement for a prompt relay operation is due to the presence of Distributed Generation (DG), since connection rules may

require that generating units stop feeding the faulty area within a limited time interval, for instance 160 ms as reported in [20]. Another advantage of transient-based algorithms is that they can be implemented for intermittent arc earthed faults.

a) Charge-voltage curves

The algorithms presented in [21], [22] evaluate the relation between the zero-sequence voltage and the zero-sequence charge, estimated as the integral of the zero-sequence current over time. In [21] the faulty feeder is identified by analyzing the shape of the charge-voltage curves over time and using a least squares and pattern recognition algorithms. While for the healthy feeders the relation between charge and voltage over time reproduces a straight line since the charge is practically proportional to the voltage, for the faulty feeder this is no longer valid. The algorithm presented in [22] establishes a numerical criterion of the above-mentioned behavior. The charge-voltage relation is approximated by a linear function based on least squares and the sum of the square of the deviations is computed. The faulty feeder is identified as the one with the largest value.

b) Energy estimation

The algorithm presented in [23] estimates the zero-sequence active energy flowing through each feeder after the fault inception and during the transient. During the transient the energy flow measured at the faulty feeder is negative due to the discharge of the capacitance of the faulty phase. At the healthy feeders instead, the energy flow is positive due to the charging of its phase capacitances.

c) Zero-sequence angle

The algorithm presented in [24] estimates the power angle from the calculation of the active and reactive power flowing through the feeders. The angle is calculated only if the magnitude of the complex power is greater than a threshold value, otherwise it is set to 0. All the estimated angles for all feeders are compared among them, and the one with the greater value determines the faulty feeder. In order to enhance the security of the algorithm, the selected feeder angle must be greater than a threshold value.

Since the angle is estimated at each time step, the algorithm outputs a decision at each time step, and no indication is given in [24] on the time interval in which the decision of operation must be taken. Indeed, there are time intervals on which the algorithm does not select any feeder as the faulty one.

d) Multi frequency neutral admittance

In the algorithm presented in [25], [26] a sum admittance phasor is used, defined as,

$$\overline{Y}_{0,sum} = \Re\left[\overline{Y}_0^1\right] + j \cdot \Im\left[\sum_{n=1}^{m} \overline{Y}_0^n\right] \tag{2.3}$$

where $\overline{Y}_0^1$ and $\overline{Y}_0^n$ are the fundamental frequency and n-th harmonic neutral admittance phasors, respectively, and m is the harmonic order considered in the algorithm.

The fundamental and harmonic admittance phasors are calculated from the respective fundamental and harmonic zero-sequence voltage and current values, which are supposed to be provided by the relay. Then, a Cumulative Phasor Summing process is implemented for which the resulting $\overline{Y}_{0,sum}$ at each time interval is cumulated through a determined time window, i.e.,

$$Y_{0,sum}^{CPS} = \sum_{t_i=t_{st}}^{t_{end}} \overline{Y}_{0,sum}(t_i) \tag{2.4}$$

An operating area defines if the fault is forward or reverse.

e) Impedance estimation

In [27] the average zero-sequence impedance is estimated from the average zero-sequence voltage and current values over a suitable time window. Mathematically,

$$Z_0 = \frac{\sum_{k=1}^{N} v_{0,k}}{\sum_{k=1}^{N} i_{0,k}} \tag{2.5}$$

where $v_{0,k}$ and $i_{0,k}$ are the instantaneous zero-sequence voltage and current k-th samples, and N is the number of samples in the time window. The time window is selected to cover the first cycle of the transient zero-sequence current.

According to [27] the polarity of the impedance is negative for the faulty feeder. Moreover its amplitude is lower since for the faulty feeder (2.5) represents the capacitive impedance of the whole background network, while for the healthy feeder it represents the capacitive impedance of the feeder itself.

f) Capacitance estimation

A variation of the previous algorithm is presented in [28]. As already stated (2.5) represents the capacitive impedance, either of the background network or of the feeder at which it is measured. Indeed, the capacitance can be derived as,

$$C = \frac{1}{2\pi \cdot f_{dom} \cdot Z_0} \tag{2.6}$$

where f_{dom} is the dominant transient frequency, obtained from the Discrete Fourier Transform (DFT) computation of i_0 and corresponding to the greatest magnitude. The calculated capacitance (scaled with respect to the total network capacitance) constitutes an indication on the directionality of the fault.

It is noticed that (2.6) is obtained by neglecting the network longitudinal impedances. At the fundamental frequency, this assumption is reasonable, since longitudinal impedances are negligible compared to the impedance of earth capacitances. However, at higher frequencies such as transient

frequencies, these impedances become meaningful. To deal with these errors a compensation factor is proposed in [29].

Moreover, (2.6) does not consider the presence of the Petersen coil in the case of compensated networks. Since the Petersen coil is transversal, the error introduced by such exclusion is larger for low frequencies, on the contrary of what happens for the longitudinal impedances. Therefore, transient signals are almost immune to the effect of the Petersen coil [30], as will be further verified in Section 3.1.1. Nevertheless, another compensation factor is proposed to deal with these errors.

In [17] some of the scenarios in which transient-based protection schemes are prone to fail are reported and include: i) asymmetrical networks; ii) 0° inception angle (i.e. the fault occurs when the faulted phase voltage is 0); iii) hybrid networks composed of overhead and underground cable lines. These scenarios will be thoroughly analyzed in Section 3.1.2.

2.2.3 Other types

Current injection-based methods, as the one presented in [31], consist in injecting a pulsating current in the network after the fault is detected. The principle is that the signal injection causes a change in the measured current just in the path of the fault, i.e., it is detected only by the measurement devices at the faulty feeder. These methods may vary in the type of signal used (e.g., sinusoidal, DC, pulse), point of signal injection (e.g. faulted phase through a voltage transformer, Petersen coil) and devices employed for the signal detection [32]. The main drawback is that an additional device is required, namely the injecting equipment, which increases the system complexity and costs. Moreover, these methods change the fault signals, which could cause the mis-operation of other devices installed in the network [30].

Travelling wave-based methods use the impulses generated at the fault location. The methods to identify the faulty feeder vary. In [33] the fact that the initial current impulse at the faulty feeder has opposite polarity with respect to the initial voltage impulse is mentioned. Another method compares the current amplitudes and polarities of all feeders at the primary substation [34]. Travelling wave-based methods are typically coupled with the implementation of discrete wave analysis to detect the moment in which the travelling wave appears [34] and for fault location purposes [35]. The main challenges regard the many reflections that come from several branches that typically are present in the distribution network, and the rather high sampling frequency required to capture the travelling waves.

Other methods include artificial intelligence, some of which can be found in [17], [36].

This Chapter has summarized the typical disturbances that can occur in a power system, namely three-phase, single-line-to-ground, line-to-line and double-line-to-ground short circuits, as well as the

evolution of single-line-to-ground faults into cross country faults. Thereafter, a literature review of the ground fault protection methods implemented in distribution systems has been presented. Since the steady state and transient-based protection methods are the most diffused, particular attention has been given to such techniques.

CHAPTER 3

A NEW TRANSIENT-BASED PROTECTION ALGORITHM

A new transient-based protection algorithm is developed in which the angle between the zero-sequence voltage and current phasors determines the directionality of the fault. The phasors are estimated at the dominant frequency of the network transient-response within the first milliseconds after the fault.

It is briefly recalled that when a single-phase-to-earth fault occurs in an unearthed or compensated neutral network, the transient that arises can be interpreted as composed by two components: a discharge component due to the lowering of the faulty phase voltage and a charge component due to the rising of the sound phases voltages [28]. The frequencies of these two transient components vary in different ranges and have different amplitudes. Following [27]–[29], that constitute the basis of the proposed protection algorithm, the charging component is adopted, corresponding to the higher amplitude and the lower frequency with respect to the discharging one.

In the following, the protection algorithm is introduced, and its performance is assessed in both radial and meshed distribution networks.

3.1 Radial networks

The network studied in [28] has been reproduced in EMTP-RV with some minor modifications and is shown in Figure 3.1a. It is a 20kV MV distribution network comprising 5 feeders. Relays are installed

at the beginning of all feeders and acquire both voltage and current signals. In practice, voltage is measured only at the bus bar, while current is measured for each feeder by using e.g., a core balance CT. The network is composed by only overhead lines with the configuration of Figure 3.1b and represented with a Frequency Dependent (FD) line model. The resulting main electrical parameters are reported in Table 3-1. The secondary of the HV/MV (HV, High Voltage) transformer has the neutral either unearthed or compensated, depending on the study case. The adopted models of all these components and those introduced hereinafter are reported in Appendix B.

For the studied network, in [28] it is reported that the transient frequencies of interest vary in the range of 100–800 Hz.

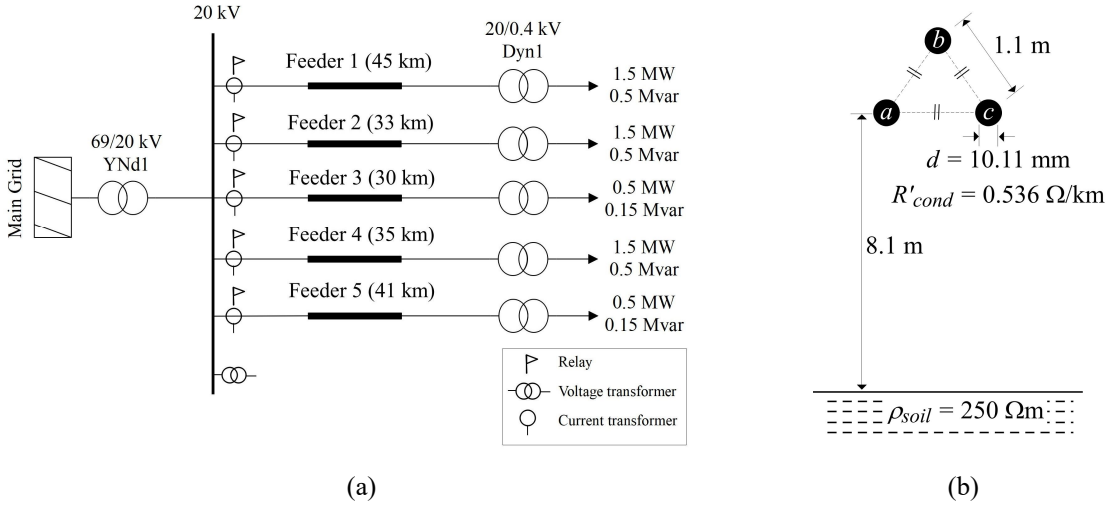

Figure 3.1 – (a) Studied network and (b) line configuration.

TABLE 3-1
OVERHEAD LINE PARAMETERS (ESTIMATED AT 811.3 HZ)

	***r'* (Ω/km)**	***l'* (mH/km)**	***c'* (nF/km)**
Positive	0.57425	1.1245	10.340
Zero	2.8612	4.6282	4.1048

3.1.1 Theoretical background

A fault is considered in feeder 5 with a resistance R_F. The circuital representation of the zero-sequence current is shown in Figure 3.2, in which the impedance relative to the grounding method has been represented as Z_N. The analysis for both unearthed and compensated networks is done in the following.

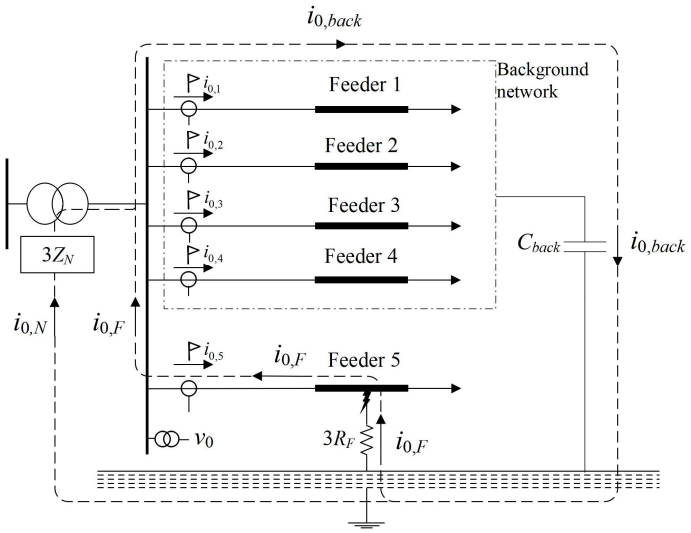

Figure 3.2 – Circuital representation of the zero-sequence current for a single phase-to-ground fault in a radial network.

a) Unearthed network

When the neutral is unearthed $Z_N = \infty$ (capacitive coupling of the transformer to ground is disregarded) and $i_{0,F} = i_{0,back}$. Assuming that the longitudinal impedances of all feeders, the impedance of the transformer and the fault resistance are negligible compared to the network capacitance, the current is entirely capacitive. The vector diagram of Figure 3.3a is obtained for the zero-sequence components of voltage and current.

The polarity of the current measured by relays is assumed positive if it goes from the bus into the line. Therefore, the direction of the fault current ($i_{0,F}$) assumed positive in the circuit of Figure 3.2 is in phase opposition to the current measured by the relay at the faulty feeder ($i_{0,5}$) and in-phase with the currents measured by the relays at the healthy ones ($i_{0,1\text{-}4}$). With these considerations, the angle θ between v_0 and i_0, measured from v_0 in anticlockwise direction, is 270° for the faulty feeder and 90° for the healthy ones.

Whether it is reasonable to neglect the longitudinal impedances of the network, since they are very small compared to the earth capacitances of the feeders, this assumption introduces some errors. Indeed, if a longitudinal inductive reactance X_L and resistance R are considered, the vector diagram becomes the one of Figure 3.3b, in which R_{back} and $X_{L,back}$ are the equivalent resistance and inductive reactance of the background network. The effect of R_{back} is deliberately overemphasized for illustrative purposes. Moreover, also R_F causes such effect on the current. It is noticed that the angles of $i_{0,1\text{-}4}$ might not be equal, but they depend mainly on the feeder impedances (e.g., if one feeder is more resistive than the others, the resistive component of its current is relatively larger). Nevertheless, their sum is always the opposite of $i_{0,5}$, thus the directionality of the fault is evident from the assessment of the phase displacement between v_0 and i_0.

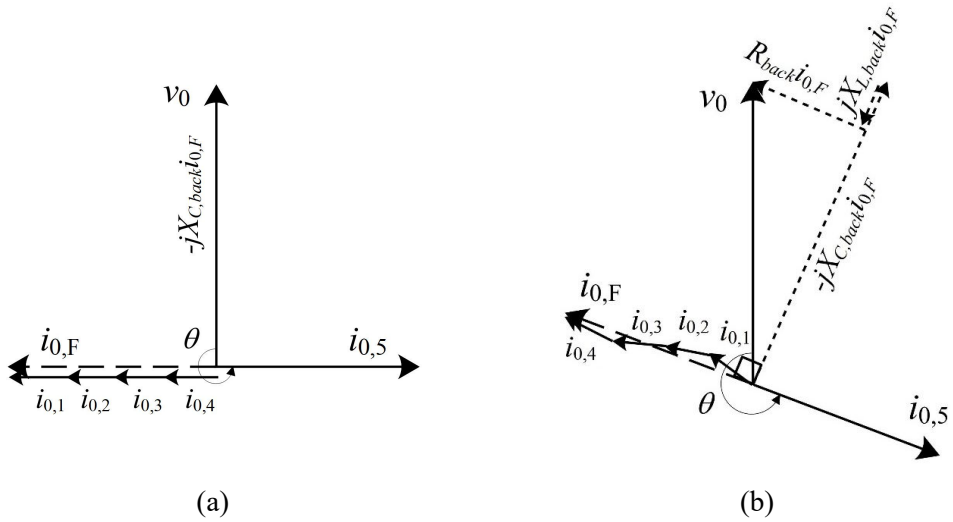

Figure 3.3 – Vectorial diagram of the zero-sequence quantities for an unearthed network, (a) neglecting and (b) considering resistances and inductances.

This characteristic is exploited in the proposed protection algorithm, for which an operation zone determined by θ_{min} and θ_{max} is selected, as schematized in Figure 3.4. If the estimated angle θ is within the operation zone, the algorithm declares the relative feeder as faulty.

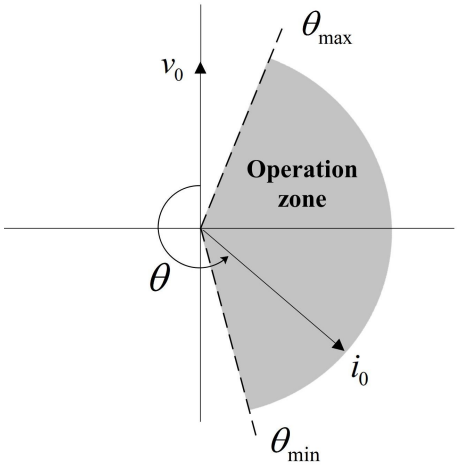

Figure 3.4 – Operation zone for faulty feeder identification [37].

b) Compensated network

When a compensated neutral is considered, a variable coil of reactance X_R in parallel to a resistor R_R is connected to the neutral of the network, as illustrated in Figure 3.5. If the LV-side of the substation transformer is wye, the star point can be directly connected to the resonant grounding; otherwise, if the LV-side is delta, the resonant grounding must be connected through a grounding transformer at the substation busbar. In both cases, the estimation of X_R is carried out without considering the resistor R_R, and results in,

$$X_R = X_N - \frac{X_{TR,0}}{3} \tag{3.1}$$

where $R_{TR,0}$ and $X_{TR,0}$ are respectively the zero-sequence resistance and reactance of the HV/MV transformer in the first case, and of the grounding transformer in the second case; $3X_N$ is the zero-sequence neutral reactance at the substation.

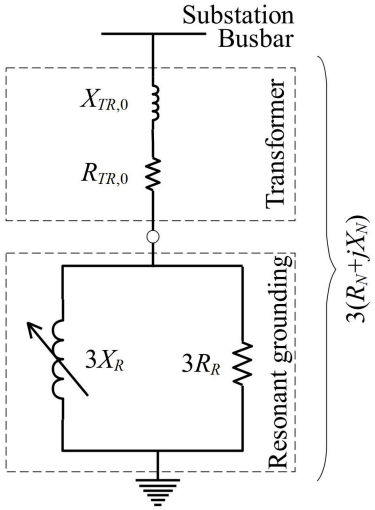

Figure 3.5 – Zero-sequence circuit of the earthing arrangement in a compensated network. The transformer can be either the main HV/MV substation transformer or the grounding one.

The grade of compensation k is defined as,

$$k = \frac{X_C}{3X_N} \tag{3.2}$$

where X_C is the capacitive reactance to ground of the entire network ($1/\omega C_0$).

From (3.1) and (3.2), the resonant grounding reactance in function of the compensation degree is,

$$X_R = \frac{1}{3}\left(\frac{X_C}{k} - X_{TR,0}\right) \tag{3.3}$$

Since the LV-side of the HV/MV transformer in the studied network is delta-connected, a grounding transformer is implemented. Based on the data reported in Table 3-1 and considering that the network is 184 km long, X_C is equal to 4.21 kΩ, corresponding to 755.1 nF and a capacitive current of 8.21 A. The main parameters of the compensated neutral arrangement are summarized in Table 3-2 with typical values of $R_{TR,0}$, $X_{TR,0}$ and R_R [38]. Three values of compensation degree are considered, namely 0.95, 1 and 1.05 which correspond to the scenarios of under-compensation, perfect compensation and over-compensation, respectively. The first scenario is the one typically adopted by the Italian Distribution System Operator (DSO) [10], [39].

TABLE 3-2
PARAMETERS OF THE COMPENSATED NEUTRAL ARRANGEMENT

Parameter values			
$R_{TR,0}$	0.3 Ω		
$X_{TR,0}$	2 Ω		
X_C	4.21 kΩ		
R_R	770 Ω		
	k = 0.95	k = 1.00	k = 1.05
X_R (≈X_N)	1.48 kΩ	1.40 kΩ	1.34 kΩ

One of the main advantages of implementing a transient-based algorithm in compensated networks is that the coil presents a high impedance for high frequencies. For this reason, during transients the compensated network behaves similarly to the unearthed network [16], [28], [29]. Indeed, considering a perfectly compensated network, i.e. k = 1, and neglecting $X_{TR,0}$, from (3.3) it is derived,

$$X_R = \frac{X_C}{3} \tag{3.4}$$

This is true at the industrial frequency. Assuming that the dominant transient frequency is m times the industrial frequency, i.e. $f_{dom} = m \cdot f$, the inductive reactance increases m times while the capacitive reactance decreases m times. Therefore, for the considered range of transient frequencies between 100–800 Hz, the capacitive current is 4–256 times the inductive one when the network is perfectly compensated. In consequence, the vectorial diagrams of Figure 3.3 are representative also for compensated networks, even in overcompensation condition.

c) Protection algorithm

Based on the vectorial diagram of Figure 3.3b, the current i_0 in faulty feeders is expected to be in the third quadrant. Considering an appropriate margin, an operation zone in the range 170°–280° is proposed.

An initial version of the protection algorithm is shown in Figure 3.6. As the earth-mode current i_0 could have very low values, particularly for high resistance faults, both current i_0 and the corresponding voltage v_0 are monitored. If one of them exceeds a predefined threshold the algorithm starts the process to identify the faulty feeder. Current and voltage earth modes i_0 and v_0 are estimated from the measurements of the phase quantities during a time window t_{win}. Since the transient duration is affected by the network parameters [17], the time window is chosen for each network depending on the expected range of transient frequencies, as will be further described. The DFT of i_0 is computed to find the dominant transient frequency f_{dom} of the fault-originated transient. The Fast Fourier Transform (FFT) method is used. Finally, the phasors of both i_0 and v_0 at the dominant transient frequency are estimated and the angular displacement θ between the phasors is used to identify the faulty feeder.

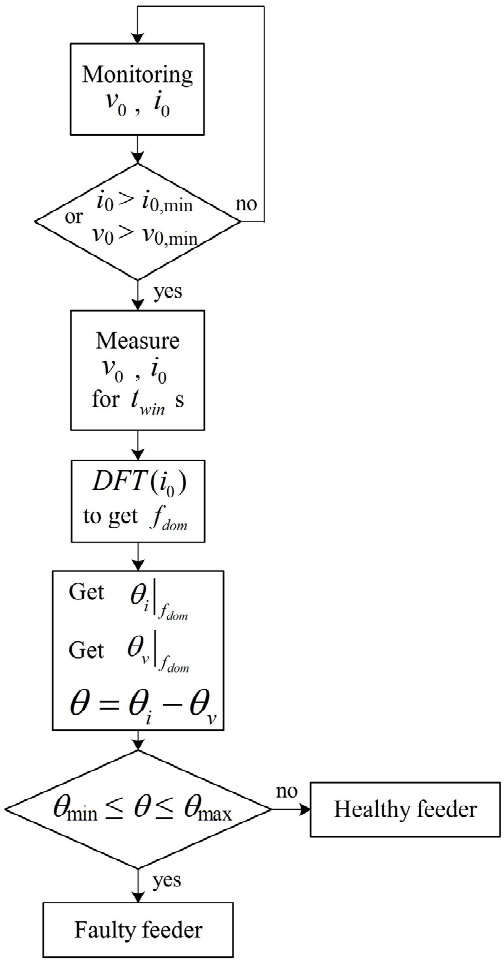

Figure 3.6 – Flowchart of the initial version of the protection algorithm.

The time window is properly selected in order to appraise at least half cycle of the signal corresponding to the minor frequency of the considered range. For this network, a time window of 5 ms is implemented. The DFT of the zero-sequence current signal is calculated over such time window and the component with the higher magnitude is the transient dominant frequency.

In the following some characteristics that must be further implemented in the algorithm are explained.

i) Zero-padding

The frequency step of the DFT is defined as,

$$f_{step} = \frac{f_s}{L} \tag{3.5}$$

where f_s is the sampling frequency and L is the length of the signal, which in turn can be expressed as,

$$L = t_{win} \cdot f_s + 1 \tag{3.6}$$

It can be noticed that f_{step} is practically independent of f_s. Indeed, for a sampling frequency of 100 kHz, L = 501 and f_{step} = 199.6 Hz, while for a sampling frequency of 8 kHz, L = 41 and f_{step} = 195.1 Hz. Considering the range of the frequencies of interest, the value of f_{step} is unacceptably high, since only

four frequency values would be possible in the range 100–800 Hz i.e., the dominant transient frequency can take only the values 195.1, 390.2, 585.3 and 780.4 Hz.

By adding a number of zeros to the analyzed signal, the frequency resolution increases i.e., f_{step} decreases. This technique is known as zero-padding [40]. A common practice is to zero-pad the signal such that it acquires a length which is a power of two, in order to speed up the FFT calculation. In this case the signal is zero-padded to have a length n,

$$n = 2^{P+2} \tag{3.7}$$

where P is the exponent of the next power of two of L i.e., P is an integer number that meets the condition,

$$2^P \geq L \tag{3.8}$$

For the case in which $L = 41$, it results in $P = 6$ since $2^6 = 64$. Then $n = 256$. For such signal length, $f_{step} = 31.25$ Hz, which is a more acceptable frequency resolution. Indeed, 22 frequency values are possible in the range 100–800 Hz i.e., a more accurate determination of the dominant transient frequency is achieved.

The influence of zero-padding in the middle of phase-*a* of Feeder 5 with a fault resistance of 0 Ω is shown in Figure 3.7.

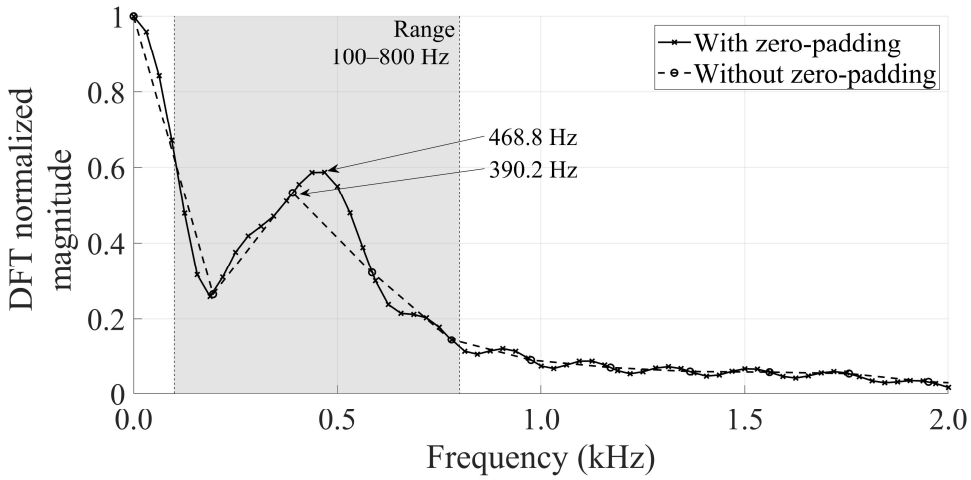

Figure 3.7 – Influence of zero-padding on the DFT computation.

ii) Filtering

One of the main issues with transient-based protection algorithms is that high-resistance faults might damp the transient components of current and voltage, affecting the sensitivity of the relay [13]. In order to assess the protection algorithm performance in this situation, the same fault as before is considered but with a 10 kΩ resistance.

The solid line of Figure 3.8 shows the DFT of $i_{0,5}$. It is difficult to clearly identify the dominant transient frequency. However, it is known that ideally, the fault resistance value does not affect the transient frequency of the signal, but only damps it. Indeed, the frequency response of an RLC circuit is independent of the resistance value and is given by,

$$f_{dom} = \frac{1}{2\pi\sqrt{L_{eq}C_{eq}}} \tag{3.9}$$

where L_{eq} and C_{eq} are the equivalent inductance and capacitance of the circuit, respectively. A filter can be implemented to i_0 before calculating its DFT.

To avoid the phase distortion provoked by the filter a zero-phase filtering can be implemented, achieved by filtering the signal in both forward and reverse directions, such as the *filtfilt* Matlab function does [41].

The dashed line of Figure 3.8 shows the DFT of the filtered signal. Now it is possible to identify the dominant transient frequency of $i_{0,5}$.

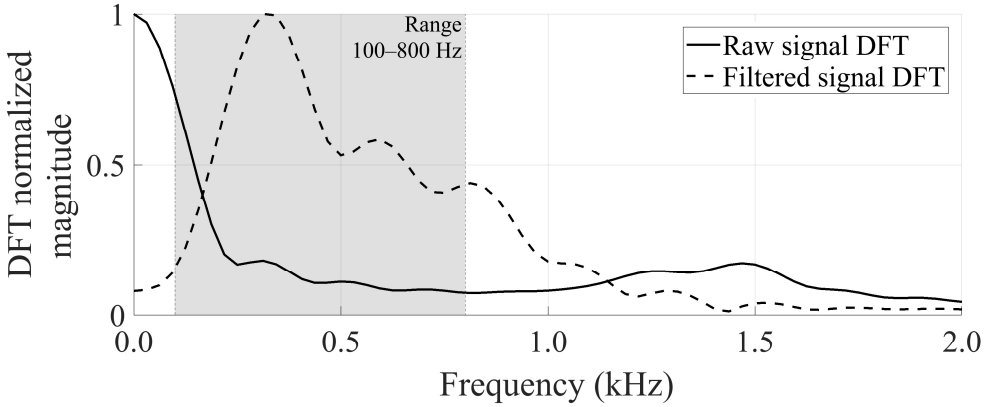

Figure 3.8 – Effect of filtering i_0 on the DFT computation.

With the above considerations, the resulting flowchart of the protection algorithm is illustrated in Figure 3.9.

The protection system parameters are summarized in Table 3-3. Consistently to the frequency range, a digital Butterworth filter centered at f_0 = 450 Hz and with a bandwidth BW = 700 Hz is implemented.

The angles estimated by the protection algorithm for the above cases in both networks unearthed and compensated (k = 0.95) are shown in Figure 3.10. The results agree with the vectorial diagrams of Figure 3.3. As the fault resistance increases, the resistive component of the current is also more relevant.

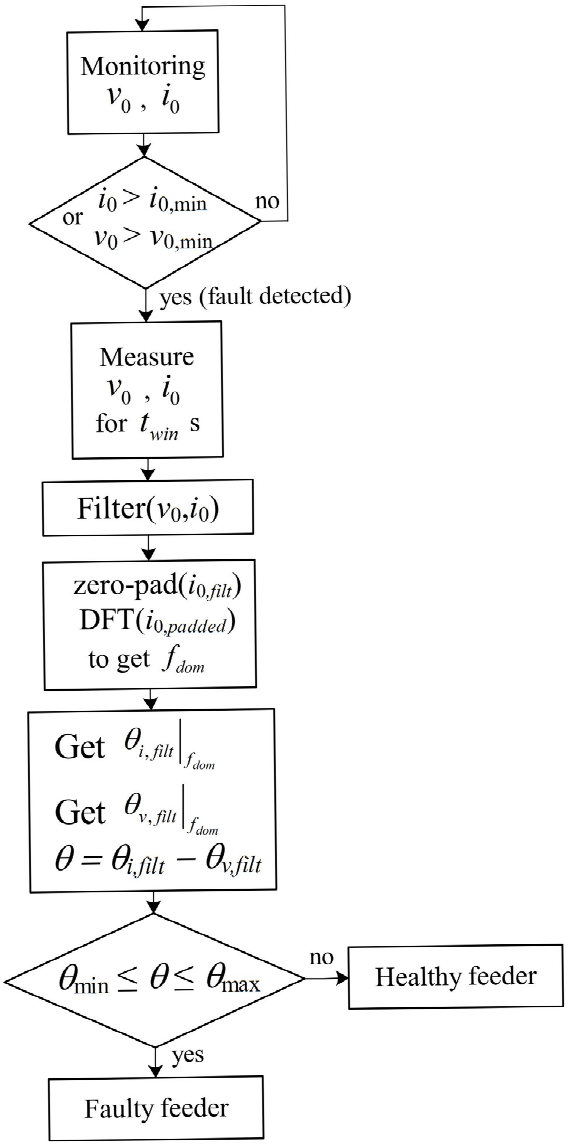

Figure 3.9 – Flowchart of the proposed protection algorithm.

TABLE 3-3
PROTECTION SYSTEM PARAMETERS

Filter f_0/BW (Hz)	450/700 Hz
t_{win} (ms)	5
$v_{0,\min}$ (kV)	1.0 (5% v_{nom})
$i_{0,\min}$ (A)	0.5
$\theta_{\min} - \theta_{\max}$	170° – 280°

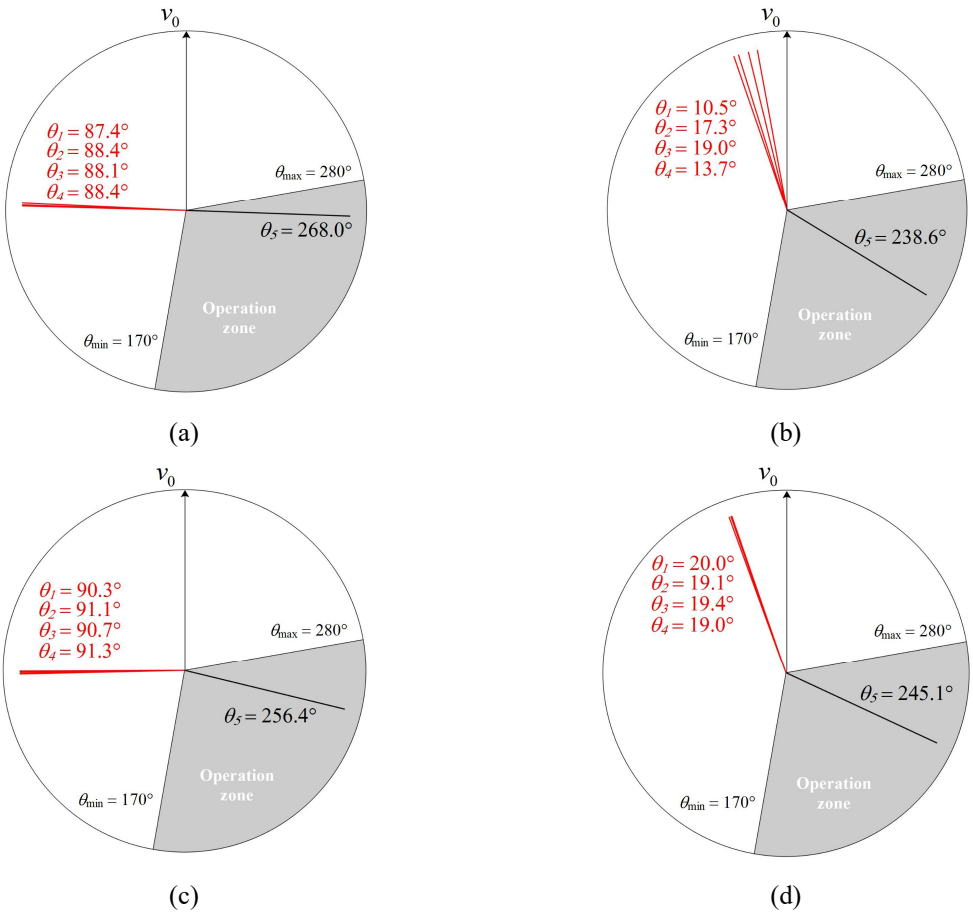

Figure 3.10 – Angles estimated by the protection algorithm for a single phase-to-ground fault when the neutral is unearthed (fault resistance equal to (a) 0 Ω and (b) 10 kΩ) and compensated (fault resistance equal to (c) 0 Ω and (d) 10 kΩ).

3.1.2 Assessment of the protection algorithm

The following analysis illustrates the influence of some parameters inherent to the fault, like the fault resistance, and inherent to the protection system, like the filter and the sampling frequency f_s. The protection system parameters are the same of Table 3-3.

a) Sensitivity analysis

In the following study cases the neutral is unearthed, since it has been shown that the compensated network has a similar behavior during the transient period.

The variation of the angles estimated for different fault resistances is illustrated in Figure 3.11 for the unearthed network. The comparison considers different sampling frequencies and the fault inception time either as known or unknown in both cases.

The comparison shows that the sampling frequency does not considerably affect the estimated angles, due to the zero-padding process. On the other hand, in practical cases the fault time is unknown, and this causes a larger angle variation, particularly at high fault resistances due to different protection triggering mechanism, e.g., for feeder 1 and $R_f \leq 5.75$ kΩ, the current threshold is activated, while for

R_f > 5.75 kΩ the voltage threshold is activated, leading to a more delayed fault detection. This effect is further illustrated in Figure 3.12 which shows the influence of $i_{0,min}$ on the angle estimation. By decreasing $i_{0,min}$, the estimated angle values approach the case in which the fault time is known. Adversely, the relay may pick up in no-fault conditions.

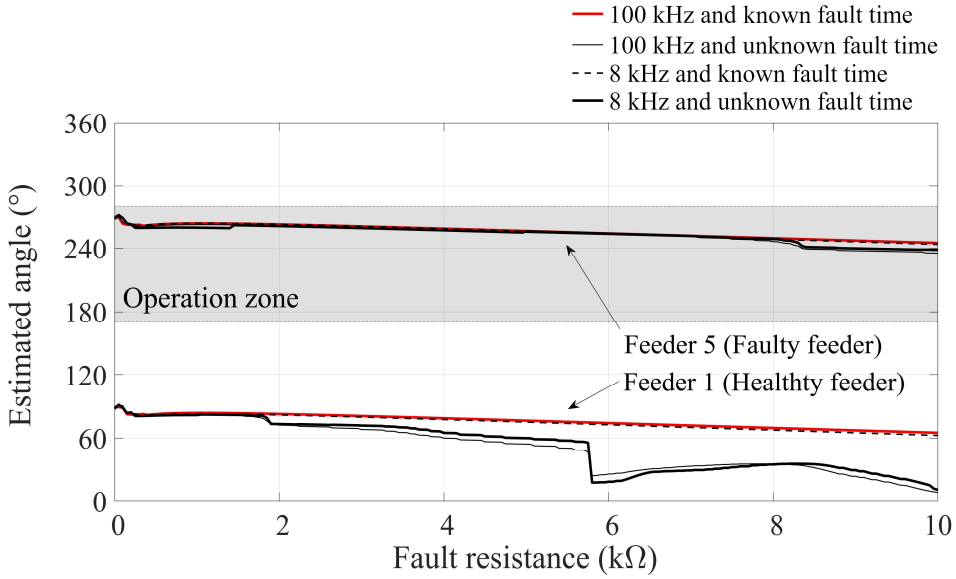

Figure 3.11 – Influence of fault resistance and other parameters inherent to the protection system on the estimated angles.

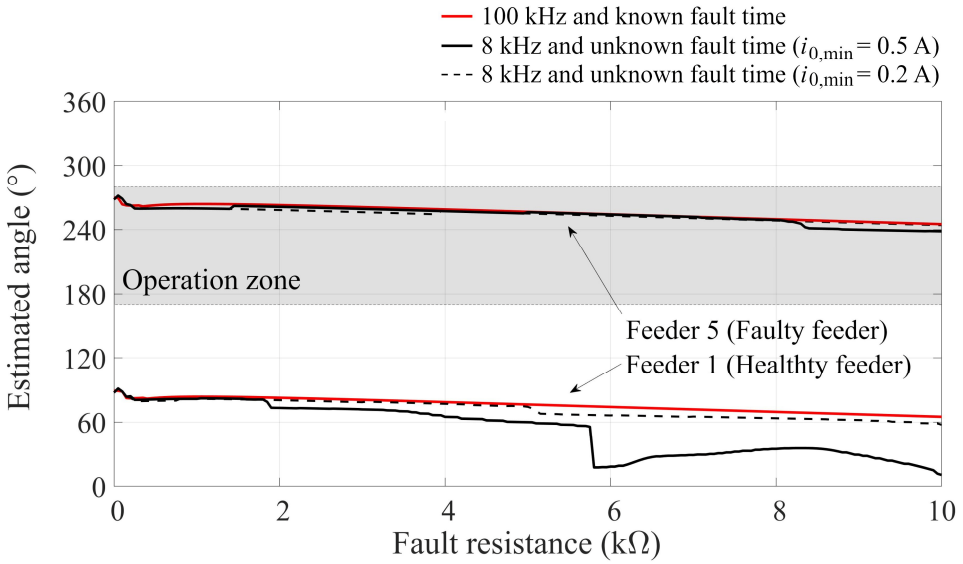

Figure 3.12 – Influence of $i_{0,min}$ on the estimated angles.

In the following, the scenarios in which transient-based protection systems might mis-operate are analyzed. A sampling rate of 100 kHz and known fault inception time are considered, in order to single out and illustrate only the influence of the characteristics inherent to each critical scenario.

i) Asymmetrical networks

One scenario is related to the capacitance-to-ground unbalance of the feeders, i.e., the inequality of the capacitance values between the single-phase conductor and ground. The asymmetry factor can be defined as [42],

$$k = \left| \frac{\overline{\mathrm{Y}}_{ag} + \alpha^2 \overline{\mathrm{Y}}_{bg} + \alpha \overline{\mathrm{Y}}_{cg}}{j\omega\left(\mathrm{C}_{ag} + \mathrm{C}_{bg} + \mathrm{C}_{cg}\right)} \right| \tag{3.10}$$

where $\overline{\mathrm{Y}}_{abcg}$ are the shunt admittances, C_{abcg} are the phase-to-ground capacitances and α is the rotational operator $e^{j2\pi/3}$. If the shunt conductances are neglected, (3.10) becomes,

$$k = \left| \frac{\mathrm{C}_{ag} + \alpha^2 \mathrm{C}_{bg} + \alpha \mathrm{C}_{cg}}{\mathrm{C}_{ag} + \mathrm{C}_{bg} + \mathrm{C}_{cg}} \right| \tag{3.11}$$

If all capacitances-to-ground are equal, then $k = 0$.

Considering $\mathrm{C}_{ag} = \mathrm{C}_{cg} = \mathrm{C}$ (see the line configuration of Figure 3.1b) and defining $\Delta\mathrm{C}_{bg} = \mathrm{C}_{bg} - \mathrm{C}$ then,

$$k = \left| \frac{\Delta\mathrm{C}_{bg}}{3\,\mathrm{C} + \Delta\mathrm{C}_{bg}} \right| \tag{3.12}$$

For the assessment of the protection performance on a network with high degree of asymmetry, an additional capacitance is connected at both ends of phase-*b* such that $k = 5$ %.

In Figure 3.13 the estimated angles are shown, when the fault occurs either in phase-*a* or *b*. Although in this study the same filter of Table 3-3 was implemented, the expected frequencies might be slightly lower due to the added capacitances [37]. For this network, the operation zone must be enlarged from 170–280° to 170–315° to obtain a proper behavior. This second proposed operation zone is further assessed also for the original network.

Another scenario that affects transient-based protection algorithms is the fault occurrence of faults when the faulted phase voltage is 0, i.e., faults with 0° inception angle. The simulations are repeated in this condition and the results are reported in Figure 3.13.

ii) Hybrid networks

The protection system is assessed in hybrid networks, i.e., composed by overhead and underground cable lines. For this purpose, the last 5 km of each feeder were replaced by underground cables with the configuration of Figure 3.14.

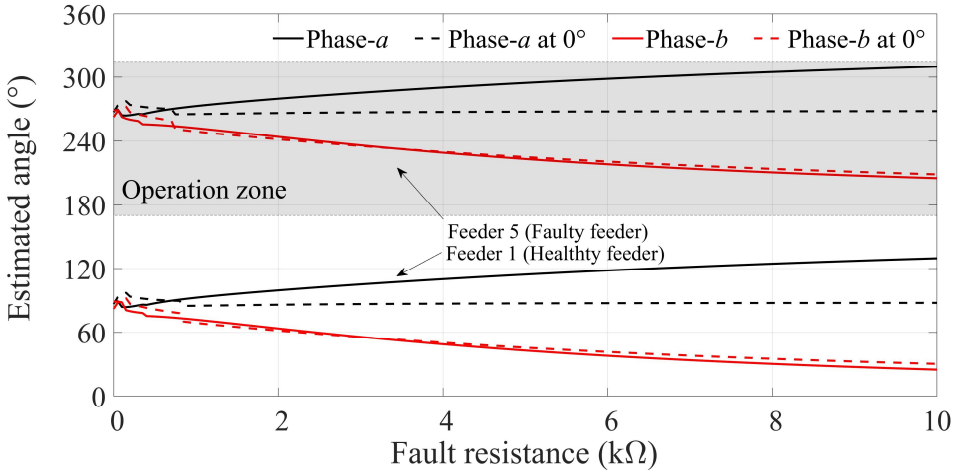

Figure 3.13 – Estimated angles for the asymmetrical network.

The estimated angles are reported in Figure 3.15, this time varying the fault location along Feeder 5 for two values of fault resistance, namely 0 and 10 kΩ. Although the protection parameters are those of Table 3-3, in this case too, the expected frequencies might be lower due to the increased capacitance of cable lines with respect to overhead ones. This effect is further illustrated in Section 3.2.3. The operation zone originally chosen within 170–280° works properly in this scenario.

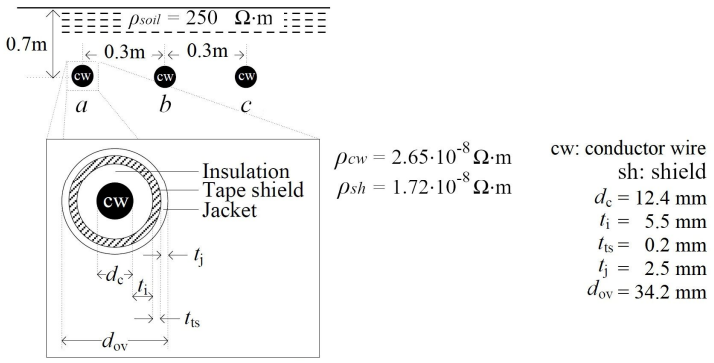

Figure 3.14 – Cable line configuration (Adapted from [43]).

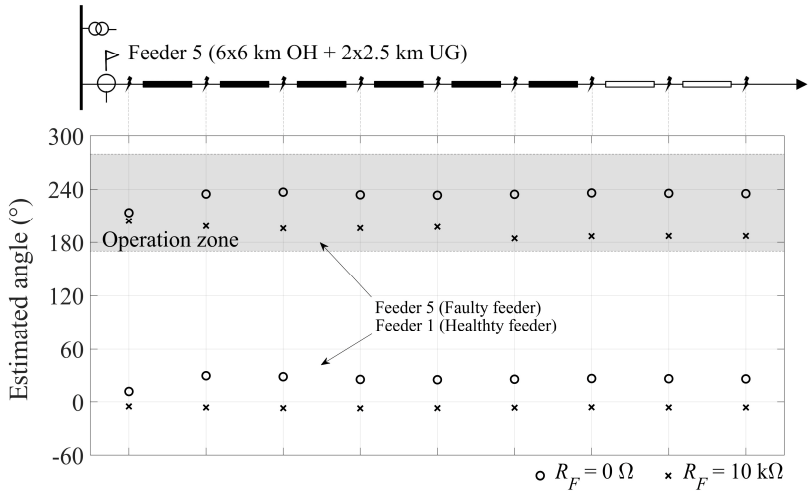

Figure 3.15 – Estimated angles in a hybrid network. Feeder 5 is divided in 6 sections of overhead (OH) line each 6 km long, and 2 sections of underground (UG) cable line each 2.5 km long. A fault is simulated at each of these points with 0 and 10 kΩ fault resistance.

b) Monte Carlo analysis

To further validate the effectiveness of the protection system and of the proposed operation zone, a Monte Carlo analysis is carried out. The original network of Figure 3.1 is studied. A set of 2000 faults randomly distributed within the entire network are simulated, by varying the fault incidence angles over one power frequency period and the fault resistances between 0 and 20 kΩ with the probability distribution shown in Figure 3.16. The characteristics of the protection system are the same of Table 3-3. The sampling frequency considered for the protection algorithm is 8 kHz, while the simulation time-step is 10 μs.

The results are reported in Table 3-4 for the unearthed network and in Table 3-5 for the compensated network with different values of compensation degree.

All the failure-to-trip cases in the compensated network are related with the threshold value and not with an angle misestimation of the algorithm. Indeed, in these cases the fault is not even detected. If $i_{0,\min}$ was set to 0.25 A, a 0 % failure-to-trip and unnecessary trip rates are obtained.

The estimated angles for the healthy and faulty feeders are reported in Figure 3.17. In 95.8% of cases the angle of the feeder is within the range 250–280° for the unearthed network and in 96.8% of cases is within 240–270° for the compensated network. By enlarging the operation zone to 170–315° as required for asymmetrical networks, the same results are obtained.

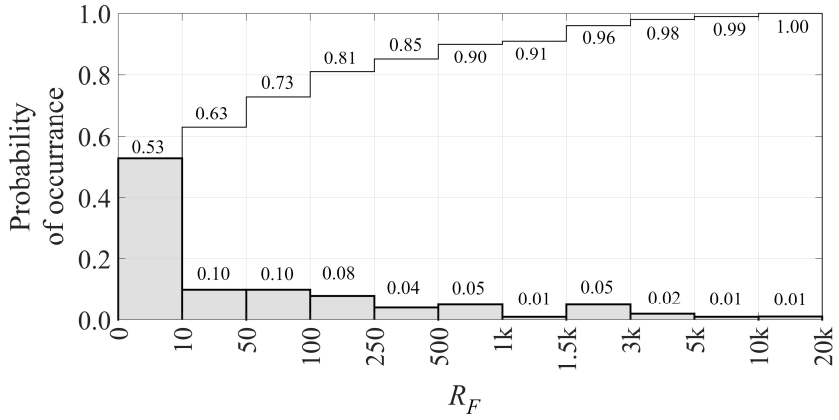

Figure 3.16 – Probability and cumulative distribution functions of the fault resistance values in a MV network, as reported in [10].

TABLE 3-4
MONTE CARLO RESULTS FOR THE UNEARTHED NEUTRAL MV NETWORK OVER 2000 FAULTS

$\theta_{\min} - \theta_{\max}$	Failure-to-trip rate	Unnecessary trip rate	Mis-operation rate[1]
170–280°	0.05 %	0.05 %	0.05 %
170–315°	0.05 %	0.05 %	0.05 %

[1]The mis-operation rate is not necessarily the sum of the failure-to-trip and unnecessary trip rates, since sometimes both events occur in a single case.

TABLE 3-5
MONTE CARLO RESULTS FOR THE COMPENSATED NEUTRAL MV NETWORK WITH DIFFERENT GRADES OF COMPENSATION OVER 2000 FAULTS

Compensation degree (k)	Failure-to-trip rate	Unnecessary trip rate	Mis-operation rate
0.95	0.65%	0.05%	0.70%
1.05	0.65%	0.05%	0.70%
1.00	0.65%	0.05%	0.70%

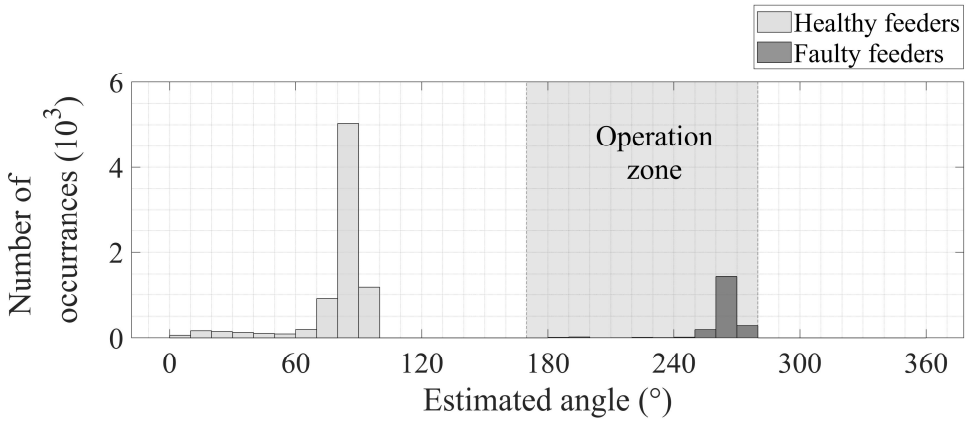

(a)

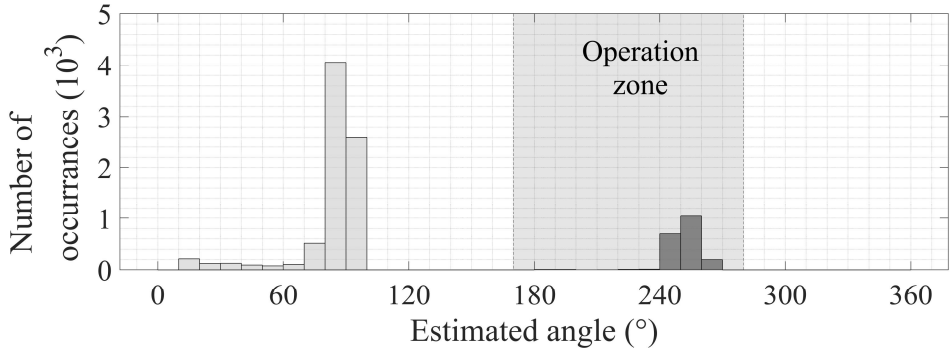

(b)

Figure 3.17 – Estimated angles obtained with the Monte Carlo analysis for both (a) unearthed and (b) compensated networks.

i) Relay operating times

The Protection Scheme Tripping Time (PSTT) is defined as the time elapsed between the fault inception and the instant when the relay sends a tripping signal to the CB (i.e., it does not include e.g. the CB operating time) [44]. It includes the pick-up time (t_{pu}), i.e., the time elapsed between the fault inception and the fault detection; the protection algorithm (t_{prot}) operating time, which is constituted by other elements; and the output device delay, as shown in Figure 3.18.

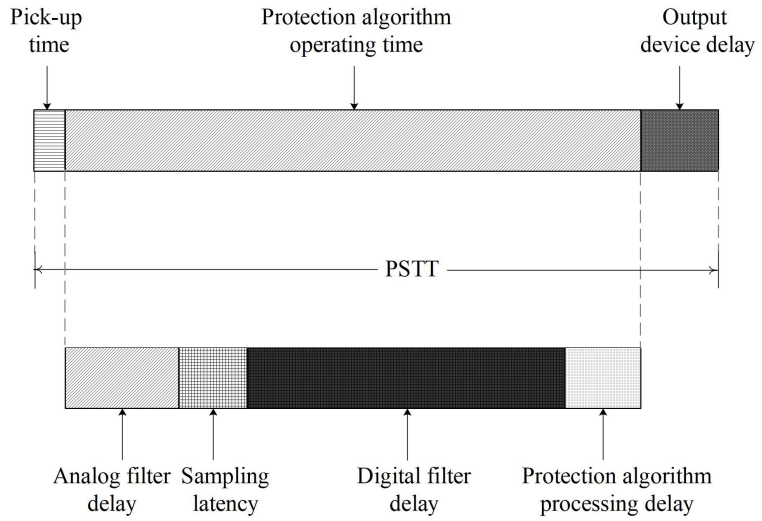

Figure 3.18 – PSTT components (Adapted from [44]).

The four components of the protection algorithm operating time are the following:

- The analog filter delay (δ_{af}) depends on the filter type and its cutoff frequency, which in turn depends on the sampling rate. Increasing the sampling frequency reduces the analog filter delay [45]. Indeed, such delay can be estimated as [46],

$$\delta_{af} = \frac{n}{8 f_c} \tag{3.13}$$

  where n is the order of the filter and f_c is the cutoff frequency of the filter, which can be assumed that it is equal to one-third the sampling rate. For a second order analog filter (3.13) becomes,

$$\delta_{af} = \frac{3}{4 f_s} \tag{3.14}$$

- The sampling latency accounts for the time that the digital filter needs to wait before the first sample is available after the event occurrence. This value varies between 0, when the event occurs in the exact moment a sample is acquired, and a sampling period, when the event occurs just after a sample has been acquired. Conservatively, a sampling period is considered, i.e., the maximum value that the sampling latency can take, e.g., 0.125 ms for a sampling frequency of 8 kHz.
- The digital filter delay is determined by the time window and the input signal magnitude. If the latter is comparable to the pickup value, the digital filter delay approaches the time window value. As the input signal magnitude is larger, the delay is smaller. Conservatively, the time window is considered, i.e., the maximum value that the digital filter delay can take.
- The protection algorithm processing delay ($\delta_{alg,proc}$) will be estimated during the tests.

The contact closing operation time of the relay is typically in the order of 10 μs for solid-state circuits [44] for which the output device delay can be neglected. Other elements included in the protection

circuitry such as interposing relays are not directly associated to the system under analysis, hence are deliberately disregarded.

The resulting protection operating time is,

$$\begin{aligned} t_{prot} &= \delta_{af} + \frac{1}{f_s} + t_{win} + \delta_{alg,proc} \\ &= \frac{7}{4 f_s} + t_{win} + \delta_{alg,proc} \end{aligned} \tag{3.15}$$

and,

$$t_{PSTT} = t_{pu} + t_{prot} \tag{3.16}$$

For the case under analysis, the protection algorithm processing delay has been estimated from the Monte Carlo analysis and its mean value is 2 ms. It accounts mainly for the DFT computation, including the zero-padding and the angle identification. It does not include the filtering process since it is supposed to be considered in the digital filter delay. Since t_{win} = 5 ms and f_s = 8 kHz, from (3.15) it can be derived that the protection operating time is around 7.2 ms from the fault detection instant.

Moreover, the pick-up time depends mainly on the thresholds other than the fault itself (e.g., fault resistance and inception angle). For the analyzed cases the time elapsed between the fault inception and the fault detection has a mean value of 0.1 ms, with maximum values of 8.1 and 3.6 ms for the unearthed and compensated networks, respectively.

The overall expected protection speed is particularly good.

3.2 Meshed unearthed networks

MV networks are typically operated in radial configuration due to straightforward control, planning, and design of the protection schemes, besides low construction costs. To improve the system reliability and reduce power losses in these networks, many approaches have been reported in literature, e.g. system reconfiguration [47] while including the radiality constraints, also in the planning problem [48]. The integration of DG might also carry benefits in terms of reduced power losses and voltage profile improvement, depending on some factors, e.g. planning (siting and sizing of DG units), DG technology and operational strategies [49], [50].

However, a fault in any part of a radial distribution network results in a customer outage, constituting the major drawback of this configuration. As most power outages in distribution systems are due to faults, the loop and meshed network configuration may improve the power quality with respect to the radial one by reducing the duration and number of interruptions [14], [51]–[53].

Moreover, due to the growing installation of DG the distribution system is becoming an active entity, which further motivates the meshed operation of the distribution networks, with benefits in terms of increased DG hosting capacity, operation flexibility and security, high reliability, voltage control and profile, as well as reduced power losses and maintenance efforts [14], [53]–[56]. Indeed, several DSOs (e.g., *e-Distribuzione*, *Florida Power Company*, *Taipower*, *Hong Kong Electric Company*, *Singapore Power*, *Korea Electric Power Corporation*, etc.) are currently operating some portions of their distribution networks with a normally closed loop configuration [55], [57]. Adversely, looped and meshed networks are more expensive since the short circuit current level of the system increases, thus requiring CBs with a larger interrupting capacity. Moreover, due to the possibility of bidirectional power flow in some portions of the network, the protection scheme design is more complex and communication and digital relays are normally required [58]. The advantages and disadvantages of both configurations are summarized in Table 3-6.

TABLE 3-6
CHARACTERISTICS OF RADIAL AND MESHED NETWORKS. ADAPTED FROM [59]

	Available sources	**Stability**	**Reliability**	**Cost**	**Voltage profile**	**Protection system**	**DER penetration**
Radial	Single	Low	Low	Low	Traditional	Simple	Problematic
Meshed	Multiple	High	High	High	Improved	Complex	Accepted. Hosting capacity is increased

Following the above-mentioned premises, the proposed protection algorithm is extended for the operation in meshed networks, and its performance is assessed.

3.2.1 Theoretical background

The analysis presented in Section 3.1.1 for radial networks is extended for meshed ones with unearthed neutral.

A simple meshed network with the topology of Figure 3.19 is considered, in which each line is protected by a couple of relays installed at both ends. Figure 3.19 shows the circuital representation of the zero-sequence current for a fault in Line 3.

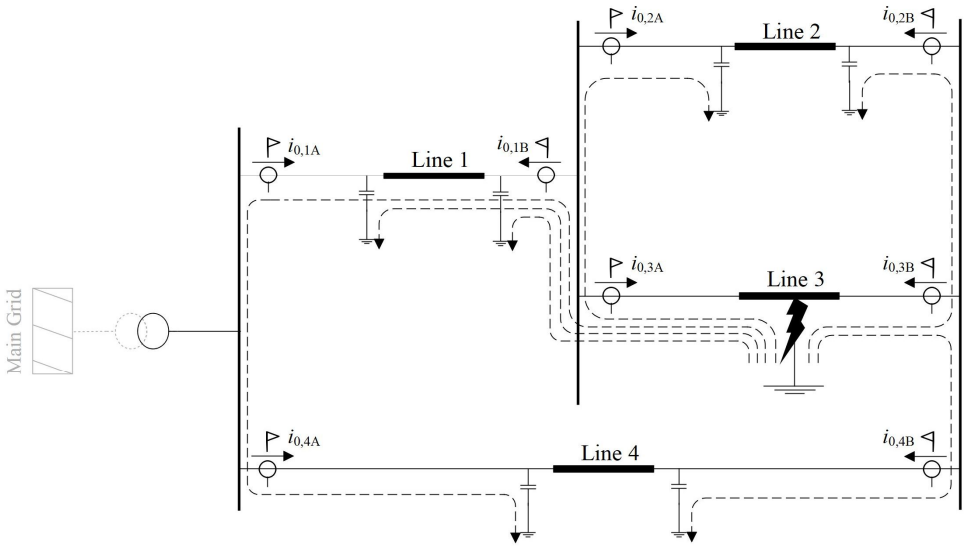

Figure 3.19 – Circuital representation of the zero-sequence current for a single phase-to-ground fault in a meshed network [37].

For a first analysis, the following two assumptions are made: i) all feeder and fault inductances and resistances are neglected, i.e. the zero-sequence current is entirely capacitive; ii) all dashed lines in Figure 3.19 represent an equal quantity $i_{0,F}$. Under these assumptions, the vectorial diagram of Figure 3.20 is obtained (similar to that of Figure 3.3a for radial networks). The following observations apply. In the faulty line, both zero-sequence currents at both line-ends (i.e. $i_{0,3A}$ and $i_{03,B}$) are lagging with respect to v_0, i.e. the angle is 270°. In healthy lines, at least one current of both line-ends is leading with respect to v_0, i.e. the angle is 90°.

The condition in which i_0 is leading v_0 can be seen by both relays at both ends of healthy lines or by only one of the two. The latter case may happen, e.g., in lines of limited length where the leakage current through the line capacitance is small, therefore the currents at both ends of the line have similar magnitude and opposite direction, but it can happen also in other cases depending on the zero-sequence current distribution, i.e., on the feeder impedances.

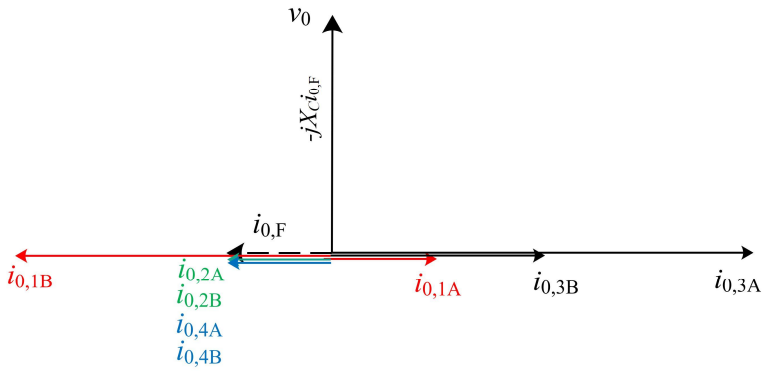

Figure 3.20 – Vectorial diagram of the zero-sequence quantities.

By considering the longitudinal impedances and the fault resistance values, a similar behavior as the one observed in Figure 3.3b would be observed.

It is evidenced from this analysis that, by implementing a communication network between relays only the faulty line can be isolated, without de-energizing the entire network and without causing any customer outage.

In the proposed protection strategy, each relay communicates to the relay at the opposite line end by exchanging permissive signals following a directional comparison permissive overreaching transfer trip (POTT) scheme [11]. One of the main advantages of the adoption of a permissive over a blocking scheme is that it allows shorter operating times [60]. This advantage is of particular interest when a transient-based protection algorithm is adopted in order to make the most of its fast operation. In blocking schemes, the coordination time, which is the minimum possible operating time for the protection, must be larger than the maximum expected latency of the blocking signal. This requirement is not needed in permissive schemes, rendering it faster. On the other hand, the loss of communication in blocking schemes leads to unnecessary trips, while in permissive schemes leads to a failure-to-trip since the permissive signal would never be transmitted. A backup protection needs to be implemented in case the communication channel is lost. This issue will be deliberately disregarded when assessing the performance of the protection algorithm. This assumption is very reasonable since, as reported in [61], the reliability of the communication network related to protection applications must be greater than 99.999%.

Moreover, one of the advantages of this scheme over differential protections is that the exchanged signals are of the on-*off* type, for which low budget communication systems can be employed. The disadvantage is that directional comparison schemes need to measure the voltage at each bus. While for radial networks the voltage was measured only at the main busbar, for meshed networks this must be replied in all the buses of the network. However, this disadvantage is minimized due to the advent of low-cost voltage dividers [62].

The estimation of the directionality of the fault by the single relay is the same as for radial networks. The relay outputs a trip signal when two conditions are met: i) it senses the fault in the forward direction and; ii) a permissive signal is received from the relay at the opposite line end. The protection algorithm scheme of Figure 3.9 is updated to obtain the one of Figure 3.21, in which changes are marked with red.

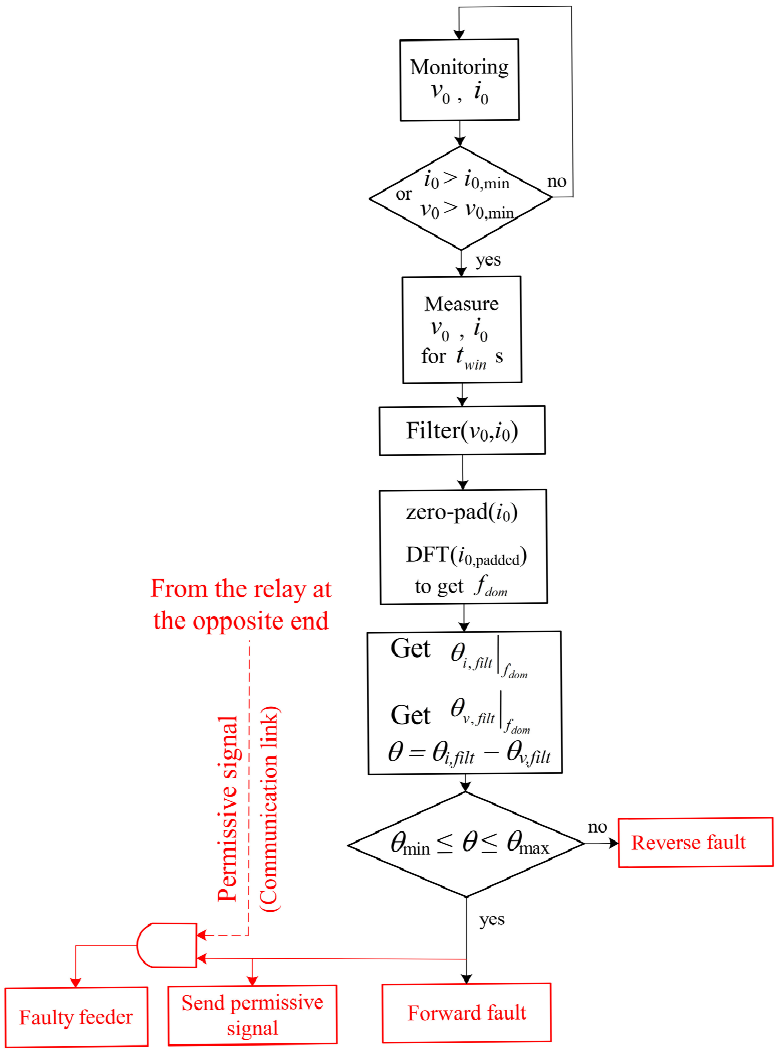

Figure 3.21 – Protection algorithm flowchart (Adapted from [37]).

a) The equivalent circuit

It is noticed from (3.9) that the dominant transient frequency depends on the values of equivalent capacitance and inductance. However, the appraisal of these parameters in a meshed network is much more complex than in a radial network. Moreover, it has been already shown in Section 3.1.1 that the estimation of the dominant transient frequency is of utmost importance for the proper operation of the protection scheme.

For the purpose of estimating the range of values that the frequencies might reach, an equivalent circuit is implemented. The reduced equivalent circuit of the network for single phase-to-ground faults is shown in Figure 3.22. It is the series of the sequence networks (see Figure 2.2) seen from the point of fault with the following considerations:

- The power system behind the faulty line has been represented at both line-ends by means of their equivalent impedances at positive, negative and zero sequences, i.e. $\overline{z}_1^{(+-)}$, $c_1^{(0)}$, $\overline{z}_2^{(+-)}$ and $c_2^{(0)}$

are the positive and negative-sequence equivalent impedances and the zero-sequence capacitances seen from the two line-ends of the faulted line.

- The faulted line has been divided in two sections at the point of fault, i.e. $\overline{z}_{line,1}^{(+-0)}$ and $\overline{z}_{line,2}^{(+-0)}$ represent the sequence impedances of the faulty line at both sides of the fault.
- Voltages $\overline{v}^{(+-0)}$ are the pre-fault sequence voltages and R_F is the fault resistance.
- The transfer impedance $\overline{z}_{transfer}^{(+-0)}$, needed in meshed networks, is also included in the equivalent circuit [63]. Such impedance represents the portion of the system surrounding the faulted line that links the two terminals as well.

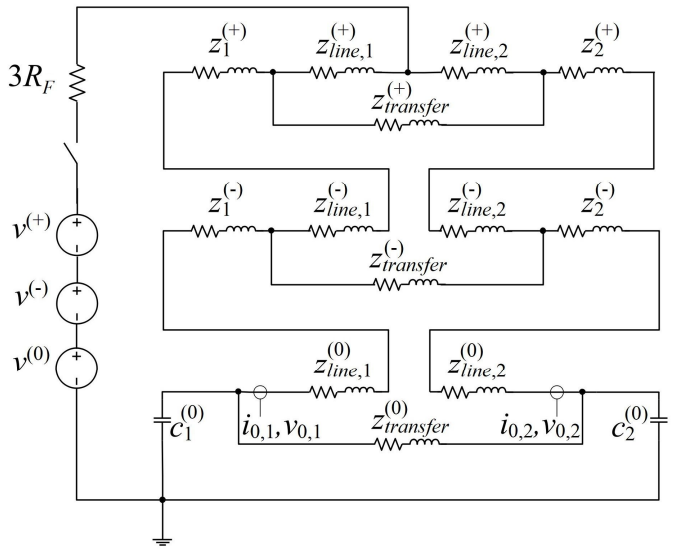

Figure 3.22 – Reduced equivalent circuit of the system in single-phase-to-ground fault condition [37].

The implementation of the equivalent circuit for the evaluation of the transient frequency is further illustrated in Section 3.2.3 in a specific case scenario.

3.2.2 The communication network

Depending on the application for which the communication network is implemented in the distribution network, the requirements are different. The IEEE Std. 2030-2011 [64] defines the smart grid evaluation criteria and the smart grid communications security categorization, both aiming at defining the performance requirements for each interface. In this Section the attention is focused on the protection application, but some aspects of other applications are reported.

Some communication network technical characteristics for typical applications of distribution networks are reported in Table 3-7. The data reported do not constitute hard technical requirements but are somewhat useful recommendations and provide a general outlook of the different network characteristics needed for the diverse applications.

TABLE 3-7
COMMUNICATION PARAMETERS FOR GENERAL APPLICATIONS. ADAPTED FROM [65]–[68]

Application	Typical response time	Maximum latency	Data size
Protection	1 – 10 ms	67 – 100 ms	Tens of bytes
Control and monitor	100 ms – 1 s	1 – 5 s	Tens to hundreds of bytes
Metering and billing	Hours to 1 day	-	Hundreds of bytes to MB
Reporting and software update	Days	-	kB to GB

The speed of the communication channels depends on many factors: the data rate of the channel, the message packet size, and the equipment latency.

Many technologies can be used for the communication between relays. Communication can be analog, e.g. Power-Line Carrier (PLC) and pilot wires (audio tones over leased telephone networks, signals over LV circuits); or digital, e.g. fiber optics, microwave, radio link and digital data services [11].

Communication over pilot wires is affected, among others, by the induction that can be established from lightning or parallel power circuits; the insulation stress that results from the voltage rise during faults, particularly high in unearthed networks; insulation failure for other reasons like physical damage.

The disadvantage of microwave is found in its tendency to fade under adverse weather conditions, in which power system faults related to wind and lightning are more prone to occur.

Digital data services available from telephone companies are not suitable for protection applications since faults near the substation can cause the loss of channel. Also, periodic interruptions have been registered through the usage of this technology.

PLC technology is not recommended for POTT schemes since during a fault, the permissive signal travelling through the channel could be interrupted or shorted by the fault, hindering the protection operation.

The remaining options are fiber optics and radio links. Both are not affected by electrical transients or ground potential rise associated to power system faults. While optic fibers are the most attractive communication technology for the implementation of protective schemes due to the high bandwidth and communication speed, the installation costs could be prohibitive for the DSOs. Radio systems instead, are a cheaper solution. In [69] it is reported that for a 20-mile link, the costs of a network with fiber optics and with radio link is, at 2012, $65.000 and $750, respectively.

Another advantage of radio systems is that they do not require any right-of-way or physical conductor, but they need line-of-sight [60], [69], [70].

For these reasons, a spread spectrum radio technology is considered on the assessment of the communication-supported protection system.

a) Influence of communication on the relay operating times

The PSTT was analyzed in Section 3.1.2 without considering the delays associated to the communication network. In addition to the protection algorithm operating time and the output device delay, the communication system delay (δ_{com}) and the relay processing delay related to the signals exchange ($\delta_{com,proc}$) must be considered, as illustrated in Figure 3.18.

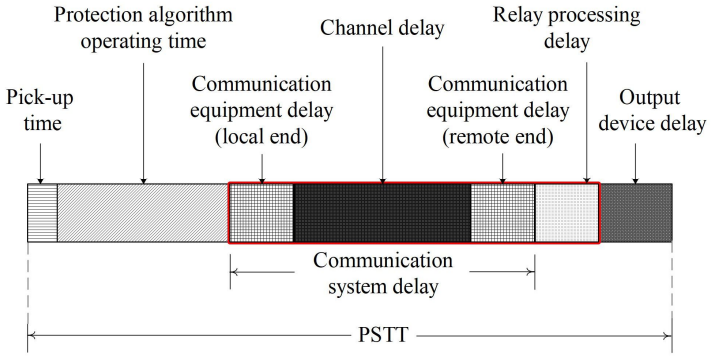

Figure 3.23 – PSTT components with communication delays. The elements related to the communication between relays are highlighted in red (Adapted from [44]).

The relay processing delay accounts for the firmware and hardware delays which are approximatively equal to 3 ms [44], and for the processing latency that follows the same principle as the sampling latency, i.e., its value varies between zero and one sampling period. Following a conservative approach, thus considering the maximum value that the processing latency can assume, it follows that,

$$\delta_{com,proc} = 3 + \frac{1}{f_s} \tag{3.17}$$

Considering these new sources of delay, (3.15) becomes,

$$t_{prot} = 3 + \frac{11}{4 f_s} + t_{win} + \delta_{alg,proc} + \delta_{com} \tag{3.18}$$

in which all times are in ms and f_s is in kHz. It is recalled that to obtain the PSTT, the pick-up time must be added to (3.18).

As for radial networks, the algorithm processing delay is estimated during the tests. While t_{win} and f_s are constants, the communication system delay δ_{com} is variable since it depends on many factors, as elucidated before.

i) Communication system delay

It is worth mentioning the following premise: to the best knowledge of the author, there are not studies in literature that describe a concise statistical analysis of the characteristics of communication systems, and even typical values differ from report to report. Under such consideration, typical values are chosen and implemented in this study, but other values could be as well used, without changing the nature of the method and the results. Moreover, if a different communication technology must be implemented,

e.g. fiber optics, the distribution and the values of typical delays might vary, but the overall methodology is still consistent.

The communications system delay includes not only the channel delay but also the equipment delays at the local and the remote ends, i.e., the sending and the receiving terminals. Typical delays of spread spectrum radio technology are between 4 and 5.6 ms, depending on the channel data rate, although encryption could add some additional delay [44], [60].

To represent this delay behavior the truncated normal distribution of Figure 3.24 is used to represent the communication delay, with mode equal to 5.6 ms. The standard deviation of the untruncated distribution is equal to 22 ms, so that the 99.9% of delays are lower than 67 ms, so the probability of exceeding the maximum delay recommended in [68] is negligible.

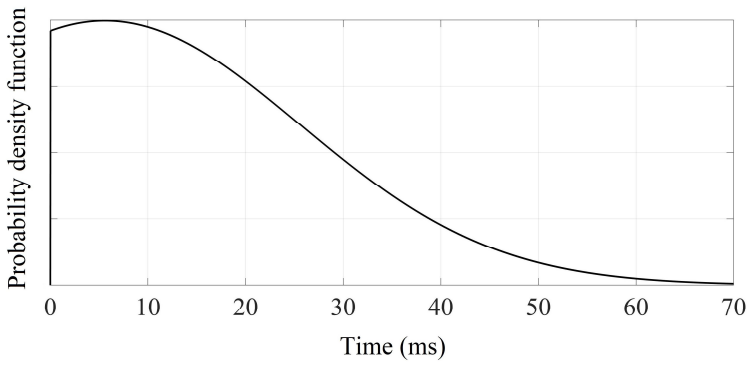

Figure 3.24 – Probability density function of time delays [37].

b) The co-simulation environment

Since the proposed protection system is supported by communication links, to assess its performance a co-simulation environment is needed. Based on [71], a tool that interfaces the Electromagnetic Transient Program (EMTP-RV) simulation environment with Matlab has been developed, hereafter called EMTP-Matlab.

The structure of the co-simulation environment is illustrated in Figure 3.25. A virtual port, namely a virtual network *socket*, is set up at the beginning of the simulation allowing the exchange of information between the two simulation environments. The information is exchanged through a Dynamic Link Library (DLL), which acts as RunTime Infrastructure (RTI). The RTI is responsible of the synchronization between simulators, and it decides when they can interact, based on information that arrives from the selfsame simulators.

In EMTP-RV (*server*) the waveshapes of the power system currents and voltages in both phase and modal domain are calculated, while in Matlab (*client*) the communication-supported protection system is modeled. A Matlab script determines the directionality of the fault and emulates the sending of permissive signals for the CB operations, considering communication delays and the other components of the PSTT.

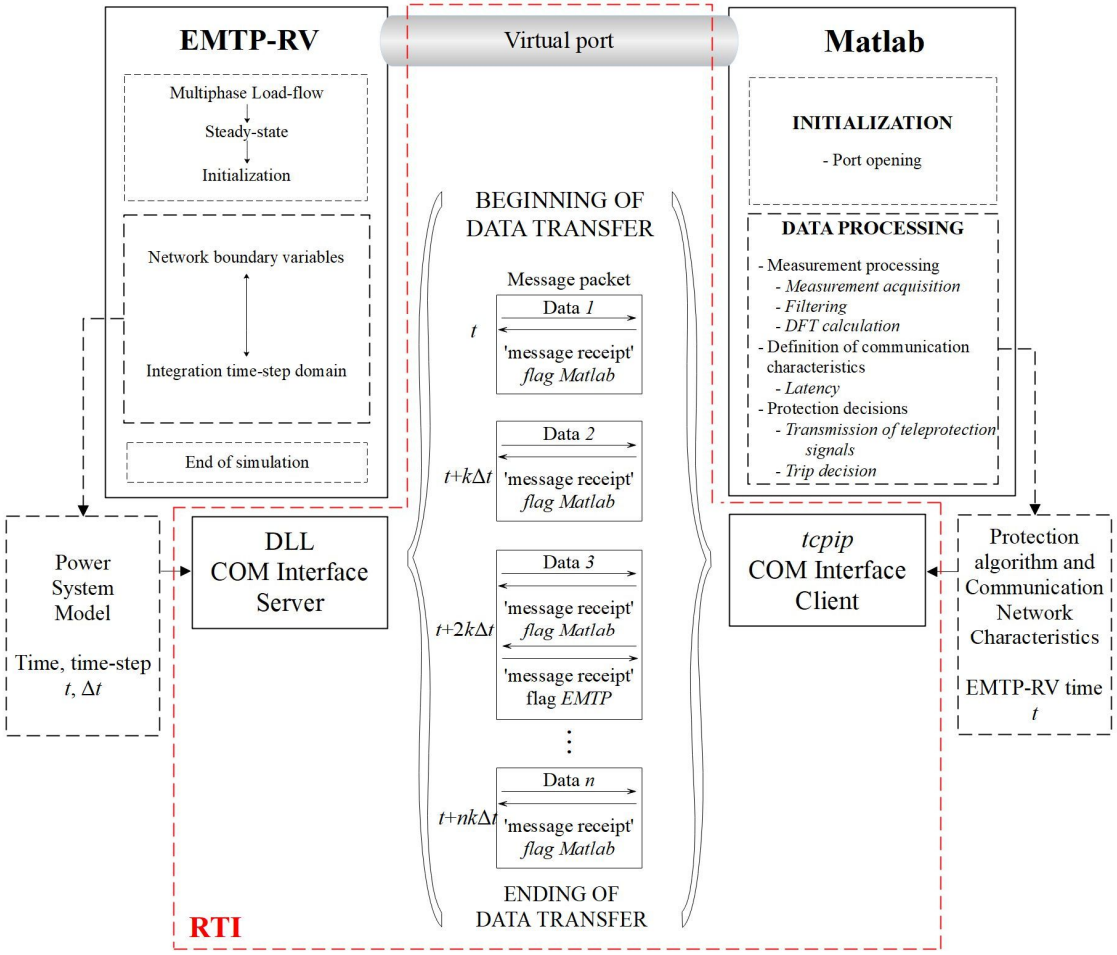

Figure 3.25 – Structure of the co-simulation environment that interfaces EMTP-RV with Matlab. The task division between both tools is illustrated (Adapted from [37]).

The virtual port is set up at the beginning of the simulation. When a fault occurs, EMTP-RV initiates to send information to Matlab at each time-step through the DLL. Vice versa Matlab sends information when necessary to EMTP-RV. Time synchronization is done by exchanging specific flag signals and time stamp information at each time-step of the RTI. When the Matlab routine completes its tasks, it closes the communication port with EMTP-RV, which then carries out the residual simulation process.

A fault clearance example is illustrated in Figure 3.26, in which the stages of the co-simulation process are exhibited.

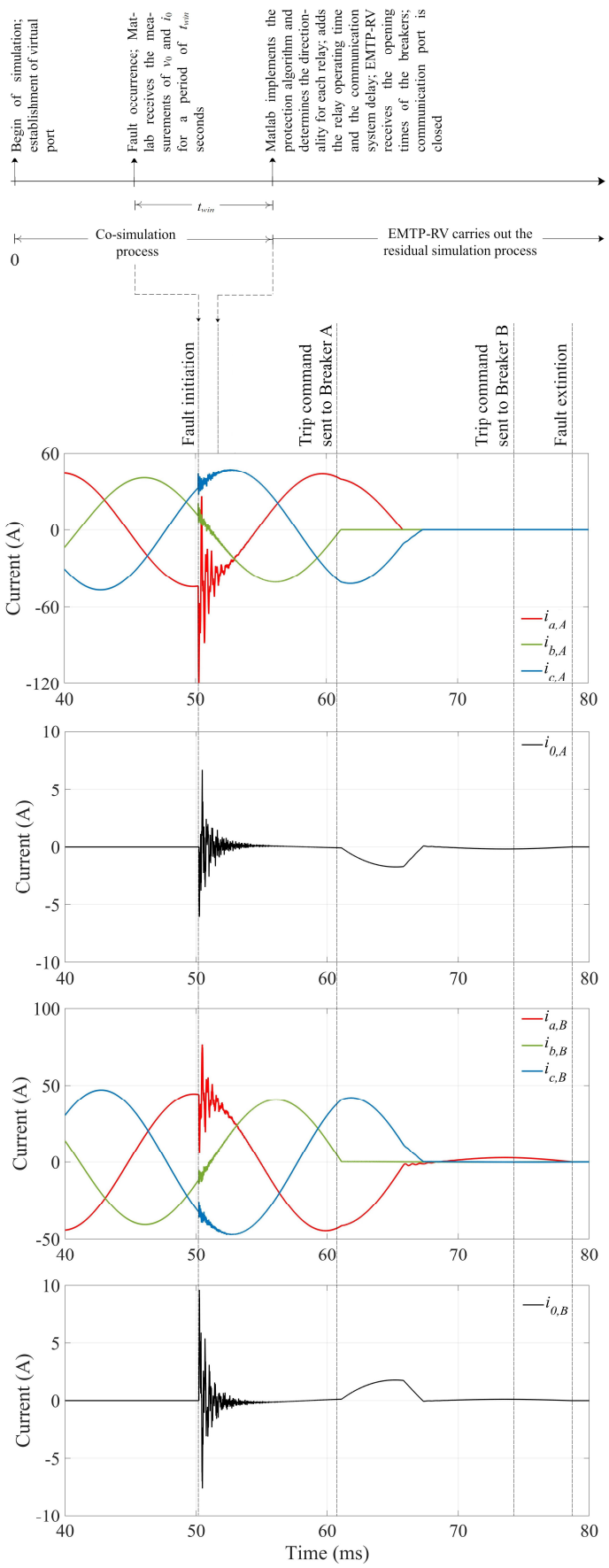

Figure 3.26 – Phase and earth mode currents for a single phase-to-earth fault. Influence of communication delays in the trip commands and the fault extinction.

In the following, in order to categorize the EMTP-Matlab tool, some characteristics relative to all co-simulation environments are described:

a) Co-simulation environments can be either static or dynamic [71]. Static environments allow the analysis of power systems under varying load conditions, in which the characteristics of communication systems are also considered. Dynamic environments instead, allow the analysis of power systems transients, e.g. when a fault occurs, thus they aim at verifying the adequacy of communication systems in such rapidly varying conditions.

Since the developed tool is for analyzing power system transients resulting from faults, a dynamic environment is chosen.

b) One of the main issues for developing co-simulation environments is the synchronization between a continuous-time type of simulator (power system) and a discrete event-based type of simulator (communication system). Four different methods of dealing with this issue can be listed [72]: i) permanent synchronization at the smallest possible time-step; ii) a priori fixed time-steps for the information exchange among all simulators; iii) user-defined model of the dynamics of the message exchange, and; iv) message delivery relaxation, in which the co-simulation is rolled-back to a previous state when an out-of-order message is delivered.

The synchronization method of EMTP-Matlab could be included in the second group. Indeed, both simulation environments execute until a preset simulation time is reached, as done in [73]. At this point, they interact through the RTI by sending/receiving the relevant messages. At each of these steps, specific flag signals and time stamp information are exchanged to ensure the synchronization, i.e., to ensure that both environments have satisfactorily sent/received the expected information and they can run into the next step. The RTI then decides the time for the next interaction i.e., an a priori fixed time-step is chosen for the exchange of information between both simulators ($k\Delta t$ in Figure 3.25), as in the second method. However, notice that in the Matlab environment no time-step is defined, but its process depends on the time-step defined in the RTI. When maximum accuracy is required, such time-step is set equal to the time-step of the EMTP-RV environment (i.e., $k = 1$), in which case the synchronization resembles the methods of the first group, since the EMTP-RV time-step is the *smallest* one.

The third method requires a scheduler, which is a rather complex task for large distribution networks and is prone to errors. Moreover, since distribution lines could be relatively short, and Constant Parameter (CP)-line or FD-line models are generally used in the analyses of the protection systems, the step-time required for the power system simulation is in the order of a few microseconds, thus the fourth method might not be adequate because it could require too many roll-backs.

c) The level of detail of the communication network can be subdivided in three groups [74], as depicted in Figure 3.27: i) no model, ii) black-box model, and iii) detailed model.

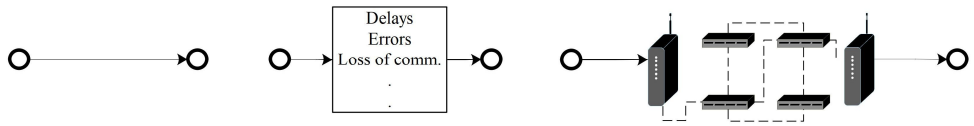

Figure 3.27 – Level of detail of the communication network models: (a) no model; (b) black-box model, and; (c) detailed model (Adapted from [74]).

For the purpose of protection system performance assessment, only the delays (and eventually the errors and/or loss of communication) are of interest. For this reason, a black-box model is implemented, in which the delays are supposed to follow the probability density function of Figure 3.24.

The EMTP-Matlab co-simulation environment is in an early stage, and it has been constructed particularly for the assessment of the proposed protection system. Therefore, many improvements are intended to be developed in the future.

3.2.3 Assessment of the protection algorithm

For the assessment of the protection system in meshed networks, different configurations are considered.

The two network topologies shown in Figure 3.28 and Figure 3.29 are analyzed, denoted as network A (Net-A) and B (Net-B), respectively. Net-A is a modified IEEE 14-bus test system with the line geometry of Figure 3.30a, that is characterized by a significant asymmetry. Net-B has the topology of the Cigré European MV distribution network benchmark [43]. It is composed of two main feeders: one denoted as Feeder A, composed by underground cables with the geometry of Figure 3.30c, the other denoted as Feeder B, composed by overhead lines with the geometry of Figure 3.30b. All lines are represented with the CP-line model. Loads in both cases, are unbalanced.

In both networks the HV-side of the transformers is wye-connected with the neutral solidly earthed, while the MV side is delta-connected.

In the next simulations a time-step of 0.2 μs was used. For the relays, a sampling frequency f_s of 8 kHz is assumed, unless otherwise specified.

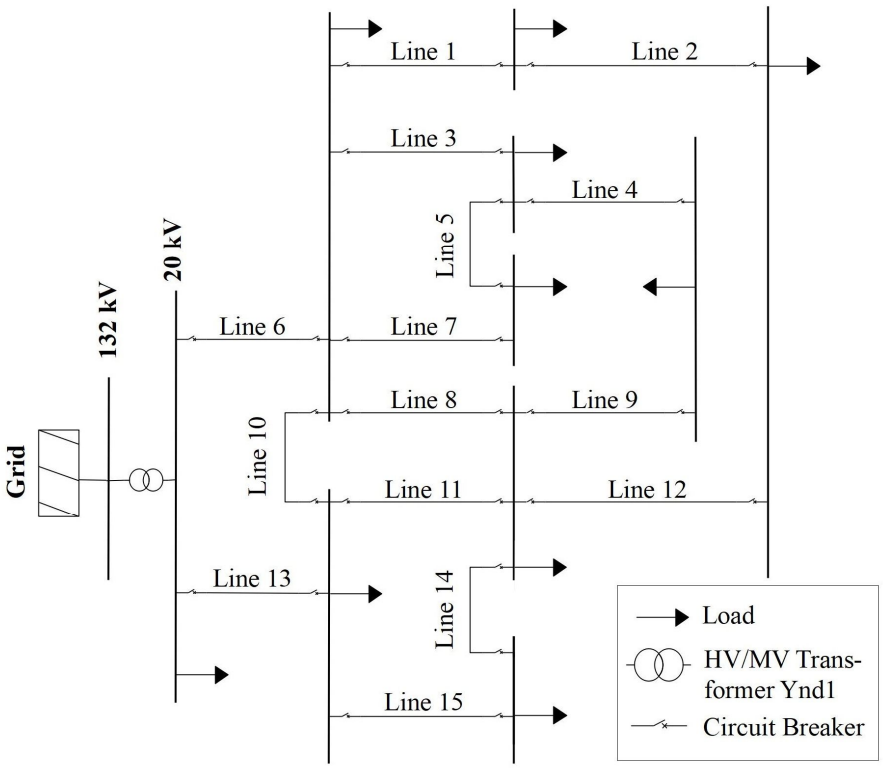

Figure 3.28 – Studied network Net-A. Modified IEEE 14-bus test network [37].

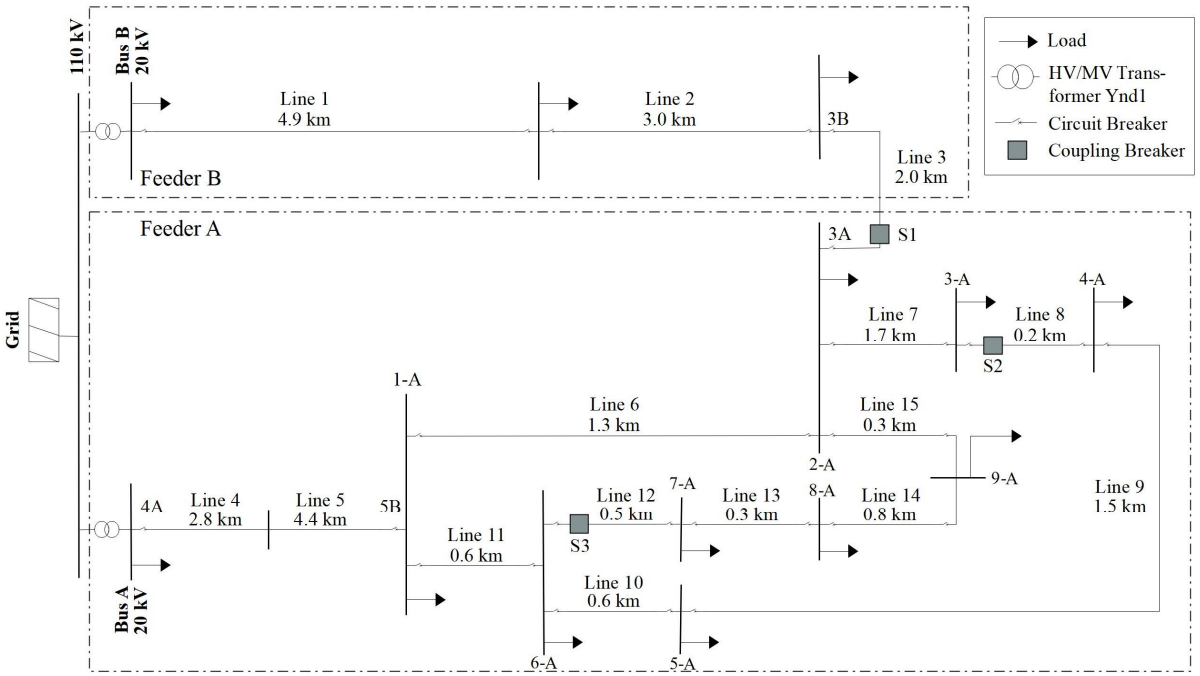

Figure 3.29 – Studied network Net-B. Cigré European MV distribution network benchmark (Adapted from [43]).

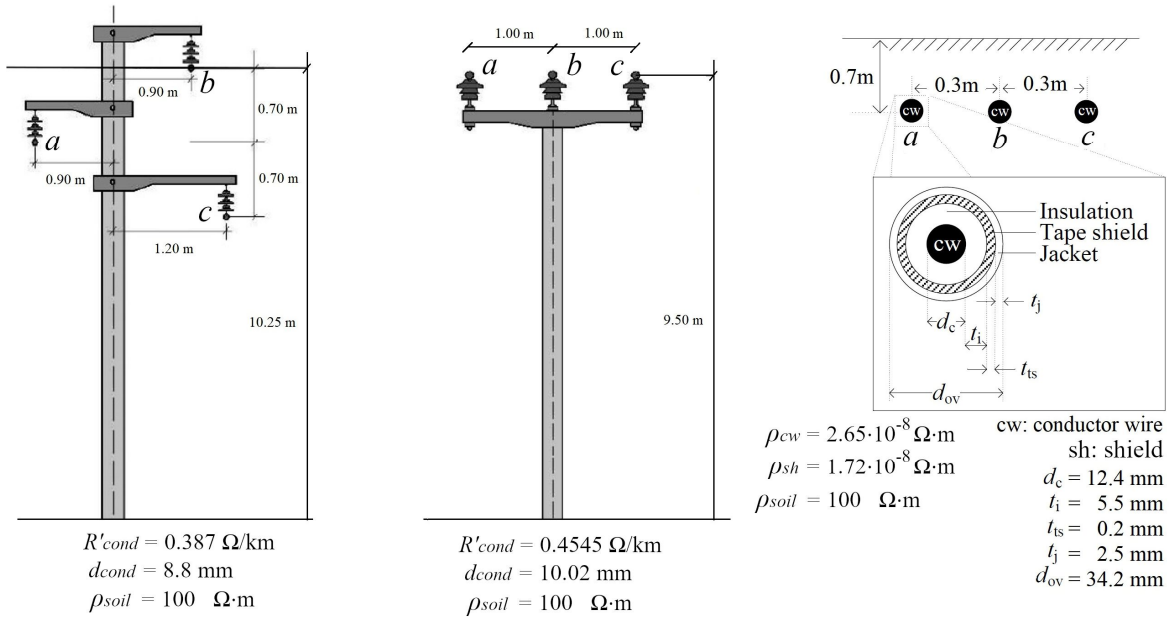

Figure 3.30 – Line configurations. (a) Overhead line of Net-A; (b) Overhead line of Net-B; (c) Cable line of Net-B (Adapted from [43], [75]).

a) Overhead line distribution networks

The performances of the protection system in Net-A are analyzed. All lines are considered to have a length of 3 km.

A preliminary analysis is carried out with the equivalent circuit described in Section 3.2.1 for a first estimation of the dominant transient frequencies.

The sequence impedances must be estimated. For such purpose, the sequence circuit of Figure 3.31 is considered, which follows the same considerations as in Figure 3.22 in absence of any fault. The following analysis is valid for each sequence, hence the super-index $^{(+-0)}$ in the variables is avoided.

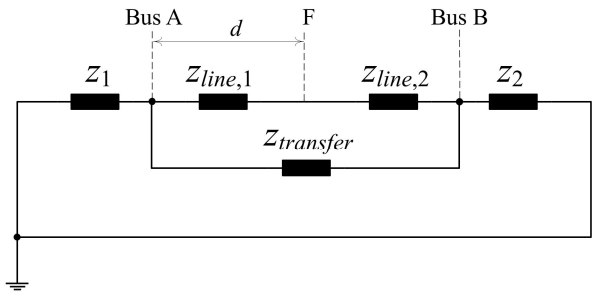

Figure 3.31 – Sequence circuit for a meshed network.

Line 9 of Figure 3.28 is taken as example. The sequence impedances are estimated with the help of the *input impedance* block in EMTP-RV [76]. This block injects a set of three-phase currents either of positive, negative or zero sequence with 1 A of magnitude. By measuring the three-phase voltages in each case, the sequence impedances can be estimated.

By disconnecting the faulted line, i.e. line 9 at both ends, and connecting the *input impedance* block between bus A and earth, the parallel between $\overline{z}_1$ and ($\overline{z}_2$+$\overline{z}_{transfer}$) is obtained for each sequence, which is defined as $\overline{z}_A$. Connecting the *input impedance* block between bus B and earth instead, the parallel between $\overline{z}_2$ and ($\overline{z}_1$+$\overline{z}_{transfer}$) is obtained, which is defined as $\overline{z}_B$. Finally, connecting the *input impedance* block between buses A and B, the parallel between $\overline{z}_{transfer}$ and ($\overline{z}_1$+$\overline{z}_2$) is obtained, which is defined as $\overline{z}_{AB}$. A three-equation system with three variables for each sequence is derived,

$$\begin{cases} \overline{z}_A = \dfrac{\overline{z}_1 \cdot \left(\overline{z}_2 + \overline{z}_{transfer}\right)}{\overline{z}_1 + \overline{z}_2 + \overline{z}_{transfer}} \\ \overline{z}_B = \dfrac{\overline{z}_2 \cdot \left(\overline{z}_1 + \overline{z}_{transfer}\right)}{\overline{z}_1 + \overline{z}_2 + \overline{z}_{transfer}} \\ \overline{z}_{AB} = \dfrac{\left(\overline{z}_1 + \overline{z}_2\right) \cdot \overline{z}_{transfer}}{\overline{z}_1 + \overline{z}_2 + \overline{z}_{transfer}} \end{cases} \tag{3.19}$$

The values of $\overline{z}_{line,1}$ and $\overline{z}_{line,2}$, as well as the pre-fault voltage $\overline{v}$ depend on the fault location F. Defining d the normalized distance from bus A to F,

$$\begin{cases} \overline{z}_{line,1} = \overline{z}_1^{'} \cdot d \\ \overline{z}_{line,2} = \overline{z}_1^{'} \cdot \left(1 - d\right) \end{cases} \tag{3.20}$$

where $\overline{z}_1^{'}$ is the line impedance per unit length.

Assuming that the voltage drop and the phase displacement along the line are uniform, by measuring the voltages at bus A ($\overline{v}_A$) and bus B ($\overline{v}_B$) the voltage magnitude and phase at the faulted point can be approximated as,

$$\left|\overline{v}\right| = \left|\overline{v}_A\right| + \left(\left|\overline{v}_B\right| - \left|\overline{v}_A\right|\right) \cdot d \tag{3.21}$$

$$\varphi_v = \varphi_{v_A} + \left(\varphi_{v_B} - \varphi_{v_A}\right) \cdot d \tag{3.22}$$

It is worth mentioning that $\overline{v}_A$ and $\overline{v}_B$ are measured with the faulted line connected to the network.

The values of impedance and voltage obtained for the case under analysis are reported in Table 3-8.

TABLE 3-8
IMPEDANCE AND VOLTAGE VALUES OBTAINED FOR THE COMPUTATION OF THE EQUIVALENT CIRCUIT PARAMETERS

Parameter	Positive	Negative	Zero
$\bar{z}_A$ (Ω)	1.222 + j2.126	1.222 + j2.126	-j1.780·10^4
$\bar{z}_B$ (Ω)	3.146 + j3.744	3.146 + j3.744	-j1.779·10^4
$\bar{z}_{AB}$ (Ω)	2.899 + j2.501	2.899 + j2.501	19.338 + j8.408
$\bar{z}'_1$ (Ω/km)	0.452 + j0.409	0.452 + j0.409	3.003 + j1.306
$\bar{v}_A$ (V)	15857.5∠28.17°	39.5∠-169.80°	421.6∠-108.65°
$\bar{v}_B$ (V)	15811.0∠28.10°	42.7∠-175.38°	421.5∠-108.58°

In order to analyze how the equivalent circuit represents the transients under analysis, a solid fault is simulated in the middle of line 9 at t = 0 s. A comparison between the real network and the equivalent circuit is reported in Figure 3.32. The equivalent circuit reproduces well the dominant transient frequency, which was in principle its main purpose. The advantages are mainly two: i) the transient in the equivalent circuit is less damped; ii) it does not represent the wave propagation, i.e. it neglects reflections that influence the waveform. These two features make it easier to extract the dominant frequency. Moreover, the latter feature rends the simulation much faster, favoring a Monte Carlo analysis in which the fault location d, the fault resistance and the fault inception angle can be varied to preliminary establish the range of the dominant frequencies expected. Indeed, with a time-step of 1 μs, 100 ms of simulation took 59.14 s and 1.11 s with the real network and the equivalent circuit, respectively[1].

The value of f_{dom} in this case is 2.64 kHz.

The study is extended by simulating a sequence of faults in the middle of lines 2, 9 and 14 of Net-A, with fault resistance varying between 0 and 100 Ω in steps of 5 Ω.

Figure 3.33 shows the dominant transient frequencies estimated by using the equivalent circuit, together with the frequencies estimated by using the real network. The latter, considered as benchmark, show the reasonable accuracy of the results provided by the equivalent circuit.

[1] Simulations were carried out on a CPU with an Intel Core i7-7500U processor running at 2.70 GHz. In the further, when reference is made to processing or simulation times, it is intended that simulations are carried out on this computer.

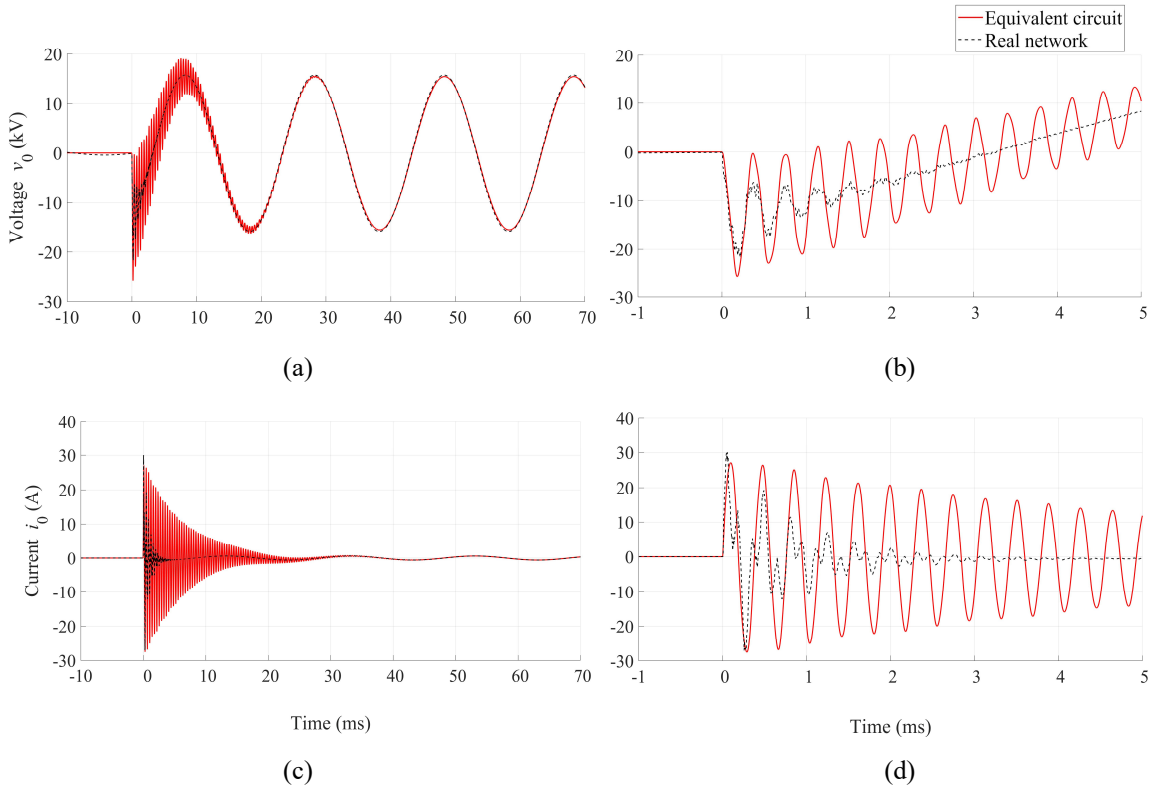

Figure 3.32 – Comparison between the equivalent circuit and the real network transient responses. Zero-sequence (a) voltages and (c) currents, zoomed in (b) and (d), respectively.

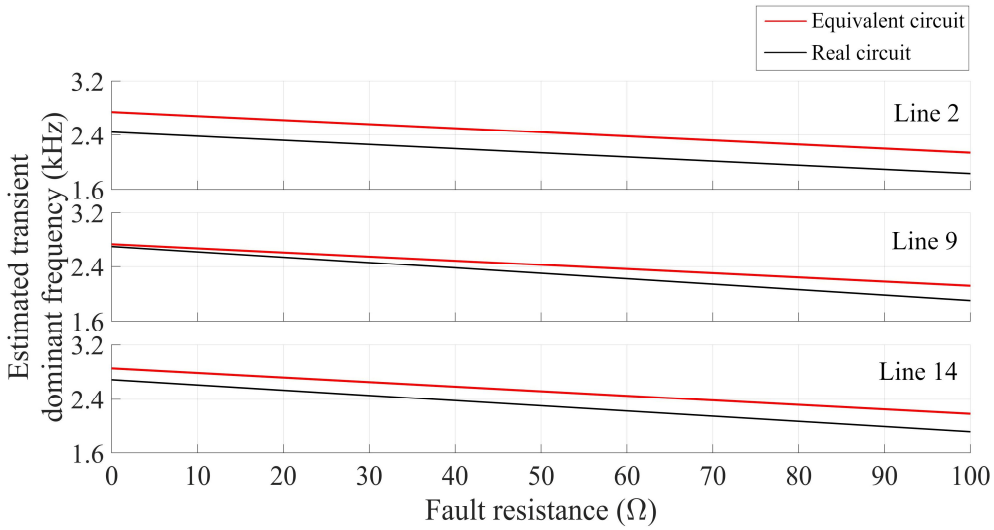

Figure 3.33 – Comparison between estimated transient dominant frequencies obtained with the real network and the equivalent circuit, for faults in different lines of Net-A [37].

The results of Figure 3.33 motivate the choice of a filter centered at 2.2 kHz (f_0) and a filter bandwidth (BW) equal to 2.2 kHz. This is also supported by the similar results obtained by repeating the analysis for all the other lines.

The time window is chosen so at least one cycle of the expected dominant transient frequency with the greatest period, i.e. the minor frequency, is framed. Due to the identified frequency range, a time window t_{win} of 1 ms is implemented.

From the analysis in radial networks, it has been established that for a fault in the forward direction, the earth-mode current at the dominant transient frequency leads the earth-mode voltage, ideally by 270°. Therefore, the *ideal* operation zone is between 180° and 360°. However, to decrease the probability of unnecessary trips a reduced operation zone is identified. This selection is done by simulating 500 faults in three different lines, namely lines 2, 9 and 14, with different fault locations, fault incidence angles and fault resistances in the range between 0 and 100 Ω. In Table 3-9 the proposed operation zone is reported, i.e. $\theta_{\min}$ and $\theta_{\max}$, that maximizes the protection performance in terms of expected rates of failures-to-trip and of unnecessary trips.

TABLE 3-9
PROTECTION SYSTEM PARAMETERS FOR NET-A

Filter f_0/BW (kHz)	2.2/2.2		
t_{win} (ms)	1.0		
$\theta_{\min} - \theta_{\max}$	220° – 350°		
$v_{0,\min}$ (kV)	1.5		
$i_{0,\min}$ (A)	0.2		
Faulted line	**Line 2**	**Line 9**	**Line 14**
Failure-to-trip rate	0.00%	0.00%	0.00%
Unnecessary trip rate	0.40%	0.00%	1.40%

To further validate the effectiveness of the considered operation zone, a Monte Carlo analysis is carried out in which a series of 2000 faults randomly distributed within the entire network are simulated. The fault incidence angles are varied over one power frequency period and the fault resistances between 0 and 100 Ω. The results show a 0.55% failure-to-trip rate and a 0.5% unnecessary trip rate.

The minimum peak values for v_0 and i_0 during the fault are 15.44 kV and 0.27 A, respectively.

Different angle values modify the results, either enhancing security by reducing the operation zone thus reducing the unnecessary trip rate; or enhancing dependability by enlarging the operation zone thus reducing the failure-to-trip rate. In Table 3-10 the results for different operation zones are summarized, obtained by varying the original angles by ±10°. The results obtained with a range between 180°–360° is also reported.

The average processing delay of the single relay was obtained from the computation time of all the simulated faults and all the relays of the network, and its mean value is equal to $\delta_{alg,proc}$ = 1.04 ms. For the evaluation of the relay operating time, it is known that f_s = 8 kHz and t_{win} = 1 ms. It follows from (3.18) that, $t_{PSTT} = t_{pu} + 5.38 + \delta_{com.}$ In Figure 3.34 the resulting histogram of the PSTTs is shown.

TABLE 3-10
MONTE CARLO RESULTS FOR NET-A OVER 2000 FAULTS

$\theta_{min} - \theta_{max}$	Failures-to-trip rate	Unnecessary trip rate	Mis-operation rate
180° – 360°	0.10%	7.55%	7.55%
220° – 350°	0.55%	0.50%	1.05%
210° – 360°	0.15%	0.95%	1.10%
230° – 340°	1.15%	0.25%	1.40%

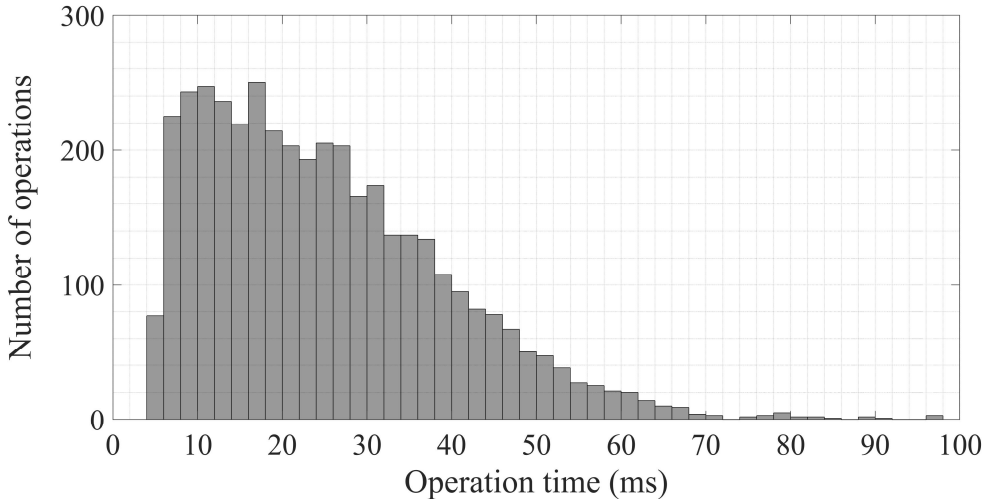

Figure 3.34 – Histogram of protection scheme tripping times for Net-A.

The protection system sends a trip signal mostly within three cycles from the fault initiation and does not exceed 100 ms even in the worst communication conditions.

i) Short lines

In order to highlight some network parameters that affect the protection performances, Net-A is again analyzed, this time considering that all lines have a length of 0.5 km instead of 3 km.

It can be seen from (3.9) that, for a specific network, shorter lines will result in both smaller equivalent capacitance and inductance, thus greater dominant frequencies. This is confirmed by the preliminary estimation of the dominant transient frequencies made with the equivalent circuit, which suggests the implementation of a filter centered at 7 kHz and with a bandwidth of 4.5 kHz.

To satisfy the Nyquist criterion the sampling frequency must be at least twice the highest expected frequency, thus a sampling frequency of 8 kHz is insufficient. A sampling frequency of 25 kHz is applied in this case.

Due to the identified frequency range, a time window t_{win} of 0.5 ms is implemented.

A Monte Carlo analysis is carried out in which again, a set of 2000 faults randomly distributed within the entire network is simulated. The fault incidence angles are varied over one power frequency period and the fault resistances between 0 and 100 Ω.

The characteristics of the protection system and the results obtained for different operation zones are reported in Table 3-11. The minimum peak values for v_0 and i_0 during the fault are 15.98 kV and 0.05 A, respectively. In this case, using a current threshold of 0.05 A or lower could result into a too sensitive protection. Hence, a larger value is used since the voltage threshold will activate the algorithm when the current is not large enough.

TABLE 3-11
PROTECTION SYSTEM PARAMETERS AND
MONTE CARLO RESULTS FOR NET-A – ALL LINES ARE 0.5 KM LONG

Filter f_0/BW (kHz)	7.0/4.5
t_{win} (ms)	0.5
$v_{0,min}$ (kV)	1.5
$i_{0,min}$ (A)	0.2

$\theta_{min} - \theta_{max}$	Failure-to-trip rate	Unnecessary trip rate	Mis-operation trip rate
180° - 360°	2.85%	12.00%	12.10%
220° - 345°	5.90%	3.50%	8.50%
210° - 355°	4.85%	6.65%	9.45%
230° - 335°	7.60%	1.55%	9.05%

The average processing delay of the single relay was obtained from the computation time of all the simulated faults and all the relays of the network, and its mean value is equal to $\delta_{alg,proc}$ = 1.32 ms. For the evaluation of the relay operating time, it is known that f_s = 25 kHz and t_{win} = 0.5 ms. It follows from (3.18) that, t_{PSTT} = 4.93 + δ_{com}. In Figure 3.35 the resulting histogram of the PSTTs is shown.

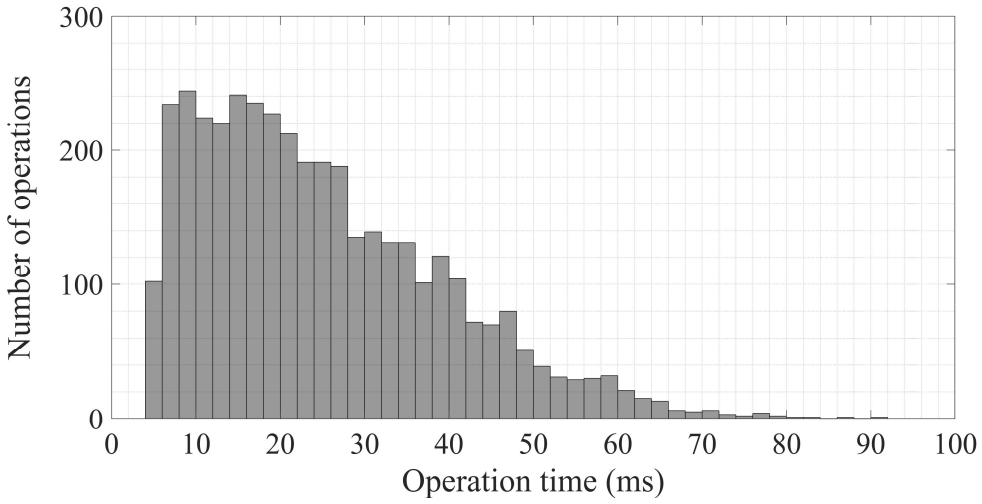

Figure 3.35 – Histogram of protection scheme tripping times for Net-A. All lines are 0.5 km long.

Also in this case, the protection system sends a trip signal in less than 100 ms even in the worst communication conditions.

b) Cable line distribution networks

The performance of the protection implemented in feeder A of Net-B in Figure 3.29 is analyzed, considering S1 open and S2 and S3 closed. Feeder A is meshed and includes only cable lines.

The analysis carried out by using the equivalent circuit suggests a filter centered at 0.5 kHz and with a bandwidth of 0.6 kHz. The lower frequencies than in the previous cases are due to the larger capacitances of the underground cables with respect to overhead lines. As a result, a time window of 5 ms is applied to consider at least one period of the lowest transient frequency.

For selecting the best operation zone, a series of 500 faults is simulated in lines 8 and 12 varying the fault incidence angle over one power frequency period, the fault resistance between 0 and 400 Ω and the fault location along the line. The main results are reported in Table 3-12.

TABLE 3-12
PROTECTION SYSTEM PARAMETERS FOR NET-B

Filter f_0/BW (kHz)	0.5/0.6	
t_{win} (ms)	5.0	
$\theta_{min} - \theta_{max}$	190° – 315°	
$v_{0,min}$ (kV)	1.5	
$i_{0,min}$ (A)	0.5	
Faulted line	**Line 8**	**Line 12**
Failures-to-trip	0.00%	0.00%
Unnecessary trips	0.00%	0.00%

For the Monte Carlo analysis[1], a set of 2000 faults randomly distributed within the entire feeder are simulated. The results show a 0.20% failure-to-trip rate and a 0.40% unnecessary trip rate. The total mis-operation rate is 0.40% since all the cases in which a failure-to-trip is verified, are also cases in which an unnecessary trip is registered. The minimum peak values for v_0 and i_0 during the fault are 7.55 kV and 1.70 A, respectively. The results obtained for different operation zones are summarized in Table 3-13.

[1] As no load is connected between them, both lines 4 and 5 of Figure 3.29 are protected by relays 4A and 5B. When a fault occurs at any point of these lines, the earth-mode current that flows through relay 4A is rather low with a very high transient dominant frequency, since values L_{eq} and C_{eq} are low as there are no other feeders connected to bus A and the relay 4A is close to the substation transformer. On the other hand, relay 4A does not need to be directional and operates whenever the measured current i0 exceeds the threshold and the permissive signal from 5B is received. The remaining setting parameters, as the time window, are equal to those of the other relays.

TABLE 3-13
MONTE CARLO RESULTS FOR NET-B OVER 2000 FAULTS

$\theta_{min} - \theta_{max}$	Failure-to-trip rate	Unnecessary trip rate	Mis-operation rate
180° – 360°	0.20%	0.85%	0.85%
190° – 315°	0.20%	0.40%	0.40%
180° – 325°	0.20%	0.60%	0.60%
200° – 305°	1.35%	0.20%	1.35%

The average processing delay of the single relay was obtained from the computation time of all the simulated faults and all the relays of the network, and its mean value is equal to $\delta_{alg,proc}$ = 1.36 ms. For the evaluation of the relay operating time, it is known that f_s = 8 kHz and t_{win} = 5 ms. It follows from (3.18) that, $t_{PSTT} = 9.70 + \delta_{com}$. In Figure 3.36 the resulting histogram of the PSTTs are shown.

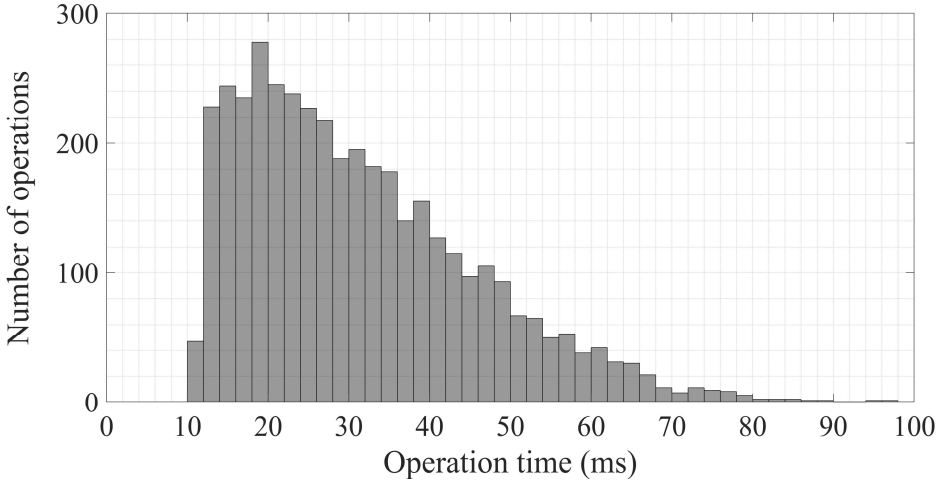

Figure 3.36 – Histogram of protection scheme tripping times for Net-B.

It is evinced from Figure 3.36 that the mean operation time is greater than in the previous cases due to the larger time window. However, the protection operates in less than 100 ms even in the worst communication conditions.

c) Hybrid distribution networks

An analysis is carried out in Net-B with all the switches closed, i.e. including overhead and cable lines.

It is worth analyzing the fault within line 3, as the earth mode current at the two line-ends has different behavior. Indeed, for such a fault, relay 3A will sense the current fed only by bus A through cable lines, while relay 3B will measure the current fed only by bus B through overhead lines. The impact of such differences is illustrated in Figure 3.37 in which the earth-mode currents at both ends of line 3 are compared when a fault occurs at 10.2 ms in the middle of phase-*a* with a 3 Ω fault resistance.

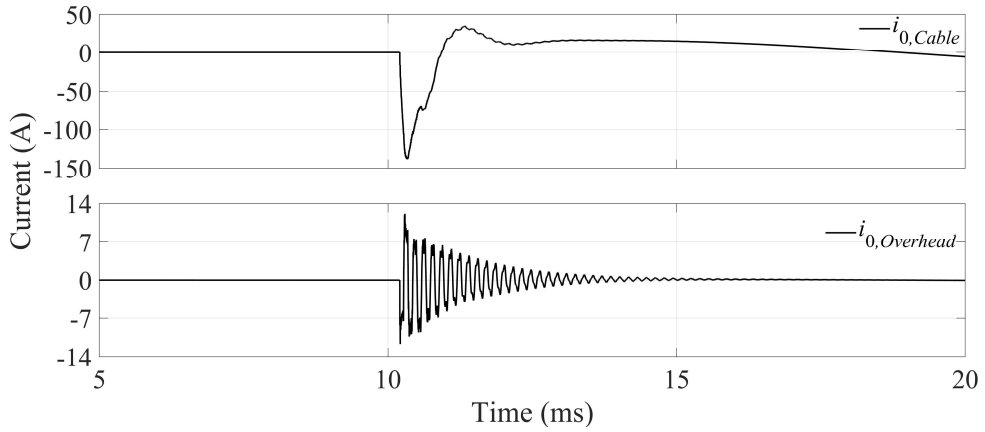

Figure 3.37 – Earth-mode currents measured at both ends of line 3 of Net-B [37].

The larger earth-mode current measured by relay 3A at the cable feeder side (the peak is about ten times that measured by relay 3B, i.e., the relay at the overhead line feeder side) is due to the lower zero-sequence impedance of cables.

The analysis carried out by using the equivalent circuit for these faults indicates the implementation of a filter in the relays of feeder B centered at 6 kHz and with a bandwidth of 3 kHz. These relays need a sampling frequency higher than 8 kHz, which is however appropriate for the relays in feeder A. Therefore, a sampling frequency of 20 kHz is used for the relays of feeder B.

A set of 500 faults is simulated varying the fault incidence angle over one power frequency period, the fault resistance between 0 and 400 Ω and the fault location along line 3. The main results are reported in Table 3-14 and show a 0.20% failure to trip rate and a 0.20% unnecessary trip rate. The total mis-operation rate is 0.20% since the fault that leads to a failure-to-trip is the same that leads to the unnecessary trip.

TABLE 3-14
PROTECTION SYSTEM PARAMETERS AND
MONTE CARLO RESULTS FOR LINE 3 OF NET-B

Relays of feeder A (cable lines)	**Filter f_0/BW (kHz)**	0.5/0.6
	t_{win} (ms)	5.0
	$\theta_{min} - \theta_{max}$	190° – 315°
	f_s (kHz)	8
	$v_{0,min}$ (kV)	1.5
	$i_{0,min}$ (A)	0.5
Relays of feeder B (overhead lines)	**Filter f_0/BW (kHz)**	6.0/3.0
	t_{win} (ms)	0.5
	$\theta_{min} - \theta_{max}$	170° – 350°
	f_s (kHz)	20
	$v_{0,min}$ (kV)	1.5
	$i_{0,min}$ (A)	0.5
	Faulted line	**Line 3**
	Failure-to-trip rate	0.20%
	Unnecessary trip rate	0.20%
	Mis-operation rate	0.20%

d) Robustness of the proposed algorithm

The influence of the operation zone has been analyzed in each case and it has been shown how by enlarging or reducing the operation zone the dependability or the security of the protection system can be enhanced.

In order to illustrate the robustness of the algorithm in front of the chosen filter both f_0 and BW are varied.

A fault in the middle of line 9 of Net-A is considered. Figure 3.38 shows the dominant transient frequency and the estimated angle for different f_0 values, estimated by a relay at one of the ends of the faulty line, and by a relay at one of the ends of Line 8, i.e., a healthy line. For the healthy line the dominant transient frequency identified by the DFT is different when $f_0 = 2.6$ kHz. The estimated angles in both relays do not vary significantly around the dominant transient frequency and do not differ considerably for filters with different f_0 values.

The value of BW has a limited influence too, as can be seen in Figure 3.39. Analogous results are obtained for the other lines and other fault locations.

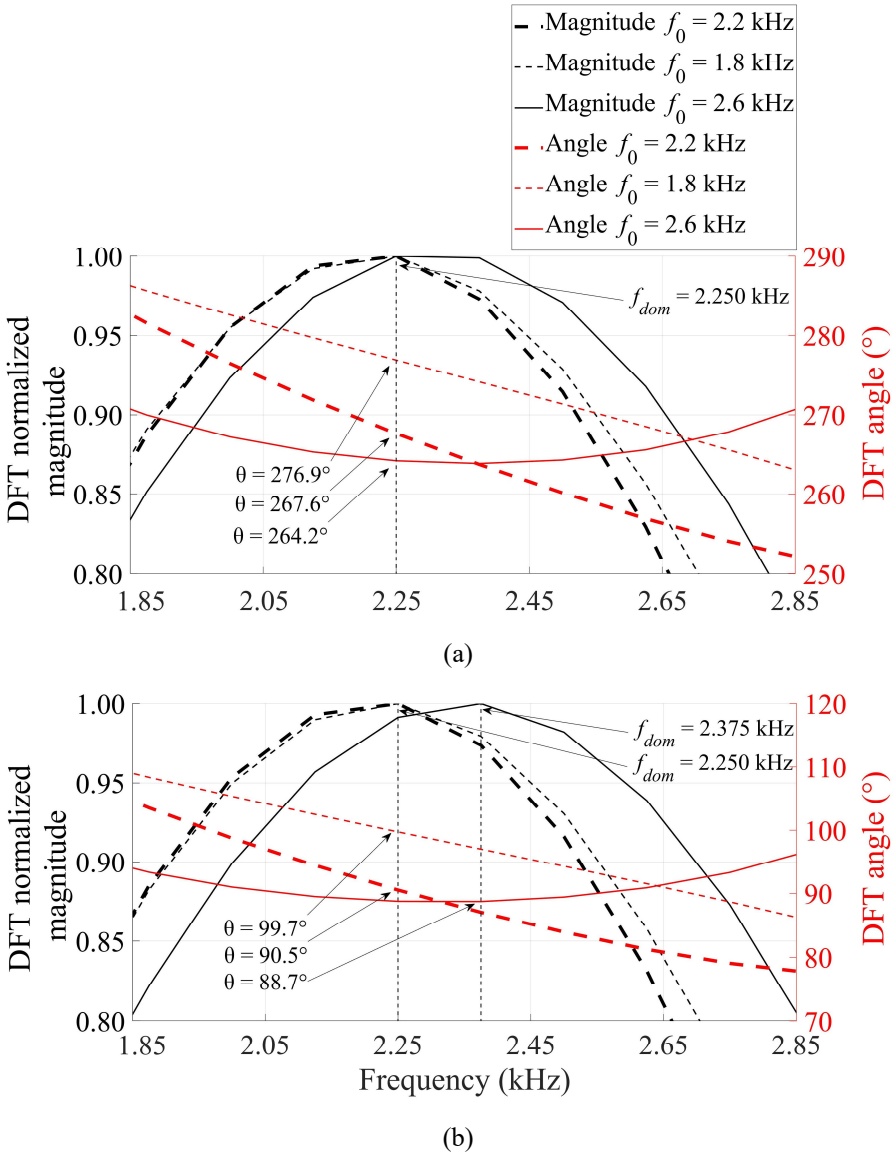

Figure 3.38 – DFT magnitudes and angles for different values of the filter center frequency f_0, estimated by relays at (a) the faulty line and (b) a healthy one. The DFT magnitude is normalized [37].

In some cases, if the *BW* value is too large then higher frequencies could be filtered in, with peaks greater than the expected transient frequency. This has been observed mainly in the radial distribution network when very high resistance faults occur.

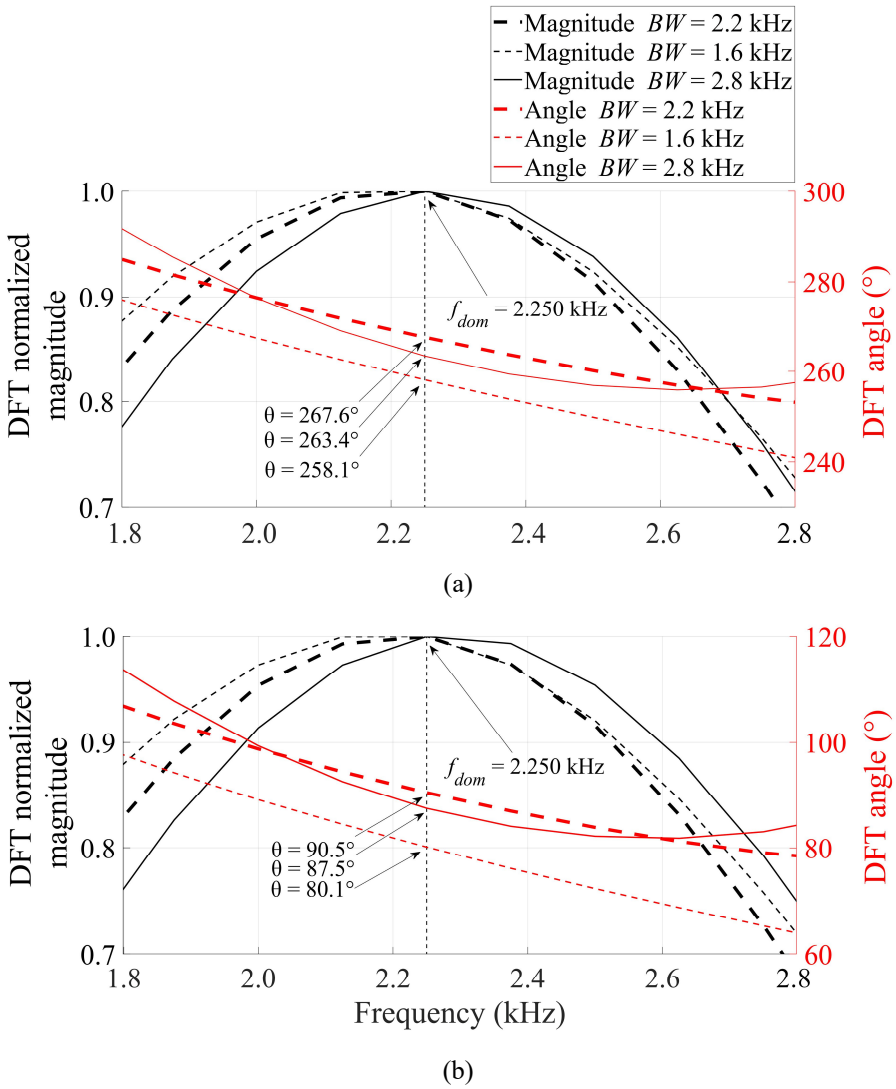

Figure 3.39 – DFT magnitudes and angles for different values of the filter bandwidth *BW*, estimated by relays at a) the faulty line and b) a healthy one. The DFT magnitude is normalized.

e) Impact of Distributed Energy Resources harmonics

In order to study the impacts of DERs on the protection algorithm, the cable feeder of Net-B is considered for the following reason. Since the filter implemented for Net-A has a center frequency of 2.2 kHz and a bandwidth of 2.2 kHz, it is expected that the filtered frequencies are between 1.1 and 3.3 kHz, which correspond to the range between the 22nd and the 66th harmonics. According to [20] harmonics introduced by DER units in this range have a maximum limit of 0.6% and 0.3% of the rated current (except for the 22th that has a limit of 1.5%), which are very low. For the cable feeder of Net-B instead, the chosen filter has a center frequency of 500 Hz and a bandwidth of 600 Hz. Thus, it is expected that the filtered frequencies are in the range between 200 and 800 Hz, which correspond to the range between the 4th and the 16th harmonics. Harmonics introduced by DER units in this range have a considerably greater maximum limit. For this reason, it is expected that the cable feeder of Net-B would be more vulnerable to the harmonics introduced by DER units (the same can be affirmed for very long overhead lines).

For a first approach, two DER units are introduced in Net-B at busses 2-A and 5-A.

Neglecting the power absorbed by the load connected at Bus A (which does not flow through any feeder branch), each DER unit feeds 11.4% of the total active power consumption.

The DER units for this study are represented by the sum of ideal current sources with different frequencies,

$$i = i_1 \cdot \cos(2\pi \cdot f + \phi) + \sum_{h=2}^{16} i_h \cdot \cos(2\pi \cdot hf + \phi) \tag{3.23}$$

where i_1 is the amplitude of the fundamental, i_h is the amplitude of the harmonic of h-th order, f is the fundamental frequency and ϕ is a phase shift.

The maximum allowed percentual values of the first 16 harmonics reported in [20] are considered, as detailed in Table 3-15. The limit of 5% given by the maximum Total Rated current Distortion (TRD) is ignored, which constitutes a conservative assumption.

TABLE 3-15
MAXIMUM HARMONIC CURRENT DISTORTION IN PERCENT OF RATED CURRENT

Harmonic order	2	3	4	5	6	7	8	9	10	11	12	13	14	15	16
Percent (%)	1	4	2	4	3	4	4	4	4	2	2	2	2	2	2

As the algorithm is based on zero-sequence quantities, it is expected that the inclusion of balanced harmonics will not have a significant effect. Therefore, also the inclusion of unbalanced harmonics is considered through multiplying factors k_a, k_b and k_c in the range 0 – 1 for phases-a, b and c, respectively, i.e.,

$$\begin{cases} i_a = i_1 \cdot \cos(2\pi \cdot f + \phi) + k_a \sum_{h=2}^{16} i_h \cdot \cos(2\pi \cdot hf + \phi) \\ i_b = i_1 \cdot \cos(2\pi \cdot f + \phi - \frac{2\pi}{3}) + k_b \sum_{h=2}^{16} i_h \cdot \cos(2\pi \cdot hf + \phi - \frac{2\pi}{3}) \\ i_c = i_1 \cdot \cos(2\pi \cdot f + \phi + \frac{2\pi}{3}) + k_c \sum_{h=2}^{16} i_h \cdot \cos(2\pi \cdot hf + \phi + \frac{2\pi}{3}) \end{cases} \tag{3.24}$$

With all the above considerations, the following 5 scenarios are studied, in which a fault is simulated in the middle of phase-a of line 12 at t = 40.6 ms:

- Scenario A: no harmonics
- Scenario B: maximum injection of balanced harmonics (k_a = 1; k_b = 1; k_c = 1)
- Scenario C: injection of current harmonics is slightly unbalanced (k_a = 1; k_b = 0.95; k_c = 0.9)

- Scenario D: injection of current harmonics is very unbalanced, with the lowest harmonic injection at the faulted phase ($k_a = 0.15$; $k_b = 0.6$; $k_c = 1$)
- Scenario E: injection of current harmonics is very unbalanced, with the highest harmonic injection at the faulted phase ($k_a = 1$; $k_b = 0.6$; $k_c = 0.15$)

The phase-*a* current injection by one DER unit and the zero-sequence current measured by one relay at the faulted line are shown in Figure 3.40. The influence of the harmonic injection on i_0 is barely noticeable. The angles estimated by all relays for all scenarios are reported in Figure 3.41.

There is no substantial influence of the harmonic injection, either in i_0 or in the angles. The greater deviations are registered in scenarios D and E, i.e., in which the unbalance of current injection is more significant. Therefore, the deviation depends mainly on the grade of harmonic unbalance rather than only the TRD.

Scenarios A and E are repeated increasing the DER penetration. Instead of two DER units, seven DER units are connected at busses 1-, 2-, 4-, 5-, 6-, 8- and 9-A, constituting 79.8% of the total active power consumption (neglecting the power consumption of the loads connected at bus A). The estimated angles are shown in Figure 3.42. The differences are still very low, and the protection operates correctly.

Other issues regarding DER units connected to distribution networks must be addressed and foment future work in this matter: i) influence of the disconnection of DER units due to the fault on the protection performances; ii) influence of the control strategies of power converter-interfaced DER units, such as e.g. fault current limiting strategies; iii) protection performance during islanding transition; iv) protection performances facing faults in islanded systems both with and without rotating generators; v) protection robustness against non-fault transients such as load rejection.

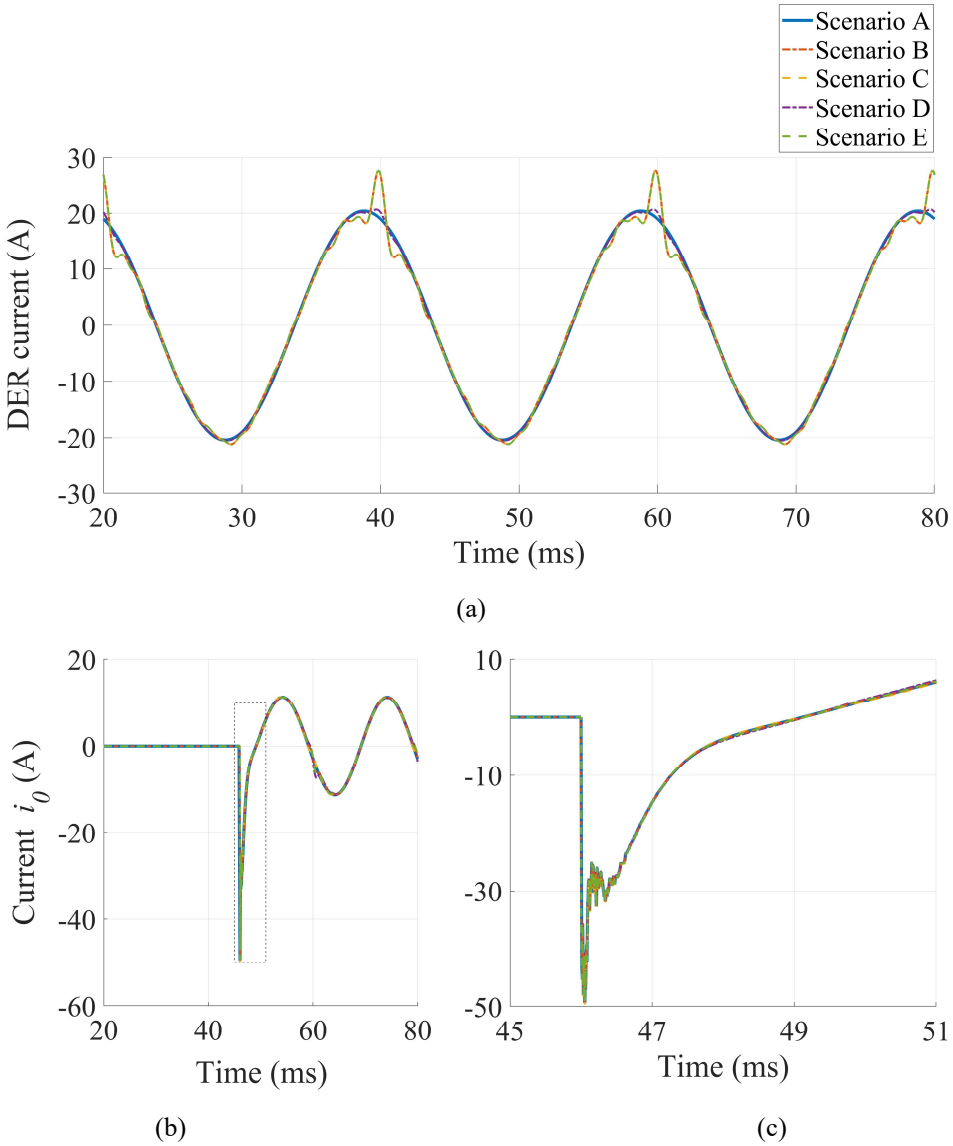

Figure 3.40 – Influence of harmonic content on (a) phase-*a* current injected by a DER unit, and; (b) zero-sequence current measured at one line-end of the faulted line, zoomed-in in (c).

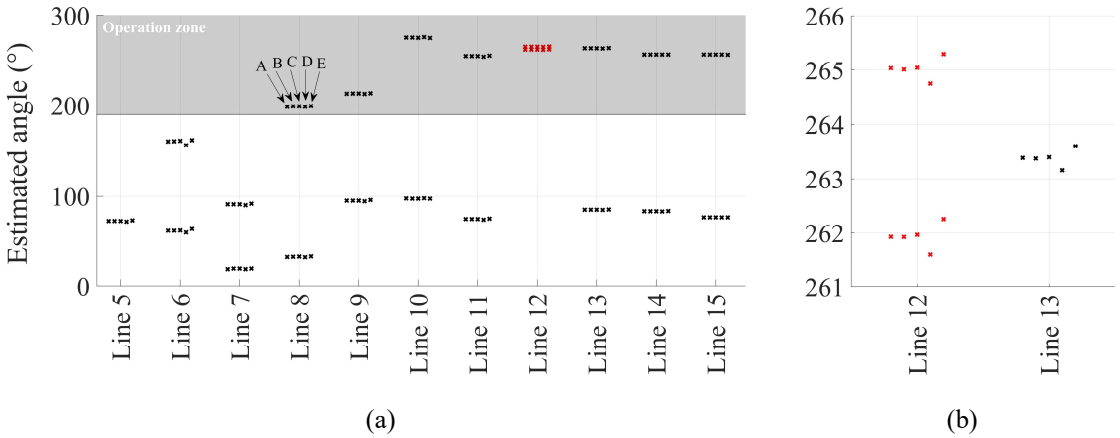

Figure 3.41 – Estimated angles by (a) all lines, and (b) the faulty and a healthy line, in all the scenarios of harmonic injection.

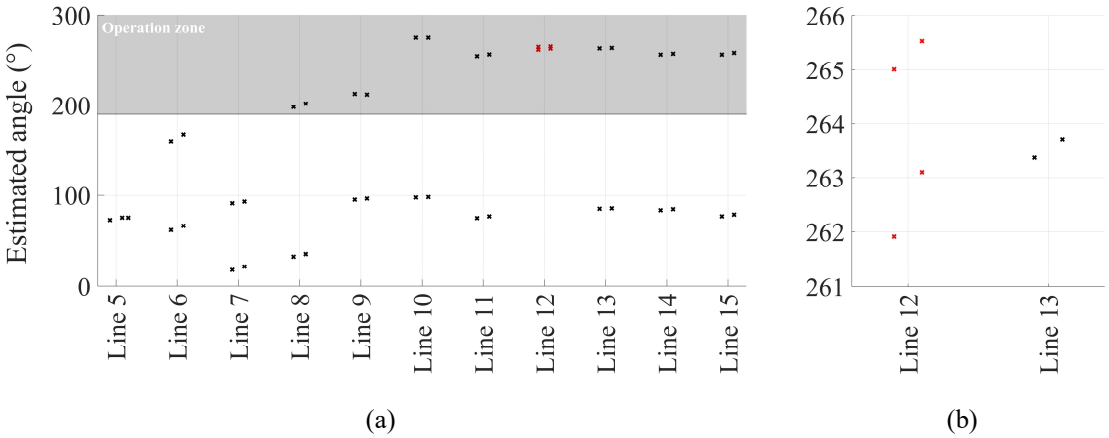

Figure 3.42 – Estimated angles by (a) all lines, and (b) the faulty and a healthy line in scenarios A and E with high DER penetration.

3.3 Real-time simulations

To further illustrate the applicability of the protection algorithm, i.e., demonstrate that the algorithm can perform all the required calculations (filtering, zero-padding, DFT, etc.) in operational times, some results obtained by performing real-time simulations are presented in this Section.

The main objective of real-time simulations is to solve the power system model equations and the relevant control and protection actions for one time-step within the same time in real world [77]. It computes the system states at certain discrete times using a fixed time-step. If the execution time is greater than such time-step size, an overrun is registered, and the performance of the simulation might be compromised. In this sense, while the objective of a typical simulation is to reduce as much as possible the *total simulation time*, the objective of real-time simulation is to reduce as much as possible the *maximum time-step* [78].

The power system and the protection algorithm are both implemented in the Opal-5600 RT simulator of the Smart Grids and Electric Vehicles Laboratory of the INESC TEC Institute. The cable feeder of Net-B is considered, i.e., the network of Figure 3.29 with switches S1 open and S2 and S3 closed.

In the following, some characteristics of the Opal-RT environment relevant to the simulations are pointed out.

3.3.1 Opal-RT simulator

The environment RT-Lab on which the Opal-RT simulator runs is fully integrated with Matlab/Simulink. Hence, the studied network has been fully reproduced in the Simulink environment.

The *ARTEMiS* (which stands for *Avanced Real-Time ElectroMechanical Simulator*) add-on enables the real-time simulation of *Simscape* models [79], which include e.g., advanced line models such as the CP or the FD ones. However, the minimum time-step attainable by the employed simulator is 20 µs. Since CP- and FD-line models would require time-steps of less than one microsecond due to the short length of the cables in the considered network, a pi-equivalent model is necessarily implemented to represent the lines. Moreover, to avoid overruns during the simulation a time-step of 62.5 µs is used.

It is worth mentioning that for the real-time simulation, relays have been simulated in all lines, i.e. 22 relays have been divided among 3 CPU cores of the Opal-RT. A fourth core was reserved for the power system model. Simulating a minor number of relays would have resulted in better performances from the time-step point of view, at the expense of analyzing the behavior of smaller portions of the network.

a) Comparison between line models

Before going further, a comparison is necessary to ascertain that the results obtained using a pi-model do not differ considerably from the simulations using more accurate models as the CP- or the FD-line ones.

For this purpose, a fault is simulated in the middle of line 8 with a 10 Ω fault resistance. The simulations with CP- and FD-models are carried out with a step time of 0.2 µs, while a step time of 62.5 µs is used for the pi-model. The zero-sequence currents measured by one side of the faulted line are shown in Figure 3.43.

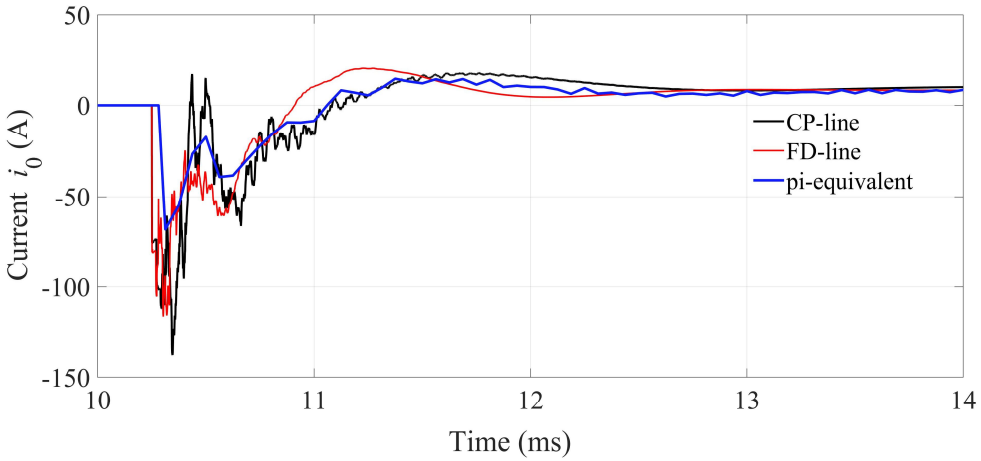

Figure 3.43 – Comparison between zero-sequence currents measured at one line-end of the faulted line by implementing different line models.

For the angle estimation a sample-rate conversion is applied to obtain a sampling frequency of 8 kHz for the relays. The estimated angles by both sides of each line are shown in Figure 3.44. A very good correspondence is found for most of the cases. Moreover, for the simulated fault, the protection operates properly, since the only line which both relays sense the fault in the forward direction are those of the faulted line, i.e., line 8.

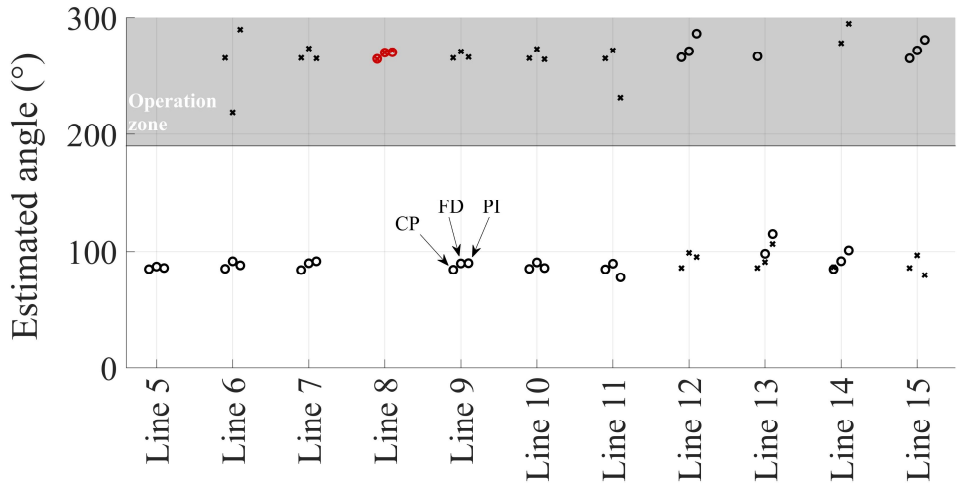

Figure 3.44 – Comparison between estimated angles by implementing different line models.

3.3.2 Assessment of the protection algorithm

For the real-time simulation, a fault is simulated in the middle of line 8 at t = 10 s with a 10 Ω fault resistance. The communication delays are also considered. In Figure 3.45 and Figure 3.46 the phase and zero-sequence currents measured at both ends of line 8 and the trip signals are reported.

When the fault occurs the current measured at both line-ends of the faulted phase flow in the same direction (from the bus into the line) as happens with phase-*a*. For the healthy phases instead, one of the ends will see the current flowing into the line, and the other end will see the current flowing into the bus, thus in opposite directions, as happens with phases-*b* and *c*.

The protection operates properly, opening only the breakers at both sides of the faulted line.

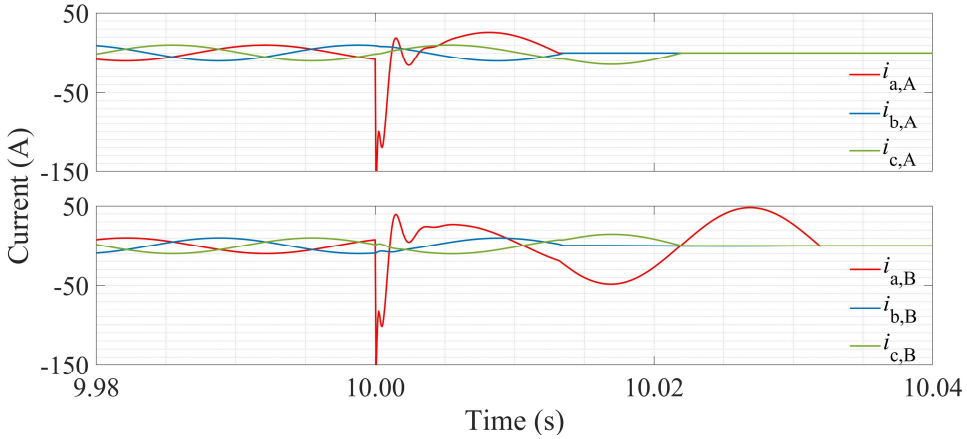

Figure 3.45 – Phase currents measured at both ends of Line 8 due to a fault in the middle of phase-*a* [37].

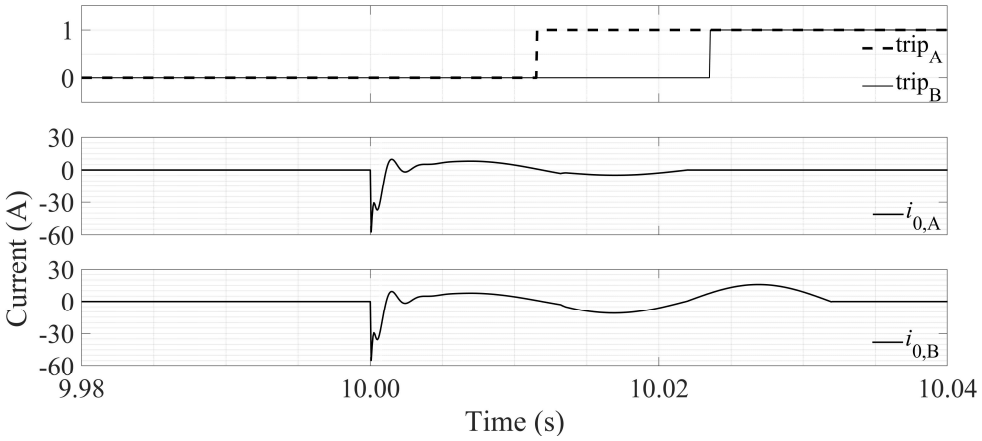

Figure 3.46 – Trip signals and zero-sequence currents measured at both ends of Line 8 due to a fault in the middle of phase-*a* [37].

3.4 Limitations and overcomes

One of the most critical limitations of the proposed algorithm is the relatively high failure-to-trip and unnecessary trip rates in very small distribution networks. Moreover, since the expected dominant transient frequencies in such networks are high, a proportionally high sampling frequency is required, since it has to comply with the sampling theorem. These two disadvantages of small distribution networks must be addressed. A possibility lays on the identification of the dominant transient frequency through other methods different from the DFT.

In meshed networks, the need of communication links can be perceived as a disadvantage. However, due to the evolution of smart grids involving other functionalities, communication networks are becoming very diffused and in constant evolution. Moreover, fiber optic networks are spreading, which brings huge advantages in terms of maximum latency, which in turn becomes advantages in terms of tripping times.

The need to install two relays per line to isolate only the faulted branch makes the proposed solution more costly, also due to the expenditures in measuring devices. However, this requirement is needed to fully exploit the benefits of the meshed network configuration. Several low-cost voltage and current sensors are available in the market, but its applicability together with the proposed protection is yet to be verified.

In this Chapter an algorithm for the protection of distribution networks against single phase-to-earth faults has been proposed and assessed. The algorithm identifies the directionality of the fault by estimating the angle between the zero-sequence voltage and current phasors at the dominant transient

frequency in the first milliseconds after the fault. The implementation of a filter and a zero-padding process to the input signals enhances the protection performance.

Different MV radial and meshed networks have been considered for the assessment of the protection performances, varying topology and line configurations, considering unbalanced loads and lines, as well as overhead and underground lines. For meshed networks a communication network has been considered in order to isolate only the faulty section without causing any customer outage.

The assessment of the performances of the protection system has been carried out by Monte Carlo simulations, varying the fault resistance, the fault incidence angle, and the fault location within the networks. The expected protection speed is particularly good for both radial and meshed networks. Furthermore, real-time simulations demonstrate that the algorithm can perform all the required processing in operational times.

CHAPTER 4

OVERVIEW OF CONTROL STRATEGIES OF DERS IN DISTRIBUTION NETWORKS AND MICROGRIDS

During the planning stage of distribution networks, they were traditionally designed to operate in all possible combination of load and generation levels in order to minimize the required control and monitoring. To accomplish this, load flow studies were carried out considering the worst-case scenarios in order to tackle all the potential issues during the planning stage and minimize the actions needed during the operation stage, resulting in passive networks. This approach is known as *fit and forget* [80], [81].

In the last couple of decades, the power system in all its levels, including MV and LV distribution networks, has been and it still is seat of a massive deployment of DER units. The *fit and forget* approach is not suitable for modern distribution networks since it limits the DER hosting capacity, and capital expenditures of the DSO for network reinforcement might increase. On the contrary, if distribution networks, and DERs with them, are integrated also in the operation stage, i.e. an ADN management strategy is implemented, many potential benefits can be obtained [49], [81]–[85]:

- Increase of DER hosting capacity – In the *fit and forget* approach the hosting capacity is estimated based on worst-case scenarios, in which e.g., the DG unit output is always maximum even in low demand conditions. In ADNs, the output of DG units and ESSs is controlled, and fundamental quantities as node voltages can be monitored. In consequence, power may be

curtailed during the worst-case scenarios, allowing the connection of more DERs at the relevant distribution network. Moreover, network reconfiguration is possible in ADN.

- Active losses could decrease, depending on the scenarios, as well as overloads – If DERs provide local loads, it could result in significant reduction of line losses, peak demands and overloads. This effect is much significant if the DER power output closely matches the local load and is located near to it. This is one reason why the sizing and siting problem of DERs is a current issue.
- Reliability improvement – DERs can be employed to supply critical loads in the case of outage of the main grid. However, proper operational strategies must be implemented in order to fully exploit such an advantage.
- Reduction of carbon emissions – With respect to fossil fuels, DERs have a minor environmental impact, whether this advantage comes from low-carbon emission systems, e.g., wind energy and PV power plants, whether it comes from enhanced efficiency, e.g., Combined Heat and Power (CHP) systems.
- Improvement of asset utilization and deferral of asset replacement – The possibility of dispatching the power coming from DERs, control the position of On-Load Tap Changers (OLTCs) and voltage regulators, reconfigure the network, among other functions inherent of ADNs optimize the asset utilization.
- Deferral of network reinforcement – The growth of load consumption might be compensated by the DG locally, avoiding e.g. the need of new transmission lines or large power plants or the upgrade of distribution transformers.

Likewise, many challenges from the power system point of view must be still dealt with. Among the main ones:

- Active losses could increase, depending on the scenarios – If DERs are located far from the substation and deliver power towards the substation or even back to the bulk transmission system, losses might increase in the distribution network. This effect is more important as more important is the reversed flux of power. On the contrary, losses would reduce on the transmission network. Proper network reconfiguration algorithms deal with this issue.
- Network reinforcement – The increase of current flows in the distribution network due to DERs could require the upgrade of the distribution system, not only in terms of power lines capacity but also CBs rating. Indeed, DG units contributes not only to the steady-state current but also to the short-circuit currents in the network.
- Voltage rise effect – In the *fit and forget* approach the load profile is assumed to follow a predictable pattern and the voltage profile is expected to regularly decrease because of load consumption along the feeder. The injection of power by DERs within the feeder changes this

paradigm modifying the voltage profile which could result in the violation of its limits at some points.

- Power quality – The main issues regarding power quality are related to voltage variations and harmonic distortion. Due to the variability of the prime source, most Renewable Energy Sources (RESs) produce voltage and power fluctuations. ESSs are an optimal solution to this problem at the expense of installation and maintenance costs. Moreover, DERs introduce harmonic and inter-harmonic components, mainly those units that are interfaced to the network through power converters.
- Protection – Many issues regarding the protection system needs to be dealt with, e.g.: i) protection coordination; ii) anti-islanding functions might be needed in several systems; iii) feeder protection from fault currents supplied by the DERs; iv) protection of the DER units against internal faults; v) directionality identification vi) protection of spot networks. Moreover, the short circuit current level varies with the integration of DER units and depends on whether the DER units are connected to the system or not, which might require a permanent adaptation of the protection settings.
- Stability – The large deployment of inverter-interfaced DERs leads to an overall decrease of the system inertia, crucial for the system stability. The stability might be also compromised due to the protection intervention of a DER unit leading to its disconnection after the occurrence of an external disturbance: the DER is disconnected in the moment in which the system most requires it to remain connected. The disturbance is not necessary a fault. As already mentioned, the intermittency of RESs units causes voltage fluctuations and voltage sags that could lead to the sudden disconnection of DERs. These effects are more harmful as higher is the disconnected DER rating and certainly the penetration level.
- Service restoration – During the normal service restoration of a distribution system in which DERs were connected before the outage, the load demand appears before DER units are reconnected. This procedure may cause overloads and other related issues during the service restoration, for which specific procedures need to be implemented.

Notice that some potential benefits are also reported among the current challenges. Indeed, the benefits are often dependent on how challenging issues are dealt with.

Moreover, there are commercial and regulatory issues which coping strategies are in constant evolution and under discussion, but they are disregarded in this thesis.

4.1 Control architecture

To cope with the challenges imposed by the increased amount of DERs connected to the distribution network, an advanced DMS needs to be implemented. It constitutes the core of ADNs, and it is aimed at controlling and optimizing the operation of the distribution network, comprehensive of the operation of DERs but also of controllable loads if present. The information coming from Advanced Metering Infrastructures (AMIs) is a resource that might be also present in the DMS. The level of complexity of DMSs and the relative functionalities vary in literature. The DMS can be very basic e.g., aimed at disconnecting the DERs, reconfiguring the network when required or changing the OLTC tap of the substation transformer; or it can be very complex in which functionalities like volt/var optimization, state estimation and dispatch optimization are implemented.

In this context, MGs constitute an active cell of the ADN that can operate in both grid-connected and standalone (islanded) operation modes [86]. The first definition of MG is given by the *Consortium for Electric Reliability Technology Solutions (CERTS)*, for which the MG is "*an aggregation of loads and microsources operating as a single system providing both power and heat. The majority of the microsources must be power electronic based to provide the required flexibility to insure operation as a single aggregated system. This control flexibility allows the CERTS MicroGrid to present itself to the bulk power system as a single controlled unit that meets local needs for reliability and security*[1]" [87]. This concept, given in 2002, was initially applied only to the LV level. However, such constraint does not longer exist in other definitions such as the one given by the IEEE Std. 2030.7 [88], and the MG concept has been extended to the MV level, whether it be MV-MGs [89], which concept is the same as LV-MGs, or MMGs [90] that cluster several LV-MGs and includes parts of the MV network mainly for interconnection purposes. MMGs have a higher architecture level in which single DER units and controllable loads not belonging to a MG can also be part of the MMG structure.

The differences between these concepts are illustrated in Figure 4.1 that shows a schematic layout of the control and management architecture of the three different systems, namely a typical distribution system, a MG (whether it is LV or MV) and a MMG [90], [91].

The typical distribution system is controlled only by the DMS. It is mainly responsible of the CB at the PCC and in some cases also of some critical loads. Notice that with this architecture, the standalone operation mode is not possible.

[1] At the moment this definition was given, the project was focused in microturbines with rating less than 500 kW, hence the *microsources* specification. However, it was already expected that larger sources could play a role in MGs.

The MG introduces a new local control level, provided by the Microgrid Central Controller (MGCC) which provides the interface between the MG and the DMS. It can control and monitor the DERs and the eventual controllable loads present in the MG. It also monitors the state of the CB at the PCC, thus the operation in grid-connected and standalone modes are possible (the standalone mode depends also on other factors as, e.g., the local energy production).

The MMG introduces another control level, provided by the Central Autonomous Management Controller (CAMC, the denomination Smart Grid System Operator can also be found in literature). Notice that the DMS can still have direct connection with other MGs, i.e., the MG and the MMG architectures are not mutually exclusive but can coexist.

In the architectures of Figure 4.1 the AMI has not been reported. Indeed, smart meters from DERs and loads could directly report to the DMS in all cases, i.e., not necessarily through the MGCC or the CAMC.

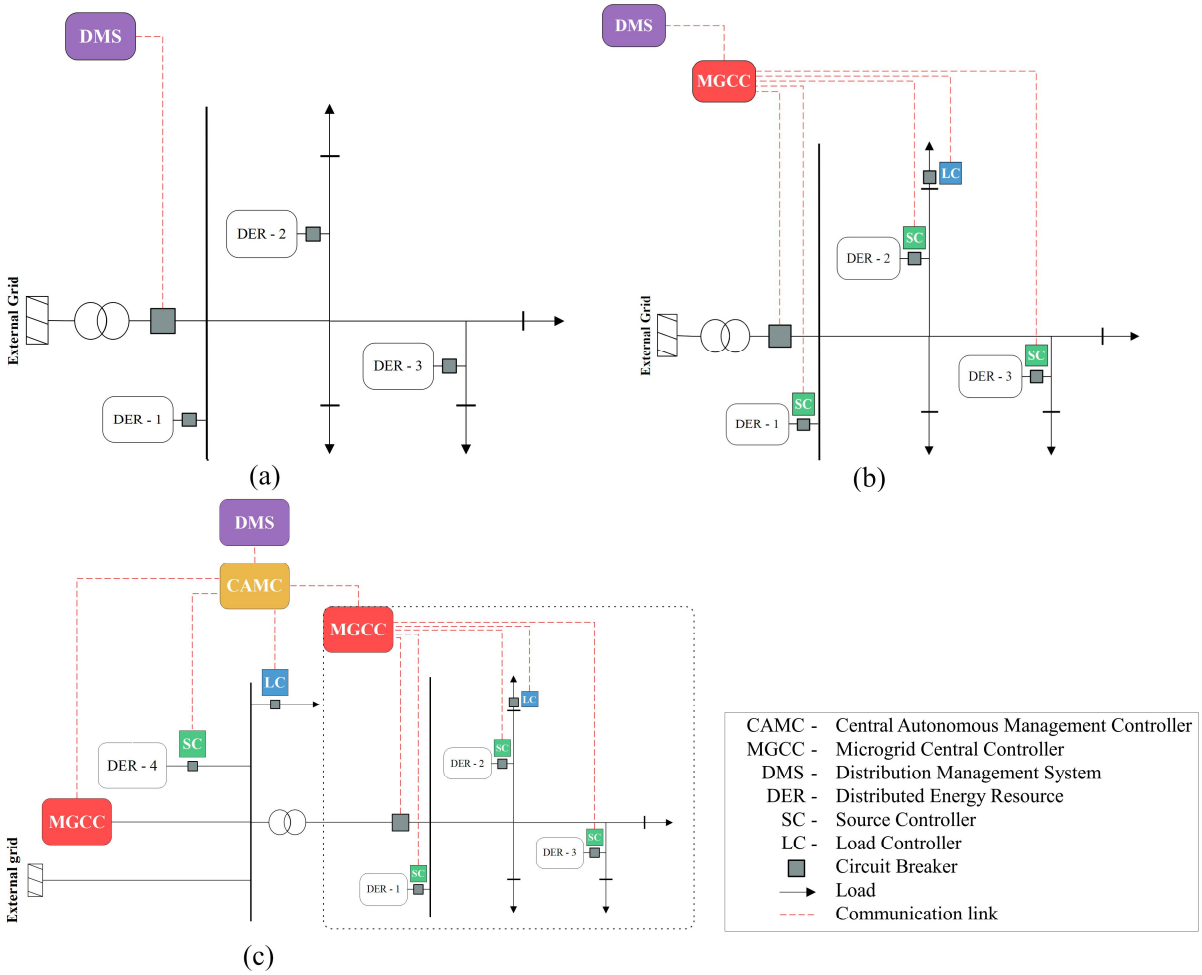

Figure 4.1 – Schematic layout of the control and management architecture of (a) a typical distribution network, (b) a MG and (c) a MMG (Adapted from [90]).

The contributions of this thesis focus on the transient response of MV-MGs for which some characteristics of the architecture of Figure 4.1b are further explored below.

The MGCC must be: i) scalable, to allow the integration of a large number of users; ii) open architecture, to allow the integration of components of a vast variety of sellers; iii) *plug and play*, to allow the easy installation of new components; iv) flexible, to allow the easy integration of new functionalities.

The MGCC is placed in the substation in which the PCC between the MG and the external grid is located. Depending on its role it can execute, as well as the DMS in traditional distribution systems, basic or advanced functionalities, e.g.: i) coordinate the local DG production by providing the relevant setpoints; ii) manage the charge/discharge of the ESSs; iii) operate the insertion of bank capacitors; iv) operate the CBs inside the MG for network reconfiguration purposes; v) operate the CB at the PCC for the transition to the standalone operation mode; among others. The setpoints could be the result e.g., of an optimization process as well as the network reconfiguration could be the result e.g., of a volt/var optimization, both carried out also by the MGCC.

To achieve all these functionalities, a typical approach is to consider a hierarchical control scheme divided in three levels as illustrated in Figure 4.2, namely a primary, a secondary and a tertiary control level, which differ one from the another by the speed of response, the time frame in which they operate and the communication requirements [6].

The primary control level performs the fastest response. It is responsible, among others, of power sharing and balancing. Since the stability of a MG is dominantly defined by the primary control [92], control strategies based on local variables such as frequency and voltage are preferred, e.g. droop-based control schemes. Indeed, fast communication links should be avoided, not only because of the expensive cost but also because the criticality they would entail.

Since primary control is performed locally, it depends only on the control scheme applied to the single DERs and eventual controllable loads that participate in the frequency and voltage control. The secondary and tertiary control level are responsible of the reliable, secure and optimal operation of MGs. The tasks of secondary and tertiary control levels are performed by the DMS, the CAMC and the MGCC, depending on the adopted strategies.

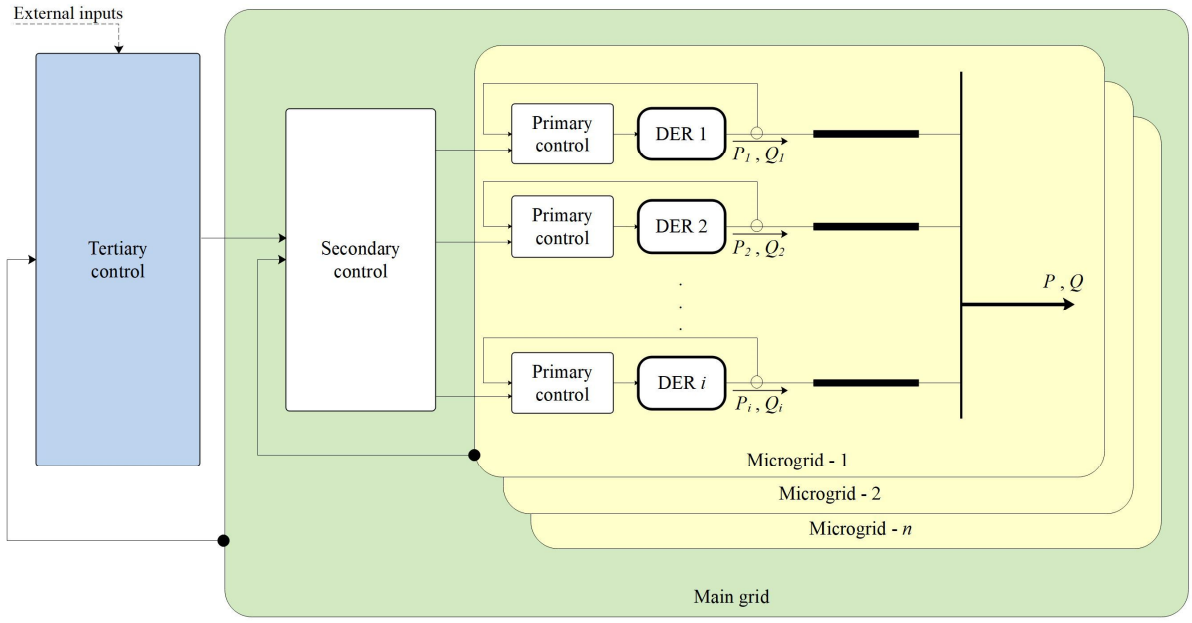

Figure 4.2 – Hierarchical control layers (Adapted from [6]).

Since the thesis focuses on transient events, the primary control and secondary control are represented, while the tertiary control is disregarded.

4.2 Microgrid operational strategies

As already stated, MGs must be able to work either in grid-connected or standalone operation modes. The control strategies needed to guarantee the MG stability depend on the operation mode. Three different scenarios can be described:

- In grid-connected mode the frequency and voltage are imposed by the external grid. Therefore, the problem of stability mainly consists of the stability of individual components such as a particular DER or a set of local loads, e.g., Induction Motors (IMs). Their impact on the system is also of interest.
- In standalone mode with at least one Synchronous Generator (SG) connected directly to the MG, it is the one that gives the frequency and voltage reference to the system using conventional exciters and governors. The inherent inertia of the rotating generator plays an important role in the primary control, as in conventional power systems.
- In standalone mode with only inverter-interfaced DERs, i.e., inertia-less MGs, for a secure operation at least one of the DERs must give the frequency and voltage references to the system.

Moreover, the transition between both operation modes must be guaranteed in both senses, i.e., from grid-connected to standalone mode (islanding) and vice versa (synchronization with the grid).

In the following, the different strategies implemented to the control of the inverters are illustrated, in order to achieve the above-mentioned objectives.

4.2.1 Power converters

Most DER units utilize Voltage-Sourced Converters (VSCs) as interface to the grid [93] which can be controlled following two different strategies:

- Grid-following control mode (*PQ*-mode): the inverter is a Current-Controlled VSC (CC-VSC), controlled to supply/absorb active and reactive power following given references. The user references (i.e., the MGCC or DMS imposed references) are not necessarily the active and reactive powers. This mainly depends on the dispatchable nature of the primary source [94]. For non-dispatchable sources, e.g. PV units, the user reference is the DC-link voltage from which the active power reference is derived from relations that are developed further in this Chapter. For dispatchable sources, e.g. microturbines or Battery Energy Storage Systems (BESSs), both active and reactive power are imposed by the user.
- Grid-forming control mode (*Vf*-mode): the inverter is a Voltage-Controlled VSC (VC-VSC) or Voltage Source Inverter (VSI), controlled in order to provide the system with voltage and frequency references. The active and reactive power supplied/absorbed will depend on the load.

Regarding the three scenarios described above, the following observations are made:

- In grid-connected mode, since the external grid provides the reference of voltage and frequency, usually inverters are controlled in the *PQ*-mode.
- The same occurs for standalone MGs with at least one SG.
- In standalone inertia-less MGs, at least one of the DERs must be controlled in the *Vf*-mode. Two control strategies are possible [95], namely single-master operation, for which only one DER is controlled in the *Vf*-mode and the rest in the *PQ*-mode, and multi-master operation in which more than one DER is controlled in the *Vf*-mode with defined droop constants.

With respect to traditional bulk systems, switching operations, load connection and disconnections, and other types of disturbances in islanded MGs result in larger frequency and voltage deviations, as can be seen in Figure 4.3. The time intervals in which the three control levels operate are also different. Indeed, the dynamics of islanded MGs are much faster.

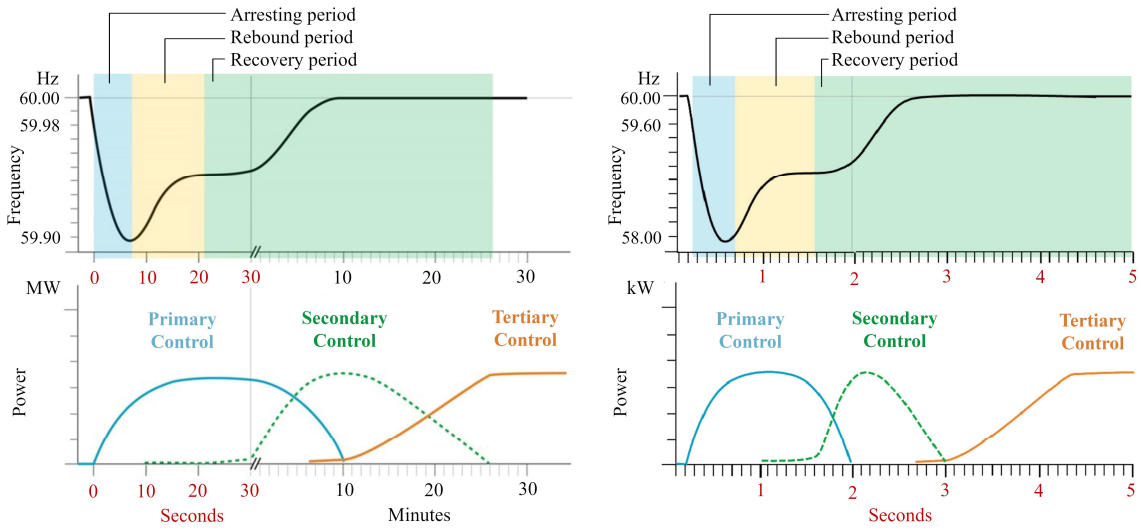

Figure 4.3 – Behavior of primary, secondary, and tertiary frequency responses following a large step-increase in load (a) in a traditional system and; (b) in a standalone MG (Adapted from [96], [97]).

a) Droop control strategy

It has been stated that for primary control, strategies based on local measurements are preferrable, e.g., a droop control strategy.

Droop control strategy can be applied for both grid-following and grid-forming modes [98], but their nature are different. In the grid-following mode the measured frequency (f) and voltage (v) modify the active and reactive power setpoints, respectively, in order to respond accordingly to generation/load variations, as follows,

$$P^* = P_{ref} + \frac{1}{k_P}\left(f_{ref} - f\right) \tag{4.1}$$

$$Q^* = Q_{ref} + \frac{1}{k_Q}\left(v_{ref} - v\right) \tag{4.2}$$

where f_{ref}, v_{ref}, P_{ref}, and Q_{ref} are the reference values for the frequency, voltage, active and reactive powers, respectively; k_P and k_Q are the droop constants for active and reactive power control, respectively; and P^* and Q^* are the reference values modified by the droop control. The droop characteristic for this control strategy is shown in Figure 4.4.

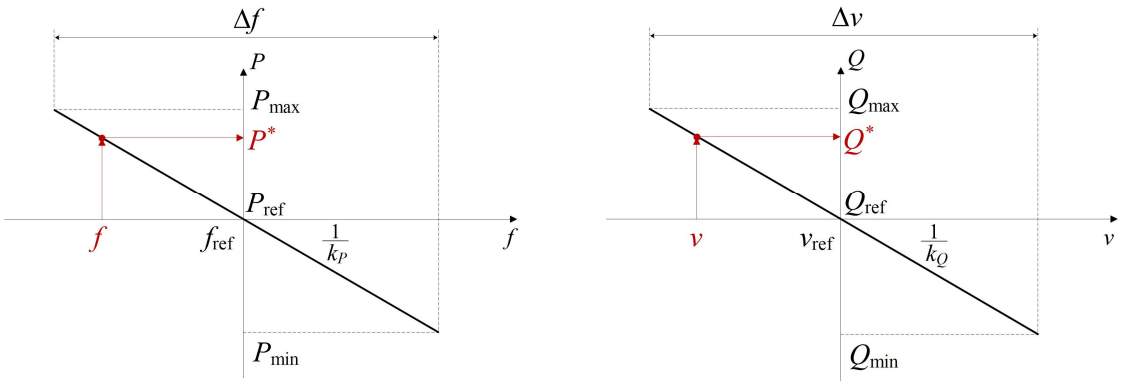

(a) (b)

Figure 4.4 – (a) Active power/frequency and (b) reactive power/voltage droop characteristics of grid-following units.

In the grid-forming mode instead, the active and reactive power modify the frequency and voltage setpoints, respectively. Indeed, the voltage and frequency references are modified as follows,

$$f^* = f_{ref} + k_P \left(P_{ref} - P \right) \tag{4.3}$$

$$v^* = v_{ref} + k_Q \left(Q_{ref} - Q \right) \tag{4.4}$$

where f^* and v^* are the reference values modified by the droop control and P and Q are the measured output active and reactive powers, respectively. The droop characteristic for this control strategy is shown in Figure 4.5. In a standalone MG, normally P_{ref} and Q_{ref} are null for grid-forming units since their task is only to keep the voltage and frequency values within operational limits [99], but could be also the result of a tertiary control layer [6].

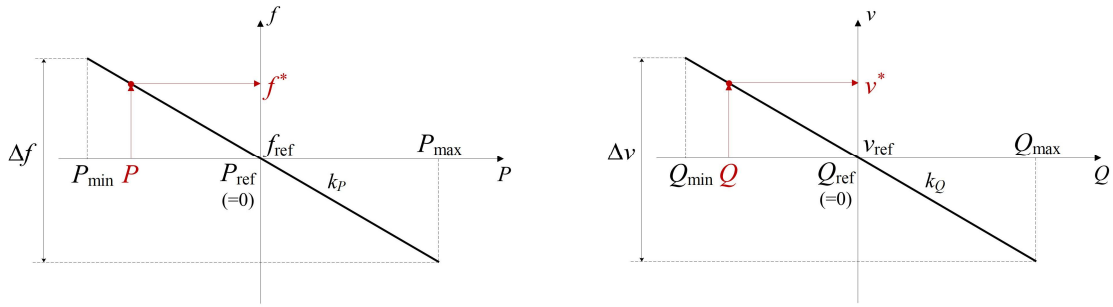

(a) (b)

Figure 4.5 – (a) Active power/frequency and (b) reactive power/voltage droop characteristics of grid-forming units.

In a multi-master operation, the droop control allows for active and reactive power distribution among units, the same way as primary frequency control of SGs in conventional power systems. In effect, assuming that the reference values for all DERs are equal, the power delivered by each unit is inversely proportional to their droop constants. Usually, unless other constraints are present, it is expected that larger units (or with greater power availability) give more power, thus a minor droop constant is imposed.

Some relevant issues regarding this control strategy are worth mentioning, although they are not directly tackled in the thesis.

Considering the equivalent circuit of several parallel inverters connected to the grid, as illustrated in Figure 4.6, the active and reactive powers injected P_i and Q_i by the i-th inverter are,

$$\begin{aligned} P_i &= \frac{VE_i}{Z_i}\cos\left(\theta_i - \delta_i\right) - \frac{V^2}{Z_i}\cos\left(\theta_i\right) \\ Q_i &= \frac{VE_i}{Z_i}\sin\left(\theta_i - \delta_i\right) - \frac{V^2}{Z_i}\sin\left(\theta_i\right) \end{aligned} \tag{4.5}$$

where δ_i is the phase angle between the output voltage of the inverter E_i and the PCC voltage V, and Z_i and θ_i are the magnitude and angle of the impedance between these two points.

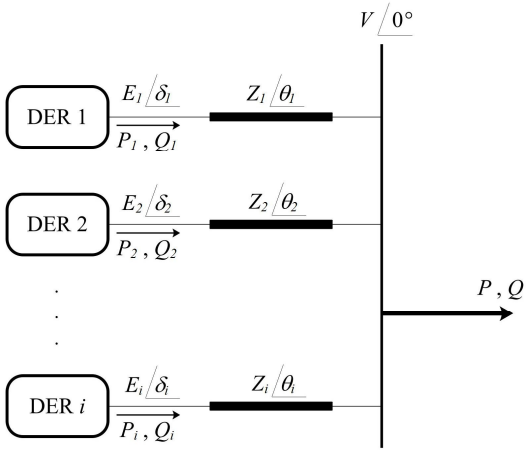

Figure 4.6 – Parallel DER units (Adapted from [100]).

The conventional droop control strategy is based on the principle that active power is mainly dependent on the angle/frequency (*P-f* dependency), and reactive power on the voltage (*Q-V* dependency), which is only true for mainly inductive systems, i.e., where $Z_i \approx X_i$ and $\theta_i \approx \pi/2$ for which,

$$\begin{aligned} P_i &= \frac{VE_i}{X_i}\sin\delta_i \\ Q_i &= \frac{VE_i\cos\delta_i - V^2}{X_i} \end{aligned} \tag{4.6}$$

In MV and LV systems this is no longer true, since the reactance-to-resistance ratio is considerably low. In consequence the *P-f* and *Q-V* controls are not completely decoupled.

Several decoupling strategies are present in literature [101]. In some cases, for LV systems (mainly resistive systems), an opposite droop strategy is implemented for which it is considered that the active power depends mainly on the voltage and the reactive power on the frequency, i.e., a dependency *P-V* and *Q-f* exists. The main disadvantages of the opposite droop are that it is not compatible either with the HV system or eventual rotating generators connected to the MG, and the active power is not

dispatchable under this paradigm. On the other hand, the conventional droop approach can still be applied for MV and LV systems due to an indirect operation of the droop characteristics [102].

Since the frequency is a global variable[1] within the MG, a proper sharing of active power can be achieved. The voltage instead, varies from node to node, and line impedances between parallel connected inverters are usually different. This results in an inaccurate reactive power sharing and a consequent circulating reactive current. If the coupling is considered, this issue affects also the active power sharing. Strategies dealing with this issue can be found in literature [103], while in this thesis a completely decoupled control between active power-frequency and reactive power-voltage is assumed.

A general scheme of both control strategies is shown in Figure 4.7. The detailed control loops are illustrated in Chapter 5.

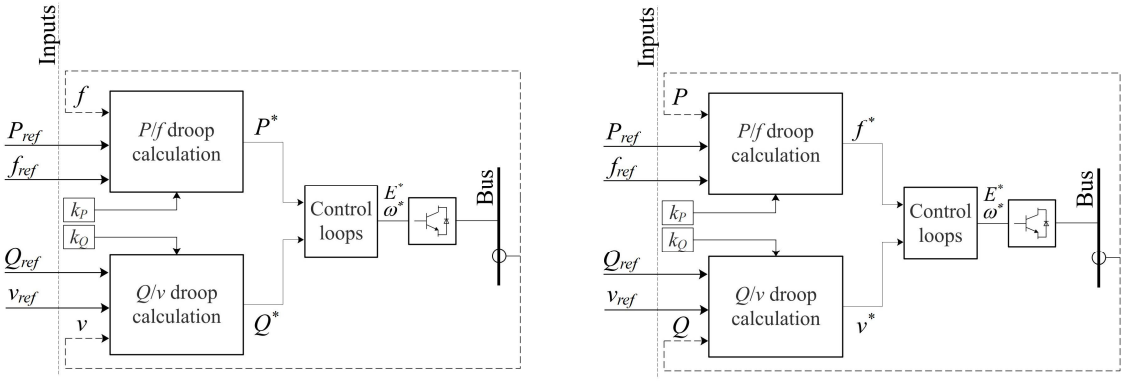

(a) (b)

Figure 4.7 – General scheme of the droop control strategy in (a) grid-following and (b) grid-forming units.

Some typical issues regarding this type of control are [6], [95], [101], [103]: i) slow transient response; ii) different (and commonly unknown or uncertain) line impedances between parallel-connected converters, which result in circulating currents among converters and inaccurate reactive power sharing; iii) inaccurate share of harmonics in the presence of non-linear loads and; iv) inherent tradeoff between frequency and voltage regulation and load sharing accuracy; v) the output current of the grid-forming unit in short-circuit conditions tends to be very high if any provision is taken, while the grid-following control mode inherently limits its output current.

b) Virtual Synchronous Machine

To cope with the stability issues arose by the inherent inertia-less characteristic of inverter-interfaced DERs, different Virtual Inertia (VI) algorithms are present in literature [104]. These implementations are introduced within the control of inverters aimed at reproducing the behavior of SGs with different levels of complexity and degrees of representation.

[1] Actually, the frequency in different points of a grid is different. However, the differences are very small and usually considered negligible, at least for the analyses of interest concerning this thesis.

The VI emulation of Virtual Synchronous Machines (VSMs) [105] aims at reproducing the dynamic properties of SGs. While the droop control mimics the steady-state characteristic of SGs, the VI emulation mimics also their transient characteristic, providing inertia support to the system and therefore enhancing the frequency stability and transient response [104], [106].

The swing equation of the SG is

$$\frac{2H \cdot S}{\omega_{ref}^2} \cdot \frac{d\omega}{dt} = T_m - T_e - D \cdot \Delta\omega \tag{4.7}$$

which in per unit can be expressed as,

$$2H \cdot \frac{d\omega'}{dt} = \frac{\Delta p}{\omega'} - k_D \cdot \Delta\omega' \tag{4.8}$$

with,

$$\Delta\omega' = \frac{\omega - \omega_{ref}}{\omega_{ref}} \tag{4.9}$$

where ω_{ref} and ω are the nominal and measured angular velocity respectively, H is the inertia constant, S is the rated power, T_m and T_e are the mechanical and electromagnetic torques, respectively, Δp is the accelerating power and D and k_D represent the damping factor.

The equivalence analysis carried out in [105], [107] between frequency droop and VSM controllers has shown that,

$$k_D = \frac{1}{k_P} \tag{4.10}$$

A general scheme is shown in Figure 4.8.

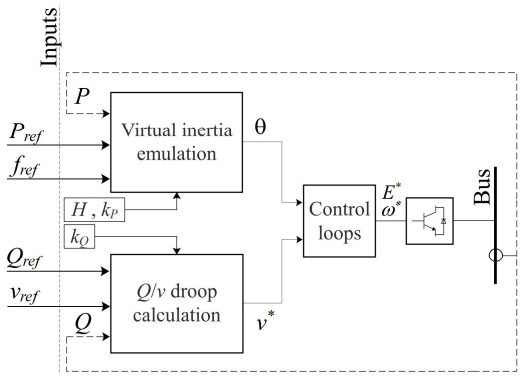

Figure 4.8 – General scheme of the VI implementation.

c) Short circuit

Inverters are normally oversized for the following reasons: i) the fast and secure operation of protection schemes installed in the distribution network in response to fault conditions rely on the presence of

large short-circuit currents, and; ii) high imbalances between load and generation in an islanded MG or during its islanding transition lead to a transient overload, particularly of grid-forming converters. In order for the MG to satisfactorily overcome these events, converters must be oversized. Nevertheless, semiconductors are only able to withstand over-currents of around twice the rated value for very short periods (around 1 ms) [108]. Therefore, the output current of inverters must be limited to avoid their disconnection from the grid. The methods for achieving this are different for grid-following and grid-forming inverters.

As mentioned before, grid-following inverters are CC-VSCs, thus they are inherently current-limited at the current reference output. In order to comply with low voltage ride-through (LVRT) capabilities and provide voltage support during disturbances, grid-following DER converters can follow different strategies [109], [110], namely: i) maintenance of pre-fault power references, in which the current limit is however respected (so-called PQM for Power Reference Maintenance); ii) maximum current compensation, in which the maximum reactive current (or active depending on the network characteristics) is injected to support the voltage; iii) maximum current compensation/maintenance of pre-fault power references, which is an hybrid of the first two strategies, i.e. the control tries to maintain the pre-fault power references and if the current does not reach the maximum level, more reactive (or active) current is injected to support the voltage until the maximum is reached; iv) no injection of current, also known as Zero Power Mode (ZPM).

Grid-forming inverters are VC-VSCs instead, thus the strategy to limit the current output is less straightforward. A Fault Current Limiter (FCL) based on the Transient Virtual Impedance (TVI) method is implemented [111]. The principle consists in emulating a large output impedance during faults that limits the current. The virtual impedance is null during normal conditions, in order to avoid unnecessary voltage drops. The magnitude of the virtual impedance $|Z_V|$ is driven by the piecewise function,

$$|Z_V| = \begin{cases} 0 & i < I_{th} \ \vee \ v > V_{th} \\ z_V & i \geq I_{th} \ \wedge \ v \leq V_{th} \end{cases} \tag{4.11}$$

where i and v are the estimated peak values of the current and voltage, and I_{th} and V_{th} are the thresholds triggering the FCL, respectively. Since the TVI modifies the voltage reference, the value of z_V is chosen such that the final voltage reference is 0 for the maximum current allowed, i.e.,

$$v_{ref} - z_V I_{\max} = 0 \tag{4.12}$$

The phase of the TVI, θ_V, is selected to be equal to the phase of the physical output impedance of the DER unit, Z_{DER}. A circuital representation of the TVI method is shown in Figure 4.9.

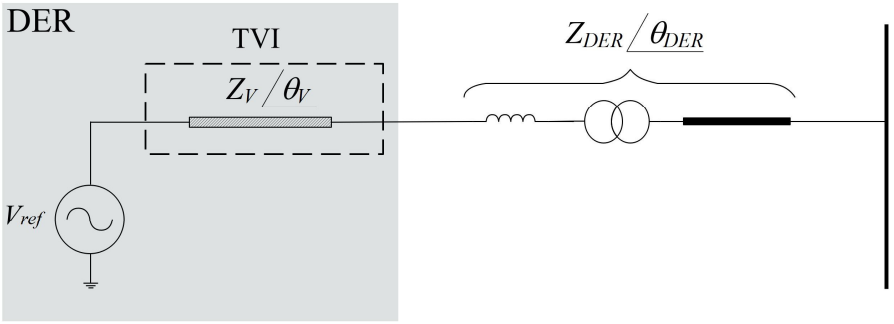

Figure 4.9 – Circuital representation of the TVI implementation.

In this Chapter an overview of the control architectures of ADNs and MGs has been presented, including an overview of the state of the art regarding the control strategies of MGs. A general schematization of the operational strategies implemented in the power converters of DERs has been presented, namely the droop control strategy and the VI implementation. The operation of power converters during short circuits has been also addressed in both grid-connected and grid-forming modes.

CHAPTER 5

STABILITY ANALYSIS OF MICROGRIDS – INFLUENCE OF LOAD MODELLING AND OF LOAD COMPOSITION

In the previous Chapter, the impacts of the large-scale integration of DERs have been mentioned and contextualized. Concerning the stability issues that arise, a main cause is that the overall inertia of the system decreases, hence large and fast frequency and voltage variations are expected due to power imbalances and electrical faults. These phenomena are prone to occur especially in MGs operating in standalone mode, or during their islanding transition. Such is the object of analysis of this Chapter.

In dynamic power system analysis performed by Transmission System Operators (TSOs) and DSOs, loads are often represented using static models. As reported by the Cigré survey results summarized in Table 5-1 [112], [113], only few DSOs consider either a dynamic representation for IMs or a detailed composite model, while the majority employ static models such as constant power, constant current, constant impedance, ZIP and exponential ones.

TABLE 5-1
SURVEY RESULTS (2014) OF LOAD MODELS USED BY DSOS IN DYNAMIC POWER SYSTEM ANALYSIS. ADAPTED FROM [112]

Load model		Constant P(Q)	Constant I	Constant Z	ZIP model	Exp. model	ZIP and IM	Exp. and IM	Detailed composite
Static studies		84	3	3	8	2	-	-	-
Dynamic studies	**Real Power**	23	19	4	19	7	16	0	10
	Reactive power	23	0	22	19	9	17	0	10

Results are expressed in percentage.

In MGs with low inertia DERs the influence of the dynamic response of loads might be of great significance. Indeed, as MGs are relatively small systems, voltage changes at DERs terminals largely influences neighboring loads. An accurate representation of the sensitivity of the loads with respect to the nodal voltage is required to evaluate the stability of the system [114], [115]. This specific characteristic of MGs is exploited in various dynamic voltage control schemes [116], [117] in which the voltage setpoint of the DERs depends on the frequency deviation. If the frequency drops, the voltage setpoint decreases in order to reduce the power consumption of the loads. Clearly the performance of such strategy is affected by the load mix. Indeed, as the voltage dependency of loads decreases, the effect of this droop voltage control becomes less efficient. As the voltage of MGs might considerably vary during unplanned islanding transitions, the load consumptions will also vary, even without any intentional voltage control, thus influencing the MG stability and the success of the islanding maneuver. Moreover, the voltage of standalone MGs fluctuates also during other types of events such as faults, connection/disconnection of load/generation/capacitor banks, etc., as well as happens for traditional power systems. However, due to the penetration of DERs, the response of standalone MGs is different and hence worth of study.

An analogous argumentation can be made concerning the frequency. Although the influence of frequency variations on the power consumption of most static loads is minor or even null within a reasonable range (e.g. 47.5 – 51.5 Hz. [118]), it could be significant on rotating loads, such as IMs.

The influence of different types of loads on the MG stability has been assessed in [92], [114], [119]–[123]. The considered study cases include varied characteristics: i) static and rotating types of loads; ii) power converter-interfaced or directly connected to the network; iii) different load power factors; iv) different mechanical torques applied to the IMs; v) different control strategies for the DERs; vi) during islanding transition, faults or load steps. In all these cases the MG includes a mix of inverter and synchronous-based DERs. While the SG has a great influence on the frequency and voltage transients

it is absent in a total inverter-based MG. Moreover, inverters controlled in grid-forming are not considered in these studies.

With the aim of contributing to fill such gaps, this chapter is mainly focused on the analysis of load dynamic response on the stability of total inverter-based MGs, and it is divided into two sections, mainly: i) analysis during islanding transition, and; ii) analysis of islanded MGs.

5.1 Islanding transition

As already stated, MGs must be able to work either in grid-connected or standalone operation modes. When an inertia-less MG is grid-connected, inverters are controlled in *PQ*-mode, and when it is standalone at least one inverter must be controlled in *Vf*-mode. Therefore, during islanding transition at least one inverter-interfaced DER needs to switch from one control mode to another. The switch can be triggered by different islanding detection methods [124], which can be classified as local methods, based on measurements at the MG side (as in [125]), and remote methods, based on signals sent by the CB relay at the point of common coupling (PCC) (as in [126], [127]) or by a central controller (as in [128]–[131]).

In literature, a few studies explicitly consider the delay in the control mode change (e.g. [128], [131], [132]), whilst most studies consider that such switching occurs simultaneously to the island formation (e.g. [126], [127], [129], [130]). For example, in [128] it has been shown that an experimental inertia-less system can avoid instability only for switching delays shorter than 470 ms. While a fast islanding switching between control modes is important to the stability of the MG, it is not instantaneous. According to the results reported in [133] the detection phase could take up to a few hundreds of milliseconds, if a local islanding detection method is employed, and several tens of milliseconds, if a signal is sent to the inverter. In consequence, the first instants after islanding, DERs continue operating in *PQ*-mode.

Since the frequency deviation can be very fast due to the absence of inertia [134], a first analysis is carried out to assess the MG stability without considering the switching between control modes, i.e. DERs are controlled in *PQ*-mode also after the CB at the PCC opens.

Moreover, the transient behavior of the MG depends not only on the control strategies of DERs but also on the load composition. As MGs are relatively small systems, voltage changes at DERs terminals largely influences neighboring loads. An accurate representation of the sensitivity of the loads with respect to the nodal voltage is required to evaluate the stability of the system [92], [115]. This specific characteristic of MGs is also exploited in various dynamic voltage control schemes, as those presented in, e.g., [116], [117].

As the voltage of the MG fluctuates during unplanned islanding transition, the load consumptions will also vary, even without any intentional voltage control, thus influencing the MG stability and the success of the islanding maneuver. A precursory analysis on the impact of load modelling techniques is required. Then, the influence of the load composition is assessed.

5.1.1 Studied system

The studied system shown in Figure 5.1 is a modified version of the Cigré benchmark for the integration of DERs in MV networks [43] and has been reproduced in EMTP-RV. It comprises the DERs and loads shown in Figure 5.2, namely a SG, a PV power station, two BESSs and a combination of stationary and rotating loads, which are further described in the following.

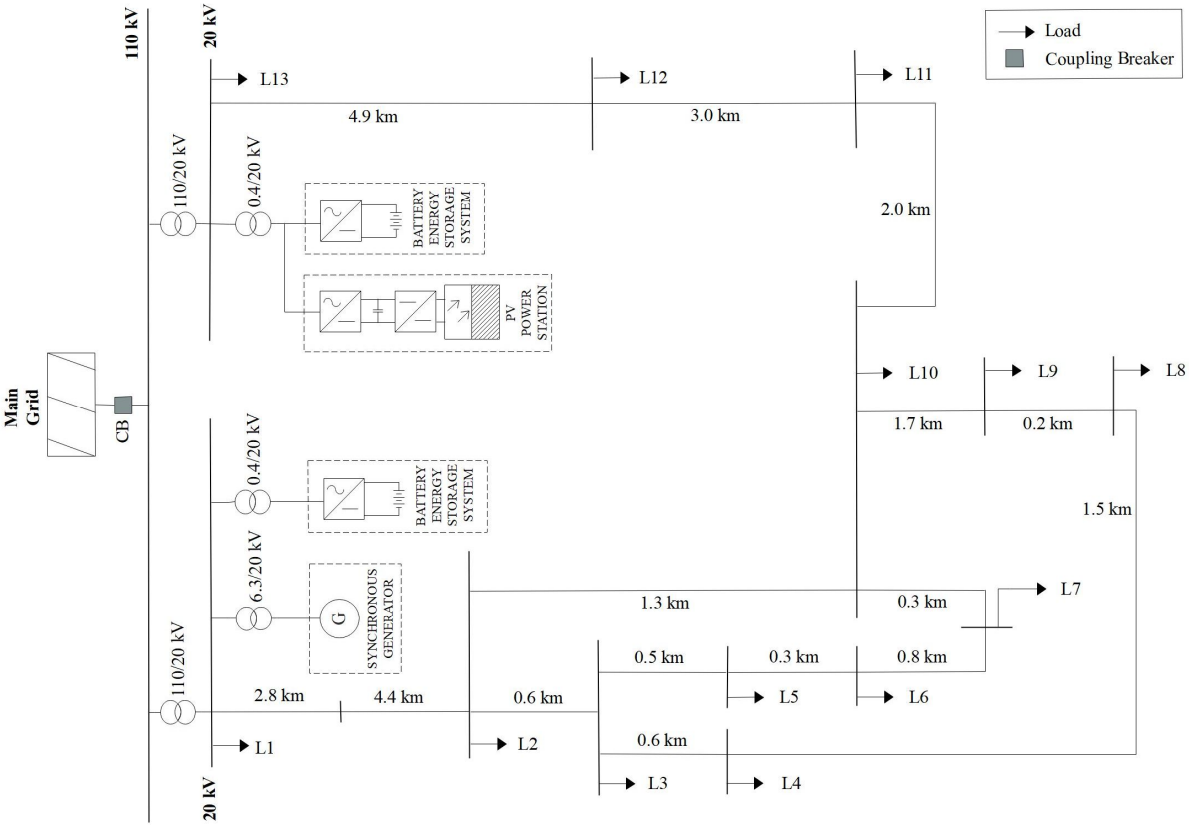

Figure 5.1 – Studied system. Cigré European MV distribution network benchmark (Adapted from [43]).

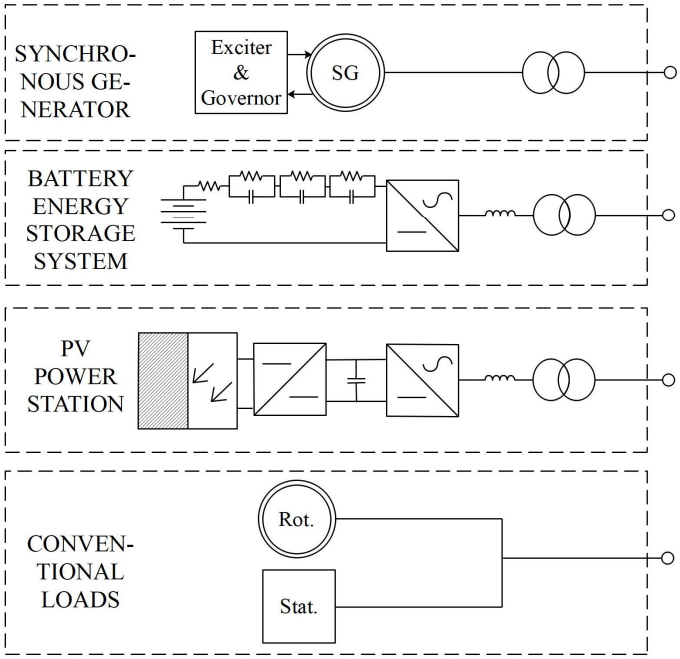

Figure 5.2 – Considered DERs and loads.

a) Synchronous Generator

The SG includes a simplified exciter [76] and an ideal governor with a droop characteristic. The parameters of the SG and its control system are reported in Table 5-2.

TABLE 5-2
PARAMETERS OF THE SG

General	
Rated Power	1 MVA
Rated Voltage	6.3 kV
Active power reference (P_{ref})	1 pu
Active power droop (k_P)	2.4 %
Inertia constant (H)	1 s
Transformer parameters	
Resistance	0.00375 pu
Reactance	0.15 pu
Impedance ratio	0.9

b) Battery Energy Storage System

The battery employed in the simulations has the characteristics reported in [135]. It is a lithium titanate battery modelled by three RC branches in series with the battery resistance, as in Figure A.19. The electrical parameters of the model depend on the State of Charge (SoC), which is assumed to remain constant during the transients considered in this thesis, as done in [136], and are reported in Table 5-3.

TABLE 5-3
BATTERY ELECTRICAL PARAMETERS.
TAKEN FROM [135]

Parameter	Value
V_{OC} (V)	733.2
R_s (Ω)	0.013
R_1 (Ω)	0.199
C_1 (F)	11234
R_2 (Ω)	0.010
C_2 (F)	2505
R_3 (Ω)	0.0006
C_3 (F)	6177.3

The control implementation of power converters in EMTP-RV is developed from [137]. Both BESSs are controlled in the grid-following mode with a droop control strategy as shown in Figure 5.3, where v_{abc} and i_{abc} are the measured voltage and current; v and f are the estimated voltage and frequency, respectively; P_{ref}, Q_{ref}, f_{ref} and v_{ref} are the reference values of active and reactive powers, frequency and voltage, respectively.

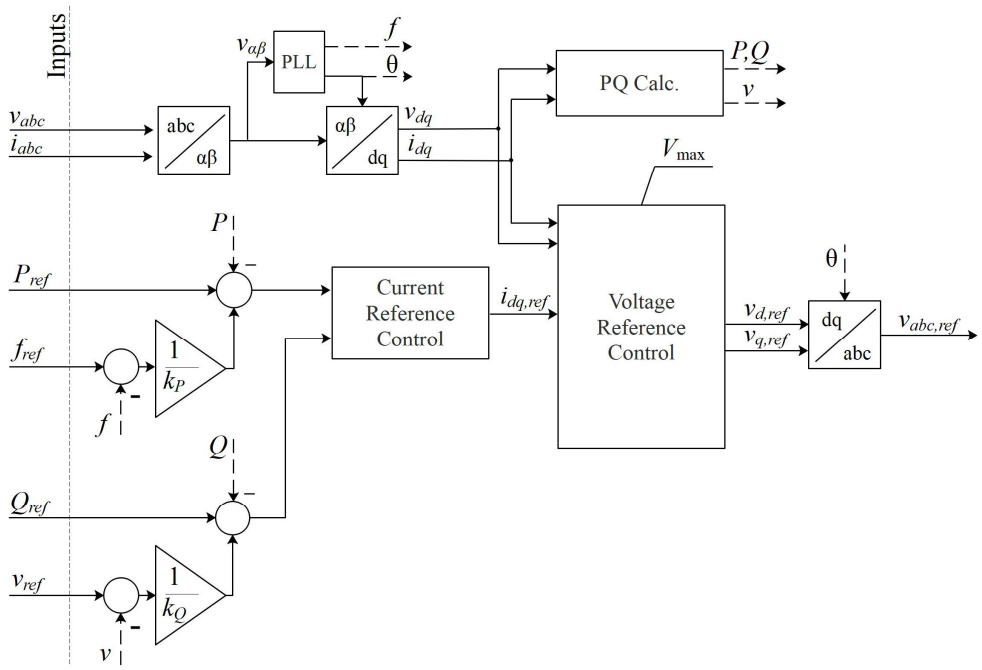

Figure 5.3 – Grid-following control strategy (Adapted from [123]).

The angle and frequency references are given by a Synchronous Reference Frame (SRF) Phase-Locked Loop (PLL) with a moving average filter [138]. The *PQ calculation* block implements (B.27) and a Low-Pass Filter (LPF) to get the active and reactive powers and the grid voltage.

The *current reference control* block implements the following calculations [137],

$$\begin{aligned} i_{d,ref} &= \frac{1}{v}\left(k_P^P + \frac{k_I^P}{s}\right)\left(P'_{ref} - P\right) \\ i_{q,ref} &= -\frac{1}{v}\left(k_P^Q + \frac{k_I^Q}{s}\right)\left(Q'_{ref} - Q\right) \end{aligned} \tag{5.1}$$

where s is the Laplace variable; k_P^P, k_I^P, k_P^Q and k_I^Q are the control parameters relative to the Proportional Integral (PI) controllers of the active and reactive powers, respectively. All PI-controllers include saturation and anti-windup blocks. P'_{ref} and Q'_{ref} are the references including the droop contribution. The other parameters are described in Figure 5.3.

The *voltage reference control* block implements the following calculations,

$$\begin{aligned} v_{d,ref} &= \left(k_P^i + \frac{k_I^i}{s}\right)\left(i_{d,ref} - i_d\right) - \omega L_{eq} i_q + v_d \\ v_{q,ref} &= \left(k_P^i + \frac{k_I^i}{s}\right)\left(i_{q,ref} - i_q\right) + \omega L_{eq} i_d + v_q \end{aligned} \tag{5.2}$$

where k_P^i, and k_I^i are the control parameters relative to the PI-controller of the current; L_{eq} is the equivalent output inductance which accounts for the transformer and the filter. The magnitude is then scaled depending on the value of v_{DC} to obtain the final reference.

The control parameters of the BESS are reported in Table 5-4.

TABLE 5-4
PARAMETERS OF THE BESS

General					
Rated power	1 MVA				
DC voltage (V_{DC})	733 V				
AC low voltage (V_{AC})	0.4 kV				
Arm reactance (X_{arm})	0.3 pu				
Control parameters					
Active power droop (k_P)	2.4 %				
Reactive power droop (k_Q)	10.0 %				
Active power reference (P_{ref})	0 pu				
Reactive power reference (Q_{ref})	0 pu				
Frequency reference (f_{ref})	50 Hz				
Voltage reference (v_{ref})	1 pu				
V_{max}	1.5 pu				
I_{max}	1.2 pu				
Transformer parameters					
Resistance	0.0175 pu				
Reactance	0.036 pu				
Impedance ratio	0.9				
PI-controllers					
k_P^P	0	k_P^Q	0	k_P^i	1.184
k_I^P	15	k_I^Q	1.5	k_I^i	925

c) Photovoltaic power plant

The PV power plant is connected to the network through a DC-DC converter in cascade with an inverter. In the former, the perturb and observe technique of the Maximum Power Point Tracking (MPPT) strategy is implemented, while the latter is controlled to maintain the voltage at the DC-link constant. The control strategy of the inverter is shown in Figure 5.4.

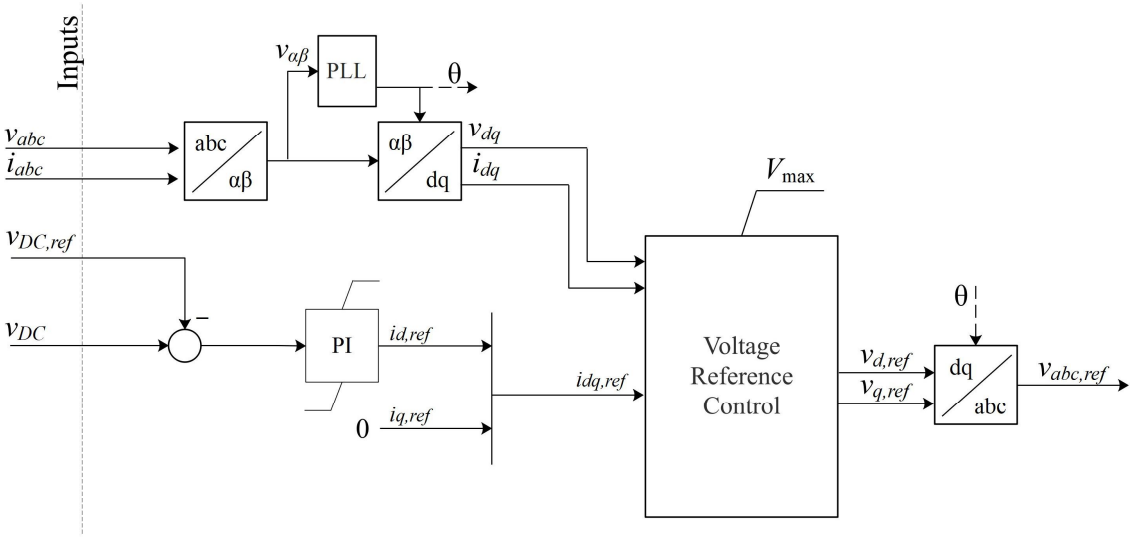

Figure 5.4 – Control scheme of the PV power plant.

The main differences with respect to the control strategy used for the BESS are: i) in this case $i_{d,ref}$ is determined by the DC-voltage reference $v_{DC,ref}$ as in (5.3), where k_P^{DC}, and k_I^{DC} are the control parameters relative to the PI-controller and v_{DC} is the measured voltage at the DC-link; ii) Q_{ref} is always zero, i.e. $i_{q,ref}$ is zero.

$$i_{d,ref} = -\left(k_P^{DC} + \frac{k_I^{DC}}{s}\right)\left(v_{DC,ref} - v_{DC}\right) \tag{5.3}$$

The PV unit is represented by the single-diode model. The parameters of the PV unit and its control system are reported in Table 5-5. The transformer is the same as for the BESS. The I-V and P-V characteristics are illustrated in Figure 5.5.

TABLE 5-5
PARAMETERS OF THE PV POWER PLANT

General			
Nominal power	1.5 MW		
DC-link voltage (V_{DC})	733 V		
AC low voltage (V_{AC})	0.4 kV		
Arm reactance (X_{arm})	0.2 pu		
Module			
Open-circuit (OC) voltage (V_{oc})	32.9 V		
Short-circuit (SC) current (I_{sc})	8.21 A		
Temp. coefficient OC ($K_{V,PV}$)	-0.123 V/°C		
Temp. coefficient SC ($K_{I,PV}$)	0.00318 A/°C		
Diode ideality factor (a)	1.025		
Num. cells in series	54		
Array			
Modules in series per string (N_s)	44		
Strings in parallel (N_p)	171		
Series resistance ($R_{s,PV}$)	0.083 Ω		
Parallel resistance ($R_{p,PV}$)	43.404 Ω		
PI-controllers			
k_P^{DC}	0.240	k_P^i	0.065
k_I^{DC}	0.367	k_I^i	3.805

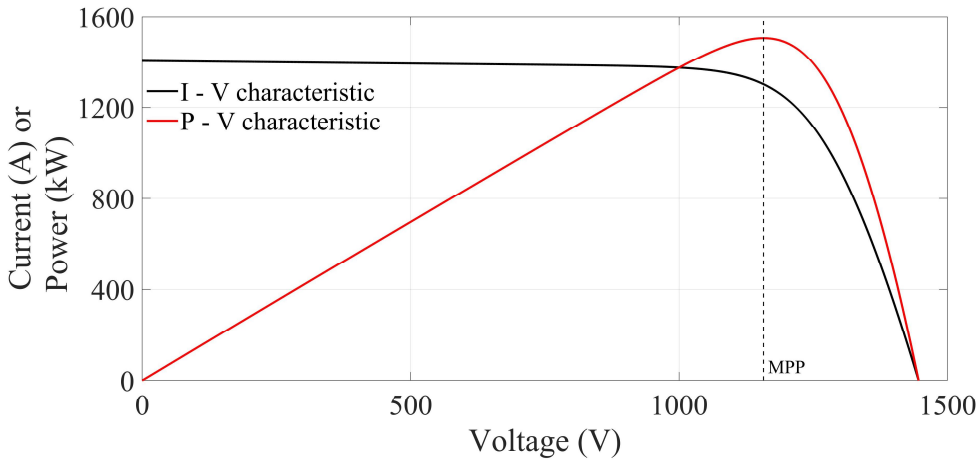

Figure 5.5 – I-V and P-V characteristics of the PV power plant. MPP corresponds to the Maximum Power Point.

All power converters are represented by the average model which is considered suitable for determining the frequency transients of the network [139].

d) Loads

Loads are categorized in four classes, namely residential, commercial, industrial, and agricultural. Each load class is supposed to be composed by different load components, as summarized in Table 5-6.

TABLE 5-6
LOAD COMPOSITION FOR EACH OF THE CONSIDERED LOAD CLASSES

Load class	Load component	Power factor	%
Residential	Fan	0.87	5.0
	Refrigeration	0.84	10.0
	Air conditioner	0.75	50.0
	Washing machine	0.65	3.0
	Dryer	0.99	3.0
	Lighting	0.90	20.0
	Resistive loads	1.00	5.0
	TV	0.77	4.0
Commercial	Fan	0.87	11.9
	Refrigeration	0.84	13.4
	Air conditioner	0.75	14.9
	Pumps and other motors	0.87	5.5
	Office equipment	1.00	13.1
	Lighting	0.90	34.5
	Resistive loads	1.00	6.7
Industrial	Small motor	0.83	20.0
	Large motor	0.89	56.0
	Lighting	0.90	19.0
	Resistive loads	1.00	5.0
Agricultural	Agricultural pump	0.85	100.0

The load compositions of residential, commercial and industrial classes are based on the data reported in [140]–[143]. The agricultural load composition is assumed to be largely dominated by pumps; hence other load components are neglected.

The total load absorbed and the load class composition at each bus of the MG before the islanding transition are reported in Table 5-7.

TABLE 5-7
LOAD COMPOSITION AND TOTAL LOAD ABSORPTION AT EACH BUS OF THE MG

Load bus	L1	L2	L3	L4	L5	L6	L7	L8	L9	L10	L11	L12	L13
Total load (kVA)	450	167	90	270	180	90	108	243	180	126	270	315	450
Class (%)													
Residential	0	0	70	100	50	100	50	40	70	50	0	0	0
Commercial	20	10	30	0	50	0	50	60	30	10	10	20	0
Industrial	80	40	0	0	0	0	0	0	0	40	50	0	80
Agricultural	0	50	0	0	0	0	0	0	0	0	40	80	20

5.1.2 Influence of load modelling

The analyzed transitory is initiated by a three-phase fault at $t = 0$ s in the upstream main grid, followed by the opening of the CB at the PCC after 50 ms. The following 6 cases are simulated, and the relevant frequency and voltage transients are compared:

- *Exp*+*EMTP*-model: Stationary loads are represented by the exponential model and rotating loads are represented by the *EMTP*-model of the IM (fifth-order model in Appendix A).
- *Exp*+*slip*-model: Stationary loads are represented by the exponential model and rotating loads are represented by the *slip*-model of the IM (first-order model in Appendix A).
- *ZIP*+*slip*-model: Stationary loads are represented by the ZIP model and rotating loads are represented by the *slip*-model of the IM.
- *Exp*-model: Stationary and rotating loads are represented by the exponential model.
- *P*-model: Stationary and rotating loads are represented as constant power loads.
- *Z*-model: Stationary and rotating loads are represented as constant impedance loads.

The load representation in the *Exp*+*EMTP*-model is the most detailed[1], therefore it is taken as benchmark.

a) Slip model

While the *EMTP*-model is embedded in the EMTP environment, the *slip*-model has been implemented from the beginning, for which a few considerations are made.

The *slip*-model consists of a circuit of passive devices, with exception of the rotor resistance, which value depends on the slip (see Figure A.9). Therefore, the slip has to be dynamically estimated during the time-domain simulations from the analysis of the motion equation (i.e., (A.34) in Appendix A)

[1] The exponential model is chosen over the ZIP model since it is less demanding from the computation point of view, since the ZIP model is simulated as three exponential models with their corresponding exponent values.

By neglecting the damping coefficients in (A.34), it can be expressed in per unit as

$$\frac{d\omega_m^{'}}{dt} = \frac{1}{2H}\left(\tau_{em} - \tau_m\right) \tag{5.4}$$

being ω'_m the mechanical angular velocity, τ_{em} and τ_m the electromagnetic and the mechanical torques and H the inertia constant, defined as the rate between the stored kinetic energy at synchronous speed Ω_{nom} and the motor rating power S_b, i.e.,

$$H = \frac{\frac{1}{2}J\Omega_{nom}^2}{S_b} \tag{5.5}$$

The per unit equation relating the powers instead of the torques is

$$\omega_m^{'}\frac{d\omega_m^{'}}{dt} = \frac{1}{2H}\left(p_{em} - p_m\right) \tag{5.6}$$

which yields,

$$\omega_m^{'}(t) = \sqrt{\frac{1}{H}\int_0^t \left(p_{em} - p_m\right)dt} \tag{5.7}$$

Therefore, the slip s can be calculated as,

$$s(t) = \frac{\omega^{'} - \omega_m^{'}(t)}{\omega^{'}} \tag{5.8}$$

where ω' is the supply voltage frequency in per unit, which is estimated by implementing a PLL. The scheme for the slip estimation is shown in Figure 5.6.

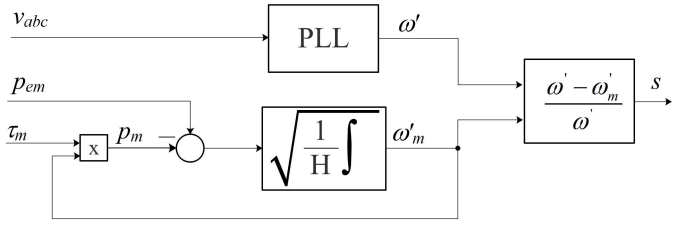

Figure 5.6 – Scheme for the slip estimation.

The load parameters of each component concerning the relevant models are reported in Table 5-8. The parameters refer to (A.19), (A.23) and Figure A.9.

TABLE 5-8
LOAD PARAMETERS.
TAKEN FROM [144]–[150]

Load component	Induction motor						Exponential model				ZIP model					
	r_s	x_s	x_m	r_r	x_r	H (s)	k_{pu}	k_{qu}	k_{pf}	k_{qf}	p_1	p_2	p_3	q_1	q_2	q_3
Lighting	-	-	-	-	-	-	0.96	7.38	1.00	-26.60	0.58	0.53	-0.11	8.04	-11.42	4.38
Resistive loads	-	-	-	-	-	-	2.00	0.00	0.00	0.00	0.92	0.10	-0.02	0.00	0.00	0.00
TV	-	-	-	-	-	-	2.00	5.20	0.00	-4.60	0.33	-0.57	1.24	19.00	-33.22	15.22
Office equipment	-	-	-	-	-	-	0.36	0.00	0.00	0.00	0.34	-0.32	0.98	0.00	0.00	0.00
Washing machine	0.110	0.120	2.0	0.110	0.130	0.69	0.08	1.60	3.00	1.80	0.05	0.31	0.63	-0.56	2.20	-0.65
Dryer	0.120	0.150	1.9	0.130	0.140	0.11	2.04	3.27	0.00	-2.63	1.96	-2.23	1.33	2.51	-2.34	0.83
Refrigerator	0.056	0.087	2.4	0.053	0.082	0.28	0.77	2.50	0.53	-1.46	1.19	-0.26	0.07	0.59	0.65	-0.24
Air conditioner	0.100	0.100	1.8	0.090	0.060	0.28	0.20	2.30	0.90	-2.67	1.60	-2.69	2.09	12.53	-21.11	9.58
Fan	0.079	0.120	3.2	0.052	0.120	0.70	0.08	1.60	2.90	1.80	0.26	0.90	-0.16	0.50	0.62	-0.12
Pumps and motors	0.079	0.120	3.2	0.052	0.120	0.70	0.08	1.60	2.90	1.80	0.46	0.73	-0.19	2.17	-3.03	1.87
Small indust. motors	0.031	0.100	3.2	0.018	0.180	0.70	0.07	0.50	2.50	1.20	1.35	-0.98	0.63	2.31	-3.72	2.40
Large indust. motors	0.013	0.067	3.8	0.009	0.170	1.50	0.07	0.50	2.50	1.20	0.48	0.78	-0.26	2.01	-2.70	1.70
Agricultural pumps	0.025	0.088	3.2	0.016	0.170	0.80	1.40	1.40	5.00	4.00	0.46	0.73	-0.19	2.17	-3.03	1.87

Dynamic loads are controlled to provide constant mechanical torque during the entire simulation.

With the *P*-model, the islanding transition leads to the system instability. For all the other models this does not occur. The frequency and voltage transients are shown in Figure 5.7 and Figure 5.8, respectively. After the islanding transition the frequency and the voltage steady state values differ from the nominal values because of the droop strategy adopted. Indeed, the frequency and voltage deviation are proportional to the active and reactive power supplied by the DER units, as can be deduced from (4.1)–(4.4) . Typically, secondary frequency and voltage control layers, not included in this study case, are responsible of taking these values back to the rated settings.

The same frequency and voltage steady state values are obtained by using all the models except the *Z*-model that presents a slightly different frequency value, as evidenced from Figure 5.7b. By using the *Exp+slip* and the *ZIP+slip*-models, the representation of the frequency transient well matches the reference one. It is worth noting that there are not significant differences between the *Exp+slip* and the *ZIP+slip*-models during the transient and in the steady state values.

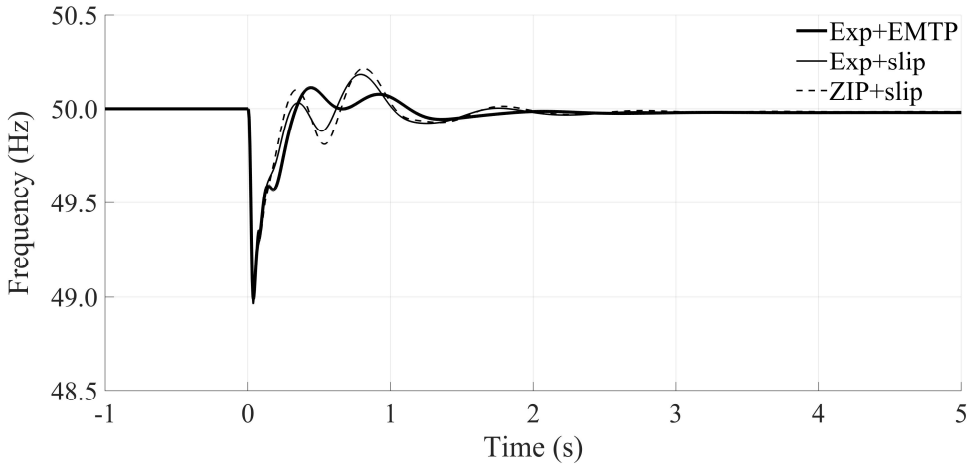

(a)

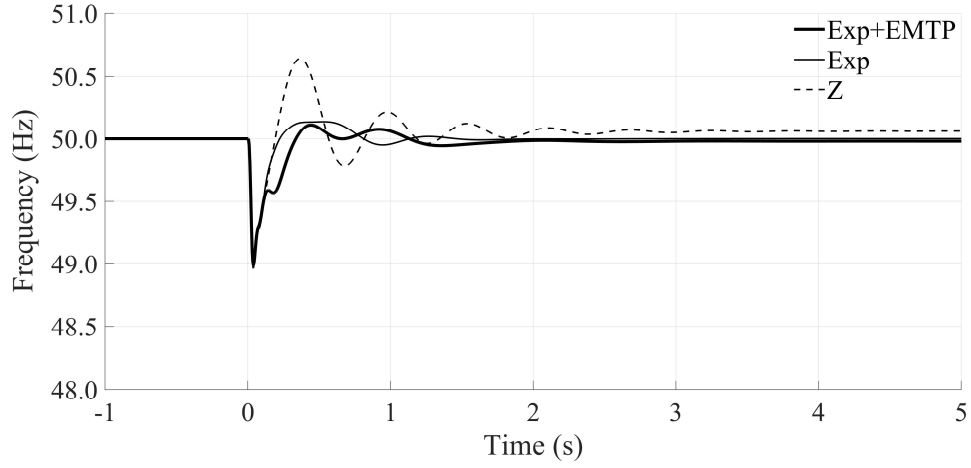

(b)

Figure 5.7 – Frequency transient during islanding transition. The SG is connected to the MG [123].

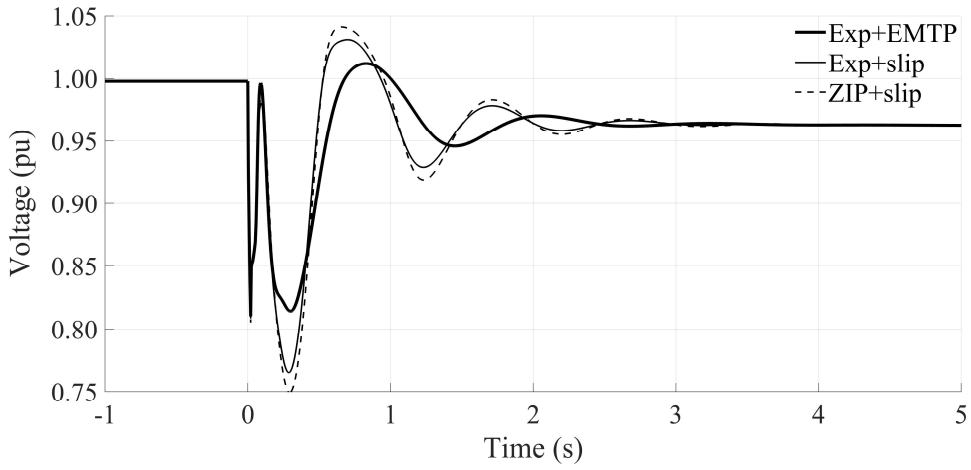

(a)

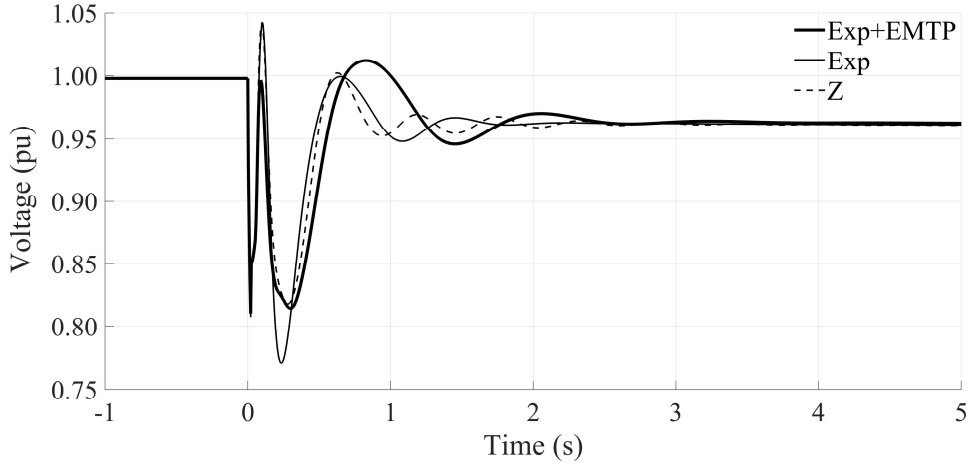

(b)

Figure 5.8 – Voltage transient during islanding transition. The SG is connected to the MG [123].

In order to analyze the frequency and voltage transients in a system in which all DER units are inertia-less, the SG is disconnected from the MG. Then, the same fault is simulated at $t = 0$ s, followed by the islanding transition after 50 ms.

As the aim is the assessment of the influence of the load dynamic response during the islanding transition of the MG, the change of control strategy of the BESS from *PQ* to *Vf*-mode is deliberately disregarded. Also, as already stated, the control strategy is not switched immediately after the opening of the CB, but it is delayed depending on the islanding detection method.

The simulation results show that when all loads are represented by some static model, namely by the *Exp*, *P* or *Z*-models, the islanding transition leads to the system instability. For the cases in which the dynamic representation of the load is included, the frequency and voltage transients are shown in Figure 5.9.

In this case, the *Exp+slip* and *ZIP+slip*-models are accurate enough to represent the transient response during the islanding transition of the considered MG. The steady state values after the disturbance are

equal for the three cases. Since the exponential model is simpler than the *ZIP*-model, the *Exp+slip*-model might be preferred.

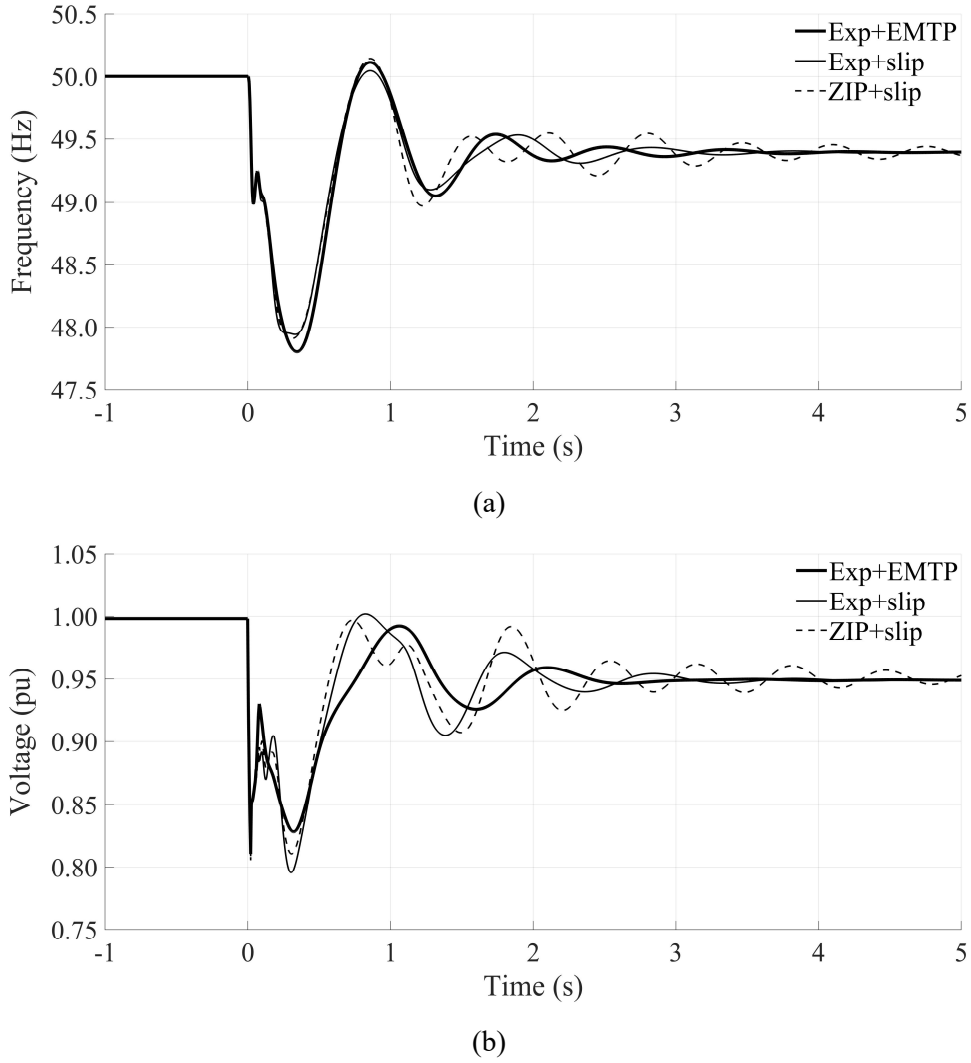

Figure 5.9 – (a) Frequency and (b) voltage transients during islanding transition. The SG is disconnected from the MG [123].

In conclusion, if a SG is connected to the MG, all models except for the *P*-model predict the stability of the MG after islanding. However, if any SG is connected to the MG, i.e. in an inertia-less MG, the *Exp* and *Z*-models predict the system instability. In such a case, only the *Exp+slip* and *ZIP+slip*-models, i.e., the models that include the rotating nature of the loads, are accurate enough to represent the stable transient response of the MG.

5.1.3 Influence of load composition – traditional loads

This Section focuses on the analysis of the influence of the load composition. First, a sensitivity analysis is carried out to assess the influence of the main load parameters in the frequency and voltage transients. Afterwards, the analysis is extended to the complete system of Figure 5.1.

a) Sensitivity analysis

The sensitivity analysis is carried out in the simple system of Figure 5.10. Loads are consisting of stationary and rotating loads, represented by the exponential and the EMTP models, respectively (i.e., the above *Exp+EMTP*-model). The base values are $k_{pu} = k_{qu} = 1$, $k_{pf} = k_{qf} = 0$, $H = 1$ s and a percentage of rotating load (η_{rot}) of 50%. Before islanding, the MG was importing both active and reactive power. To isolate the influence of the load from other intricacies, the fault in this case is not simulated, and the islanding transition begins with the automatic opening of the CB.

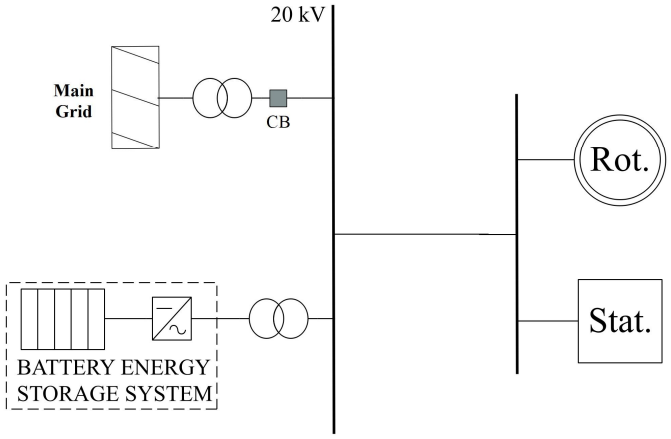

Figure 5.10 – Simple system for the sensitivity analysis.

The influence of the inertia constant of rotating loads is analyzed. The minimum values of frequency and voltage during the islanding transition are shown in Figure 5.11. Both increase as the inertia constant increases, although the voltage increase is limited. For values of H less than 0.5, the system is unstable.

The influence of the percentage of rotating load η_{rot} is carried out assuming $H = 1.5$ s. The minimum values of frequency and voltage are shown in Figure 5.12. Both increase with the increasing of the rotating load percentage. For load compositions with less than 35% of rotating load, the system is unstable.

Moreover, the influence of k_{pu}, k_{qu}, k_{pf} and k_{qf} are analyzed. From Figure 5.13 to Figure 5.16 the minimum values of frequency and voltage during the islanding transition are shown for the variations of the different parameters. The minimum frequency increases when k_{pu} or k_{pf} increases and decreases when k_{qu} or k_{qf} increases. The increase of k_{pu}, k_{qu} or k_{qf} leads to an increase of the minimum voltage, while k_{pf} has a negligible influence on it.

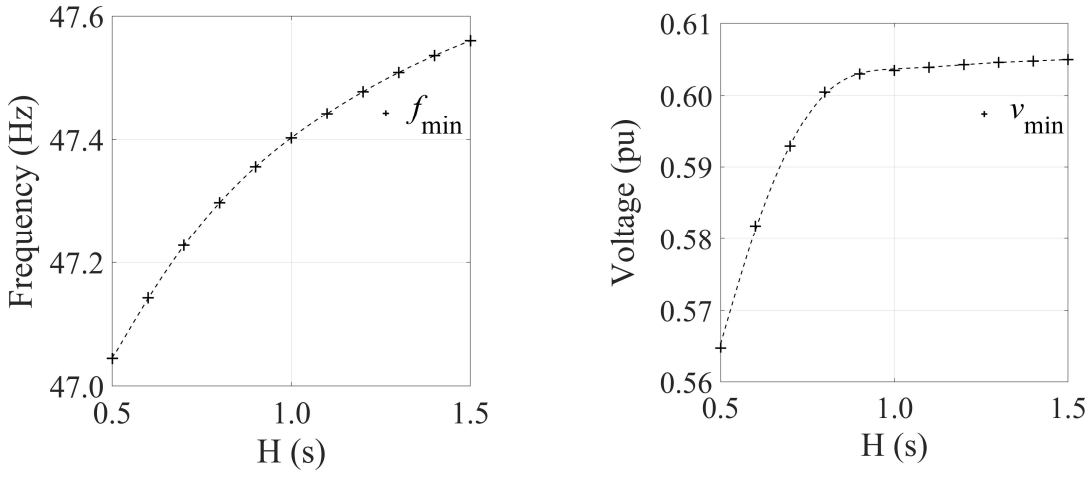

(a) (b)

Figure 5.11 – Influence of inertia constant H on the (a) frequency and (b) voltage transients during the islanding transition [123].

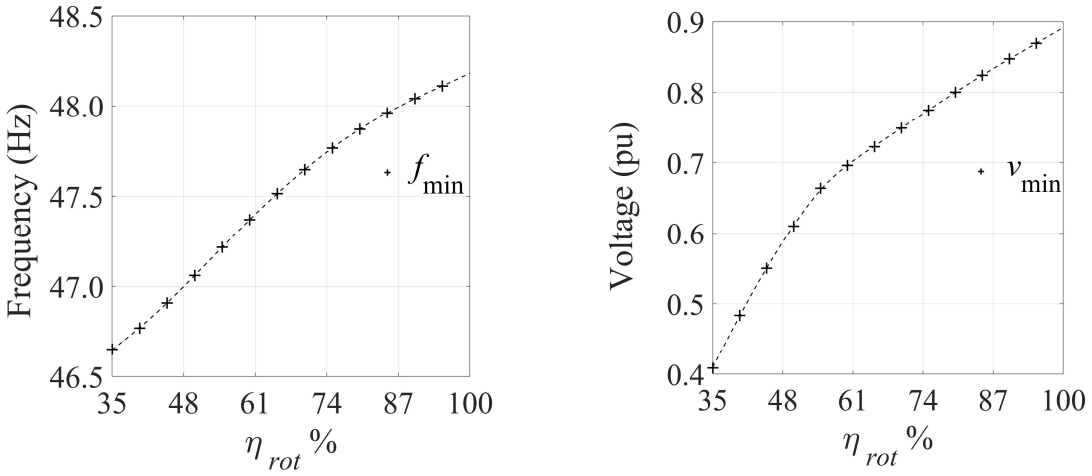

(a) (b)

Figure 5.12 – Influence of the percentage of rotating load η_{rot} on the (a) frequency and (b) voltage transients during the islanding transition [123].

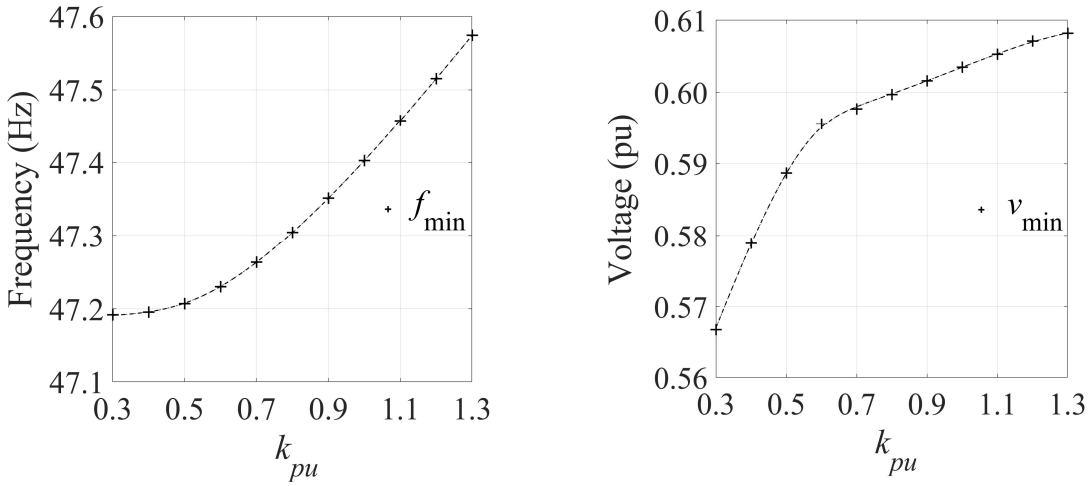

(a) (b)

Figure 5.13 – Influence of the parameter k_{pu} on the (a) frequency and (b) voltage transients during the islanding transition [123].

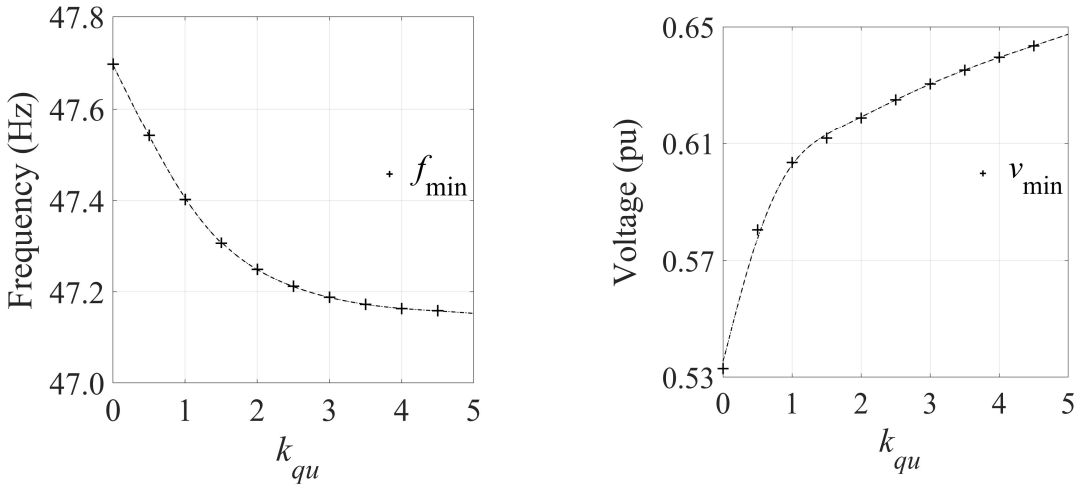

(a) (b)

Figure 5.14 – Influence of the parameter k_{qu} on the (a) frequency and (b) voltage transients during the islanding transition [123].

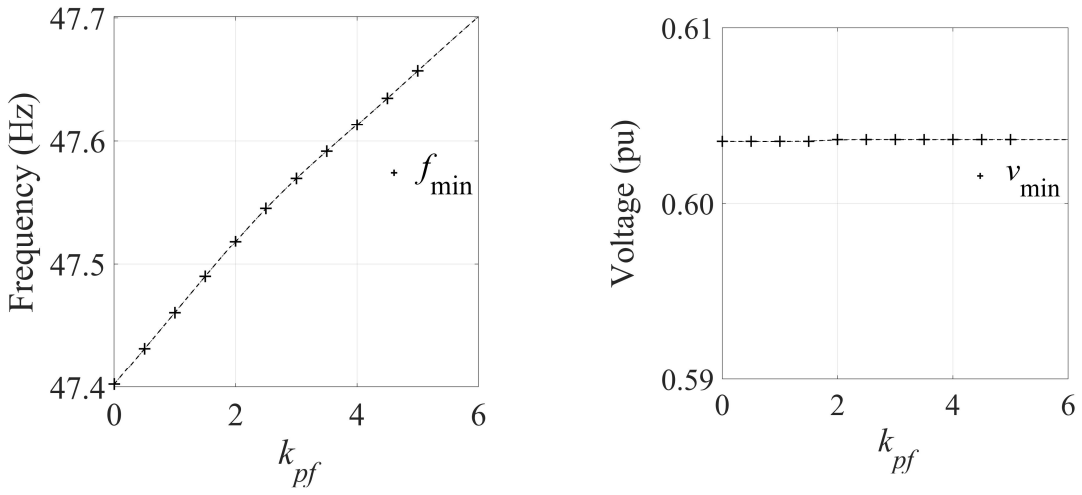

(a) (b)

Figure 5.15 – Influence of the parameter k_{pf} on the (a) frequency and (b) voltage transients during the islanding transition [123].

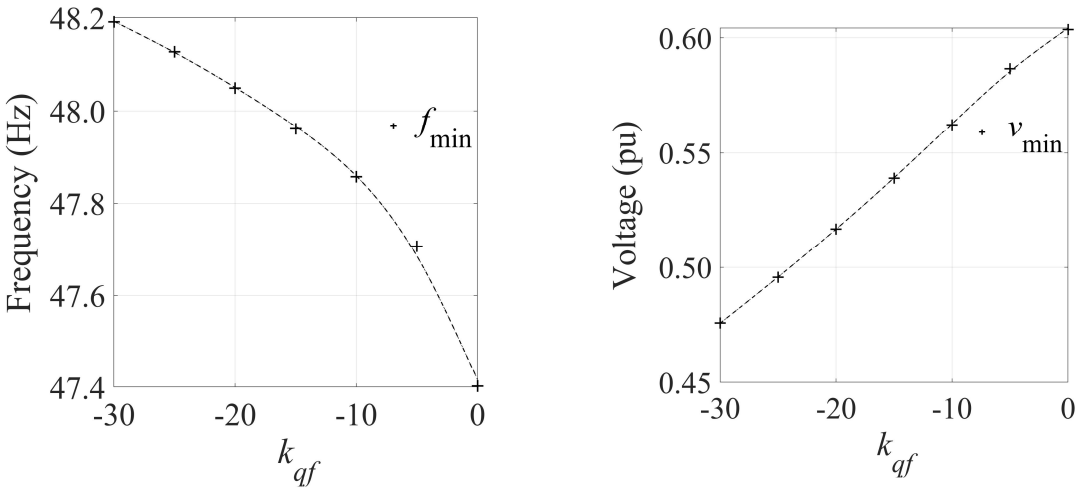

(a) (b)

Figure 5.16 – Influence of the parameter k_{qf} on the (a) frequency and (b) voltage transients during the islanding transition [123].

b) Study cases

The analysis is extended to the network of Figure 5.1 in which the percentages of load classes in each bus were varied keeping constant the total load.

The eight different cases reported in Table 5-9 are analyzed.

TABLE 5-9
LOAD COMPOSITION AND TOTAL LOAD ABSORPTION AT EACH BUS OF THE MG

Load bus		L1	L2	L3	L4	L5	L6	L7	L8	L9	L10	L11	L12	L13
Total load (kVA)		450	167	90	270	180	90	108	243	180	126	270	315	450
Class (%)														
Case A	Residential	0	0	30	60	10	60	10	0	30	30	0	0	0
	Commercial	60	50	70	40	90	40	90	100	70	50	50	60	40
	Industrial	40	20	0	0	0	0	0	0	0	20	30	0	60
	Agricultural	0	30	0	0	0	0	0	0	0	0	20	40	0
Case B	Residential	0	30	30	90	10	90	10	30	30	60	0	0	30
	Commercial	30	20	40	10	60	10	60	70	40	20	20	30	10
	Industrial	70	20	30	0	30	0	30	0	30	20	60	30	60
	Agricultural	0	30	0	0	0	0	0	0	0	0	20	40	0
Case C	Residential	0	50	30	80	0	80	0	30	30	60	20	30	30
	Commercial	20	0	0	0	30	0	30	50	20	0	0	0	0
	Industrial	80	20	40	0	40	0	40	0	30	40	60	30	70
	Agricultural	0	30	30	20	30	20	30	20	20	0	20	40	0
Case D	Residential	0	70	0	70	30	60	30	50	30	60	20	30	30
	Commercial	0	0	0	0	0	0	0	0	0	0	0	0	0
	Industrial	100	0	70	30	40	20	40	30	30	40	60	30	70
	Agricultural	0	30	30	0	30	20	30	20	40	0	20	40	0
Case E	Residential	40	40	100	100	90	100	90	80	100	90	40	40	40
	Commercial	0	0	0	0	10	0	10	20	0	0	0	0	0
	Industrial	60	25	0	0	0	0	0	0	0	10	35	0	60
	Agricultural	0	35	0	0	0	0	0	0	0	0	25	60	0
Case F	Residential	0	0	30	60	10	60	10	0	30	30	0	0	0
	Commercial	60	50	70	40	90	40	90	100	70	50	50	60	40
	Industrial	40	20	0	0	0	0	0	0	0	20	30	0	60
	Agricultural	0	30	0	0	0	0	0	0	0	0	20	40	0
Case G	Residential	0	0	50	60	30	60	30	20	50	20	0	0	0
	Commercial	0	0	10	0	30	0	30	40	10	0	0	0	0
	Industrial	100	80	40	40	40	40	40	40	40	80	90	40	100
	Agricultural	0	20	0	0	0	0	0	0	0	0	10	60	0
Case H	Residential	0	0	50	60	30	60	30	20	50	35	0	0	0
	Commercial	0	0	10	0	30	0	30	40	10	0	0	0	0
	Industrial	60	10	0	0	0	0	0	0	0	25	20	0	40
	Agricultural	40	90	40	40	40	40	40	40	40	40	80	100	60

The characterization of each case is done by estimating equivalent values for H, k_{pu}, k_{qu} k_{pf} and k_{qf}. The equivalent inertia constant H_{eq} is estimated, according to [151], as

$$H_{eq} = \sum_i s_{i,rot} H_i \tag{5.9}$$

where $s_{i,rot}$ is the portion of load (apparent power) of type i with inertia H_i with respect to the total rotating load. It is worth noting that this equivalent is referred only to the rotating load. The inertia constant of the entire system instead, would be expressed as

$$H_{sys} = \sum_i s_i H_i = H_{eq} \eta_{rot} \tag{5.10}$$

where s_i is the portion of load of type i with inertia H_i with respect to the total load. The exponential parameters $k_{pu,eq}$, $k_{qu,eq}$, $k_{pf,eq}$ and $k_{qf,eq}$ are estimated from an equivalent characteristic such that,

$$V^{k_{pu,eq}} = \sum_i p_{i,st} V^{k_{pu,i}} \tag{5.11}$$

$$V^{k_{qu,eq}} = \sum_i q_{i,st} V^{k_{qu,i}} \tag{5.12}$$

$$1 + k_{pf,eq}\,\Delta f = \sum_i p_{i,st} (1 + k_{pf,i}\,\Delta f) \tag{5.13}$$

$$1 + k_{qf,eq}\,\Delta f = \sum_i q_{i,st} (1 + k_{qf,i}\,\Delta f) \tag{5.14}$$

where $p_{i,st}$ ($q_{i,st}$) is the portion of active (reactive) power absorbed by the load of type i with exponential parameters $k_{pu,i}$, $k_{qu,i}$, $k_{pf,i}$ and $k_{qf,i}$ with respect to the total stationary active (reactive) power. The resulting equivalent parameters and percentage of rotating load of the residential, commercial, industrial, and agricultural classes of load are shown in Table 5-10.

TABLE 5-10
EQUIVALENT PARAMETERS OF ALL LOAD CLASSES

Class	H_{eq} (s)	η_{rot} (%)	H_{sys} (s)	$k_{pu,eq}$	$k_{qu,eq}$	$k_{pf,eq}$	$k_{qf,eq}$
Residential	0.320	71.0	0.227	1.21	6.94	0.69	-21.62
Commercial	0.440	45.7	0.201	0.86	7.38	0.61	-26.60
Industrial	1.289	76.0	0.980	1.14	7.38	0.77	-26.60
Agricultural	0.800	100.0	0.800	-	-	-	-

Cases A to D are configured in order to gradually increase the parameters that, according to the sensitivity analysis, improve the system stability, i.e. H_{eq}, η_{rot}, k_{pu}, k_{pf}, and in order to decrease the parameters that, on the contrary, worsen the stability, i.e. k_{qu} and k_{qf}. Cases E to H instead, have a 40% increase of residential, commercial, industrial, and agricultural loads with respect to the *base* case of Table 5-7. Therefore, cases E to H can be considered as predominantly residential, commercial, industrial, and agricultural MGs, respectively.

The islanding transition begins with the automatic opening of the CB. The equivalent parameters and the obtained results in terms of minimum frequency and voltage for all cases are presented in Table 5-11.

TABLE 5-11
STUDY CASES.
EQUIVALENT PARAMETERS AND MINIMUM FREQUENCY AND VOLTAGE VALUES

Case	H_{eq} (s)	η_{rot} (%)	H_{sys} (s)	$k_{pu,eq}$	$k_{qu,eq}$	$k_{pf,eq}$	$k_{qf,eq}$	f_{min} (Hz)	v_{min} (pu)
A	0.689	59.2	0.408	0.91	7.33	0.64	-26.02	48.83	0.810
B	0.796	67.6	0.538	1.00	7.26	0.67	-25.19	48.97	0.819
C	0.844	75.1	0.634	1.08	7.21	0.70	-24.62	49.04	0.825
D	0.893	78.3	0.699	1.17	7.18	0.74	-24.23	49.08	0.830
E	0.622	74.6	0.464	1.17	7.05	0.70	-22.85	48.95	0.800
F	0.689	59.2	0.408	0.91	7.33	0.64	-26.02	48.83	0.810
G	1.037	75.0	0.778	1.10	7.28	0.73	-25.46	49.11	0.842
H	0.796	86.4	0.688	1.07	7.19	0.69	-24.43	49.05	0.826

As expected, from cases A to D, the frequency and the voltage responses improve in terms of minimum reached values.

Although Case F has a larger H_{eq} than Case E, the minimum frequency is smaller. This can be attributed mainly to the lower value of rotating load, but also to the lower value of $k_{pu,eq}$ and the larger value of $k_{qu,eq}$. The best case in terms of minimum frequency and voltage is Case G, in which the industrial load is predominant. Such result might be attributed to the very large H_{eq} and the relatively high percentage of rotating load. Case H too, in which the agricultural load is predominant, results in a smaller frequency deviation.

In Figure 5.17 the frequency and voltage minimum values with respect to H_{sys} are shown. The minimum frequency increases with the increasing of the total system inertia, regardless of the other parameters. The same occurs for the minimum voltage, except for case E. The parameter that could lead to such behavior in case E is $k_{qu,eq}$ which is indeed the lowest compared to all the other cases.

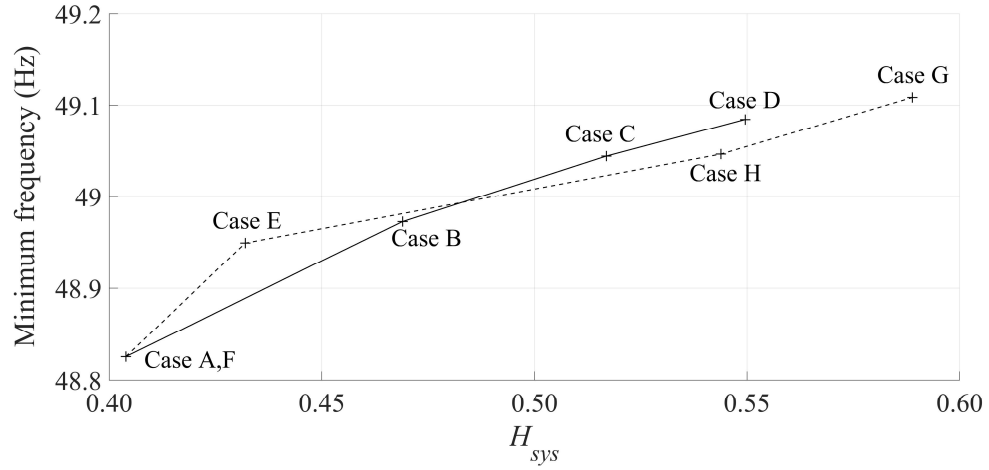

(a)

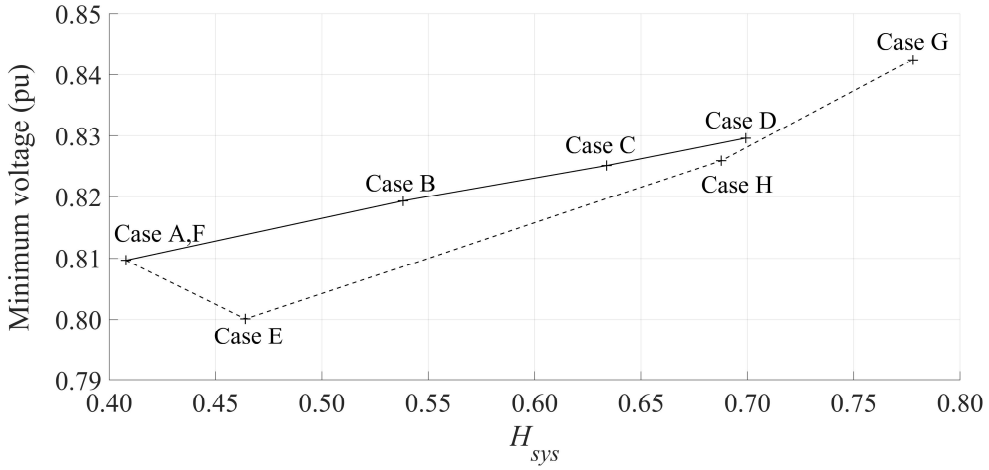

(b)

Figure 5.17 – Minimum (a) frequency and (b) voltage values reached during the islanding transition, as reported in Table 5-11 [123].

5.2 Islanded Microgrids

It has been shown how the dynamic response of loads has a significant influence on the stability of inertia-less MGs during islanding transition. Such analysis is extended in this section to MGs operating in standalone mode, comprising a DER unit operating in grid-forming mode that provides voltage and frequency references to the MG.

In this Section the dynamics of a standalone MG after a three-phase fault are analyzed. The main contribution with respect to the current state of the art regards the analysis of the MG in absence of rotating generators and with a BESS working in the grid-forming mode. The exclusion of any rotating generator is expected to heighten the load influence on the dynamics of the system. Moreover, besides conventional loads (i.e., uncontrollable loads such as resistive loads, lighting loads, fans, refrigerators,

etc.) modern controllable loads are considered, namely an Electric Vehicle (EV) Charging Station (CS) and variable speed Heat Pumps (HPs) [152], [153].

5.2.1 Studied system

As done in Section 5.1.3 for the analysis of the influence of load composition during the islanding transition, a sensitivity analysis is carried out first in a simple system and then it is extended to a more complex network. The DERs and loads considered for both cases are shown in Figure 5.18 and are further described in the following.

Since real time simulations are also carried out, as described at the end of the Section, all components are implemented in the Simulink environment, which is fully integrated with the Opal-RT. In [154] a comparative analysis between EMTP-RV and Simulink is carried out, in which some differences in the simulation of the dynamic response of MGs are shown.

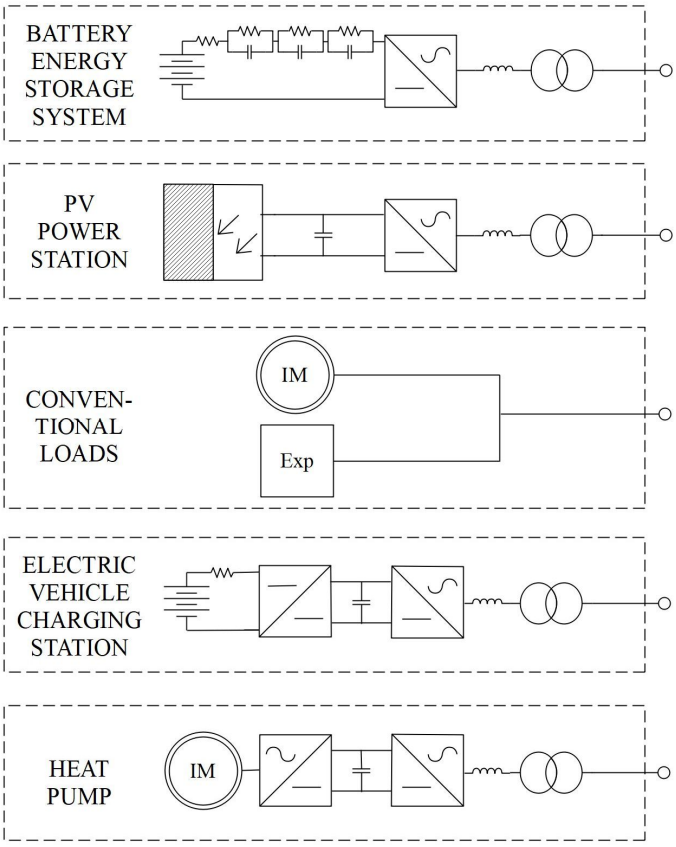

Figure 5.18 – Considered DERs and loads.

a) Battery Energy Storage System

The battery is represented as in Section 5.1.1b with the same parameters of Table 5-3.

The grid-following mode is the same as the one illustrated in Figure 5.3 with the parameters of Table 5-4, with the following considerations: i) during short-circuits the PQM strategy is adopted; ii) a modified SRF-PLL is implemented.

With respect to a standard SRF-PLL, the modified SRF-PLL of Figure 5.19 considers: i) the adaptive mechanism proposed in [155] that improves the transient performance of the PLL against phase angle jumps due to system faults that cause large and fast transients of the estimated frequency; ii) the frequency is estimated from the integrator output, since it results in a more damped transient response [138]. The constants $k_{PI,P}$ and $k_{PI,I}$ are parameters of the PLL.

The modified SRF-PLL is implemented also in the exponential load model (see Figure A.6). The response improvement is further shown.

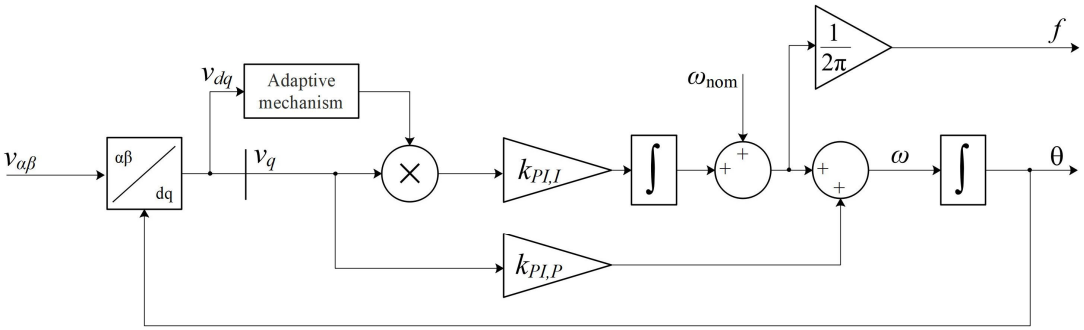

Figure 5.19 – Modified PLL structure.

The grid-forming control scheme is illustrated in Figure 5.20.

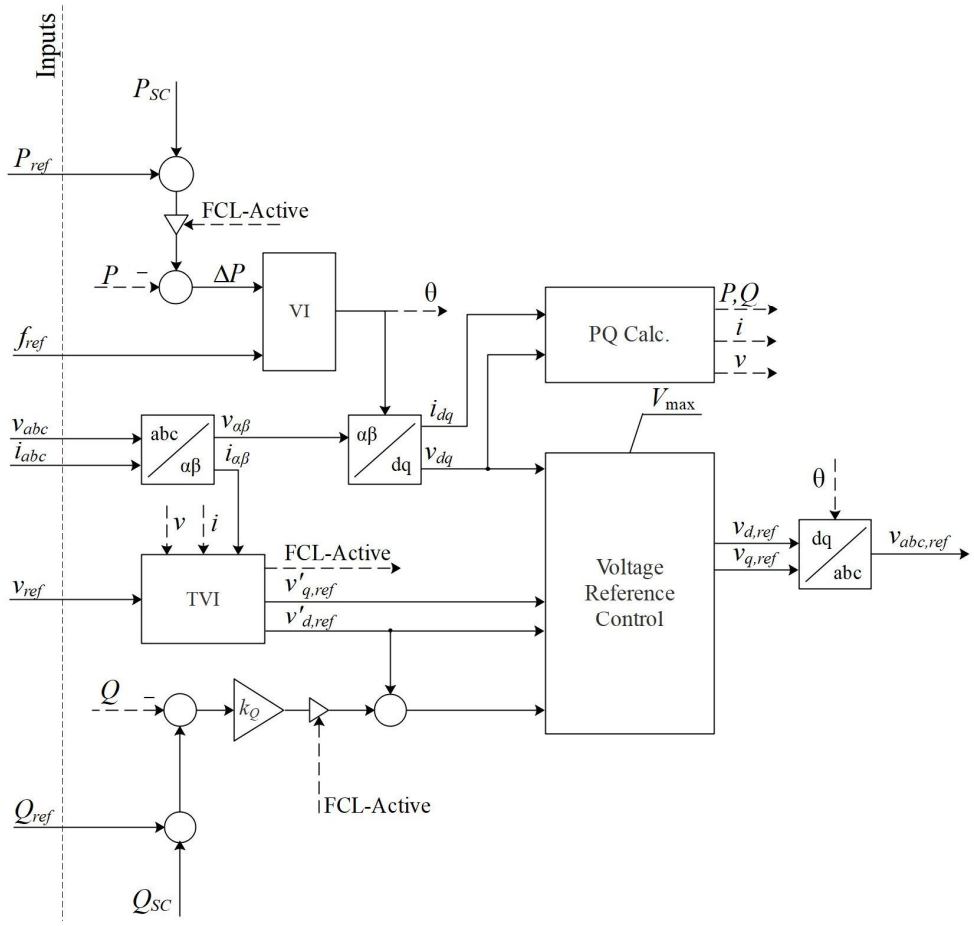

Figure 5.20 – Grid-forming control strategy.

The *voltage reference control* block implements a simple integral controller that rejects high-frequency disturbances [156], with a v_d feed-forward for good dynamic response [125].

The *PQ calculation* block, other than the active and reactive powers and the grid voltage, estimates also the current amplitude required for the implementation of the FCL algorithm.

The *VI* block is where the VSM strategy described in Section 4.2.1b is implemented. The control scheme is illustrated in Figure 5.21, where H_V is the VI constant, f_{nom} is the nominal frequency and ω_{ref} is the reference angular velocity, which in pu is equal to f_{ref}.

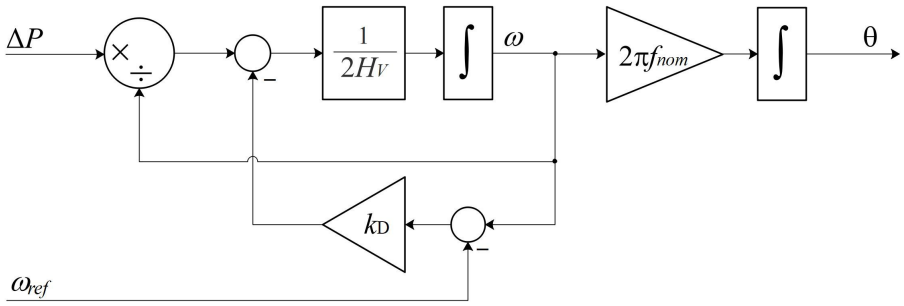

Figure 5.21 – Virtual Synchronous Machine implementation.

Due to the absence of a current controller in Figure 5.20, the current cannot be directly limited. To overcome this issue, the *TVI* block implements the FCL as described in Section 4.2.1c and its scheme is illustrated in Figure 5.22. The Z_V block implements (4.11) to establish the state and value of the virtual impedance.

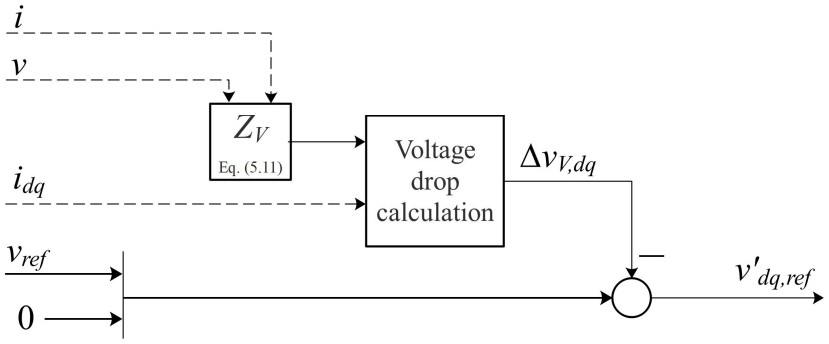

Figure 5.22 – TVI implementation.

The voltage drop across the TVI can be expressed in the *dq*-frame as [157],

$$\begin{aligned} \Delta v_{V,d} &= R_V \cdot i_d - X_V \cdot i_q \\ \Delta v_{V,q} &= R_V \cdot i_q + X_V \cdot i_d \end{aligned} \tag{5.15}$$

Signals P_{SC} and Q_{SC} account for the frequency and voltage secondary control. Secondary load-frequency control can be performed locally, by using a PI-controller at each source responsible of providing the system with the frequency reference, or in a centralized way [95], [158]. In any case, when more than one source participates in the secondary control, participation factors are applied.

The same logic can be applied for the voltage control [94]. In such case, the voltage measuring point should be the same for all sources.

It is noticed that the secondary control is deactivated when the FCL is activated, otherwise the voltage secondary control loop conflicts with the voltage drop implemented in the TVI [111]. Moreover, since during faults the voltage drops considerably, the current increases proportionally to such drop so the BESS injects/absorbs a certain amount of power. To avoid the rising of the current, also the contribution of power references (which is not always null as seen in Section 4.2.1) is brought to zero, as in a ZPM strategy. Therefore, the grid-forming unit is entirely committed to maintain the MG synchronized within acceptable limits.

The parameters of the grid-forming BESS are the same of Table 5-4 with the extension of those reported in Table 5-12. The transformer parameters are the same for all DERs and controllable loads, with the proper nominal voltages.

TABLE 5-12
PARAMETERS OF THE GRID-FORMING BESS

VSM	
Virtual inertia (H_V)	1 s
FCL – TVI	
Maximum current (I_{max})	1.5 pu
Output impedance (Z_{DER})	0.0175 + j0.1860 Ω

A value of I_{max} equal to 1.5 pu is used in this report [108], [159], which is more conservative with respect to the range 3-5 pu sometimes suggested in the literature [95]. However, some effects of such choice are further assessed.

b) Photovoltaic power plant

In this study the PV generator is connected to the grid only through an inverter in which the MPPT is implemented. In such way, the scheme of Figure 5.4 is still representative, where $v_{DC,ref}$ is not an independent input, but it is determined by the MPPT algorithm.

The main parameters of the PV plant, which are taken from the "*SunPower SPR-415E-WHT-D*" built-in model available in Simulink [160], are reported in Table 5-13. The I-V and P-V characteristic is illustrated in Figure 5.23.

TABLE 5-13
PARAMETERS OF THE PV POWER PLANT

General			
Nominal power	500 kW		
DC voltage (V_{DC})	480 V		
AC low voltage (V_{AC})	0.23 kV		
Arm inductance (X_{arm})	0.3 pu		
Module			
Open-circuit (OC) voltage (V_{oc})	85.3 V		
Short-circuit (SC) current (I_{sc})	6.09 A		
Temp. coefficient OC ($K_{V,PV}$)	-0.229 %/°C		
Temp. coefficient SC ($K_{I,PV}$)	0.030706 %/°C		
Diode ideality factor (a)	0.87223		
Num. cells per module	128		
Array			
Modules in series per string (N_s)	7		
Strings in parallel (N_p)	175		
Series resistance ($R_{s,PV}$)	0.5371 Ω		
Parallel resistance ($R_{p,PV}$)	419.7813 Ω		
PI-controllers			
k_P^{DC}	2	k_P^i	0.3
k_I^{DC}	400	k_I^i	20

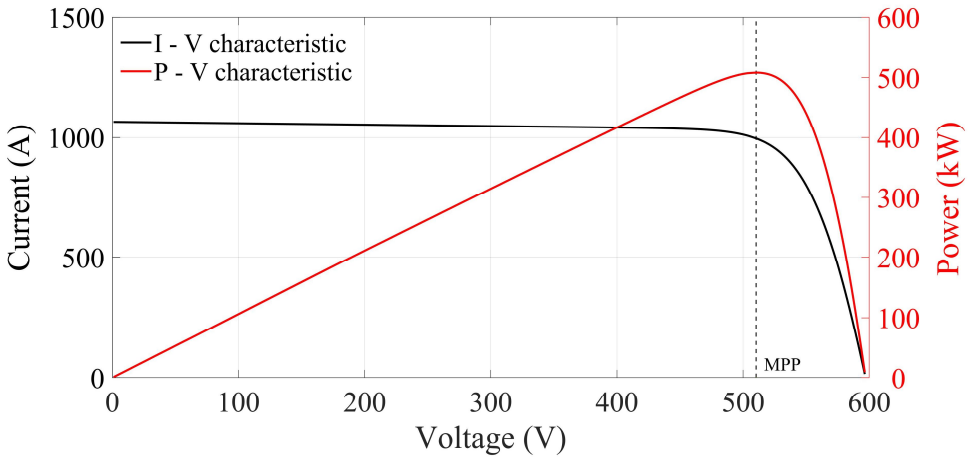

Figure 5.23 – I-V and P-V characteristics of the PV power plant. MPP corresponds to the Maximum Power Point.

c) Conventional Loads

Following the conclusions of Section 5.1.2 for which the rotating nature of loads must be considered, conventional loads are represented as a combination of stationary loads and IMs.

Stationary loads are represented through the exponential model, in which the frequency-dependence has been neglected, i.e., their behavior is described by (A.21).

Since the load within a MG normally comprises very different types and classes of loads, the full representation of such heterogeneity leads to a high computational burden, which could be critical particularly for real-time simulations. Therefore, a load aggregation process is applied in order to reduce a group of loads with different characteristics into *one single* exponential load plus *one single* IM.

The equivalent inertia (referred to only the rotating load) and the equivalent parameters of the exponential load were already addressed in (5.9), (5.11) and (5.12). The remaining equivalent parameters of the IM are calculated by using the following expressions [161],

$$\frac{1}{R_{s,eq} + jX_{s,eq}} = \sum_i \frac{s_{i,rot}}{R_{s,i} + jX_{s,i}} \tag{5.16}$$

$$\frac{1}{X_{m,eq}} = \sum_i \frac{s_{i,rot}}{X_{m,i}} \tag{5.17}$$

$$\frac{1}{R_{r,eq} + jX_{r,eq}} = \sum_i \frac{s_{i,rot}}{R_{r,i} + jX_{r,i}} \tag{5.18}$$

The rated power of the equivalent exponential load and IM is simply the sum of the correspondent rated powers.

To validate the aggregation process, a fault and its clearance process is simulated in a system connecting a SG to a residential load through an impedance. In one case the load is represented in detail, i.e., by 5 IMs and 3 exponential loads. The time required to carry 2 seconds of simulation was 110.29 s. In a second case, the load is aggregated, thus represented by one IM and one exponential load. The time required to carry 2 seconds of simulation was 29.28 s., i.e., almost four times less than for the first case. The system frequency, the voltage at the terminals of the load and the current absorbed by it are illustrated in Figure 5.24, showing a good equivalence.

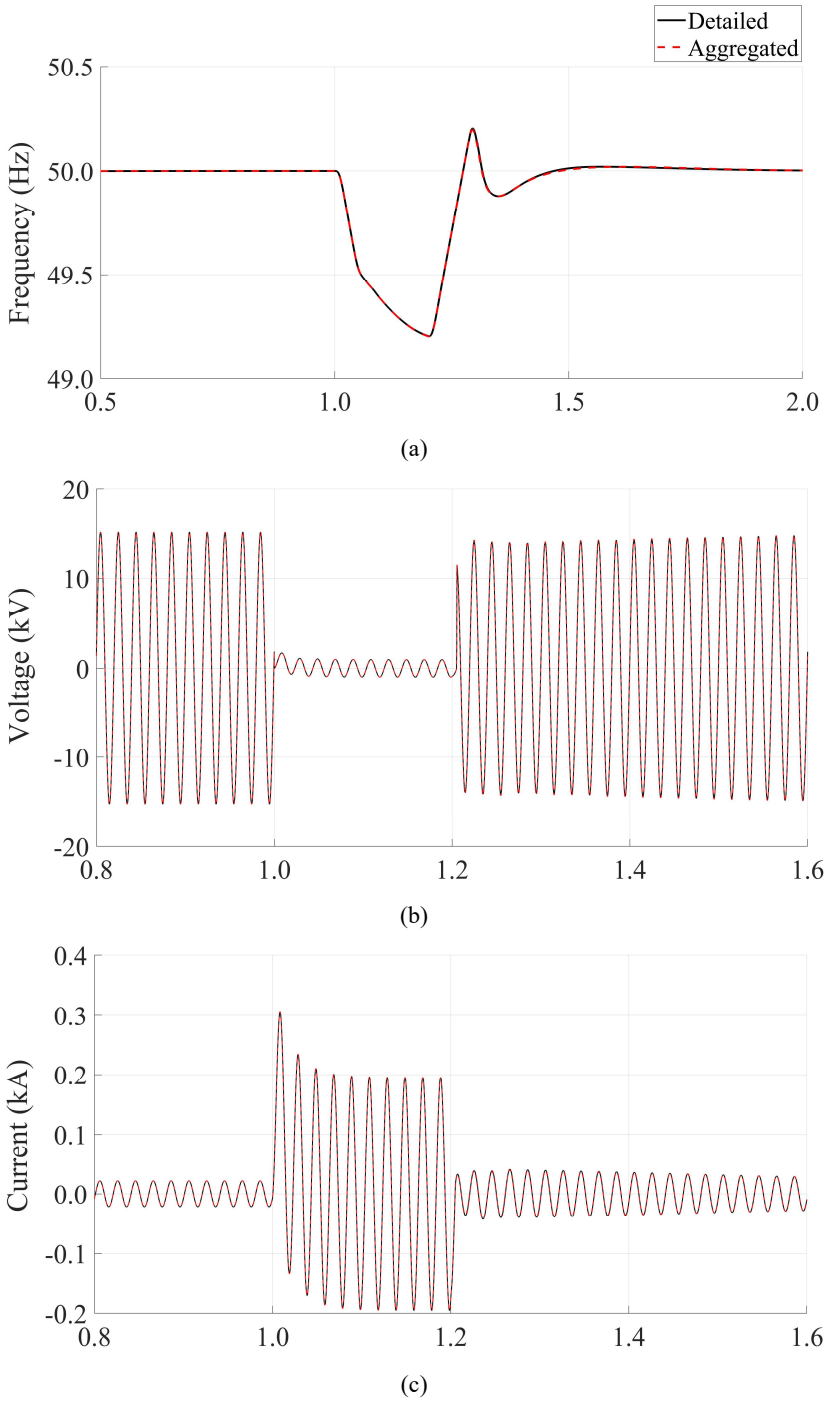

Figure 5.24 – Comparison between a detailed load model and its aggregated equivalent. (a) Frequency, (b) voltage and (c) current at the load terminals during a three-phase fault.

The same classes and types of loads of Table 5-6 are considered.

d) Electric vehicle – charging station

The batteries belonging to EVs constitute a power reserve that can help to the frequency and voltage control of the MG, particularly when it is islanded. Different strategies can be adopted to accomplish this. In this section, a control strategy based on the one presented in [162] is adopted.

The EV-CS is modelled as a DC ideal source in series to a resistance and a boost converter in cascade with an inverter, as shown in Figure 5.18. The boost converter is controlled to maintain the voltage at the DC-link constant. The inverter is controlled the same way as the inverter of the BESS in the grid-following mode (Figure 5.3), comprising the droop control strategy with the following considerations.

- In order to guarantee the longevity of the batteries, a dead band is added to the droop characteristics in which EVs do not respond to frequency and voltage deviations, as shown in Figure 5.25, in which $f_{db,uf}$, $f_{db,of}$, $v_{db,uv}$ and $v_{db,ov}$ refer to the frequency and voltage dead bands for under and over frequency and under and over voltage, respectively, for which the droop constants $k_{P,uf}$, $k_{P,of}$, $k_{Q,uv}$ and $k_{Q,ov}$ are considered. It is noticed that the curves of Figure 5.25 are reversed with respect to the ones of Figure 4.4, since the load sign convention is considered for the EV-CS, in opposition to the generator sign convention implemented for the BESSs.
- The reactive power reference is always set to zero. Unlike PV plants for which $i_{q,ref}$ is always zero, a voltage-reactive power droop is implemented to the EV-CS such that it can absorb or inject reactive power if voltage is outside the dead band.

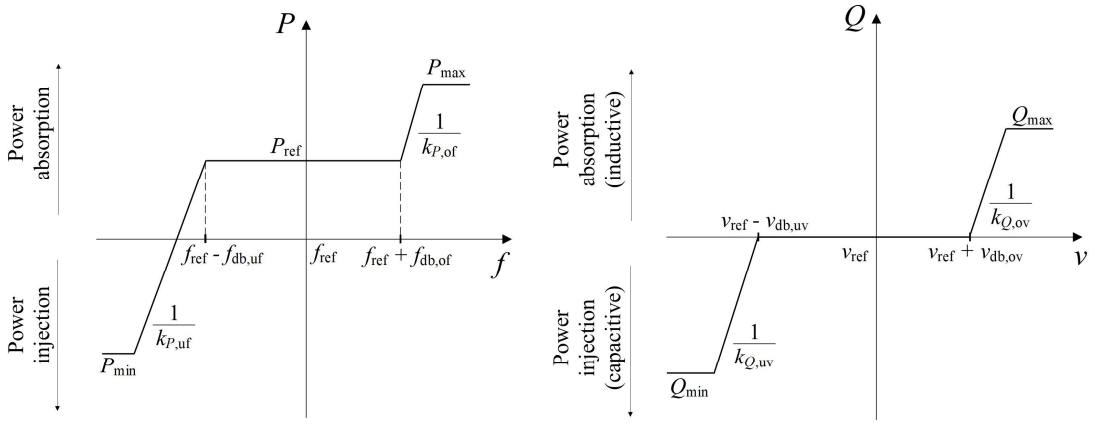

(a) (b)

Figure 5.25 – Droop characteristics of the EV-CS (Adapted from [162]).

Some parameters of the EV-CS are reported in Table 5-14, while others (e.g., the dead band) are specified in each study case.

The parameters relative to the droop characteristics are mainly defined according to the power system characteristics. They might also account for the SoC of the vehicles, e.g. to prevent over-charging (over-discharging) the batteries when they are already full (empty) [163]. Moreover, if the converter does not allow power injection to the grid, a controllable charging mode can still be applied by setting $P_{min} = 0$ [162].

TABLE 5-14
PARAMETERS OF THE EV-CS

General					
Battery voltage (e_{DC})	325 V				
Series resistance (R_s)	0.013 Ω				
DC-link voltage (V_{DC})	733 V				
AC low voltage (V_{AC})	0.4 kV				
Arm reactance	0.3 pu				
Droop control					
Under frequency active power droop ($k_{P,uf}$)	2.4 %				
Over frequency active power droop ($k_{P,of}$)	4.8 %				
Under voltage reactive power droop ($k_{Q,uv}$)	10 %				
Over voltage reactive power droop ($k_{Q,ov}$)	20 %				
PI-controllers					
k_P^P	0.1	k_P^Q	0	k_P^i	1.185
k_I^P	15	k_I^Q	0.75	k_I^i	925

Since the EV-CS normally constitutes a load, during faults the ZPM is adopted.

e) Variable speed heat pumps

Variable speed HPs are constituted by an IM interfaced to the network through a back-to-back converter, as shown in Figure 5.18. The grid-side converter is controlled to maintain the voltage at the DC-link constant, as in Figure 5.4. The motor-side converter is governed to follow a constant V/Hz control [164], feeding the motor with a voltage proportional to the frequency for frequencies minor than the rated value and maintaining the voltage constant for greater frequencies .

As HPs could alter their behavior depending on the system frequency, other than the temperature, they can contribute to the frequency regulation, e.g. as proposed in [152], [165]. A combination based on two different strategies is adopted: i) a controller compares the frequency of the system f with two thresholds f_{ON} and f_{OFF}, as done in [152]. If f rises higher than f_{ON} the HP is switched on. On the contrary if f drops lower than f_{OFF} the HP is switched off. Both thresholds are settled dynamically depending on the temperature; ii) a VI control is implemented as in [165], for which the power reference in per unit is modified by,

$$\Delta P_{ref} = H_V \frac{df}{dt} + k_D \left(f - f_{ref} \right) \tag{5.19}$$

For simplicity, the damping factor will be expressed through the droop constant, considering their relation evidenced by (4.10).

The combination of both strategies allows HPs to respond to system over-frequencies by increasing their active power demand: in part by turning on and in part by increasing their power setpoint. Vice versa, they respond to system under-frequencies by decreasing their demand: in part by turning off and in part by decreasing their power setpoint. This control scheme is shown in Figure 5.26.

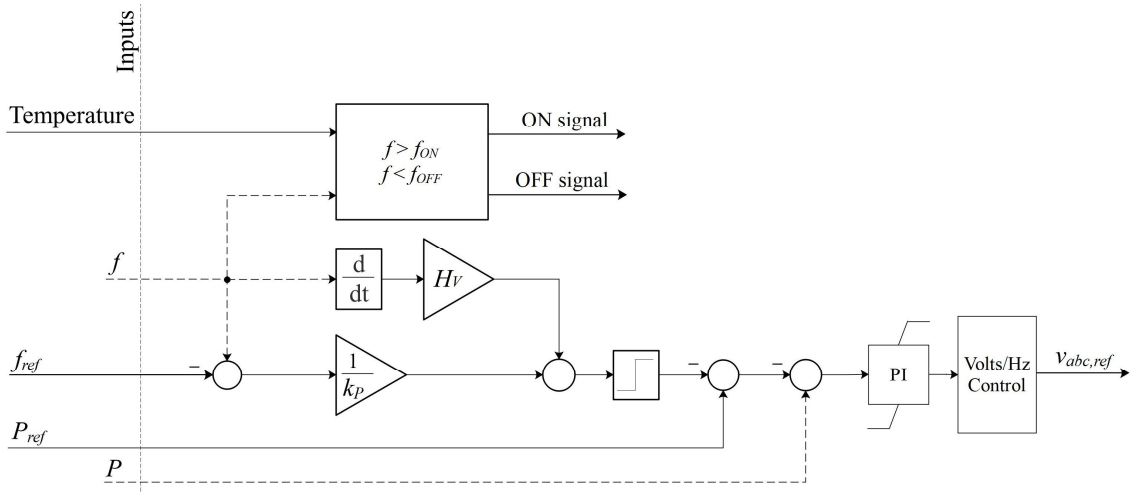

Figure 5.26 – Control scheme of HPs for the motor side converter.

In order to prevent input over-currents and DC-link over-voltages during the acceleration/deceleration of the IM [166], the grid-side converter (which controls the DC-link voltage) is faster than the motor-side converter (which controls the power and in which the VI is implemented).

During faults, in order to replicate a ZPM strategy, the reference $i_{d,ref}$ for the grid-side converter is brought to 0. However, if the control of the motor-side converter would remain invariant, the IM would withdraw energy from the DC-link, reducing drastically the DC-link voltage. In order to prevent that, during faults, also reference $v_{abc,ref}$ of the motor-side converter is brought to 0.

In the time horizon of the considered short transients, the temperature of a building could barely change, hence the thermal model of the buildings is avoided. Instead, different temperature conditions are assumed for different scenarios.

The parameters of the HP are shown in Table 5-15.

TABLE 5-15
PARAMETERS OF THE HPS

General					
AC motor-side voltage ($V_{AC,M}$)	380 V				
AC grid-side low voltage ($V_{AC,G}$)	380 V				
DC-link voltage (V_{DC})	733 V				
IM Inertia (H)	0.3 s				
Arm reactance	0.3 pu				
Virtual inertia					
Droop constant (k_P)	2.4 %				
Virtual inertia (H_V)	0.5 s				
PI-controllers					
Motor-side converter		**Grid-side converter**			
k_P^P	0	k_P^{DC}	2.4	k_P^i	1.8
k_I^P	0.318	k_I^{DC}	80	k_I^i	925

All power converters are represented by the average model.

5.2.2 Influence of load composition

a) Sensitivity analysis

A sensitivity analysis is carried out considering the system of Figure 5.27 to assess the impact of some parameters of both conventional and controllable loads on the minimum values reached by frequency and voltage during fault-generated transients. A three-phase fault with a 5 Ω fault resistance is simulated in line 2 at $t = 4$ s, followed by the opening of the CBs after 200 ms. The BESS is controlled in the grid-forming mode and the load is specified for each study case.

All the simulations are carried out in the Simulink environment.

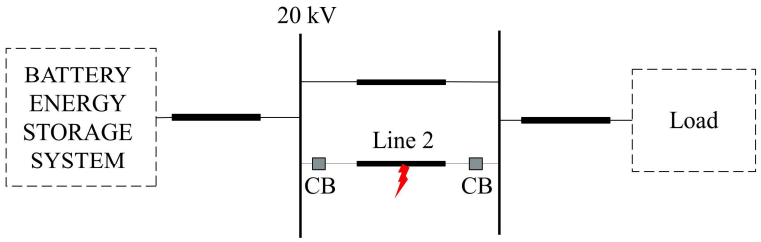

Figure 5.27 – Simple system for the sensitivity analysis.

i) Phase-locked loop response

The impact of the PLL on the system stability is already investigated in the literature [114]. It is briefly addressed here only for the case of interest, i.e., for the analysis of the MG dynamic response during short circuits.

A grid-following BESS is connected to the same bus of the grid-forming BESS feeding a mix of stationary and rotating loads.

The frequency estimated by the conventional PLL (as the one implemented in Section 5.1) and the modified one (Figure 5.19) is shown in Figure 5.28. The frequency of the grid-forming unit is also shown as reference, since it is the frequency imposed to the MG. During the short circuit phase, a much more accurate response is obtained with the modified PLL and the same PI parameters (denoted with (a) in Figure 5.28), since the modified PLL can avoid the undesired behavior due to phase jumps. Moreover, the dynamic response can be further improved by modifying the PI parameters (curve (b) in Figure 5.28).

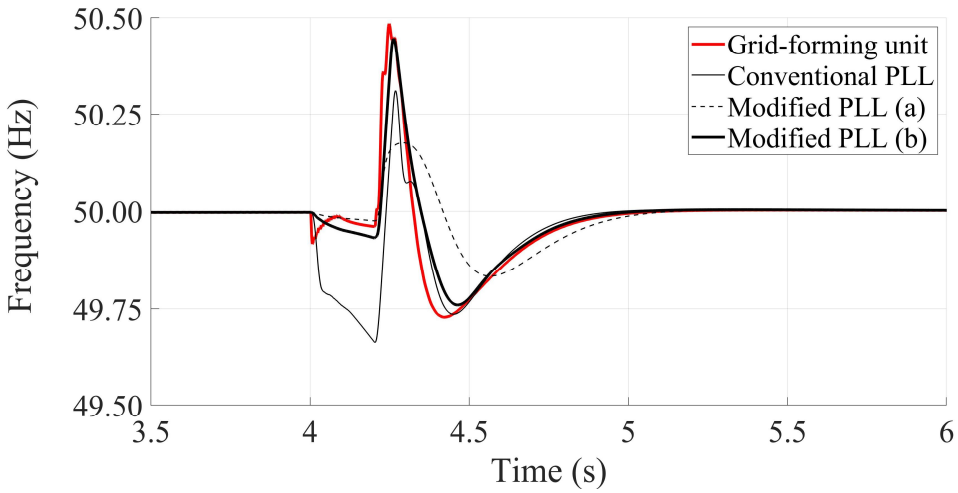

Figure 5.28 – PLL response.

Also the dynamics of exponential loads depend on the estimation of the voltage and current phasor angles through a PLL (see Appendix A). Therefore, the implementation of the modified PLL in the exponential load model improves the numerical stability of the simulations.

ii) Conventional loads

The load connected to the system is composed by a combination of five exponential loads and five IMs. Some of the relevant parameters are kept constant and are reported in Table 5-16.

TABLE 5-16
LOAD PARAMETERS

IMs and exponential loads	
Rated power	5x 70 kVA
Power factor	0.87
IMs	
Stator resistance (r_s)	0.025 pu
Stator reactance (x_{ls})	0.088 pu
Magnetizing inductance (x_m)	3.2 pu
Rotor resistance (r_r)	0.016 pu
Rotor reactance (x_{lr})	0.17 pu

In a first case study, k_{pu} and k_{qu} are kept constant and equal to 1. The influence of the inertia constant H of the IMs on the frequency and voltage after the fault is illustrated in Figure 5.29. A greater frequency variation can be observed when H is greater. This is because during the fault, the IMs decelerate. After that, when the fault is cleared, the IM with greater inertia absorbs more active power to accelerate and return to the steady-state velocity. The IM with less inertia reaches a lower speed at the end of the fault, thus the acceleration process takes more time, and it absorbs more reactive power causing the voltage sag of Figure 5.29b.

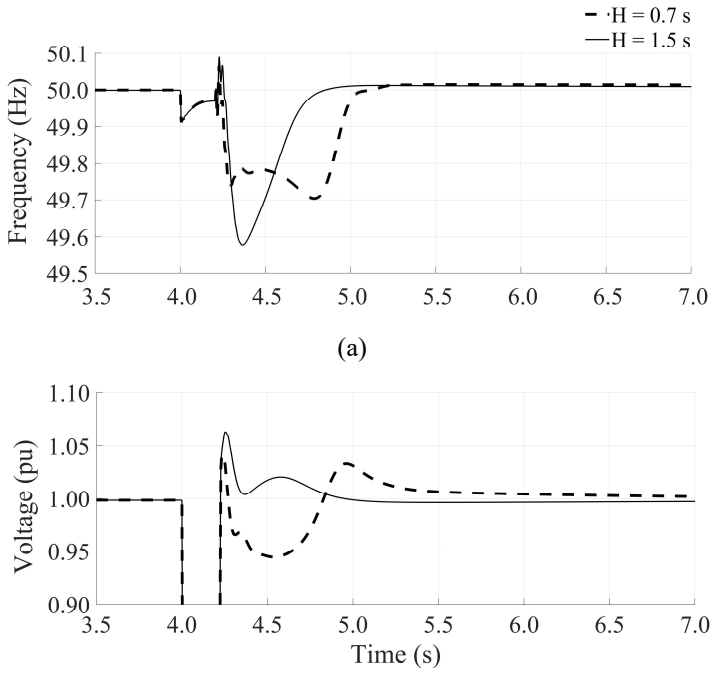

Figure 5.29 – Influence of the inertia constant H on the (a) frequency and (b) voltage transients during a fault.

This behavior is not observed always in the same way changing the parameter values. After a certain value of H, the minimum frequency starts to increase. Moreover, the rotor resistance R_r has been

observed to have an influence both in the minimum frequency and in the value of H in which the behavior reverses, as can be seen in Figure 5.30.

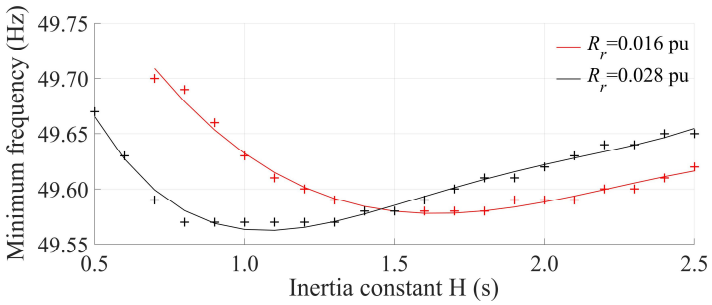

Figure 5.30 – Influence of the rotor resistance r_r and H on the minimum value of frequency during a fault.

The influence of the exponential load parameters is analyzed, at first, by keeping k_{qu} constant and equal to 1 while increasing k_{pu}, then, by keeping k_{pu} constant and equal to 1 while increasing k_{qu}. A range of values for k_{pu} and k_{qu} considering typical loads [167] is examined.

The impact of the exponential loads is greater as greater is the deviation of the voltage from its rated value. Considering this, when H = 1.5 s, the voltage deviation after the fault clearance is not very conspicuous (see Figure 5.29b). Therefore, in such case, the influence of k_{pu} and k_{qu} is negligible, as can be seen in Figure 5.31.

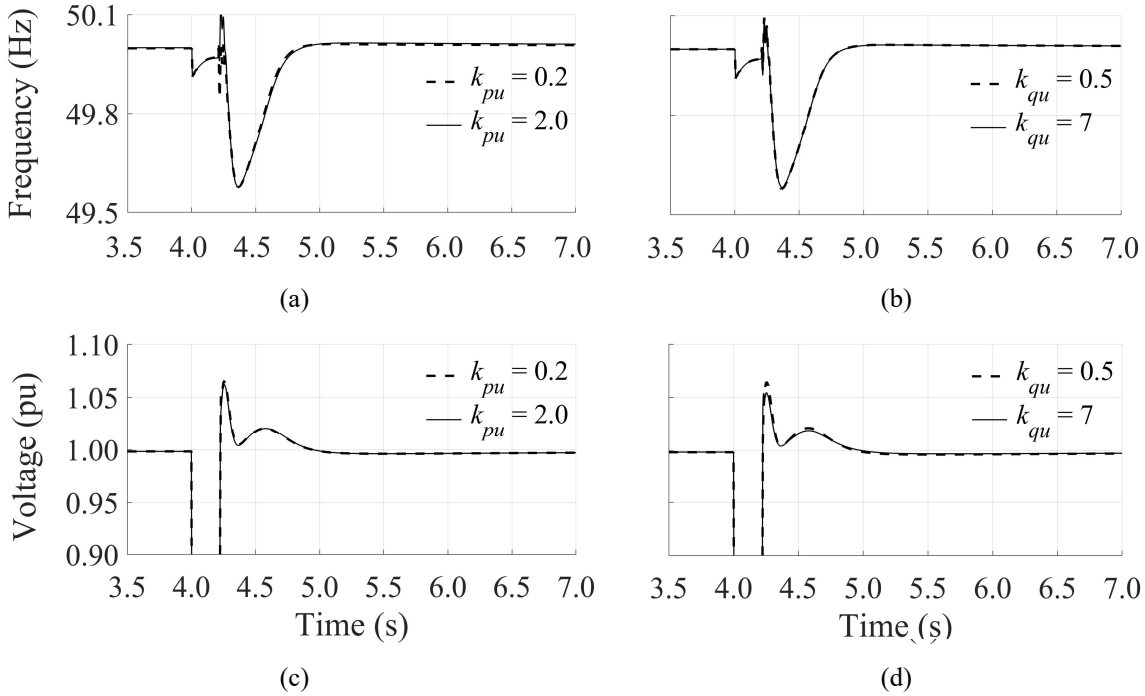

Figure 5.31 – Influence of the exponential load parameters on (a) and (b) the frequency and (c) and (d) the voltage transients during a fault when H = 1.5 s.

The same analysis is carried out for H = 0.7 s, for which the voltage deviation is greater (see Figure 5.29b). The results are shown in Figure 5.32 and can be summarized as follows: i) Greater values of k_{pu} and k_{qu} lead to minor frequency and voltage deviations, respectively, as shown by Figure 5.32a and Figure 5.32d. Since greater values of the exponential parameters lead to a minor load consumption

during the voltage sag, hence there are minor frequency and voltage deviations; ii) The influence of k_{pu} and k_{qu} on the voltage and frequency, respectively, is almost negligible as shown by Figure 5.32c and Figure 5.32b. A greater value of k_{pu} leads to a slightly greater frequency deviation, hence the slip of IMs is minor for a given speed reached during the fault, thus its recovery is slower (Figure 5.32c); a greater value of k_{qu} leads to a minor voltage deviation, which in turn leads to a greater active power load consumption, hence a minor frequency (Figure 5.32b).

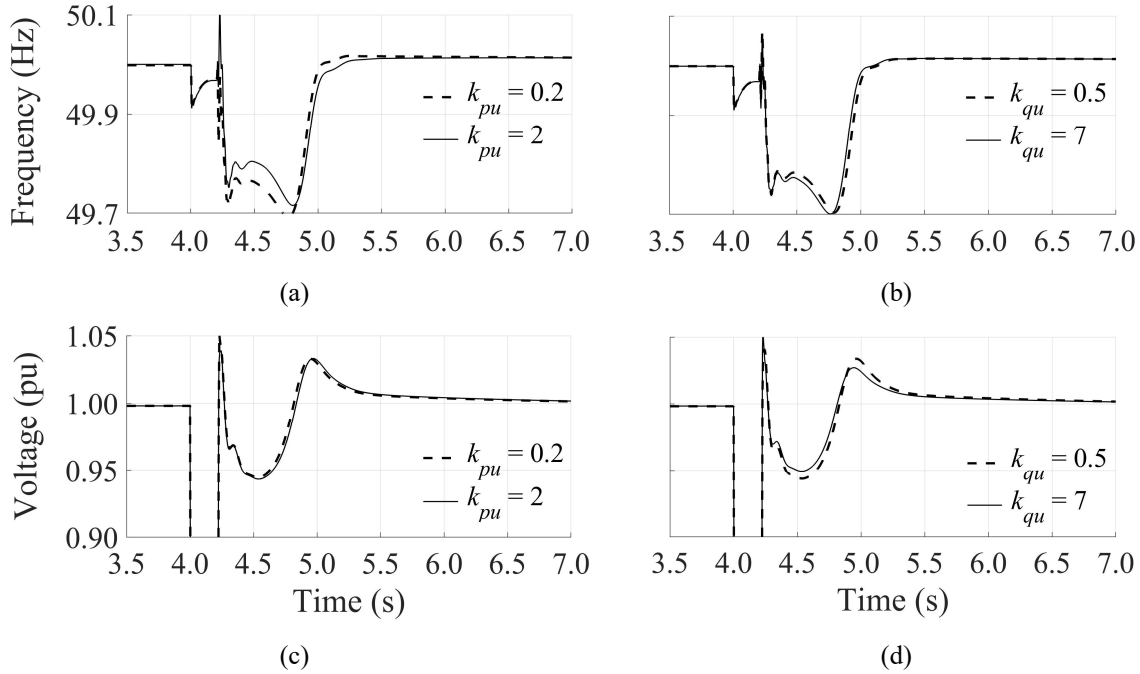

Figure 5.32 – Influence of the exponential load parameters on (a) and (b) the frequency and (c) and (d) the voltage transients during a fault when H = 0.7 s.

iii) Grid-forming unit

In Figure 5.33 the influence of the VI constant of the BESS (H_V) on the frequency is illustrated. A greater H_V results in a minor frequency deviation, as expected, while the influence on the voltage is negligible.

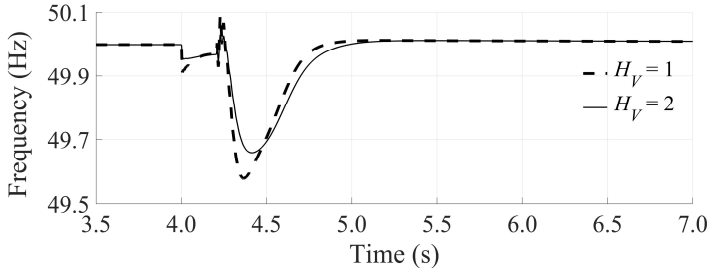

Figure 5.33 – Influence of the VI constant H_V on the frequency transient during a fault.

An analysis is carried out to show the influence of the FCL, considering H = 0.7 s and $k_{pu} = k_{qu}$ = 1. In Figure 5.34 the frequency, voltage and current behavior for different values of $I_{\max}$ is shown. As $I_{\max}$ increases, the frequency during the fault and just after the fault clearance decreases. The speed of IMs is also shown in Figure 5.34. When the allowed current is increased, more power is delivered by the

BESS, hence IMs accelerate faster reaching the steady state faster. This latter effect could have a great influence on the IMs in some cases, e.g. if the fault lasts longer or if the mechanical load of the IM is greater, in which case an I_{max} of 1.5 pu is not be able to restore the speed of the IMs while an I_{max} of 5 pu guarantees their recovery, as shown in Figure 5.35.

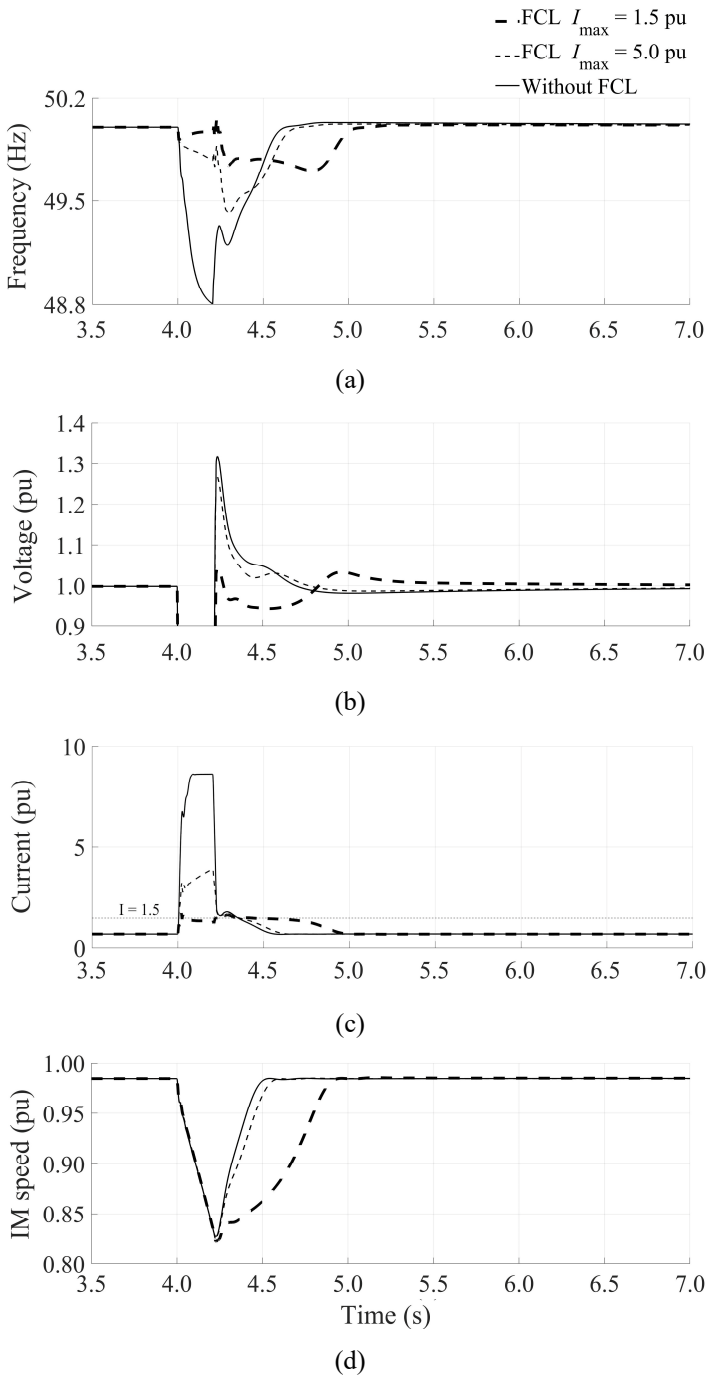

Figure 5.34 – Influence of the FCL implementation and the maximum current value on the (a) frequency, (b) voltage, (c) current and (d) motor speed transients during a fault.

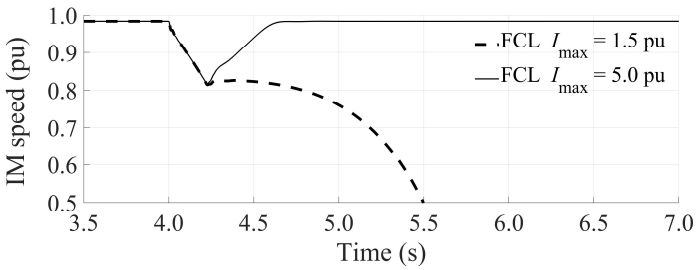

Figure 5.35 – Influence of the maximum current on a particular case.

iv) Electric vehicle charging station

An EV-CS is included in the load composition, as reported in Table 5-17, in order to study the influence of its control parameters on the minimum frequency and voltage. The electrical parameters of the exponential loads and the IMs are the same reported in Table 5-16.

TABLE 5-17
LOAD PARAMETERS

IMs		**Exponential loads**	
Rated power	5x 70 kVA	**Rated power**	5x 70 kVA
Inertia (H)	0.7 s	k_{pu} **and** k_{qu}	1
EV-CS			
Rated power	1 MVA		
Active power reference (P_{ref})	-0.1 pu		

The influence of the EV-CS droop control on the frequency and voltage is shown in Figure 5.36 in which two dead-bands are compared: a wider dead-band, i.e. $f_{db,uf} = f_{db,of} = 0.2$ and $v_{db,uv} = v_{db,ov} = 0.05$ and a narrower dead-band, i.e. $f_{db,uf} = f_{db,of} = 0.1$ and $v_{db,uv} = v_{db,ov} = 0.025$.

The influence of the droop control strategy is particularly important for the voltage since it reduces the depth and the duration of the voltage sag after the fault clearance. Such voltage sag, as already mentioned, is a consequence of the reactive power absorbed by the IMs during the acceleration. The contribution of EV-CS could be crucial in some cases. In Figure 5.37 it is illustrated a case in which the IM is not able to recover after the fault clearance without the contribution of EV-CS.

The contribution to the system restoration after the fault is greater as narrower is the dead-band. The activation of a narrow dead-band after a fault condition is detected while keeping a wide dead-band in normal conditions, might limit the negative effects on the EV battery usage while guaranteeing a considerable contribution to the system stability during faults.

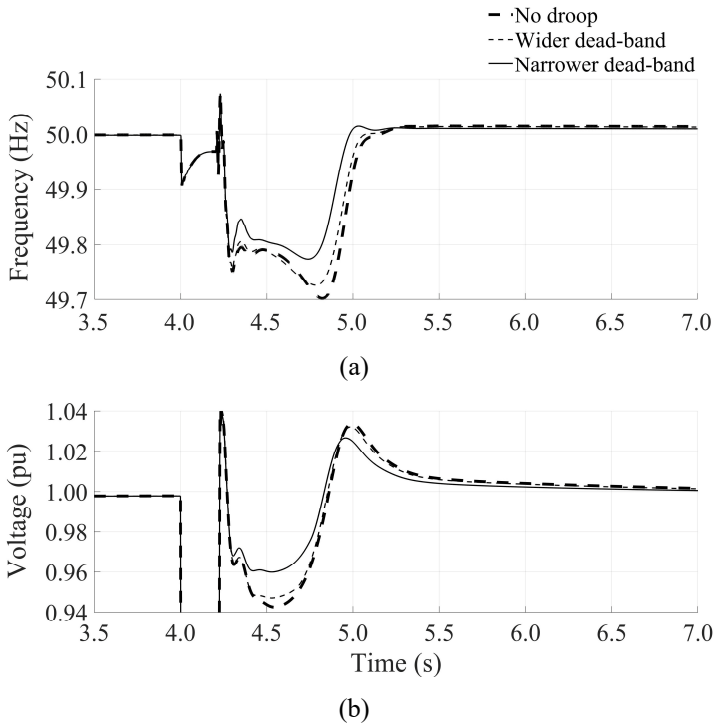

Figure 5.36 – Influence of the droop control and its dead-band on the (a) frequency and (b) voltage transients during a fault.

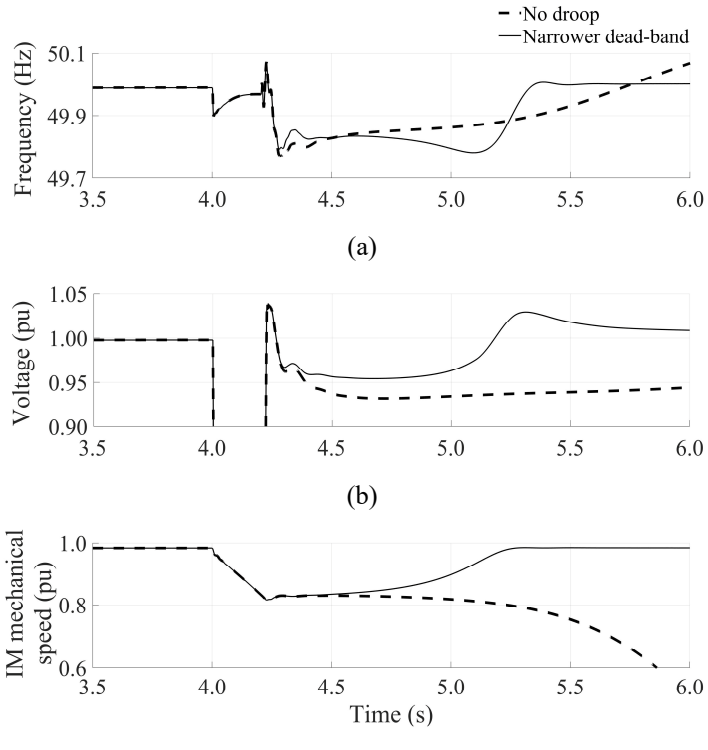

Figure 5.37 – Influence of the droop control on the (a) frequency, (b) voltage and (c) motor speed transients during a fault for a particular case.

The droop constants, as it is expected, have a direct influence on the frequency and voltage deviations. This effect is shown in Figure 5.38.

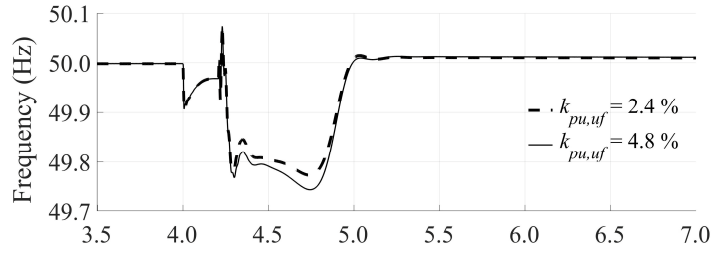

(a)

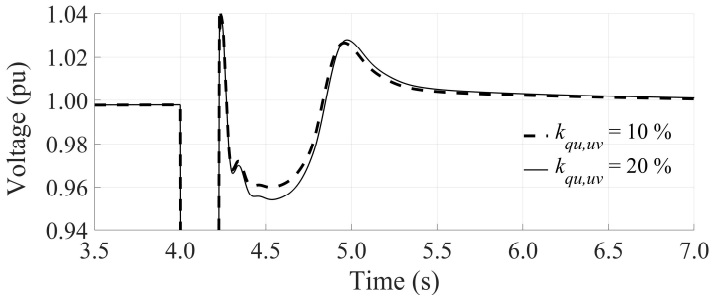

(b)

Figure 5.38 – Influence of the droop constants on the (a) frequency and (b) voltage transients during a fault.

v) Heat Pumps

In this scenario, part of the load is composed by HPs as reported in Table 5-18, in order to study the influence of its control parameters on the minimum frequency and voltage values. The electrical parameters of the exponential load and the IMs are the same reported in Table 5-16.

TABLE 5-18
LOAD PARAMETERS

IMs		**Exponential loads**	
Rated power	5x 50 kVA	**Rated power**	5x 50 kVA
Inertia (H)	1.5 s	k_{pu} **and** k_{qu}	1
HP			
Total power	400 kVA		
Active power reference (P_{ref})	-0.8 pu		

First, the impact of the VI implementation on the transient after the fault is assessed, assuming that any load is disconnected from the MG due to the frequency deviation. The results are shown in Figure 5.39. The contribution of the VI implementation is almost negligible concerning the immediate response of the MG. This is because the dynamics during the first instants after the fault clearance are mainly driven by the DC voltage control loop of the grid-side converter which, as stated before, is faster than the dynamics of the motor-side converter in which the VI is implemented. The DC voltage and the relative *d*-axis current reference are shown in Figure 5.40.

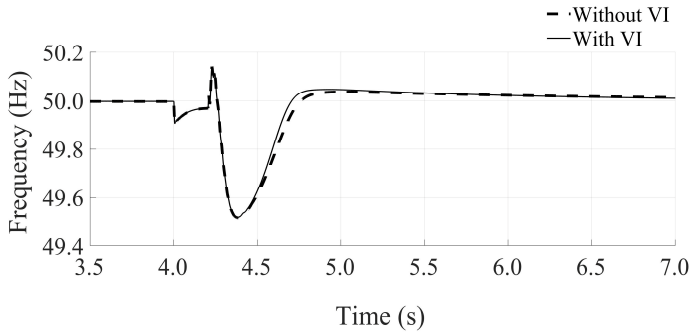

Figure 5.39 – Influence of the VI of HPs on the frequency transients during a fault.

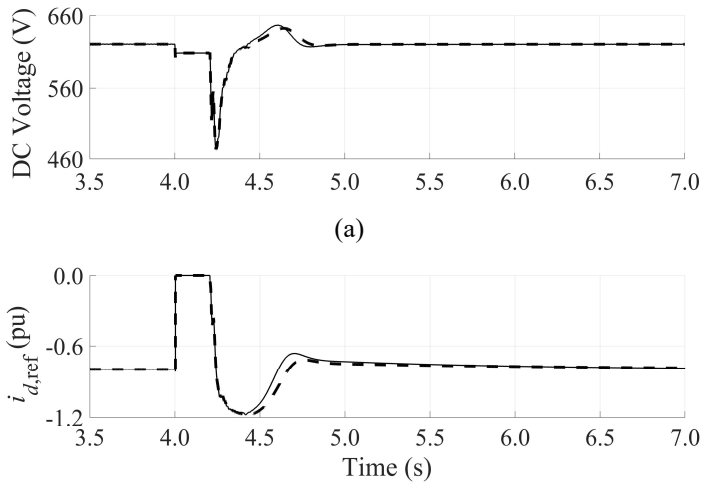

Figure 5.40 – (a) DC voltage and (b) $i_{d,ref}$ transients of HPs during a fault.

In Figure 5.41 the frequency is shown assuming a disconnection of the 50% and the 100% of the HPs at $f = 49.75$ Hz. The actual disconnection takes place at a minor frequency. This is because the frequency shown in Figure 5.41 is the frequency computed by the VSM, while the frequency measured by the PLL of the HP is slightly different during the transient, as shown in Figure 5.42. When the PLL measures 49.75 Hz, the actual frequency is 49.55 Hz. Therefore, the effectiveness of this strategy, particularly when fast frequency changes occur, is very much dependent on the ability of the PLL to follow the frequency transient. The conventional PLL could lead to the undesired disconnection of HPs during the short circuit due to a frequency misestimation (see Figure 5.28).

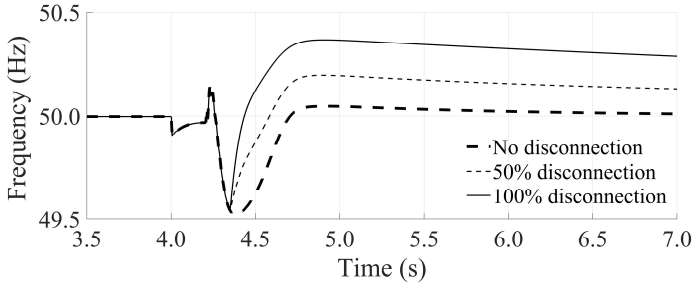

Figure 5.41 – Influence of the disconnection of HPs on the frequency transient.

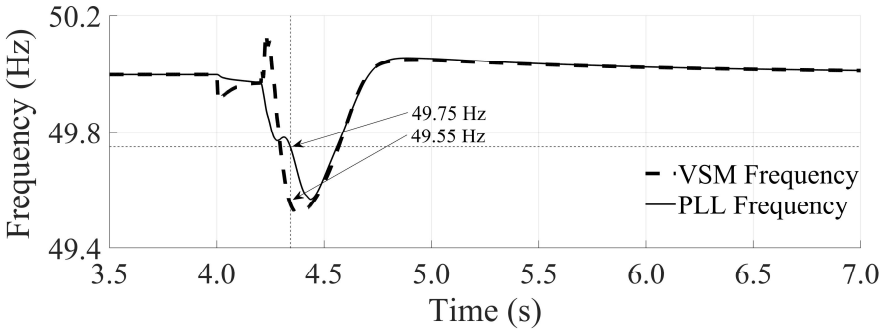

Figure 5.42 – Frequencies from the grid-forming unit and estimated by the HP.

TABLE 5-19
SUMMARY OF THE INFLUENCE OF SOME PARAMETERS RELEVANT TO THE GRID-FORMING BESS AND TO BOTH CONVENTIONAL AND CONTROLLABLE LOADS

Parameter			Frequency deviation	Voltage deviation	Recovery time
BESS	H_V	↑	↓	–	↑↑
	I_{max}	↑	↑↑↑	↓↓↓	↓↓↓
IM†	$H < H'$	↑	↑↑	↓↓↓	↓↓↓
	$H > H'$	↑	↓	–	↑
Exponential load	k_{pu}	↑	↓	–	↑↑
	k_{qu}	↑	–	↓	–
EV-CS	Dead-band	Narrower††	↓	↓↓	↓↓
	$k_{P,uf}$	↑	↑	–	–
	$k_{Q,uv}$	↑	–	↑	–
HP	Virtual Inertia		–	–	↓
	Disconnection		↓↓↓ †††	–	↓↓↓

†The behavior of the IMs is not monotonous as observed from Figure 5.30, and depends if the inertia is greater or lower than a certain value, defined here as H' and which is dependent on other parameters of the motor (e.g., on the rotor resistance as previously illustrated).

††While this characteristic might not be in general very influent on the frequency and voltage deviation, it could be determinant in some cases to prevent the motor stalling, as seen in Figure 5.37.

†††Depends on the moment in which HPs are disconnected and on the amount of disconnected power. However, the contribution can be very considerable.

b) Power-Hardware-in-the-Loop simulations

This section presents the results of PHIL simulations. All tests were carried out in the Smart Grid and Electric Vehicles Laboratory of INESC TEC.

The PHIL system consists of an Opal-RT real-time simulator and a 15kVA power amplifier. In the Opal-RT the grid is simulated, which comprises also the DERs and loads, while the amplifier modulates

the voltage at a certain point of the grid to feed a determined physical load, which in this case is either a motor or a passive resistive-inductive load. The currents absorbed by the physical load are measured and fed back to the Opal-RT.

The parameters of the motor were estimated in [168] and are reported in Table 5-20 for convenience. The power seen by the simulated system can be amplified accordingly through appropriate gain values applied to the Opal-RT current inputs coming from the power amplifier.

TABLE 5-20
PARAMETERS OF IM AT INESC TEC
TAKEN FROM [168]

Rated power (kW)	R_s (Ω)	X_s (Ω)	X_m (Ω)	R_r (Ω)	X_r (Ω)	H (s)
4	1.44	2.56	56.17	1.37	2.56	0.198

i) Simple system

The system of Figure 5.43 is tested. The parameters of the DERs and simulated loads are reported in Table 5-21. The load fed by the power amplifier is varied between the IM and a passive resistive-inductive load, ensuring that the steady state active and reactive powers absorbed are the same in both cases. A three-phase fault with a 5 Ω fault resistance is simulated in line 2 followed by the opening of the CBs after 200 ms. The results are shown from Figure 5.44 to Figure 5.48. Results are reported as if the fault occurred when t = 0 s.

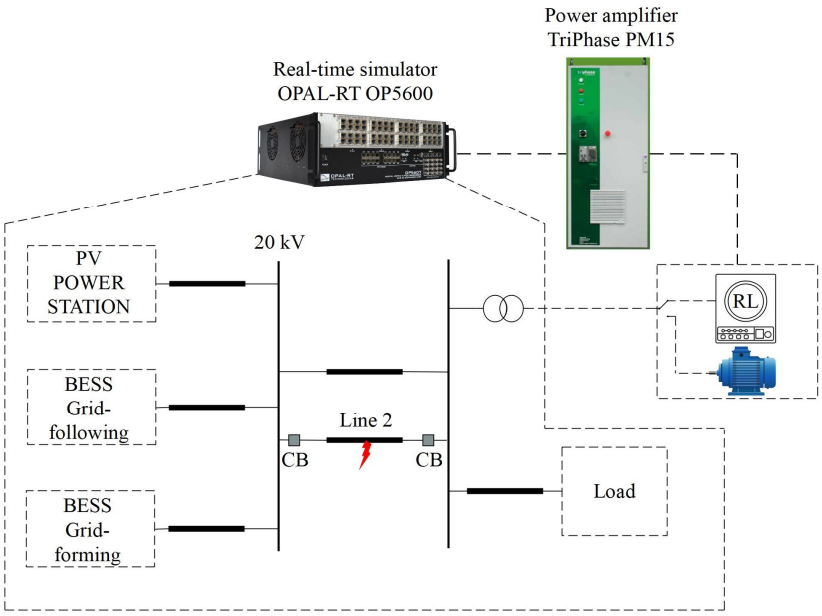

Figure 5.43 – PHIL set-up of a simple system.

TABLE 5-21
LOAD AND DER PARAMETERS

IMs		Exponential loads	
Rated power	5x 70 kVA	**Rated power**	5x 70 kVA
Inertia (*H*)	0.7 s	**k_{pu} and k_{qu}**	1
EV-CS			
Rated power		1 MVA	
Active power reference (P_{ref})		-0.2 pu	
HP			
Rated power		600 kVA	
Active power reference (P_{ref})		-0.8 pu	
BESS (grid-following)			
Active power reference (P_{ref})		0.40 pu	
Reactive power reference (Q_{ref})		0.55 pu	

In Figure 5.44 the frequency and voltage are shown for both cases when the grid-following BESS, the EV-CS and the HP do not participate in the frequency and voltage regulation. When the IM is connected, the minimum reached frequency is lower than when the passive load is connected. When both BESSs and the controllable loads participate in the frequency and voltage regulation, the results are shown in Figure 5.45. In this case too, the frequency reaches a minor value when the IM is connected, but the recovery is faster and the voltage sag is minor, as can be better evinced in Figure 5.46 in which the above results when the IM is connected are compared. As already mentioned, this contribution might become substantial in some situations, as the one shown in Figure 5.47 in which only the participation ensures the system integrity.

Figure 5.48 shows the effect of the disconnection of the HPs for different off-frequency thresholds (f_{OFF}), with respect to the base case in which no disconnection is considered. When the IM is connected, all the considered cases lead to the disconnection of the HPs, while when the passive load is connected, just the last two cases lead to the disconnection of the HPs, i.e., when f_{OFF} is greater or equal than 49.6 Hz.

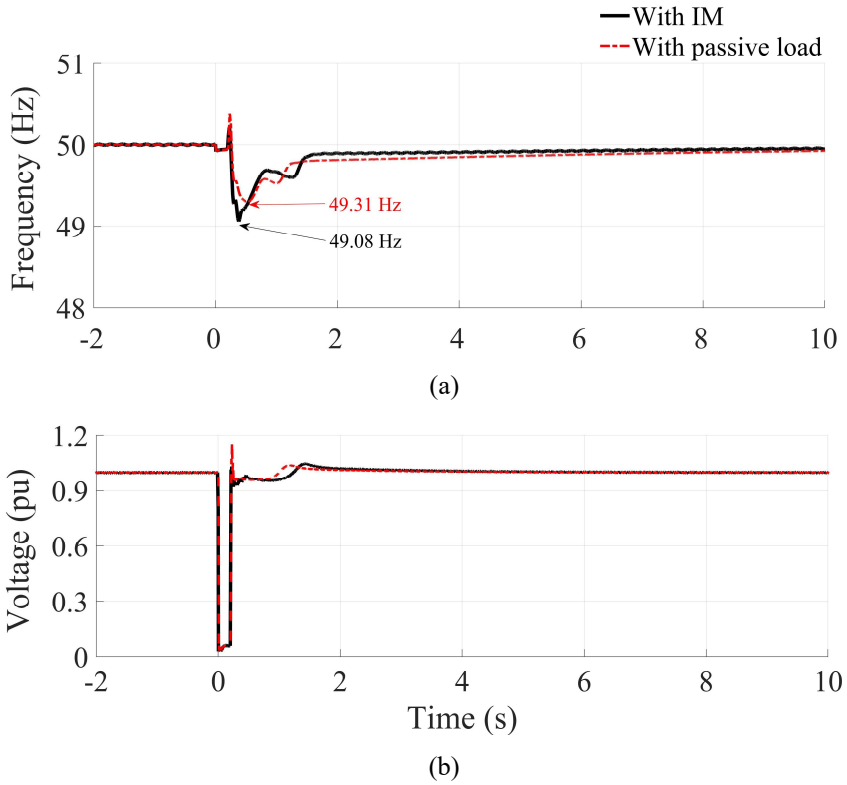

Figure 5.44 – (a) Frequency and (b) voltage for different types of physical loads connected to the MG. The grid-following BESS and the controllable loads do not participate in the frequency and voltage regulation.

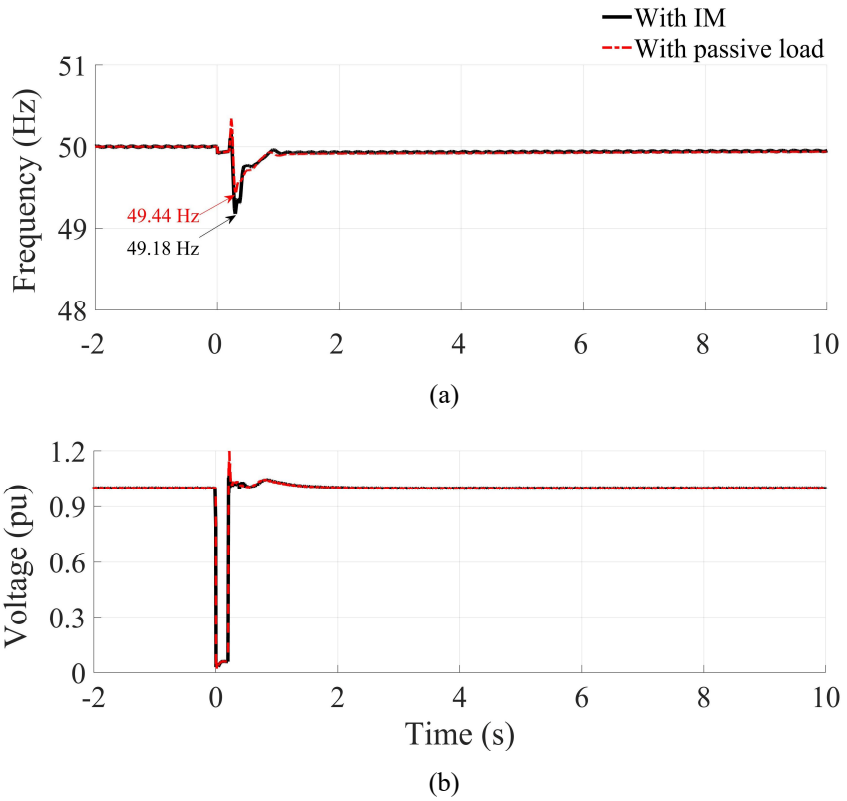

Figure 5.45 – (a) Frequency and (b) voltage for different types of physical loads connected to the MG. The grid-following BESS and the controllable loads participate in the frequency and voltage regulation.

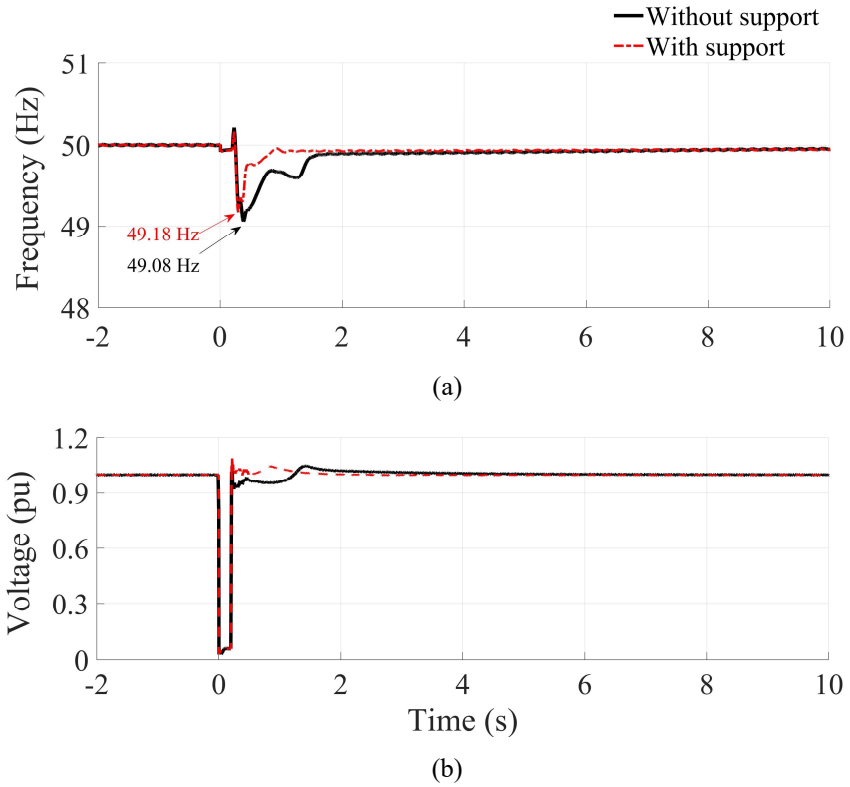

Figure 5.46 – (a) Frequency and (b) voltage with and without the participation in the regulation of the grid-following BESS and the controllable loads.

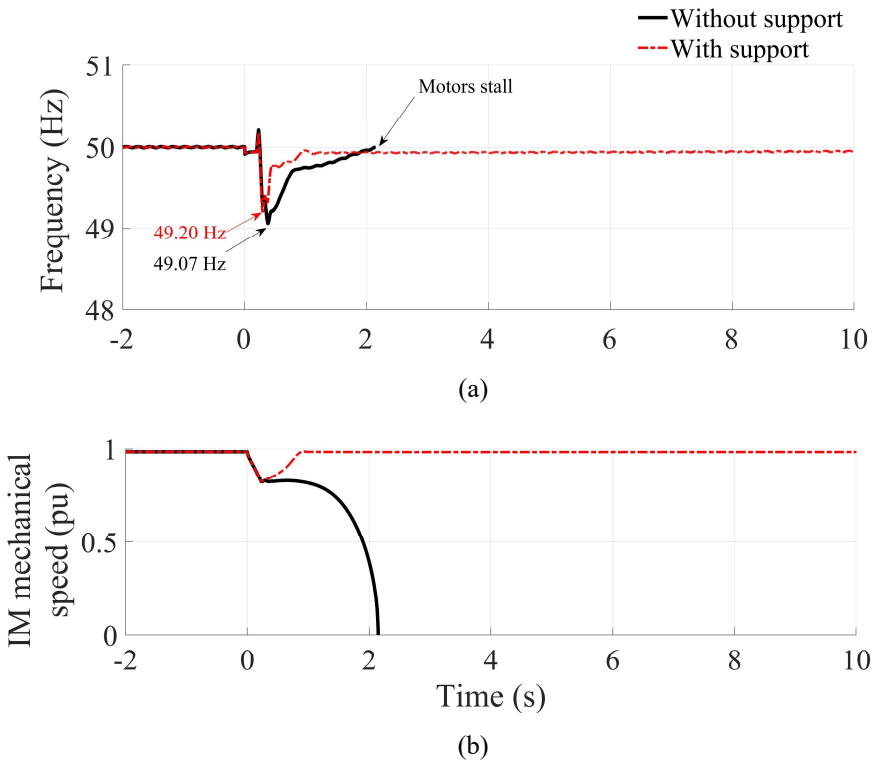

Figure 5.47 – (a) Frequency and (b) voltage with and without the participation in the regulation for a particular case.

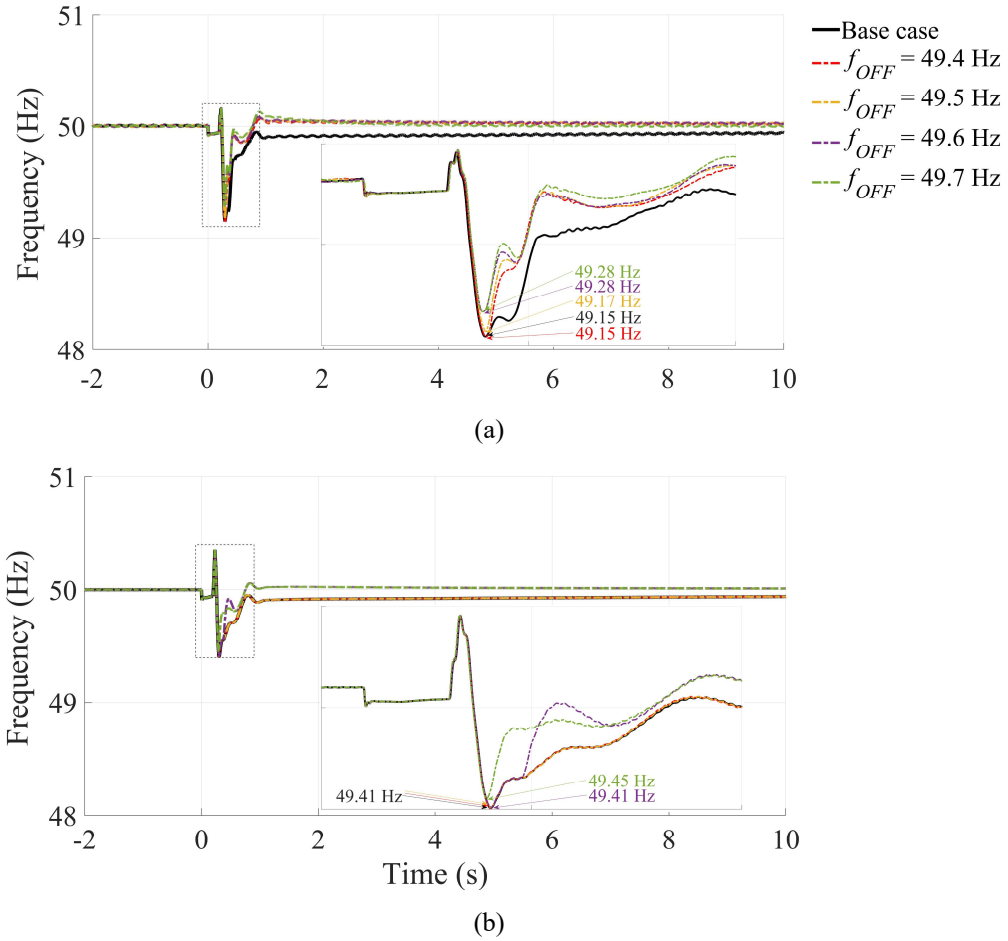

Figure 5.48 – Frequency for different values of f_{OFF} of HPs when (a) the IM and; (b) the passive load is connected to the MG.

ii) Cigré benchmark

The analysis is extended to a more complex network, namely a modified version of the Cigré benchmark for the integration of DERs in MV distribution networks [43], in order to verify the results obtained in the sensitivity analysis and appraise the interaction between all the analyzed components.

The modified Cigré network of Figure 5.49 is tested. The parameters of the DERs are the same as for the previous case, except for the PV which nominal power is halved. The load composition is the same reported in Table 5-6. The load parameters are the same of Table 5-8 except for the air conditioner for which the parameters of the physical INESC IM of Table 5-20 are implemented.

Four cases are tested considering the preponderance of each load class for each case, resulting in mostly residential, commercial, industrial, and agricultural MGs. The load at each bus is composed by 70% of the preponderant class, and 10% of the remaining classes.

The total load at each bus is reported in Table 5-22. On this basis, the load consumed by each component in each bus is calculated, and then the aggregation process introduced in Section 5.2.1c) is implemented. The result of this process is an equivalent IM and an equivalent exponential load for each bus. Since for the single case under analysis the percentage of each class is the same for all buses, the same equivalent

is obtained for all buses, but the total absorbed powers vary. For example, in the residential MG all busses have one IM and one exponential load with the same parameters but with different nominal powers. The values of the parameters for each case are reported in Table 5-23.

In order to perform the PHIL simulations, the physical INESC IM is connected at bus 1 as shown in Figure 5.49. This load represents just a portion of the total rotating load connected to that bus, i.e., a portion is still simulated through an equivalent IM. Just for this bus the equivalent IM has no longer the parameters reported in Table 5-23, but the ones reported in Table 5-24.

TABLE 5-22
TOTAL LOAD AT EACH BUS OF THE MODIFIED CIGRÉ NETWORK (IN KVA)

L1	L2	L3	L4	L5	L6	L7	L8	L9	L10	L11	L12	L13
175	64.75	35	105	70	35	42	94.5	70	49	105	122.5	175

TABLE 5-23
EQUIVALENT PARAMETERS OF THE AGGREGATED LOADS FOR EACH CASE

Case	IM						Exp		H_{sys} (s)
	r_s (pu)	x_{ls} (pu)	x_m (pu)	r_r (pu)	x_{lr} (pu)	H (s)	k_{pu}	k_{qu}	
Residential	0.0380	0.0765	1.8678	0.0419	0.0869	0.455	1.127	7.044	0.327
Commercial	0.0400	0.0846	2.2852	0.0445	0.1010	0.580	0.892	7.342	0.329
Industrial	0.0207	0.0768	3.0659	0.0279	0.1500	1.073	1.079	7.323	0.804
Agricultural	0.0269	0.0859	2.9194	0.0281	0.1516	0.779	1.004	7.240	0.696

TABLE 5-24
EQUIVALENT PARAMETERS OF THE AGGREGATED LOADS AT BUS 1 FOR EACH CASE

Case	IM					
	r_s (pu)	x_{ls} (pu)	x_m (pu)	r_r (pu)	x_{lr} (pu)	H (s)
Residential	0.0386	0.0948	2.8323	0.0512	0.1358	0.720
Commercial	0.0410	0.0956	2.9857	0.0482	0.1277	0.723
Industrial	0.0189	0.0777	3.4538	0.0196	0.1671	1.156
Agricultural	0.0256	0.0878	3.1892	0.0214	0.1661	0.8246

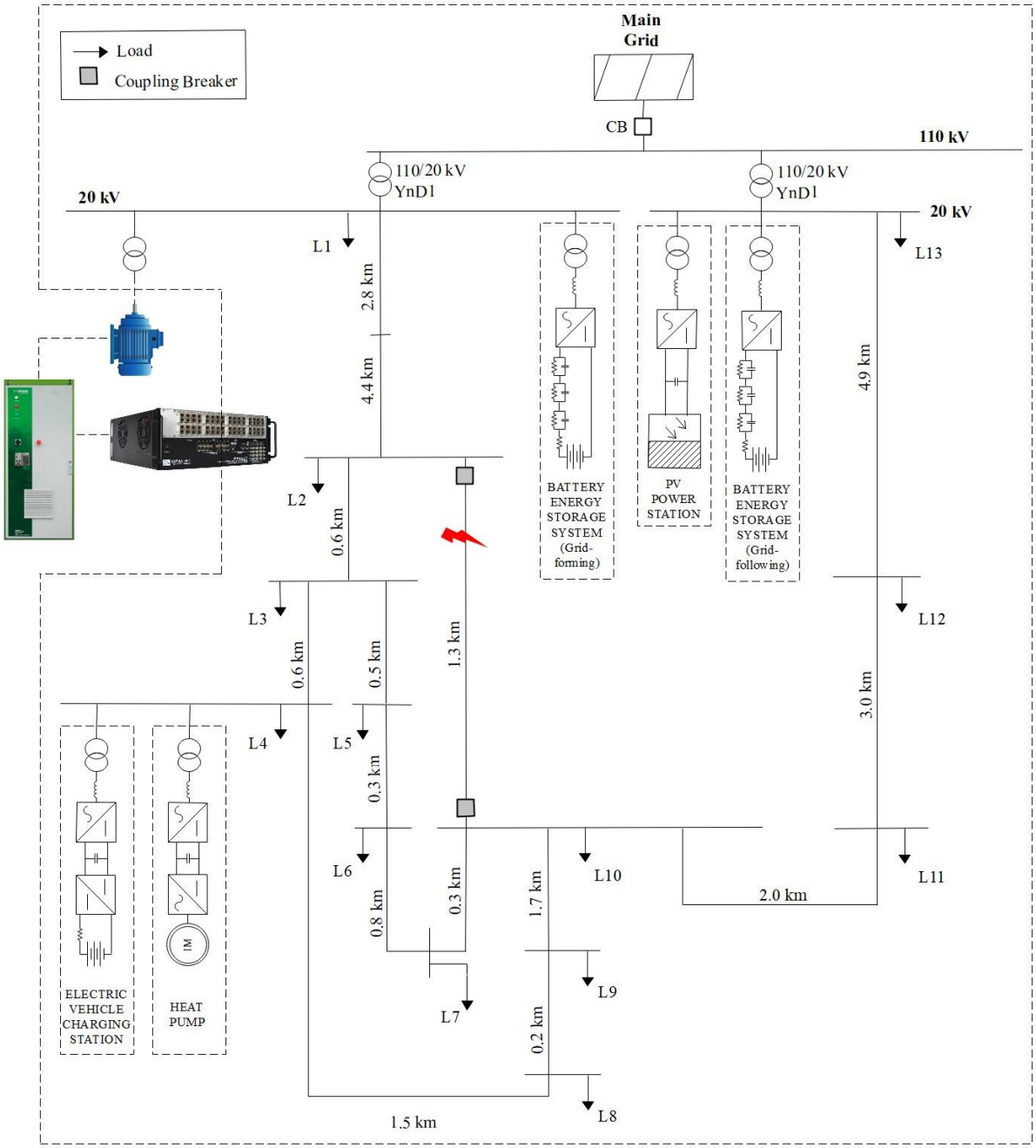

Figure 5.49 – PHIL set-up of the modified Cigré Network with DERs and controllable loads.

A three-phase fault with a 5 Ω fault resistance is simulated in the line between buses 2 and 10 followed by the opening of the corresponding CBs at both ends after 200 ms.

The results are shown in Figure 5.50 and Figure 5.51 for the 4 cases. In Figure 5.50 the results are reported when the grid-following BESS and the controllable loads do not participate in the frequency and voltage regulation, while Figure 5.51 shows the results when they do. The residential case presents the worst response in terms of frequency nadir, while the commercial, industrial and agricultural cases present similar results between them. The industrial and agricultural cases present deeper voltage sags during the recovery, which are more evident when the BESS and the controllable loads do not

participate in the regulation. Such participation does not have a great influence on the frequency nadir but on the voltage sag during the recovery process. It also allows a faster recovery.

The simulations were repeated considering three minimum frequency thresholds for the HPs, namely 49.2, 49.4, and 49.6 Hz. In none of the cases the first threshold operated. For the second threshold the HPs were disconnected only for the residential and the commercial cases. Finally, HPs were disconnected in all cases when considering the third threshold. Therefore, for the considered residential, commercial, industrial and agricultural classes of loads, HPs are more prone to be disconnected in MGs with preponderant residential and commercial loads than with industrial and agricultural ones.

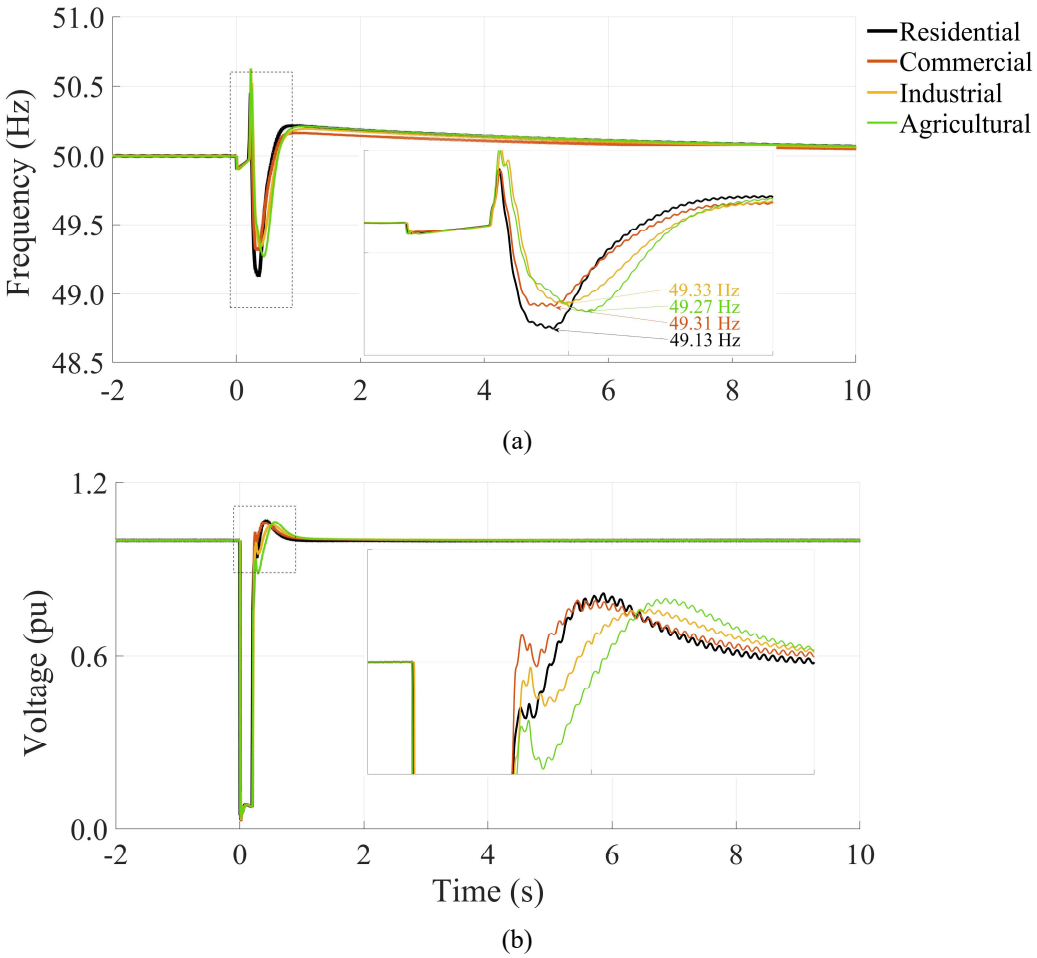

Figure 5.50 – (a) Frequency and (b) voltage for different load compositions. The grid-following BESS and the controllable loads do not participate in the frequency and voltage regulation.

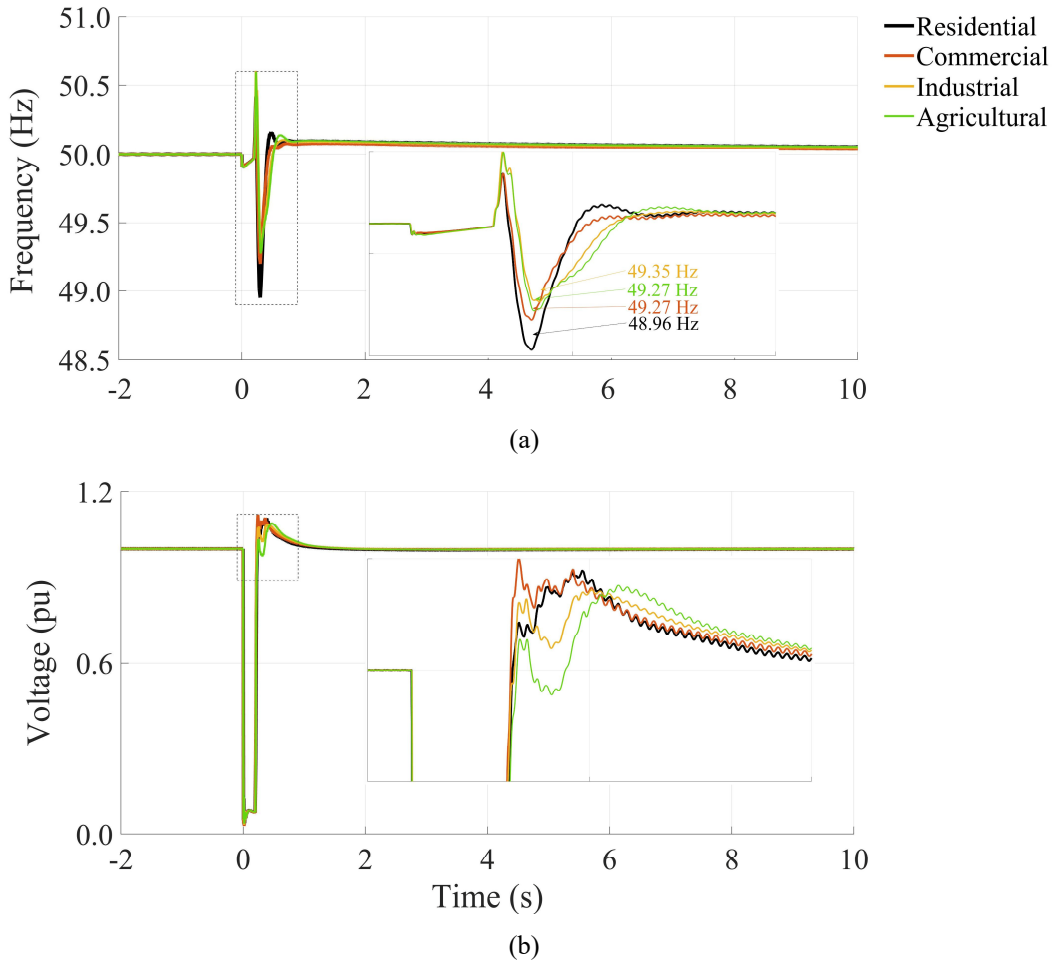

Figure 5.51 – (a) Frequency and (b) voltage for different load compositions. The grid-following BESS and the controllable loads participate in the frequency and voltage regulation.

In this Chapter the influence of load modelling on the transient stability of a MG during islanding transition has been analyzed, by considering the most common approaches of modelling conventional loads, resulting in the necessity of representing the rotating nature of loads such as IMs, particularly when all DERs are power converter-interfaced.

Moreover, the influence of the load composition has been also analyzed by considering two scenarios, namely the islanding transition of a MG and the disturbance caused by a fault in a standalone MG. The control schemes of all DER units and controllable loads have been described in detail. The results obtained constitute a guideline of the overall load influence on the dynamics of the MG in the studied scenarios.

Finally, PHIL simulations have been carried out by alternating the physical connected load between an IM and a resistive-inductive load, depending on the case study.

CHAPTER 6
CONCLUSIONS

The large deployment of Distributed Energy Resources (DERs) has a significant impact on the operation of electrical power systems and constitutes a challenge in many aspects. Not only the unpredictable and distributed nature of these resources rises complications, but most types of DERs are electronically interfaced to the grid, through power converters that behave completely different with respect to traditional power plants equipped with alternators. As a consequence, the traditional way of dealing with the main technical issues regarding the secure operation of distribution networks is evolving, in terms of protection strategies, as well as of frequency and voltage control. This thesis has dealt with such relevant issues, with particular reference to distribution networks and MicroGrids (MGs).

First, a transient-based protection system against single-phase-to-ground has been developed, for the protection of Medium Voltage (MV) networks with unearthed or compensated neutral. The algorithm identifies the directionality of the fault by estimating the angle between the zero-sequence voltage and current phasors at the dominant transient frequency in the first milliseconds after the fault. The implementation of a filter and a zero-padding process to the input signals enhances the protection performance.

The sensitivity analysis relevant to the influence of the characteristics of the protection algorithm shows that a fast fault detection is important to contain the deviation of the estimated angles with respect to the expected values, particularly for high resistance faults. Due to the zero-padding process during the Discrete Fourier Transform (DFT) computation of the zero-sequence current, the sampling frequency does not produce a significant impact on the protection performance, as long as it complies with the

sampling theorem, hence low sampling frequencies attainable by modern relays may be implemented. The influence of the filter characteristics and the zero-padding process has been addressed too. The filter center and its bandwidth do not affect particularly the performance of the protection system, while the zero-padding process allows a better identification of the dominant transient frequency and hence a more accurate angle estimation.

Another important result is that the range of variation of the expected dominant transient frequencies has been shown to depend on the network characteristics, mainly on the equivalent capacitance and inductance. For networks with very short overhead lines, i.e., networks with a very low total capacitance-to-earth, a high sampling frequency might be required. This limitation affects all the transient-based protection algorithms that use a DFT approach to calculate the dominant transient frequency. As the network includes additional feeders and longer or prevalent capacitive lines like cables, the expected dominant frequencies are relatively low and such limitation is less significant.

Different MV radial and meshed networks have been considered for the accomplished analysis, varying topology and line configurations, considering unbalanced loads and lines, as well as overhead and underground lines.

For radial networks an operation zone within 170–280° is proposed. For networks with a very high degree of asymmetry, the operation zone might need to be enlarged to 170–315°. However, the latter operation zone is adequate also for the former system. The presence of underground cable lines does not affect particularly the performances of the protection system.

For meshed networks, relays are installed at both line-ends of each line. A communication network allows each relay to exchange permissive signals with the relay at the opposite line-end, thus isolating only the faulty section without causing any customer outage. The proper operation zone has been estimated through several simulations for each analyzed network. The effects of the communication network latencies on the protection system operation have been evaluated. Although the need to install two relays per line to isolate only the faulted branch makes the proposed solution costlier, this requirement is needed to fully exploit the benefits of the meshed network configuration. The protection system has demonstrated to be secure in front of harmonic injection due to the presence of DERs in the network, even at high levels of penetration.

A further assessment of the performances of the protection system has been carried out by Monte Carlo simulations, varying the fault resistance, the fault incidence angle, and the fault location within the networks. The expected protection speed is particularly good for both radial and meshed networks.

Finally, real-time simulations demonstrate that the algorithm can perform all the required processing in operational times.

The future work on this subject should aim at:

- Improving the identification of the dominant transient frequency by exploring other techniques, especially for small overhead networks. It is preferable that such techniques do not require a particularly high sampling frequency.
- Assess the protection performances by taking into account the model of measurement devices, such as potential and current transformers. Since the algorithm works with relatively high frequencies, the effect of the noise in the measures must be addressed.
- Assess the interaction of the protection system with DER units modelled in detail, i.e., accounting for the power conversion stage and their protective devices and control systems.
- Field tests are required to further fulfill the protection system validation.

The second part of the thesis has investigated and assessed the influence of load modelling and composition on the transient stability assessment and limits, respectively, of a MV-MG.

In particular, the influence of load modelling in the transient stability assessment of the MG during islanding transition has been addressed, by considering the most common approaches of modelling conventional loads. The transition is initiated by the opening of the Circuit Breaker (CB) after a fault occurs in the main power system. Two different scenarios for MGs have been considered: with and without a Synchronous Generator (SG). In the second case, i.e., when all DERs connected to the MG are inherently inertia-less, the representation of the rotating nature of rotating loads, e.g., Induction Motors (IMs), is mandatory.

If the SG is connected to the MG, all models except for the constant power (*P*-model) predict the stability of the MG after islanding. However, if the SG is not connected to the MG, also the exponential (*Exp*-model) and constant impedance (*Z*-model) models predict the system instability. In such case, only the models that represent the IMs whether through the fifth order (*EMTP*-model) or first order (*slip*-model) models are accurate enough to represent the stable transient response of the MG, where stationary loads are still represented through the *Exp*- and *ZIP*-models. The *Exp*-model is preferred for the representation of stationary loads in dynamic simulations, since it is simpler and less demanding from the computational point of view.

Concerning the influence of the load composition on the transient stability limits, two scenarios have been analyzed, namely the islanding transition of a MG and the disturbance caused by a fault in a standalone MG.

By carrying out a sensitivity analysis, the impact of several parameters inherent to the load characteristics and to the control strategies has been derived. The results obtained constitute a guideline of the overall load influence on the dynamics of the MG in the studied scenarios, and they append to the existing literature on this subject. They can be summarized as follows:

- During the islanding transition: the increase of the inertia constant of IMs (H), the voltage exponential parameter of the active power (k_{pu}) and the percentage of rotating load improves

the stability during the islanding maneuver in terms of minimum frequency and voltage variations. The increase of the voltage exponential parameter of the reactive power (k_{qu}) instead, worsens the voltage profile but improves the frequency nadir.

- When a fault occurs in a standalone MG: the influence of H is not monotonous but depends on a critical value H', which in turn depends mainly on the rotor resistance. If $H < H'$, the increase of H produces a larger frequency deviation but a much lower voltage sag, after the fault clearance. On the other hand, if $H > H'$, the increase of H barely improves the frequency nadir and has a negligible effect on the voltage. Also, the influence of k_{pu} and k_{qu} has been found to be scarce.

  Regarding the control parameters of the grid-forming unit, the increase of the virtual inertia (H_V) improves the frequency nadir while it has no sensible effect on the voltage. The increase of the maximum current allowed ($I_{\max}$) worsens the frequency nadir but reduces considerably the voltage sag and the recovery time of IMs. However, this value is subjected to inherent limitations of the power converters, an issue deliberately not addressed here.

  Controllable loads, mainly an Electric Vehicle Charging Station (EV-CS) and variable speed Heat Pumps (HPs), have been included in the second scenario, and their contribution to frequency and voltage control has been assessed. It can be concluded that in general the contribution of the EV-CS is not of importance on the frequency and voltage deviation. However, it allows a faster recovery of the system after the fault and could therefore be crucial to prevent the motor stalling in some cases. The influence of the virtual inertia of HPs is practically negligible in the frequency nadir but allows a faster recovery after the fault. On the other hand, the disconnection of HPs for underfrequency transients, might have a great impact on both the frequency deviation and the recovery time, depending on the moment in which the disconnection occurs and on the amount of disconnected power.

  Power-Hardware-In-The-Loop (PHIL) simulations have been carried out by alternating the physical connected load between an IM and a resistive-inductive load, depending on the case study.

The above analysis was extended to the modified version of a Cigré benchmark system. For such a purpose, conventional loads have been categorized in four classes, namely residential, commercial, industrial and agricultural, in which each load class is composed by different stationary and rotating load components.

During the islanding transition, the considered industrial and agricultural classes of load are more prone to ease the islanding transition with respect to the residential and commercial classes, due to their larger values of equivalent inertia and percentage of rotating load.

For the case of a fault in a standalone MG, only PHIL simulations have been carried out. The considered residential case presents the worst response in terms of frequency nadir, while the commercial,

industrial and agricultural cases present similar results between them. The industrial and agricultural cases present deeper voltage sags during the recovery. The participation of DERs and controllable loads in the frequency and voltage control influences mainly the voltage sag during the recovery process by reducing it, while it does not have a great influence on the frequency nadir. It also allows a faster recovery.

The influence of load composition and load dynamics on the stability of the MG is a very wide area of research. Future work could consider the following points:

- Since the load composition influences the stability of the MG, it would be useful to be able to dynamically characterize it through online measurements e.g., of voltage and current during transients. It is accounted that some of the load parameters seem to have a higher and sometimes predominant influence on the stability of the MG, e.g., the inertia of IMs and their percentage of the total load.
- It has been observed that different types of loads, and more in general different classes of loads, contribute differently to the MG stability. During important disturbances in which load shedding is inevitable to maintain the system in service, it could be preferable to shed some specific types or classes of loads. This hypothesis goes along with the previous point, since it would be needed to have the system already characterized and possibly divided into zones. An analogous treatment can be accomplished for the system restoration i.e., it could be preferable to energize some classes of loads first.

APPENDIX A
ADOPTED MODELS

A traditional electric power system is organized in 3 main parts which transmit power in a unidirectional manner, as shown in Figure A.1a:

- Generation, that comprises the power plants in which electricity is generated by the conversion of natural primary sources of energy such as fossil, hydraulic and nuclear. This is achieved by setting in motion a SG. Power plants are connected to the transmission network through step-up transformers.
- Transmission, which aims at interconnecting all generating stations and consumption areas. It is mainly composed by transformers and power lines.
- Sub transmission and distribution, which can be divided into three systems, mainly the HV, MV and LV distribution systems. All of them aim at distributing the power withdrawn from the transmission network to the final customers at different voltage levels, depending on the customer requirements and characteristics, e.g., industrial, commercial and residential. As well as the transmission level, it is mainly composed by transformers and power lines, but also of several different types of loads.

To these parts, which represent the power layer, are added the communication and coupling layer, and the decision layer [169].

Concerning modern electric power systems, as earlier mentioned, they include new energy sources, mostly from renewables, and new types of storage systems, mostly distributed, in addition to classical pump-hydro stations, as schematically shown in Figure A.1b. These new energy sources do not necessarily achieve the energy conversion through SGs, as different technologies are implemented, for

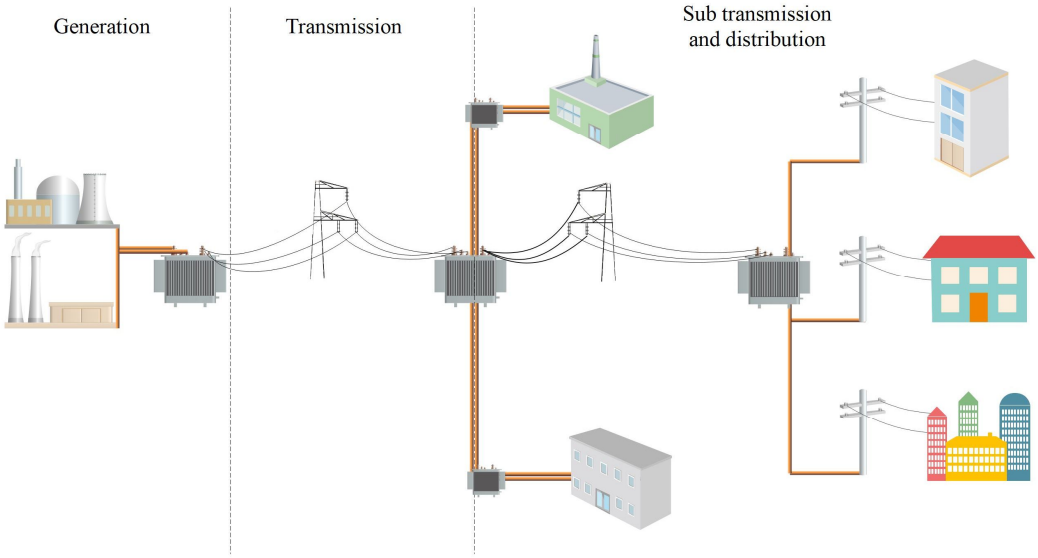

(a)

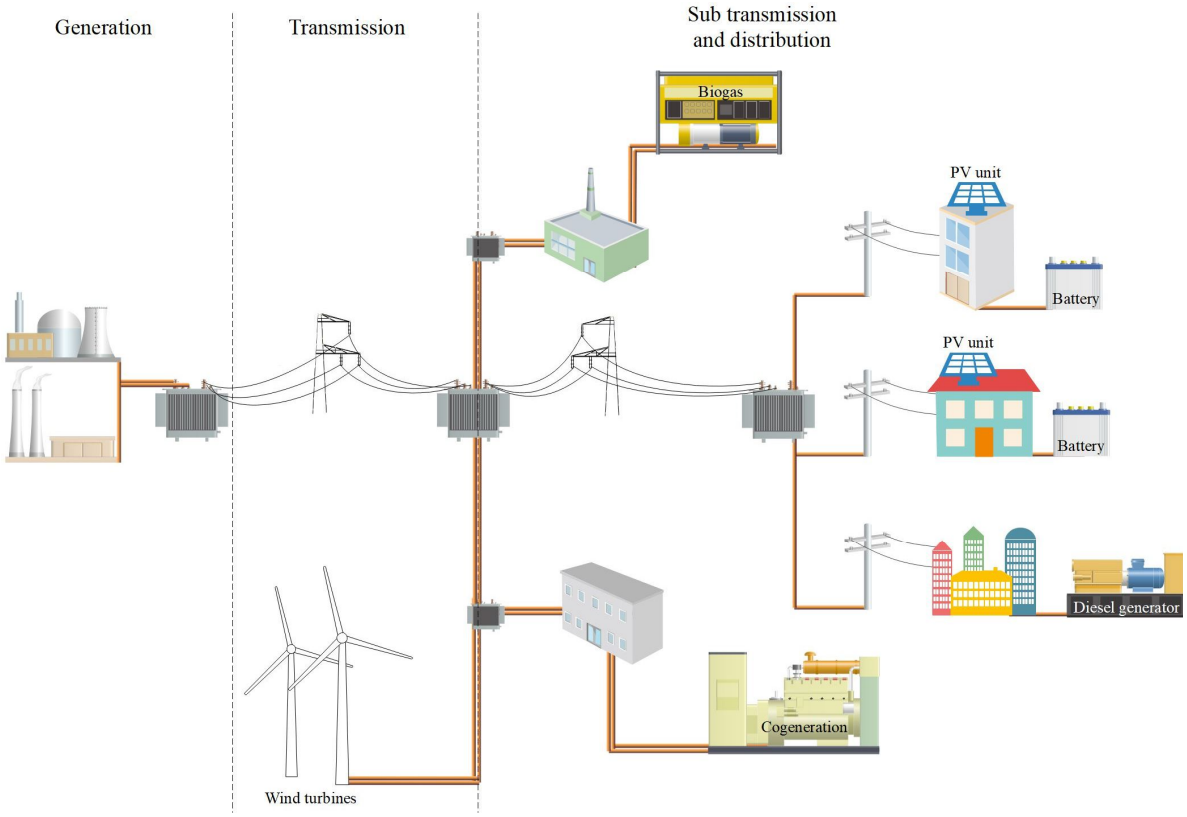

(b)

Figure A.1 – (a) Traditional and (b) modern electric power system structure.

which the utilization of electronic power converters is required. Moreover, they are not necessarily connected to the transmission network, but could be coupled to the sub transmission and distribution level, hence the power flow becomes bidirectional. Some controllable loads such as HPs and EVs are also becoming relevant in modern power systems.

Additional components of a power system are protection devices and CBs, synchronous compensators, series and shunt capacitor banks, reactors and tap-changers.

In the following, the main above-mentioned components are described. The aim is to explore and acknowledge the currently implemented dynamic models for representing such components in distribution networks, with particular emphasis in electromagnetic transient simulations, which is the main tool used in this thesis.

A.1 Line

Power is transferred between two points through overhead and cable lines, which are characterized by the following parameters: resistance R', inductance L', conductance G' and capacitance C' per unit length.

The telegrapher's equations are,

$$\begin{aligned} \frac{\partial v(x,t)}{\partial x} + R'i(x,t) + L'\frac{\partial i(x,t)}{\partial t} = 0 \\ \frac{\partial i(x,t)}{\partial x} + G'i(x,t) + C'\frac{\partial v(x,t)}{\partial t} = 0 \end{aligned} \tag{A.1}$$

The single-phase equivalent circuit of a differential element of the line is shown in Figure A.2.

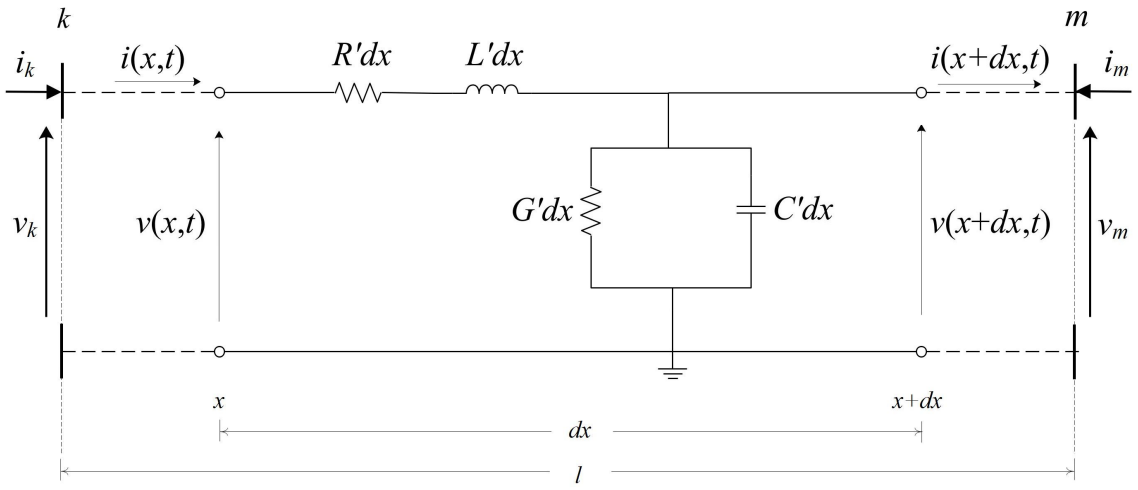

Figure A.2 – Differential line element with distributed parameters.

By applying the Laplace transformation to (A.1),

$$\begin{aligned} \frac{dV(x,s)}{dx} = -Z'I(x,s) \\ \frac{dI(x,s)}{dx} = -Y'V(x,s) \end{aligned} \tag{A.2}$$

where $Z' = R' + sL'$ and $Y' = G' + sC'$. By imposing the boundary conditions at both line-ends it follows that,

$$V(x,s) = V_k \cosh(\gamma x) - Z_c I_k \sinh(\gamma x)$$
$$I(x,s) = \frac{1}{Z_c} V_k \sinh(\gamma x) - I_k \cosh(\gamma x) \tag{A.3}$$

where Z_c and γ are the characteristic impedance and the propagation constant, respectively, and are expressed as,

$$Z_c = \sqrt{\frac{R' + sL'}{G' + sC'}} \tag{A.4}$$

$$\gamma = \sqrt{(R + sL')(G + sC')} \tag{A.5}$$

Then, the voltage and current at both line ends are,

$$V_k - Z_c I_k = \left[V_m + Z_c I_m\right] A_p$$
$$V_m - Z_c I_m = \left[V_k + Z_c I_k\right] A_p \tag{A.6}$$

known as the delay equations, where l is the line length and $A_p = e^{-\gamma l}$ is the propagation function.

A.1.1 Constant Parameter line model

The implementation of the CP-line model considers all the electrical parameters as frequency independent, i.e., R', L', G' and C' are constant values. Moreover, in a first approximation the line is considered lossless, i.e., $R' = G' = 0$. With these assumptions, the time-domain solution of (A.6) is the following,

$$v_k(t) - Z_c i_k(t) = v_m(t-\tau) + Z_c i_m(t-\tau)$$
$$v_m(t) - Z_c i_m(t) = v_k(t-\tau) + Z_c i_k(t-\tau) \tag{A.7}$$

where,

$$Z_c = \sqrt{\frac{L'}{C'}} \tag{A.8}$$

and τ is the travelling time given by,

$$\tau = l\sqrt{L'C'} \tag{A.9}$$

The line circuit model obtained is depicted in Figure A.3, in which $i_{k,h}$ and $i_{m,h}$ represent the history terms which consider the wave propagation, and are given by the voltage and current values at the opposite line-end τ seconds earlier, i.e.,

$$
\begin{aligned}
i_{k,h} &= \frac{v_m(t-\tau)}{Z_c} + i_m(t-\tau) \\
i_{m,h} &= \frac{v_k(t-\tau)}{Z_c} + i_k(t-\tau)
\end{aligned}
\tag{A.10}
$$

Such terms are already known at the instant *t*.

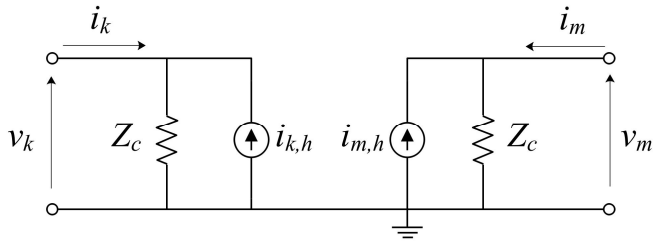

Figure A.3 – Lossless line model for time-domain simulations (Adapted from [170]).

The losses are then included by dividing the line into two identic lossless sections and distributing the line resistance *r* at both line-ends and in the middle point, while the conductance *G* is still neglected.

In a multi-phase system, a modal transformation matrix is applied to the voltage and current vectors such that the resulting modal quantities are decoupled. Therefore, they can be treated as independent single-phase circuits and the above treatment can be implemented separately for each circuit. In the modal domain (A.2) is still valid in matrix form and for modal quantities, i.e.,

$$
\begin{aligned}
\frac{d\hat{\boldsymbol{V}}(x,s)}{dx} &= -\widehat{\boldsymbol{Z}}'\hat{\boldsymbol{I}}(x,s) \\
\frac{d\hat{\boldsymbol{I}}(x,s)}{dx} &= -\widehat{\boldsymbol{Y}}'\hat{\boldsymbol{V}}(x,s)
\end{aligned}
\tag{A.11}
$$

in which bold letters represent vectors or matrices and the hatted vectors are modal quantities and are obtained from,

$$
\begin{aligned}
\hat{\boldsymbol{V}} &= \boldsymbol{T}_v^{-1}\boldsymbol{V} \\
\hat{\boldsymbol{I}} &= \boldsymbol{T}_i^{-1}\boldsymbol{I} \\
\widehat{\boldsymbol{Z}}' &= \boldsymbol{T}_i^{\mathrm{T}}\boldsymbol{Z}'\boldsymbol{T}_i \\
\widehat{\boldsymbol{Y}}' &= \boldsymbol{T}_v^{\mathrm{T}}\boldsymbol{Y}'\boldsymbol{T}_v
\end{aligned}
\tag{A.12}
$$

and,

$$
\begin{aligned}
\widehat{\boldsymbol{Z}_c} &= \boldsymbol{T}_i^{\mathrm{T}}\boldsymbol{Z}_c\boldsymbol{T}_i \\
\widehat{\boldsymbol{A}_p} &= \boldsymbol{T}_i^{-1}\boldsymbol{A}_p\boldsymbol{T}_i
\end{aligned}
\tag{A.13}
$$

The transformation matrixes $\boldsymbol{T}_v$ and $\boldsymbol{T}_i$ are not independent but $\boldsymbol{T}_i = \left(\boldsymbol{T}_v^{\mathrm{T}}\right)^{-1}$.

A.1.2 Frequency Dependent line model

For the FD- line model, R' and L' are considered to vary with the frequency. Therefore, the characteristic impedance Z_c and the propagation function A_p in (A.6) are FD, and such dependency is approximated by rational functions. The circuit of Figure A.3 is still representative, but Z_c is no longer a resistance given by (A.8) but a series of RC branches representing the defined rational function, and the equivalent history current sources $i_{k,h}$ and $i_{m,h}$ consider voltages and currents at the opposite line-end not only τ seconds earlier, but also at other instants through a weighting function.

For multi-phase systems, the matrix $\boldsymbol{T}_i$ (hence also $\boldsymbol{T}_v$) for the modal transformation is approximated to be constant and real for the representation of overhead lines (as well as for the CP-line model) [170], while it is FD for the representation of cable lines [171]. The frequency dependence in the latter case is approximated by rational functions, as done for $\boldsymbol{Z}_c$ and $\boldsymbol{A}_p$.

A.1.3 Pi-equivalent line model

By expressing voltages and currents in (A.3) as phasors and referring them to both line-ends, it yields,

$$\begin{aligned} \overline{V}_m &= \overline{V}_k \cosh(\gamma l) - \overline{Z}_c \overline{I}_k \sinh(\gamma l) \\ \overline{I}_m &= \frac{\overline{V}_k}{Z_c} \sinh(\gamma l) - \overline{I}_k \cosh(\gamma l) \end{aligned} \tag{A.14}$$

where,

$$\begin{aligned} Z_c &= \sqrt{\frac{R' + j\omega L'}{G' + j\omega C'}} \\ \gamma &= \sqrt{(R + j\omega L')(G + j\omega C')} \end{aligned} \tag{A.15}$$

The pi-equivalent circuit is shown in Figure A.4, for which the following relation can be written,

$$\overline{V}_m = \overline{V}_k \left(1 + \frac{ZY}{2}\right) - \overline{Z}\,\overline{I}_k \tag{A.16}$$

A similar analysis can be carried out for V_k. By comparing both (A.14) and (A.16), it yields,

$$\begin{aligned} Z &= Z_c \sinh(\gamma l) \\ \frac{Y}{2} &= \frac{1}{Z_c} \tanh\left(\frac{\gamma l}{2}\right) \end{aligned} \tag{A.17}$$

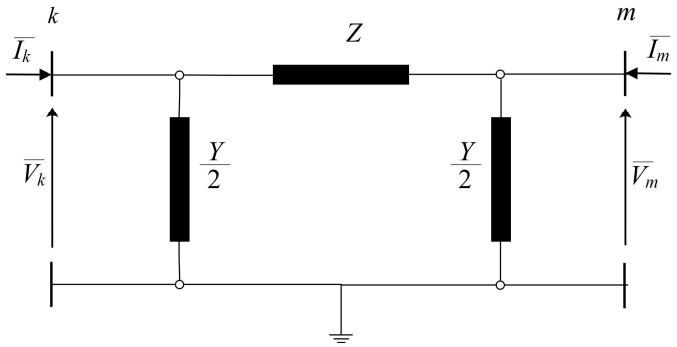

Figure A.4 – Pi-equivalent line model.

This analysis was carried out considering voltages and currents as phasors, although it could be repeated in the frequency domain, thus obtaining the same pi-equivalent circuit valid in the frequency domain.

If $\gamma l << 1$, (A.17) can be approximated as,

$$Z = Z'l$$
$$\frac{Y}{2} = \frac{Y'}{2}l \tag{A.18}$$

The three-phase representation is constituted by three pi-equivalent circuits coupled between them.

A.2 Transformer

The equivalent circuit of a single-phase two-winding transformer is depicted in Figure A.5. Resistances R_1 and R_2 represent the losses due to Joule effect in both windings, while inductances L_1 and L_2 account for the leakage flux. The shunt inductance L_{mag} accounts for the magnetization current and it considers also the core saturation effect. Finally, the shunt resistance R_{mag} accounts for the core losses due to eddy currents and hysteresis. The factor k is the transformation ratio $V_{nom,1}/V_{nom,2}$, and it is equal to the ratio between the number of turns of both windings.

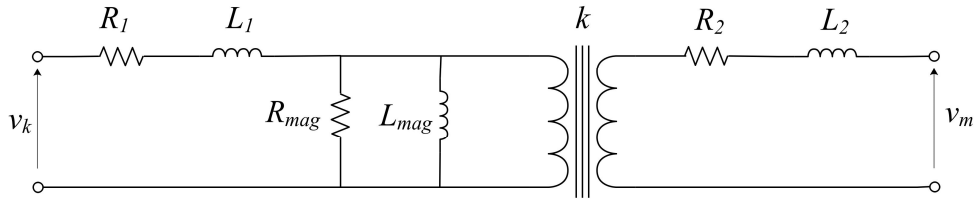

Figure A.5 – Equivalent circuit of a single-phase two-winding transformer.

The magnetizing curve is defined as the flux in function of the current. The core saturation is represented in such curve. The corresponding L_{mag} thus, is a non-linear inductance, which value depends on the current. Moreover, if hysteresis is represented the magnetizing curve is a double-valued function, while an ideal (i.e., anhysteretic) magnetizing curve is represented through a single-valued function.

Three-phase transformers are then represented as three single-phase units, which connection depends on the type and group of the transformer.

A.3 Loads

Electrical load models are traditionally classified into two categories, i.e., static and dynamic models.

A.3.1 Static models

Static models represent the load power absorption[1] at any instant through defined algebraic functions, depending on the voltage magnitude and frequency at such instant.

One of the most used models is the exponential one, which can be generally expressed as,

$$\begin{aligned} P &= P_n \left(\frac{V}{V_n} \right)^{k_{pu}} \left(1 + k_{pf} \Delta f \right) \\ Q &= Q_n \left(\frac{V}{V_n} \right)^{k_{qu}} \left(1 + k_{qf} \Delta f \right) \end{aligned} \tag{A.19}$$

where P and Q are the active and reactive powers consumed by the load when it is fed by a voltage of magnitude V and frequency f; P_n and Q_n are the nominal active and reactive powers relative to the rated voltage V_n and frequency f_n; k_{pu}, k_{qu}, k_{pf} and k_{qf} are the parameters of the exponential model for the load; Δf is the frequency deviation in pu, i.e.,

$$\Delta f = \frac{f - f_n}{f_n} \tag{A.20}$$

A variant of this model is the frequency-independent exponential model, for which (A.19) becomes,

$$\begin{aligned} P &= P_n \left(\frac{V}{V_n} \right)^{k_{pu}} \\ Q &= Q_n \left(\frac{V}{V_n} \right)^{k_{qu}} \end{aligned} \tag{A.21}$$

An alternative, also widely implemented, is given by the polynomial model, most commonly known as ZIP model as it is composed by a constant impedance (Z), a constant current (I) and a constant power (P) components i.e.,

[1] Since the load sign convention is adopted, a positive reactive power represents an inductive behavior. Vice versa a negative reactive power represents a capacitive behavior. On the other hand, active power is always positive, although during transients some loads (rotating loads) could inject power to the grid.

$$P = P_n\left[p_1\left(\frac{V}{V_n}\right)^2 + p_2\left(\frac{V}{V_n}\right) + p_3\right]\left(1 + k_{pf}\Delta f\right)$$
$$Q = Q_n\left[q_1\left(\frac{V}{V_n}\right)^2 + q_2\left(\frac{V}{V_n}\right) + q_3\right]\left(1 + k_{qf}\Delta f\right) \quad \text{(A.22)}$$

where parameters p_1, p_2, p_3 and q_1, q_2 and q_3 represent the weights of the Z, I and P components for the active and reactive power, respectively. Analogously, the frequency-independent version of the ZIP model is given by,

$$P = P_n\left[p_1\left(\frac{V}{V_n}\right)^2 + p_2\left(\frac{V}{V_n}\right) + p_3\right]$$
$$Q = Q_n\left[q_1\left(\frac{V}{V_n}\right)^2 + q_2\left(\frac{V}{V_n}\right) + q_3\right] \quad \text{(A.23)}$$

These models are not realistic at very low values of voltage, for which a constant impedance model is normally employed when V is minor than a defined threshold.

To account for the load dynamics, a transfer function can be included within the power calculation equations e.g., from (A.21) it follows

$$P = P_n\left(\frac{V}{V_n}\right)^{k_{pu}}\frac{F_{P1}(s)}{F_{P2}(s)}$$
$$Q = Q_n\left(\frac{V}{V_n}\right)^{k_{qu}}\frac{F_{Q1}(s)}{F_{Q2}(s)} \quad \text{(A.24)}$$

where F_{P1}, F_{P2}, F_{Q1} and F_{Q2} are functions in the Laplace domain that control the dynamics of active and reactive power.

To simulate the behavior of any of the above representations in dynamic simulations, the relevant procedures may differ. A general scheme is shown in Figure A.6.

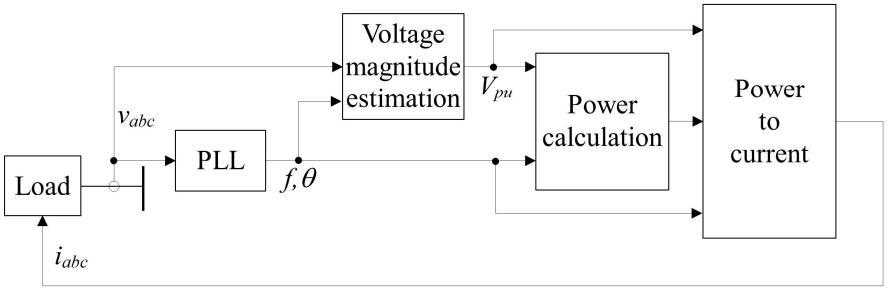

Figure A.6 – General scheme of static load models for dynamic time-domain simulations.

The PLL block estimates the frequency and the phase of the voltage. The *Power calculation* block implements one of (A.19) to (A.24), i.e. calculates the power that the load should absorb at the given values of voltage and frequency at each instant, and the *Power to current* block calculates the relative

current. The scheme could be implemented separately for each single-phase or directly for the three-phase system by implementing a proper reference transformation (e.g., Clarke or Park transformations which are illustrated in the Appendix B). In the former case (e.g., EMTP-RV), powers are equally divided in each of the single phases, while in the latter case (e.g., Simulink) currents are equally divided, thus power flows depend on the voltage of each phase.

It follows that the load can be represented as a controlled current source by itself or as a controlled current source in parallel to a resistor and an inductor/capacitor for which the current sources act as a compensation element. Diverse filters are included in the scheme to exclude the high-frequency components, which also influence the dynamic behavior of the load.

A.3.2 Dynamic models

Dynamic types of load include not only rotating loads such as induction or synchronous motors, but also thermostatic loads and on-load tap changers. The operation of protective relays also causes changes in the load that cannot be represented through static models.

However, motors (mainly IMs) are responsible of 60% to 70% of the load consumption of a traditional power system [146], for which the attention is focused on the representation of this type of load.

The electromagnetic dynamics can be analyzed as follows. Starting from a general consideration, for a generic winding it can be written

$$v_k(t) = R_k i_k(t) + \frac{d}{dt}\lambda_k(t) \tag{A.25}$$

where R_k is the winding resistance and λ_k is the flux linkage of the winding. The load sign convention is still adopted. If more than one winding is considered, (A.25) can be expressed in vectorial form as,

$$\boldsymbol{v} = \boldsymbol{R}\boldsymbol{i} + \frac{d}{dt}\boldsymbol{\lambda} \tag{A.26}$$

where $\boldsymbol{R}$ is a diagonal matrix of winding resistances and $\boldsymbol{\lambda} = \boldsymbol{L}\boldsymbol{i}$, where $\boldsymbol{L}$ is a matrix with self-inductance coefficients in its diagonal and mutual-inductance coefficients in the off-diagonal parts.

For a generic three-phase system three windings are considered, and the magnitude-invariant Park's transformation[1] is applied to (A.26). Since

$$\frac{d}{dt}\left\{\boldsymbol{T}_{dq0}\boldsymbol{\lambda}\right\} = \left[\frac{d}{dt}\boldsymbol{T}_{dq0}\right]\boldsymbol{\lambda} + \boldsymbol{T}_{dq0}\frac{d}{dt}\boldsymbol{\lambda} \tag{A.27}$$

[1] As seen in Appendix B, the Park transformation implemented considers the *q*-axis leading the *d*-axis. Some relevant literature, e.g. the EMTP Theory Book [76], considers the *q*-axis lagging the *d*-axis for this analysis which leads to some sign variations.

it is yield,

$$\boldsymbol{v}_{dq0} = \boldsymbol{R}\boldsymbol{i}_{dq0} + \frac{d}{dt}\boldsymbol{\lambda}_{dq0} - \left[\frac{d}{dt}\boldsymbol{T}_{dq0}\right]\boldsymbol{T}_{dq0}^{-1}\boldsymbol{\lambda}_{dq0} \tag{A.28}$$

Since,

$$\left[\frac{d}{dt}T_{dq0}\right]T_{dq0}^{-1} = \omega\begin{bmatrix} 0 & 1 & 0 \\ -1 & 0 & 0 \\ 0 & 0 & 0 \end{bmatrix} \tag{A.29}$$

Therefore,

$$\begin{bmatrix} v_{d,k} \\ v_{q,k} \\ v_{0,k} \end{bmatrix} = R\begin{bmatrix} i_{d,k} \\ i_{q,k} \\ i_{0,k} \end{bmatrix} + \frac{d}{dt}\begin{bmatrix} \lambda_{d,k} \\ \lambda_{q,k} \\ \lambda_{0,k} \end{bmatrix} + \begin{bmatrix} -\omega\lambda_{q,k} \\ \omega\lambda_{d,k} \\ 0 \end{bmatrix} \tag{A.30}$$

where ω is the electrical angular speed of the reference frame (equal to that of the supply voltage). The zero sequence fluxes are not coupled at all.

In order to apply these general considerations to the single cage IM, the armature and rotor windings must be considered. The armature is composed of three windings *a*, *b* and *c*, symmetrical with respect to each other. The rotor consists of a set of bars short circuited by two circular end caps. Since the rotor is short-circuited the voltages in (A.30) are null[1] and rotor windings produce a field that has the same number of poles as the stator, i.e., it can be modelled as an equivalent three-phase winding.

Let be Ω the mechanical angular speed of the rotor and ω_r the respective angular speed in electrical radians, i.e., $\omega_r = p\Omega$ where p is the number of polar pairs. Thus, considering that the angular speed of the reference frame with respect to the rotor is $\omega - \omega_r$, the equations for both stator and rotor are derived from (A.26) and (A.30),

$$\begin{bmatrix} v_{d,s} \\ v_{q,s} \\ v_{0,s} \\ v_{d,r} \\ v_{q,r} \end{bmatrix} = \begin{bmatrix} \boldsymbol{R}_s & 0 \\ 0 & \boldsymbol{R}_r \end{bmatrix}\begin{bmatrix} i_{d,s} \\ i_{q,s} \\ i_{0,s} \\ i_{d,r} \\ i_{q,r} \end{bmatrix} + \frac{d}{dt}\begin{bmatrix} \lambda_{d,s} \\ \lambda_{q,s} \\ \lambda_{0,s} \\ \lambda_{d,r} \\ \lambda_{q,r} \end{bmatrix} + \begin{bmatrix} -\omega\lambda_{q,s} \\ \omega\lambda_{d,s} \\ 0 \\ -(\omega-\omega_r)\lambda_{q,r} \\ (\omega-\omega_r)\lambda_{d,r} \end{bmatrix} \tag{A.31}$$

The single cage IM representation is shown in Figure A.7.

[1] In the following, $v_{d,r}$ and $v_{q,r}$ are kept in their variable form instead of replacing them by a zero, to maintain some generality.

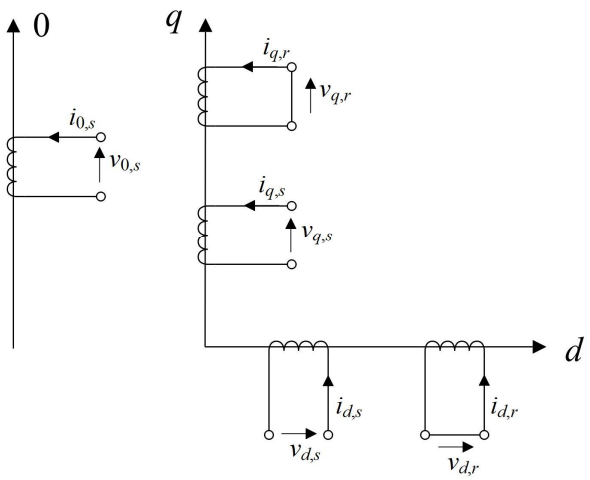

Figure A.7 – Single cage IM model in the *dq*0-frame.

Some further considerations are: i) the resistance of each winding is constant; ii) the rotor is isotropic hence the self-inductances are constant; iii) magnetic circuits are linear, thus effects of hysteresis and saturation are neglected; iv) effects of eddy currents are negligible; v) The permeance of each part of the magnetic circuit is constant.

The (A.31) can be rewritten separately for the *dq*-axis,

$$\begin{bmatrix} v_{d,s} \\ v_{d,r} \end{bmatrix} = \begin{bmatrix} R_s & 0 \\ 0 & R_r \end{bmatrix} \begin{bmatrix} i_{d,s} \\ i_{d,r} \end{bmatrix} + \begin{bmatrix} L_{d,ss} & M_{d,sr} \\ M_{d,sr} & L_{d,rr} \end{bmatrix} \frac{d}{dt} \begin{bmatrix} i_{d,s} \\ i_{d,r} \end{bmatrix} + \begin{bmatrix} -\omega \lambda_{q,s} \\ -(\omega - \omega_r) \lambda_{q,r} \end{bmatrix} \tag{A.32}$$

$$\begin{bmatrix} v_{q,s} \\ v_{q,r} \end{bmatrix} = \begin{bmatrix} R_s & 0 \\ 0 & R_r \end{bmatrix} \begin{bmatrix} i_{q,s} \\ i_{q,r} \end{bmatrix} + \begin{bmatrix} L_{q,ss} & M_{q,sr} \\ M_{q,sr} & L_{q,rr} \end{bmatrix} \frac{d}{dt} \begin{bmatrix} i_{q,s} \\ i_{q,r} \end{bmatrix} + \begin{bmatrix} \omega \lambda_{d,s} \\ (\omega - \omega_r) \lambda_{d,r} \end{bmatrix} \tag{A.33}$$

As for transformers, referring the rotor quantities to the stator implies that there is a main flux equally linked with both windings on each axis, i.e. a given stator current produces the same magnetomotive force as the same equivalent rotor current [164].

Due to the symmetry assumption, inductances in the *d* and *q*-axis are the same, i.e. $L_{d,ss} = L_{q,ss} = L_s$, $L_{d,rr} = L_{q,rr} = L_r$ and $M_{d,sr} = M_{q,sr} = M$, which represent the self-induction coefficients of the stator and rotor circuits and the mutual induction between them, all in the *dq*-axis.

Considering that the stator leakage reactance X_{ls} is derived from $L_s - M$; the rotor leakage reactance X_{lr} is derived from $L_r - M$; and the magnetizing reactance X_m is derived from M; then, the equivalent circuits of Figure A.8 are obtained.

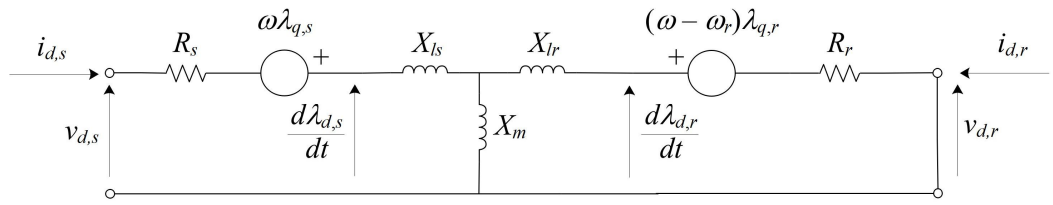

(a)

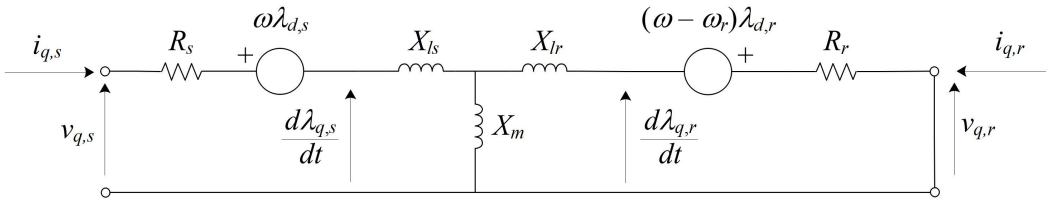

(b)

Figure A.8 – Equivalent circuits of a single cage IM along the *dq*-axes. Rotor quantities are referred to the stator.

If a double cage motor is considered, an additional pair of windings must be considered in the *dq*-frame of Figure A.7, and an additional branch in the rotor side of the *dq*-equivalent circuits of Figure A.8, parallel to the existent one. If a wound rotor is considered instead, the *dq*-voltages at the rotor side in Figure A.7and Figure A.8 are no longer short circuited. Moreover, a zero-sequence circuit for the rotor is added in Figure A.7.

The mechanical dynamics are expressed through the motion equation, which general form is,

$$J\frac{d\Omega}{dt}+D\,\Omega=T_{em}-T_m \tag{A.34}$$

where J is the inertia of the motor, D the damping coefficient, Ω the mechanical angular speed of the motor, and T_{em} and T_m the electromagnetic and mechanical torques, respectively.

The (A.32)–(A.34) constitute the fifth-order model of the single cage IM, and it is the most accurate model.

A simplified model can be derived if the electromagnetic dynamics of both stator and rotor are neglected, i.e. the derivative terms in (A.32) and (A.33) are neglected. By doing so, and knowing that $v_s = v_{d,s} + jv_{q,s}$ (analogous for the current and for the rotor), the following is obtained,

$$\begin{aligned} v_s &= R_s i_s + j\omega L_s i_s + j\omega M i_r \\ v_r &= R_r i_r + j\left(\omega-\omega_r\right)L_r i_r + j\left(\omega-\omega_r\right)M i_s \end{aligned} \tag{A.35}$$

Defining the slip as

$$s=\frac{\omega-\omega_r}{\omega} \tag{A.36}$$

and putting $v_r = 0$ in the second of the (A.35), it yields,

$$
\begin{aligned}
v_s &= R_s i_s + j\omega L_s i_s + j\omega M i_r \\
0 &= \frac{R_r}{s} i_r + j\omega L_r i_r + j\omega M i_s
\end{aligned}
\tag{A.37}
$$

Expressing the resistances and reactances in per unit, the equivalent circuit of Figure A.9 is obtained, in which again all rotor quantities are referred to the stator. This model considers only the dynamics given by (A.34), i.e. the mechanical phenomena, therefore it is also referred to as the first-order model. The reactances in Figure A.9 have been referred to the supply voltage frequency f' since it might be different from the nominal one for which reactances are defined.

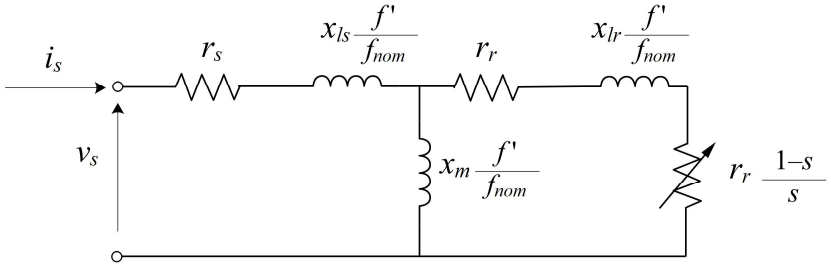

Figure A.9 – Slip-model of the IM.

A.4 Power converters

Power converters can be modelled through detailed or so-called average models. Detailed models include the full representation of all components, switching devices among them, which operate at very high switching frequencies. For this reason, normally very small numerical integration time-steps are required to accurately represent fast switching events, thus high computational times. Moreover, the size and complexity of the simulated system rapidly increases when more power converters are added, or if multilevel converters are employed since the switching devices might be thousands in these types of converters. The advantages of detailed models are in terms of high accuracy, capability to account for special switching states, direct representation of unbalanced conditions in the converters, and establishment of a reference model [172]. On the other hand, average models eliminate the computation burden imposed by detailed models, even for multilevel converters, while replicating the average response of switching devices by using controlled sources. Other intermediate models, e.g. detailed equivalent and arm switching function-based models [173], still consider the high frequency due to the presence of switching devices, hence are not considered.

A.4.1 DC-AC Converter

The most common type of DC-AC converter used in power system applications is the VSC [174], which is based on Insulated-Gate Bipolar Transistors (IGBTs) and Pulse-Width Modulation (PWM)

techniques. The analysis presented here is carried out for a two-level VSC, but the principle is the same also for multilevel converters.

The detailed circuital representation of a VSC is depicted in Figure A.10. The inductor L_{arm} is added on each arm to limit circulating currents, current harmonics and fault currents.

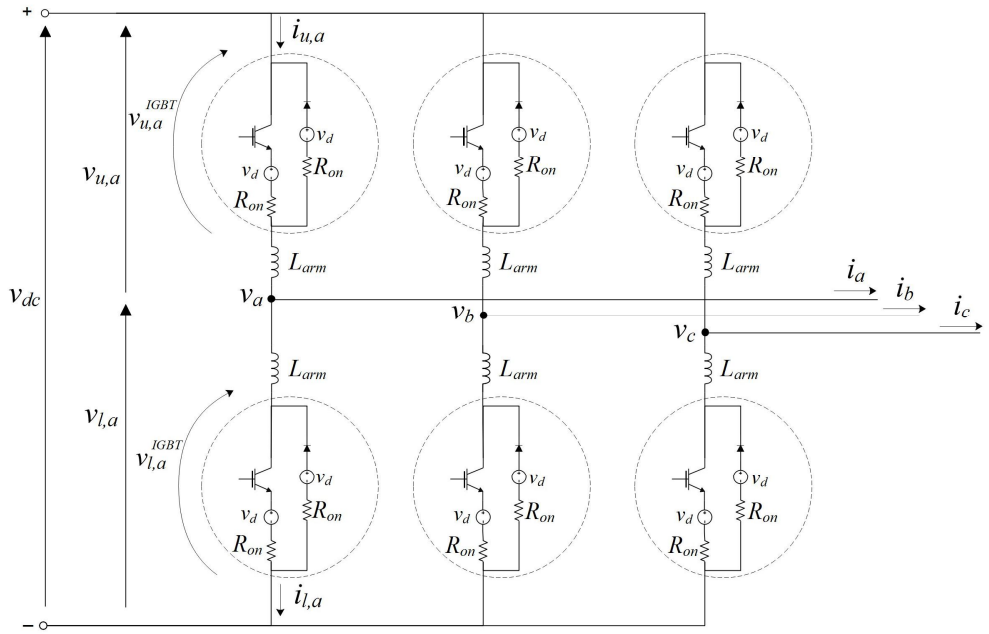

Figure A.10 – Detailed circuit model of a two-level voltage-sourced converter (Adapted from [174]).

In the average model IGBTs are not explicitly modelled, but the overall converter behavior is represented through controlled sources. The average model is obtained by analyzing Figure A.10 for which the following relations are evident for any phase-*j*,

$$\begin{aligned} v_{u,j} &= v_{u,j}^{IGBT} + L_{arm}\frac{di_{u,j}}{dt} \\ v_{l,j} &= v_{l,j}^{IGBT} + L_{arm}\frac{di_{l,j}}{dt} \\ v_j &= -v_{u,j} + \frac{v_{dc}}{2} = v_{l,j} - \frac{v_{dc}}{2} \\ i_j &= i_{u,j} - i_{l,j} \end{aligned} \tag{A.38}$$

in which circulating currents have been neglected. By defining,

$$e_j = \frac{-v_{u,j}^{IGBT} + v_{l,j}^{IGBT}}{2} \tag{A.39}$$

from (A.38) it is yield,

$$e_j = v_j + \frac{L_{arm}}{2}\frac{di_j}{dt} \tag{A.40}$$

This equivalent circuit for the ac-side is shown in Figure A.11, where L_{ac} = ½ L_{arm}. The expression obtained is valid also for multilevel converters, in which instead of considering the single IGBT, all the modules are taken into account.

Finally, e_j is obtained from,

$$e_j = \frac{v_{dc}}{2} v_{j,ref} \tag{A.41}$$

where $v_{j,ref}$ is the voltage reference or modulation index of phase-j, i.e. the output signal of the control system [175].

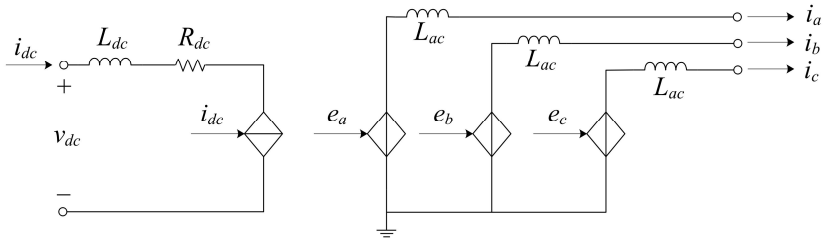

Figure A.11 – Average circuit model of a two-level VSC (Adapted from [173]).

The equivalent representation of the dc-side is obtained by considering the principle of power conservation, for which

$$v_{dc} i_{dc} = \sum_{j=a,b,c} e_j i_j \tag{A.42}$$

Therefore, i_{dc} is the current imposed to the controlled current source in the dc-side, obtained by replacing (A.41) in (A.42). It is worth mentioning that, while e_j and i_{dc} are controlled sources, v_{dc} and i_j are measured quantities.

The remaining equivalent electrical parameters R_{dc} and L_{dc} are obtained from an analysis of the circuit of Figure A.10 considering that ⅓ of the dc-current flows in each arm and that the same current flows in the upper and lower arms of each phase,

$$\begin{aligned} R_{dc} &= \frac{2}{3} R_{on} \\ L_{dc} &= \frac{2}{3} L_{arm} \end{aligned} \tag{A.43}$$

If a multilevel converter is considered, the number of modules must be considered when calculating R_{dc}.

A.4.2 DC-DC Converter

The detailed and average models of the DC-DC converter are shown in Figure A.12.

In the average model, i_a and u_b are the current and voltage measured at the LV and HV sides, respectively, and e_a is the controlled value, which could be an output signal of a controller. In PV units e.g., such signal is the output of the MPPT controller.

To calculate the value of the controlled current source i_b, the same principle of power balance used for the inverter is applied, i.e.,

$$e_a i_a = u_b i_b \tag{A.44}$$

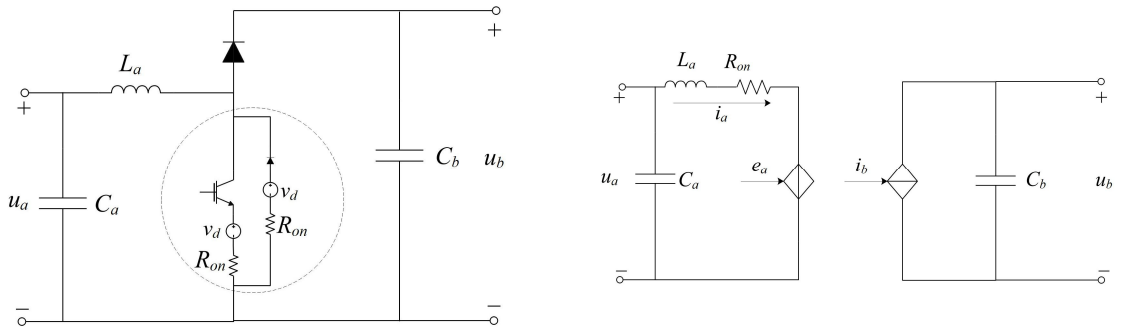

(a) (b)

Figure A.12 – (a) Detailed and (b) average circuit models of a DC/DC converter (Adapted from [176]).

A.5 The Distributed Energy Resources

In this Section, the most common technologies used for the distributed supply of electrical power are outlined. However, particular emphasis is given to the technologies employed in the thesis.

A.5.1 Synchronous and induction generators

DERs directly connected to the grid such as small hydro power plants, diesel and gas units, biomass and geothermal power plants, employ a SG or and Induction Generator (IG) for the mechanical-to-electrical energy conversion.

Since the aim is to go through the modelling of electric components, in the following analysis the mechanical power available at the generator shaft is considered known.

The analysis done for IMs in Section A.3.2 is applicable also for IGs, while the analysis of SGs is similar.

The following considerations are made for the analysis of SGs:

- The stator field rotates at the same electrical speed as the rotor, for which $\omega = \omega_r$.
- The generator convention is implemented for the stator windings.

By considering the following windings in the *dq*-axis:

- *d*,*s* and *q*,*s* that represent the three armature windings
- *f* that represents the field winding which produces flux only on the *d*-axis
- *d*,*r* and *q*,*r* that represent the damper circuit[1]
- *r*2 that represents the effect of rotor eddy-currents on the *q*-axis (negligible in salient pole SGs)

the winding representation in the *dq*-frame of the SG is that of Figure A.13. The (A.31) becomes,

$$\begin{bmatrix} v_{d,s} \\ v_{q,s} \\ v_f \\ v_{d,r} \\ v_{q,r} \\ v_{r2} \end{bmatrix} = \begin{bmatrix} R_s & 0 & \cdots & & & 0 \\ 0 & R_s & & & & \\ \vdots & & R_f & & & \\ & & & R_{d,r} & & \vdots \\ & & & & R_{q,r} & 0 \\ 0 & & & \cdots & 0 & R_{r2} \end{bmatrix} \begin{bmatrix} -i_{d,s} \\ -i_{q,s} \\ i_f \\ i_{d,r} \\ i_{q,r} \\ i_{r2} \end{bmatrix} + \frac{d}{dt} \begin{bmatrix} \lambda_{d,s} \\ \lambda_{q,s} \\ \lambda_f \\ \lambda_{d,r} \\ \lambda_{q,r} \\ \lambda_{r2} \end{bmatrix} + \begin{bmatrix} -\omega\lambda_{q,s} \\ \omega\lambda_{d,s} \\ 0 \\ 0 \\ 0 \\ 0 \end{bmatrix} \tag{A.45}$$

where the meaning of all variables is self-explanatory. The speed voltages appear only for the stator windings.

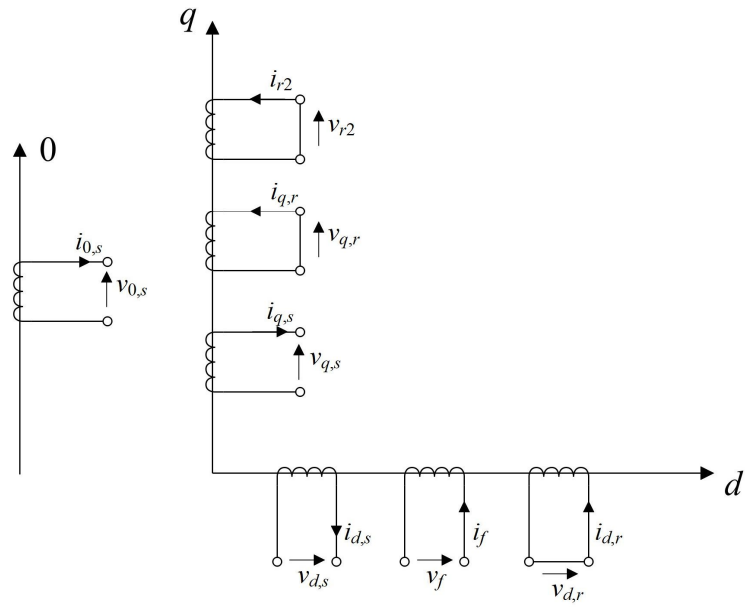

Figure A.13 – SG windings in the *dq*0-frame.

Expressing (A.45) separately for each axis, and considering self and mutual inductances, yields

$$\begin{bmatrix} v_{d,s} \\ v_f \\ 0 \end{bmatrix} = \begin{bmatrix} R_s & 0 & 0 \\ 0 & R_f & 0 \\ 0 & 0 & R_{d,r} \end{bmatrix} \begin{bmatrix} -i_{d,s} \\ i_f \\ i_{d,r} \end{bmatrix} + \begin{bmatrix} L_{d,s} & M_{d,sf} & M_{d,sr} \\ M_{d,fs} & L_f & M_{d,fr} \\ M_{d,rs} & M_{d,rf} & L_{d,r} \end{bmatrix} \frac{d}{dt} \begin{bmatrix} -i_{d,s} \\ i_f \\ i_{d,r} \end{bmatrix} + \begin{bmatrix} -\omega\lambda_{q,s} \\ 0 \\ 0 \end{bmatrix} \tag{A.46}$$

[1] It might be required to represent more than one damper circuit. In the following analysis, increasing such number is straightforward.

$$\begin{bmatrix} v_{q,s} \\ 0 \\ 0 \end{bmatrix} = \begin{bmatrix} R_s & 0 & 0 \\ 0 & R_{q,r} & 0 \\ 0 & 0 & R_{r2} \end{bmatrix} \begin{bmatrix} -i_{q,s} \\ i_{q,r} \\ i_{r2} \end{bmatrix} + \begin{bmatrix} L_{q,s} & M_{q,sr} & M_{q,sr2} \\ M_{q,rs} & L_{q,r} & M_{q,rr2} \\ M_{q,r2s} & M_{q,r2r} & L_{r2} \end{bmatrix} \frac{d}{dt} \begin{bmatrix} -i_{q,s} \\ i_{qr} \\ i_{r2} \end{bmatrix} + \begin{bmatrix} \omega \lambda_{d,s} \\ 0 \\ 0 \end{bmatrix} \quad \text{(A.47)}$$

By implementing a reciprocal per unit system [146], the mutual inductances between different windings are reciprocal and the mutual inductances between stator and rotor are equal between them in each axis. They are denoted as $x_{d,m}$ and $x_{q,m}$.

Moreover, similarly to what has been done for the IM and considering $x_{d,s}$ the reactance in per unit relative to the self-inductance $L_{d,s}$, then $x_{d,s} - x_{d,m} = x_{ls}$, which represents the stator leakage reactance that is nearly equal in both axes. A similar procedure can be applied to all other windings, thus obtaining the equivalent circuits in per unit of Figure A.14.

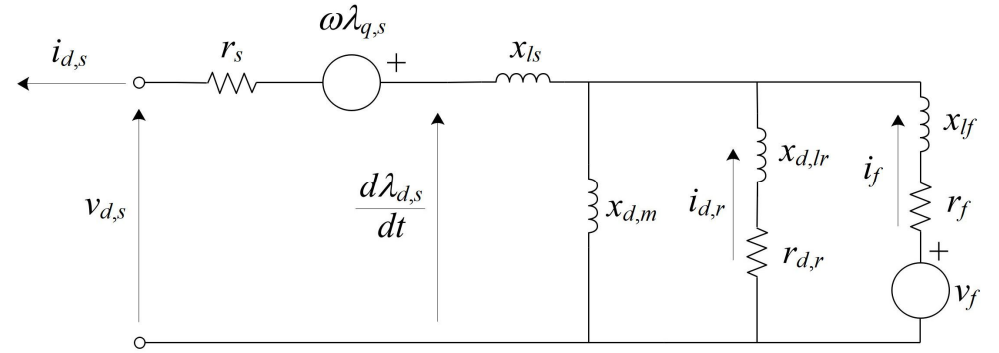

(a)

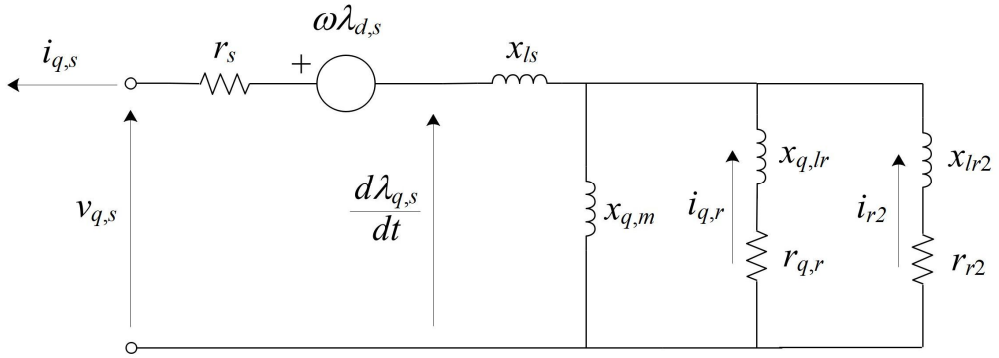

(b)

Figure A.14 – Equivalent circuits of a SG in the (a) *d*-axis and (b) *q*-axis. All magnitudes are expressed in per unit in a reciprocal system.

The mechanical dynamics are expressed through the motion equation i.e., (A.34) already introduced for the IM. Multi-mass models might be more adequate in some cases, represented by lumped masses with different inertias and damping constants, connected through shafts with stiffness K_i. The (A.34) becomes, in matrix form to consider all masses,

$$\boldsymbol{J}\frac{d^2\boldsymbol{\theta}}{dt^2} + \boldsymbol{D}\frac{d\boldsymbol{\theta}}{dt} + \boldsymbol{K}\,\boldsymbol{\theta} = \boldsymbol{T}_{em} - \boldsymbol{T}_m \quad \text{(A.48)}$$

in which the vector of angular velocities $\boldsymbol{\Omega}$ has been replaced by the vector of angular positions $\boldsymbol{\theta}$. Matrices $\boldsymbol{D}$ and $\boldsymbol{K}$ are not diagonal but tridiagonal, since they consider the influences of the adjacent lumped masses [76].

A.5.2 Microturbines

Microturbines are small gas combustion turbines. They can be grouped into single-shaft and split-shaft units [177].

In the case of single-shaft units, they are equipped with a permanent magnet SG mounted on the same shaft as the turbine, spinning at very high speed, typically between 50,000 and 120,000 rpm. Therefore, they generate electric power at a very high frequency, for which a back-to-back converter is employed to interface them with the grid.

In the case of split-shaft units, the turbine spins at 3,000 rpm and is connected to a conventional SG or IG through a gear box. Therefore, the back-to-back converter is not needed in this type of units.

It is straightforward that the modelling of single-shaft microturbines for electric transient studies is achieved by combining whether an SG or an IG with a back-to-back converter, as e.g. done in [178]. Since split-shaft microturbines implement only the electrical generator, reference is made to Section A.5.1. Moreover, even if the microturbine is of the split-shaft type, it is suitable to model it as a single-shaft unit, i.e. the mechanical part is modelled as a single-mass lumped model [179].

The efficiency of the microturbine is around 30%, which can be increased to values around 80% by adding a recuperator to recover waste heat. However, the recuperator is normally excluded from the model since its only purpose is to raise the microturbine efficiency.

A.5.3 Photovoltaic power plants

The single-diode model of a PV unit is shown in Figure A.15.

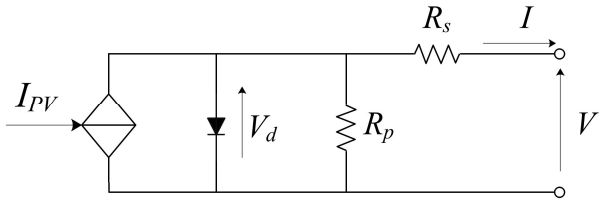

Figure A.15 – Single-diode equivalent circuit of a PV cell.

The expression that describes the ideal PV cell characteristic is obtained by ignoring R_s and R_p, i.e.

$$I = I_{PV,cell} - I_{0,cell}\left(e^{\frac{qV}{kT}} - 1\right) \tag{A.49}$$

where $I_{PV,cell}$ is the current generated by the incident light, and the second right term is the current at the diode, given by the Shockley equation, in which q is the electron charge, k is the Boltzmann constant and T is the temperature of the cell.

In order to consider a real PV cell, the resistances can no longer be ignored. Moreover, the ideality factor of the cell a is included, which accounts for the recombination mechanisms inside the diode. By considering an array composed by N_s cells in series and N_p modules in parallel, (A.49) becomes

$$I = I_{PV} - I_0\left(e^{\frac{V_d}{aV_t}} - 1\right) - \frac{V + R_s I}{R_p} \tag{A.50}$$

where $I_{PV} = N_p I_{PV,cell}$, $I_0 = N_p I_{0,cell}$, V_d is the voltage at the diode terminals, and V_t is the thermal voltage of the array, given by

$$V_t = N_s \frac{kT}{q} \tag{A.51}$$

The model is improved by taking into account the irradiance and temperature effect on I_{PV}. Given the nominal current generated by the cell at nominal conditions $I_{PV,cell,nom}$, i.e. when the irradiance is G_{nom} and temperature is T_{nom} (usually 1000 W/m^2 and 25°C), the current $I_{PV,T}$ generated by the array when the irradiance is G and temperature is T is yield from

$$I_{PV,T} = N_p\left[I_{PV,cell,nom} + K_{I,PV}\left(T - T_{nom}\right)\right]\frac{G}{G_{nom}} \tag{A.52}$$

where the parameter $K_{I,PV}$ is the short-circuit current temperature coefficient. Normally $I_{PV,cell,nom}$ is not known, but the short-circuit current of the cell $I_{sc,nom}$ is. It is often considered that $I_{PV,cell,nom} = I_{sc,nom}$ since the value of R_p is great. However, for a better accuracy, the value of $I_{PV,cell,nom}$ can be derived from,

$$I_{PV,cell,nom} = \frac{R_p + R_s}{R_p} I_{sc,nom} \tag{A.53}$$

The model is further improved by imposing

$$I_0 = N_p\left[\frac{I_{sc,nom} + K_{I,PV}\left(T - T_{nom}\right)}{e^{\frac{V_{oc,nom} + K_{V,PV}\left(T - T_{nom}\right)}{aV_t}} - 1}\right] \tag{A.54}$$

where $V_{oc,nom}$ is the open-circuit voltage of the cell at nominal conditions and $K_{V,PV}$ is the open-circuit voltage temperature coefficient. The relation expressed in (A.54) was obtained from experimental data [180].

Therefore, the PV array can be simulated as a controlled current source which implements

$$I_{source} = I_{PV,T} - I_0 \left(e^{\frac{V_d}{aV_t}} - 1 \right) \tag{A.55}$$

where $I_{PV,T}$ is obtained from (A.52) and I_0 from (A.54). Moreover, the equivalent resistances for the model are given by,

$$\begin{aligned} R_{s,PV} &= R_s \frac{N_s}{N_p} \\ R_{p,PV} &= R_p \frac{N_s}{N_p} \end{aligned} \tag{A.56}$$

The circuit model is depicted in Figure A.16.

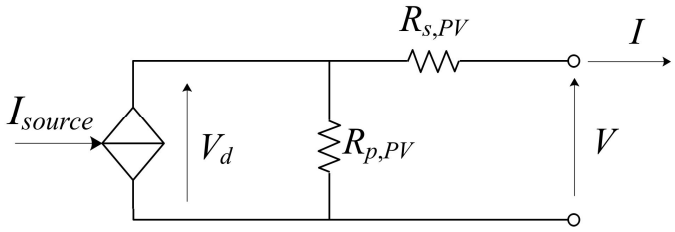

Figure A.16 – Circuit model of a PV array.

A.5.4 Wind generators

There are mainly 4 types of wind generators as shown in Figure A.17.

The main electrical components are: a generator, which can be either a squirrel cage or a wounded rotor IG or a permanent magnet SG, depending on the topology; a bank of resistances; a soft-starter; a back-to-back converter; a capacitor bank; and a transformer. The modelling of generators and transformers was already illustrated in previous subsections. Therefore, only the remaining components are described in the following.

The variable resistances of the wind turbine of type – 2 are added to the rotor circuit in order to control the output power for a speed range above the synchronous speed typically in the range from 0 to 10%, but also values of 60% can be achieved [181]. The total rotor resistance might be varied by controlling an IGBT-based converter which short circuits partially the resistances, therefore controlling the rotor current and slip hence the power output. The overall system is placed directly on the rotor, which eliminates the presence of rings and brushes. It can be simulated through a variable resistance properly controlled, in series to the intrinsic rotor resistance of Figure A.8 and Figure A.9.

The soft-starter limits the current during the startup of the generator by modulating the magnitude of the voltage supply. It consists of two anti-parallel thyristors for each phase, which firing angle is controlled during the startup, and are by-passed in normal operating conditions. Depending on the study case, it can be modelled in detail or represented with a controlled voltage source [182].

Capacitor banks are useful to compensate for the reactive power withdrawn by IGs. They are connected only in turbines of type 1 and 2, since in those of type 3 and 4, the power converter covers their role. Capacitor banks are represented as a lumped shunt capacitance placed at the stator terminals of Figure A.8 and Figure A.9.

The back-to-back converter is employed in both type 3 and type 4 wind turbines. It is composed by two bi-directional AC/DC converters in cascade connected either between the wound rotor of the IG and the transformer, in case of a Doubly Fed Induction Generator (DFIG); or between the generator stator winding and the transformer, in case of a Full-Scale Converter (FSC) wind turbine. In both cases, the converters are of VSC-type with IGBTs, as the ones described in Section A.4.

When a voltage dip occurs at the generator terminals of a type – 3 wind turbine, large currents might rise in the rotor winding connected to the rotor-side converter that could damage the converter switches. The crowbar circuit connected to the rotor winding prevents such phenomenon. It might be constituted by thyristors or by an IGBT-based controlled circuit [183]. The crowbar can be modelled as a set of resistances connected to the rotor winding through a controllable breaker ignited by the crowbar protection scheme. In the model, the resistances are placed in series to the intrinsic rotor resistance, as for the variable resistances in type – 2 wind turbines.

The mechanical system involves the blades, the hub and the slow and fast shafts coupled through the gear box (if existent) and the generator. The inertia of the gear is often neglected and only the transformation ratio of the gear system is included, while the turbine and the generator rotors provide a considerable inertia to the system [184]. A single mass model as the one adopted for synchronous-based resources is not accurate even in absence of the gear box, due to the particularly low stiffness of the shaft system of wind turbines. Therefore, a two-mass model representation with a connecting shaft is normally implemented. It consists of two masses with different inertia and own friction coefficients, coupled by a torsional stiffness and damping link. To simplify the model, the friction and damping coefficients can be neglected.

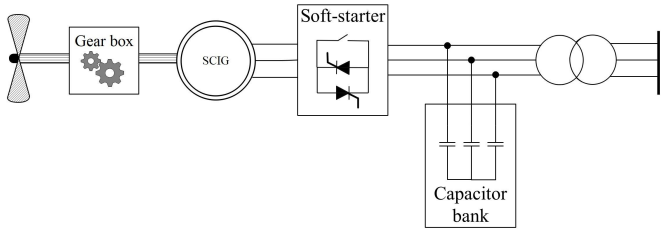

(a)

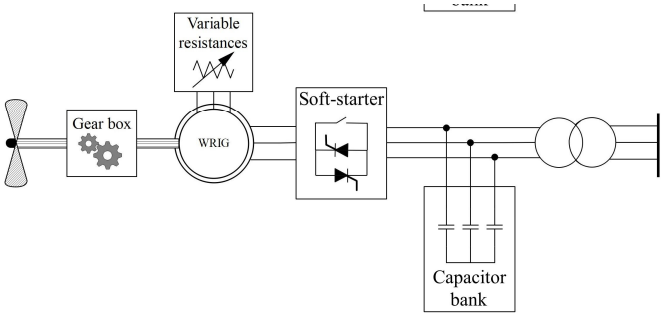

(b)

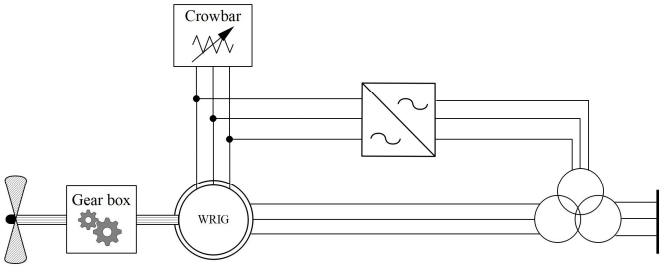

(c)

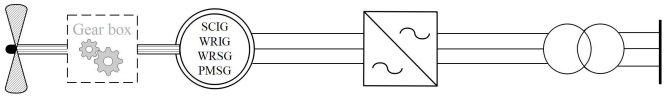

(d)

SCIG: Squirrel Cage Induction Generator WRSG: Wound Rotor Synchronous Generator
WRIG: Wound Rotor Induction Generator PMSG: Permanent Magnet Synchronous Generator

Figure A.17 – Typical wind turbine electrical configurations: (a) type 1 – fixed-speed; (b) type 2 – limited variable-speed; (c) type 3 – variable speed with partial scale frequency converter or doubly fed induction generator; and (d) type 4 – variable speed with full-scale frequency converter (Adapted from [185]).

A.5.5 Storage systems

a) Batteries

There is a wide variety of batteries with very different characteristics from the point of view of energy density, power density, efficiency, life cycle, operational temperature among others [186]. The main technologies are lead acid, high-temperature (or molten salt e.g., NaS), lithium ion (Li-ion), nickel-based and flow batteries (e.g., vanadium redox). While the lead acid is the oldest and most mature technology, the Li-ion is one of the most promising technologies due to high power and energy densities, high efficiency and life cycle.

Many battery models exist in literature and can be divided into three categories: i) electrochemical models, ii) mathematical models, and iii) electrical models. Electrochemical models are very complex, and they aim at optimizing the physical aspects of batteries. Mathematical models employ empirical relations to predict the battery behavior in terms of efficiency, capacity and run time, hence are not practical for circuital representation. Electrical models employ a combination of electrical elements such as voltage sources, resistors and capacitors. For this reason, electrical models are the most suitable for the scope of the studies related to electrical transients, such as the ones carried out in this thesis.

Electrical models can be divided in turn into three categories: i) Thévenin-based models, ii) impedance-based models, and iii) runtime-based models.

- Thévenin-based model

The Thévenin-based model in its simplest form is shown in Figure A.18, in which V_{oc} represents the open-circuit voltage, R_s, R_t and C_t the battery conduction losses and its transient response.

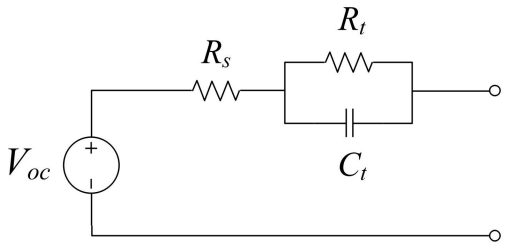

Figure A.18 – Thévenin-based model of the battery in its simplest form (Adapted from [187]).

The major drawback of this models is that it considers all parameters as constants, thus failing at reproducing the steady-state voltage variations (dc-response) and the runtime information. In practice, all parameters are nonlinear functions of the SoC, temperature and C-rate.

Several other models have been developed from the simple circuit of Figure A.18, some of them aim at dealing with the above-mentioned issues, some others aim at improving the battery transient response representation. Regarding the first group, models are quite complex and however do not predict the battery runtime accurately [187]. Regarding the second group, in order to reproduce dynamics that take place in different temporal ranges some authors add a second and even a third RC branch in series, as shown in Figure A.19, while disregarding or simplifying the issues related to the steady-state voltage variations and the runtime information.

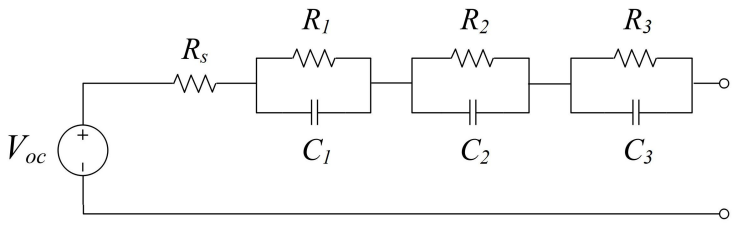

Figure A.19 – Thévenin-based model of the battery with three RC branches (Adapted from [188]).

To cope to some degree with the dependency of the parameters, the parameter estimation is performed for different ranges of SoC [188], [189], while the effect of the temperature and the C-rate is usually disregarded.

Further, a resistor can be added in parallel to the voltage source to reproduce the effect of self-discharge. Moreover, if different parameters are considered for the charge and discharge processes, they can be connected in parallel with anti-parallel ideal diodes, only to represent the difference between both processes. Depending on the battery technology, different Thévenin-based models might be employed [190].

- Impedance-based models

Impedance-based models are similar to the Thévenin-based model from the circuital point of view. They obtain an equivalent impedance model in the frequency domain from an electrochemical impedance spectroscopy through fitting process which mechanism is very complicated. It suffers of the same flaws that the Thévenin-based models, i.e. they cannot inherently predict the dc-response or runtime. Moreover, the accuracy of its transient response is limited [191].

- Runtime-based models

Runtime-based models use a combination of inter-dependent equivalent circuits as shown in Figure A.20, which very well simulate the battery dc-response and runtime for a constant discharge current. For these models too, the accuracy of its transient response is limited.

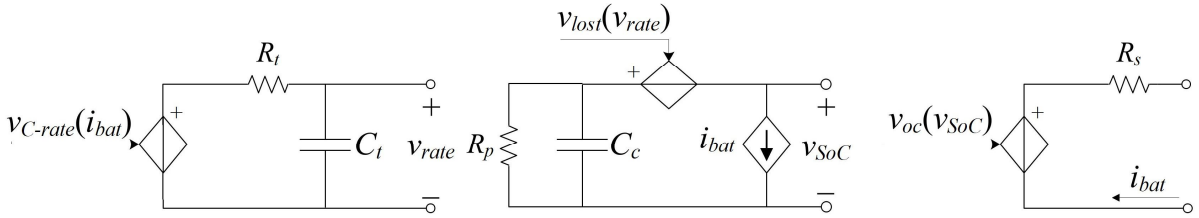

Figure A.20 – Runtime-based model of the battery (Adapted from [187]).

Combined models can be also derived, for example combining the characteristics of runtime-based and Thévenin-based models [191]. The main differences between the characteristics of these three types of electrical models are reported in Table A-1.

TABLE A-1
COMPARISON OF ELECTRICAL MODELS OF BATTERIES.
ADAPTED FROM [187]

Predicting capability	Thévenin-based	Impedance-based	Runtime-based
DC response	No	No	Yes
AC response (frequency)	Limited	Yes	No
Transient response	Yes	Limited	Limited
Runtime	No	No	Yes

For their accuracy at representing the transient response of batteries, a Thévenin-based model is adopted in this thesis.

b) Supercapacitors

Supercapacitors are often modelled using equivalent circuits composed of resistors and capacitors, as shown in Figure A.21. In the classical model shown in Figure A.21a, as for batteries, the series resistance R_s represents the conduction losses, while C represents the supercapacitor itself and R_p the self-discharge. An inductive element might be added to account for aspects mainly related to the metallic cover of the supercapacitor, which may become important at frequencies typically above 100 Hz [192].

The dynamic model shown in Figure A.21b includes a series of RC branches for which any continuous distribution of time constants can be generated. It might employ an electrochemical impedance spectroscopy aiming at describing its behavior in a wide frequency range.

The three-stage ladder model shown in Figure A.21c, which actually is flexible as for the number of stages, aims at reproducing the distributed nature of the capacitance and resistance in a supercapacitor.

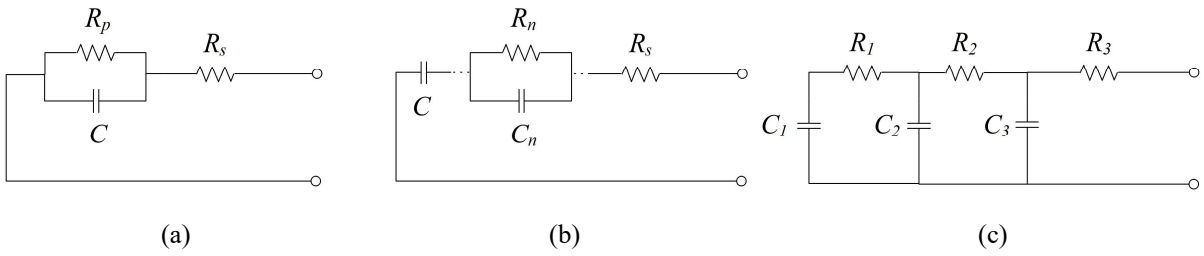

Figure A.21 – Supercapacitor equivalent circuits: (a) classical model; (b) dynamic model and; (c) three-stage ladder model (Adapted from [193]).

Other than equivalent circuit models, there are electrochemical, fractional-order (similar to impedance-based models of batteries) and intelligence-based models [193].

For completeness, although they have not been used in the simulations of this thesis, it is worth mentioning other relevant ESSs that include pumped hydro, compressed air, flywheels, superconducting magnetics and fuel cells [194].

- Pumped hydro storage is the most important form of storage for electric power systems and is still the most widely deployed. Energy is stored in the form of gravitational potential energy by pumping water from one reservoir to another placed at a higher level. A pump/turbine unit is attached to a reversible electric generator/motor unit that pumps water towards the upper reservoir when the demand is low and vice versa generates electricity when the demand is high.

- Compressed air systems store energy in the form of potential elastic energy by compressing air in a reservoir. When the demand is low, a motor drives a compressor to store air at high pressures in a

reservoir, vice versa releases the compressed air to drive a turbine/generator unit to generate electricity when the demand is high. The air heats up when compressed while cools down when released, so proper measures are taken to deal with this issue.

- Flywheel systems store energy in the form of kinetic energy by spinning a flywheel. The flywheel is attached to a reversible electric generator/motor unit in a vacuum chamber that draws electricity from the grid to spin the flywheel up to the nominal speed when the demand is low and vice versa generates electricity when the demand is high.

- Superconducting magnetic systems store energy in the form of magnetic field by driving a direct current flow in a superconducting coil. The superconducting coil is attached to a power conditioning system that absorbs energy from the grid to feed the coil when the demand is low and vice versa releases energy when required by the power system. Superconducting magnetic systems store low amounts of energy, as well as the supercapacitors, for which when implemented are normally used during transient events when the power system requires it, i.e., not in function of the load demand.

- Fuel cells, as well as batteries, store energy in the form of electrochemical energy. One of the most interesting fuel cells are the hydrogen ones. The fuel cell withdraws electricity from the grid to generate hydrogen through electrolysis when the demand is low and vice versa generates electricity due to the reaction of the hydrogen with oxygen when the demand is high. Hydrogen can also be provided from outside. The principle of other fuel cells is the same.

ESSs that can properly deal with power quality-related issues require high cyclability and fast response rates [195]. From the above-mentioned technologies, batteries, flywheels, supercapacitors and superconducting coils are the most adapted. Different ESSs can be also combined to obtain the desired response at different time scales, as done e.g. in [196].

APPENDIX B
SPACE-VECTOR TRANSFORMATIONS

For control design and implementation purposes, it is preferred to deal with real-valued functions of time rather than phasor and complex-valued functions. Moreover, the speed response of the controllers of power converters makes impractical the application of rms and average measurements of quantities such as powers, voltage and current. Instead, it is desired to estimate the instantaneous values of these quantities.

The two most popular transformations applied to three-phase systems to deal with the above-mentioned issues are briefly illustrated, namely the Clarke and the Park transformations [197]–[200]. All the control schemes implemented in this thesis use these two transformations.

B.1 Clarke transformation

The Clarke or $\alpha\beta$0-transformation is defined in [197] as,

$$\begin{bmatrix} u_\alpha \\ u_\beta \\ u_0 \end{bmatrix} = \begin{bmatrix} 1 & -1/2 & -1/2 \\ 0 & \sqrt{3}/2 & -\sqrt{3}/2 \\ 1 & 1 & 1 \end{bmatrix} \begin{bmatrix} u_a \\ u_b \\ u_c \end{bmatrix} \tag{B.1}$$

The $\alpha\beta 0$-transformation can be seen as the result from the decomposition of the positive-sequence of a three-phase quantity in its real (α) and imaginary (β) parts, plus the zero-component (0). Indeed, the positive sequence of a three-phase voltage $\boldsymbol{u}_{abc}$ is,

$$u^{+} = \begin{bmatrix} 1 & a & a^2 \end{bmatrix} \begin{bmatrix} u_a \\ u_b \\ u_c \end{bmatrix} \tag{B.2}$$

where a is the rotational operator equal to $e^{j2\pi/3}$. The $\alpha\beta 0$-transformation results from considering the real part for α and the imaginary part for β [198], i.e.,

$$\boldsymbol{u}_{\alpha\beta 0} = \begin{bmatrix} 1 & \Re\{a\} & \Re\{a^2\} \\ 0 & \Im\{a\} & \Im\{a^2\} \\ 1 & 1 & 1 \end{bmatrix} \boldsymbol{u}_{abc} \tag{B.3}$$

which results in (B.1).

The $\alpha\beta 0$-transformation can be written in general form as,

$$\boldsymbol{u}_{\alpha\beta 0} = k_1 \begin{bmatrix} 1 & -1/2 & -1/2 \\ 0 & \sqrt{3}/2 & -\sqrt{3}/2 \\ k_0 & k_0 & k_0 \end{bmatrix} \boldsymbol{u}_{abc} \tag{B.4}$$

in which the parameters k_0 and k_1 determine the relation between the two systems.

Assuming that $\boldsymbol{u}_{abc}$ is a symmetrical tern of voltages, each of magnitude U, the magnitude of both $\alpha\beta$-components is,

$$U_\alpha = U_\beta = \frac{3}{2} k_1 \cdot U \tag{B.5}$$

Therefore, for the magnitudes of the sinusoidal signals in the $\alpha\beta$- and abc-frames to be equal, $k_1 = 2/3$. Moreover, from (B.4) the 0-component is coincident with the homopolar sequence if $k_0 = 1/2$ such that $k_1 \cdot k_0 = 1/3$. However, k_0 is kept as a variable and its value is further chosen.

Under such considerations, the transformation and anti-transformation matrices $\boldsymbol{T}_{\alpha\beta 0}$ and $\boldsymbol{T}_{\alpha\beta 0}^{-1}$ can be expressed as,

$$\boldsymbol{T}_{\alpha\beta 0} = \frac{2}{3}\begin{bmatrix} 1 & -1/2 & -1/2 \\ 0 & \sqrt{3}/2 & -\sqrt{3}/2 \\ k_0 & k_0 & k_0 \end{bmatrix}$$
$$\boldsymbol{T}_{\alpha\beta 0}^{-1} = \begin{bmatrix} 1 & 0 & 1/2k_0 \\ -1/2 & \sqrt{3}/2 & 1/2k_0 \\ -1/2 & -\sqrt{3}/2 & 1/2k_0 \end{bmatrix} \tag{B.6}$$

The apparent power is,

$$S = \boldsymbol{u}_{abc}{}^{T}\boldsymbol{i}_{abc} \tag{B.7}$$

which results in,

$$\begin{aligned} S &= \left(\boldsymbol{T}_{\alpha\beta 0}^{-1}\boldsymbol{u}_{\alpha\beta 0}\right)^{T}\left(\boldsymbol{T}_{\alpha\beta 0}^{-1}\boldsymbol{i}_{\alpha\beta 0}\right) \\ &= \boldsymbol{u}_{\alpha\beta 0}{}^{T}\left(\boldsymbol{T}_{\alpha\beta 0}^{-1}\right)^{T}\left(\boldsymbol{T}_{\alpha\beta 0}^{-1}\right)\boldsymbol{i}_{\alpha\beta 0} \end{aligned} \tag{B.8}$$

And,

$$\left(\boldsymbol{T}_{\alpha\beta 0}^{-1}\right)^{T}\left(\boldsymbol{T}_{\alpha\beta 0}^{-1}\right) = \frac{3}{2}\begin{bmatrix} 1 & 0 & 0 \\ 0 & 1 & 0 \\ 0 & 0 & 1/2k_0{}^{2} \end{bmatrix} \tag{B.9}$$

By choosing $k_0 = 1/\sqrt{2}$ (B.7) results in,

$$S_{abc} = \frac{3}{2}S_{\alpha\beta 0} \tag{B.10}$$

If $k_0 = ½$ was chosen, a further factor would have been needed to account for the power due to the zero-sequence components in the power equivalence.

Then, (B.6) becomes,

$$\boldsymbol{T}_{\alpha\beta 0} = \frac{2}{3}\begin{bmatrix} 1 & -1/2 & -1/2 \\ 0 & \sqrt{3}/2 & -\sqrt{3}/2 \\ 1/\sqrt{2} & 1/\sqrt{2} & 1/\sqrt{2} \end{bmatrix}$$
$$\boldsymbol{T}^{-1}_{\alpha\beta 0} = \begin{bmatrix} 1 & 0 & 1/\sqrt{2} \\ -1/2 & \sqrt{3}/2 & 1/\sqrt{2} \\ -1/2 & -\sqrt{3}/2 & 1/\sqrt{2} \end{bmatrix} \quad \text{(B.11)}$$

This is the magnitude-invariant form of the *αβ0*-transformation, since the transformation of a symmetrical system in the *abc*-frame results in sinusoidal *αβ*-signals with the same amplitude.

The power-invariant form of the transformation considers a gain of $\sqrt{2}/3$ in the anti-transformation matrix, such that the product $\left(\boldsymbol{T}^{-1}_{\alpha\beta 0}\right)^T \left(\boldsymbol{T}^{-1}_{\alpha\beta 0}\right)$ in (B.9) equals the identity matrix and in consequence (B.10) results in $S_{abc} = S_{\alpha\beta 0}$.

The resulting matrices are,

$$\boldsymbol{T}_{\alpha\beta 0} = \sqrt{\frac{2}{3}}\begin{bmatrix} 1 & -1/2 & -1/2 \\ 0 & \sqrt{3}/2 & -\sqrt{3}/2 \\ 1/\sqrt{2} & 1/\sqrt{2} & 1/\sqrt{2} \end{bmatrix}$$
$$\boldsymbol{T}^{-1}_{\alpha\beta 0} = \sqrt{\frac{2}{3}}\begin{bmatrix} 1 & 0 & 1/\sqrt{2} \\ -1/2 & \sqrt{3}/2 & 1/\sqrt{2} \\ -1/2 & -\sqrt{3}/2 & 1/\sqrt{2} \end{bmatrix} \quad \text{(B.12)}$$

In this case, the norm of the resulting vectors in both systems are equal, i.e.,

$$U_a^2 + U_b^2 + U_c^2 = U_\alpha^2 + U_\beta^2 + U_0^2 \quad \text{(B.13)}$$

B.1.1 The per-unit form

A per unit analysis is done, with the peak phase voltage and the peak line current as base quantities. The power base in the *abc*-system is,

$$S_B = \sqrt{3} V_{nom} I_{nom} \quad \text{(B.14)}$$

where V_{nom} is the rms line-to-line voltage and I_{nom} the rms line current. Follows that the base values in a wye-system are,

$$\begin{aligned} V_B &= \frac{\sqrt{2}\,V_{nom}}{\sqrt{3}} \\ I_B &= \sqrt{2}\,I_{nom} \end{aligned} \tag{B.15}$$

Then,

$$S_B = \frac{3}{2} V_B I_B \tag{B.16}$$

When calculating the per unit power as,

$$\begin{aligned} s'_{abc} &= \frac{S}{S_B} \\ &= \frac{2}{3} \boldsymbol{u}'^{\,T}_{\alpha\beta 0} \left(\boldsymbol{T}^{-1}_{\alpha\beta 0}\right)^T \left(\boldsymbol{T}^{-1}_{\alpha\beta 0}\right) \boldsymbol{i}'_{\alpha\beta 0} \end{aligned} \tag{B.17}$$

from (B.7) results in,

$$s'_{abc} = \frac{2}{3} \boldsymbol{u}'^{\,T}_{\alpha\beta 0} \left(\boldsymbol{T}^{-1}_{\alpha\beta 0}\right)^T \left(\boldsymbol{T}^{-1}_{\alpha\beta 0}\right) \boldsymbol{i}'_{\alpha\beta 0} \tag{B.18}$$

in which primed variables are per unit quantities.

By implementing the magnitude-invariant form, i.e., with $k_1 = ⅔$, it follows from (B.11) that,

$$\frac{2}{3}\left(\boldsymbol{T}^{-1}_{\alpha\beta 0}\right)^T \left(\boldsymbol{T}^{-1}_{\alpha\beta 0}\right) = \begin{bmatrix} 1 & 0 & 0 \\ 0 & 1 & 0 \\ 0 & 0 & 1 \end{bmatrix} \tag{B.19}$$

Then,

$$s'_{abc} = s'_{\alpha\beta 0} \tag{B.20}$$

The magnitude-invariant transformation matrices in per unit are also power-invariant.

If the zero-component is disregarded, as in the controls implemented in this thesis, the transformation matrices for the per unit system are,

$$\boldsymbol{T}_{\alpha\beta} = \frac{2}{3}\begin{bmatrix} 1 & -1/2 & -1/2 \\ 0 & \sqrt{3}/2 & -\sqrt{3}/2 \end{bmatrix}$$
$$\boldsymbol{T}_{\alpha\beta}^{-1} = \begin{bmatrix} 1 & 0 \\ -1/2 & \sqrt{3}/2 \\ -1/2 & -\sqrt{3}/2 \end{bmatrix} \tag{B.21}$$

The magnitudes of major interest for the control of power converters are the voltage, the current, and the active and reactive powers, which in terms of $\alpha\beta$-quantities can be expressed in per unit as,

$$\begin{aligned} v &= \sqrt{v_\alpha^2 + v_\beta^2} \\ i &= \sqrt{i_\alpha^2 + i_\beta^2} \\ p &= v_\alpha i_\alpha + v_\beta i_\beta \\ q &= -v_\alpha i_\beta + v_\beta i_\alpha \end{aligned} \tag{B.22}$$

B.2 Park transformation

The vector $\boldsymbol{u}_{\alpha\beta0}$ resulting from the $\alpha\beta0$-transformation is a vector $\boldsymbol{u}_{\alpha\beta}$ rotating in the $\alpha\beta$-plane orthogonal to the 0-axis, as can be seen in Figure B.1a. The Park or $dq0$-transformation establishes a rotating dq-frame still orthogonal to the 0-axis, as can be seen in Figure B.1b. The d-axis is aligned with the a-axis (known as cosine-based Park transformation), which in the analysis here exposed is also the α-axis.

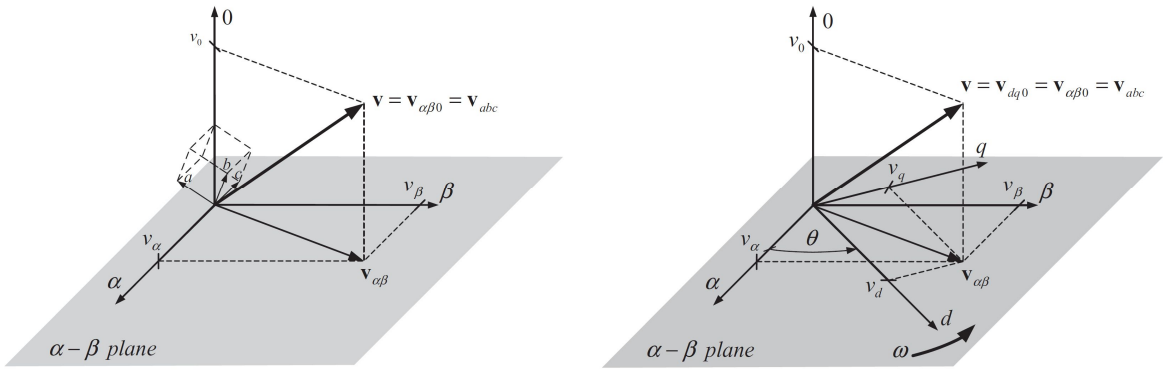

(a) (b)

Figure B.1 – Graphical representation of (a) the $\alpha\beta0$ and, (b) the $dq0$-frames (From [198]).

The transformation and anti-transformation matrices applied to the $\alpha\beta0$-system are,

$$\boldsymbol{T}_{dq0}\Big|_{\alpha\beta0} = \begin{bmatrix} \cos(\omega t) & \sin(\omega t) & 0 \\ -\sin(\omega t) & \cos(\omega t) & 0 \\ 0 & 0 & 1 \end{bmatrix}$$
$$\boldsymbol{T}_{dq0}^{-1}\Big|_{\alpha\beta0} = \begin{bmatrix} \cos(\omega t) & -\sin(\omega t) & 0 \\ \sin(\omega t) & \cos(\omega t) & 0 \\ 0 & 0 & 1 \end{bmatrix} \tag{B.23}$$

If instead, they are applied to the *abc*-system,

$$\boldsymbol{T}_{dq0}\Big|_{abc} = \frac{2}{3}\begin{bmatrix} \cos(\omega t) & \cos\left(\omega t - \frac{2\pi}{3}\right) & \cos\left(\omega t + \frac{2\pi}{3}\right) \\ -\sin(\omega t) & -\sin\left(\omega t - \frac{2\pi}{3}\right) & -\sin\left(\omega t + \frac{2\pi}{3}\right) \\ 1/\sqrt{2} & 1/\sqrt{2} & 1/\sqrt{2} \end{bmatrix}$$
$$\boldsymbol{T}_{dq0}^{-1}\Big|_{abc} = \begin{bmatrix} \cos(\omega t) & -\sin(\omega t) & 1/\sqrt{2} \\ \cos\left(\omega t - \frac{2\pi}{3}\right) & -\sin\left(\omega t - \frac{2\pi}{3}\right) & 1/\sqrt{2} \\ \cos\left(\omega t + \frac{2\pi}{3}\right) & -\sin\left(\omega t + \frac{2\pi}{3}\right) & 1/\sqrt{2} \end{bmatrix} \tag{B.24}$$

which constitute the magnitude-invariant version of the *dq*0-transformation. Regarding the power, an analog analysis as the one for the Clarke transformation can be done. Indeed from (B.24) follows,

$$\left(\boldsymbol{T}_{dq0}^{-1}\right)^T\left(\boldsymbol{T}_{dq0}^{-1}\right) = \frac{3}{2}\begin{bmatrix} 1 & 0 & 0 \\ 0 & 1 & 0 \\ 0 & 0 & 1 \end{bmatrix} \tag{B.25}$$

And the relation expressed in (B.10) is valid also for the *dq*0-system.

Following the same reasoning as for the Clarke transformation, the matrices in the power-invariant version are,

$$\boldsymbol{T}_{dq0} = \sqrt{\frac{2}{3}} \begin{bmatrix} \cos(\omega t) & \cos\left(\omega t - \frac{2\pi}{3}\right) & \cos\left(\omega t + \frac{2\pi}{3}\right) \\ -\sin(\omega t) & -\sin\left(\omega t - \frac{2\pi}{3}\right) & -\sin\left(\omega t + \frac{2\pi}{3}\right) \\ 1/\sqrt{2} & 1/\sqrt{2} & 1/\sqrt{2} \end{bmatrix}$$

$$\boldsymbol{T}_{dq0}^{-1} = \sqrt{\frac{2}{3}} \begin{bmatrix} \cos(\omega t) & -\sin(\omega t) & 1/\sqrt{2} \\ \cos(\omega t - \frac{2\pi}{3}) & -\sin(\omega t - \frac{2\pi}{3}) & 1/\sqrt{2} \\ \cos(\omega t + \frac{2\pi}{3}) & -\sin(\omega t + \frac{2\pi}{3}) & 1/\sqrt{2} \end{bmatrix} \tag{B.26}$$

B.2.1 The per-unit form

The magnitude-invariant matrices of (B.24) are also power-invariant if the per unit system is employed, with the base values of (B.15) and (B.16).

Neglecting the 0-component, the magnitudes of interest for the control of power converters can be expressed as,

$$\begin{aligned} v &= \sqrt{v_d^2 + v_q^2} \\ i &= \sqrt{i_d^2 + i_q^2} \\ p &= u_d i_d + u_q i_q \\ q &= -u_d i_q + u_q i_d \end{aligned} \tag{B.27}$$

BIBLIOGRAPHY AND REFERENCES

[1] International Renewable Energy Agency (IRENA), *Global Energy Transformation: A Roadmap to 2050*. 2019.

[2] Directorate-General for Energy (European Commission), "Clean energy for all Europeans," *Euroheat and Power*, 2019.

[3] Terna SpA e Gruppo Terna, "Contesto ed evoluzione del sistema elettrico," Italy, 2019.

[4] ANIE Rinnovabili, "Osservatorio Sistemi di Accumulo," Italy, 2020.

[5] "Piano Nazionale Integro per l'Energia e il Clima," 2019.

[6] D. E. Olivares, A. Mehrizi-Sani, A. H. Etemadi, C. A. Cañizares, R. Iravani, M. Kazerani, A. H. Hajimiragha, O. Gomis-Bellmunt, M. Saeedifard, R. Palma-Behnke, G. A. Jiménez-Estévez, and N. D. Hatziargyriou, "Trends in microgrid control," *IEEE Trans. Smart Grid*, 2014.

[7] J. J. Grainger and W. D. Stevenson, *Power System Analysis*. Singapore: McGraw-Hill, Inc., 1994.

[8] *IEEE Recommended Practice for Protection and Coordination of Industrial and Commercial Power Systems (Buff Book)*. New York: The Institute of Electrical and Electronics Engineers, Inc., 2001.

[9] F. M. Gatta, A. Geri, S. Lauria, and M. Maccioni, "Analytical prediction of abnormal temporary overvoltages due to ground faults in MV networks," *Electr. Power Syst. Res.*, 2007.

[10] A. Cerretti, F. M. Gatta, A. Geri, S. Lauria, M. MacCioni, and G. Valtorta, "Ground fault temporary overvoltages in MV networks: Evaluation and experimental tests," *IEEE Trans. Power Deliv.*, 2012.

[11] J. L. Blackburn and T. J. Domin, *Protective Relaying: Principles and Applications*. CRC Press, 2006.

[12] "IEEE Standard Definitions for Power Switchaear," *IEEE Std C37.100-1992*, 1992.

[13] J. Roberts, H. J. Altuve, and D. Hou, "Review of ground fault protection methods for grounded, ungrounded, and compensated distribution systems," *27th Annu. West. Prot. Relay Conf.*, 2001.

[14] A. Capasso, R. Calone, R. Lama, S. Lauria, and A. Santopaolo, "Ground Fault Protection in ENEL Distribuzione's Experimental MV Loop Line," in *12th IET International Conference on Developments in Power System Protection (DPSP 2014)*, Copenhagen, Denmark, 2014.

[15] A. Wahlroos and J. Altonen, "Performance of novel neutral admittance criterion in MV-feeder earth-fault protection," in *IET Conference Publications*, 2009.

[16] M. Lehtonen, R. J. Millar, and C. J. Kim, "The Impact of the Distribution Network Type and Configuration on the Transient Behavior of the Fault and Neutral Points during Earth Faults," in *International Conference on Power Systems Transients*, Delft, Netherlands, 2011.

[17] K. Pandakov, H. K. Høidalen, and J. I. Marvik, "Misoperation analysis of steady-state and transient methods on earth fault locating in compensated distribution networks," *Sustain. Energy, Grids Networks*, vol. 15, pp. 34–42, 2018.

[18] Z. Xinhui, X. Bingyin, P. Zhencun, and W. Peiyu, "Study on single-phase earthed faulty feeder selection methods in non-solidly grounded systems," in *3rd International Conference on Deregulation and Restructuring and Power Technologies, DRPT 2008*, 2008.

[19] S. Hänninen and M. Lehtonen, "Characteristics of earth faults in electrical distribution networks with high impedance earthing," *Electr. Power Syst. Res.*, vol. 44, no. 3, pp. 155–161, 1998.

[20] "IEEE Std. 1547-2018. Standard for Interconnection and Interoperability of Distributed Energy Resources with Associated Electric Power Systems Interfaces," *IEEE Std 1547-2018 (Revision of IEEE Std 1547-2003)*. 2018.

[21] G. Druml, A. Kugi, and O. Seifert, "A new directional transient relay for high ohmic earth faults," in *CIRED 17th International Conference on Electricity Distribution*, 2003.

[22] T. Henriksen, "Faulty feeder identification in high impedance grounded network using charge-voltage relationship," *Electr. Power Syst. Res.*, vol. 81, no. 9, pp. 1832–1839, 2011.

[23] M. Loos, S. Werben, M. Kereit, and J. C. Maun, "Fault direction method in compensated network using the zero sequence active energy signal," in *IEEE EuroCon 2013*, 2013.

[24] P. Balcerek, M. Fulczyk, J. Izykowski, E. Rosolowski, and P. Pierz, "Centralized substation level protection for determination of faulty feeder in distribution network," in *IEEE Power and*

Energy Society General Meeting, San Diego, CA, USA, 2012.
[25] A. Wahlroos, J. Altonen, U. Uggla, and D. Wall, "Application of novel cumulative phasor sum measurement for earth-fault protection in compensated MV-networks," in *22nd International Conference on Electricity Distribution (CIRED)*, 2013.
[26] A. Wahlroos and J. Altonen, "Application of novel multi-frequency neutral admittance method into earth-fault protection in compensated MV-networks," in *12th IET International Conference on Developments in Power System Protection, DPSP 2014*, 2014.
[27] M. F. Abdel-Fattah and M. Lehtonen, "A transient fault detection technique with varying fault detection window of earth modes in unearthed MV systems," in *6th International Conference - Power Quality and Supply Reliability*, 2008.
[28] M. F. Abdel-Fattah and M. Lehtonen, "A New Transient Impedance-Based Algorithm for Earth Fault Detection in Medium Voltage Networks," in *International Conference on Power Systems Transients*, 2009.
[29] M. F. Abdel-Fattah and M. Lehtonen, "Transient algorithm based on earth capacitance estimation for earth-fault detection in medium-voltage networks," *IET Gener. Transm. Distrib.*, vol. 6, no. 2, pp. 161–166, 2012.
[30] P. Liu and C. Huang, "Detecting single-phase-to-ground fault event and identifying faulty feeder in neutral ineffectively grounded distribution system," *IEEE Trans. Power Deliv.*, 2018.
[31] G. Druml, C. Raunig, P. Schegner, and L. Fickert, "Fast selective earth fault localization using the new fast pulse detection method," in *IET Conference Publications*, 2013.
[32] G. Buigues, V. Valverde, I. Zamora, J. Mazón, and E. Torres, "Signal injection techniques for fault location in distribution networks," *Renew. Energy Power Qual. J.*, 2012.
[33] X. Dong, J. Wang, S. Shi, B. Wang, B. Dominik, and M. Redefern, "Traveling wave based single-phase-to-ground protection method for power distribution system," *CSEE J. Power Energy Syst.*, 2015.
[34] N. Davydova and G. Hug, "Traveling wave based protection for medium voltage grids with distributed generation," in *2017 IEEE Manchester PowerTech, Powertech 2017*, 2017.
[35] A. Borghetti, M. Bosetti, M. Di Silvestro, C. A. Nucci, and M. Paolone, "Continuous-wavelet transform for fault location in distribution power networks: Definition of mother wavelets inferred from fault originated transients," *IEEE Trans. Power Syst.*, 2008.
[36] A. Farughian, L. Kumpulainen, and K. Kauhaniemi, "Review of methodologies for earth fault indication and location in compensated and unearthed MV distribution networks," *Electric Power Systems Research*. 2018.
[37] J. D. Rios Penaloza, A. Borghetti, F. Napolitano, F. Tossani, and C. A. Nucci, "A New Transient-Based Earth Fault Protection System for Unearthed Meshed Distribution Networks," *IEEE Trans. Power Deliv. (Early Access)*, 2020.
[38] ENEL Distribuzione S.p.A., "Criteri di protezione della rete MT di distribuzione - DK 4451 Ed. 2.1," 2005.
[39] M. Brenna, E. De Berardinis, L. Delli Carpini, P. Paulon, P. Petroni, G. Sapienza, G. Scrosati, and D. Zaninelli, "Petersen coil regulators analysis using a real-time digital simulator," *IEEE Trans. Power Deliv.*, 2011.
[40] J. Arrillaga and N. R. Watson, *Power system harmonics*. John Wiley & Sons Ltd., 2003.
[41] The Mathworks Inc., *Signal Processing Toolbox: User's Guide*. Natick, MA, 2018.
[42] V. Leitloff, L. Pierrat, and R. Feuillet, "Study of the neutral-to-ground voltage in a compensated power system," *Eur. Trans. Electr. Power*, 1994.
[43] CIGRE Working Group C4.605, "Benchmark Systems for Network Integration of Renewable and Distributed Energy Resources," CIGRE, Paris, France, Tech. Rep. C6.04.02, 2014.
[44] H. J. Altuve, K. Zimmerman, and D. Tziouvaras, "Maximizing line protection reliability, speed, and sensitivity," in *69th Annual Conference for Protective Relay Engineers*, College Station, TX, USA, 2016, pp. 1–28.
[45] E. O. Schweitzer and D. Hou, "Filtering for protective relays," in *Communications, Computers and Power in the Modern Environment*, 1993.
[46] S. J. Elliott, *Signal Processing for Active Control*, 1st ed. Academic Press, 2001.
[47] S. Civanlar, J. J. Grainger, H. Yin, and S. S. H. Lee, "Distribution Feeder Reconfiguration for Loss Reduction," *IEEE Trans. Power Deliv.*, 1988.

[48] M. Lavorato, J. F. Franco, M. J. Rider, and R. Romero, "Imposing radiality constraints in distribution system optimization problems," *IEEE Transactions on Power Systems*. 2012.
[49] L. F. Ochoa, C. J. Dent, and G. P. Harrison, "Distribution network capacity assessment: Variable DG and active networks," *IEEE Trans. Power Syst.*, 2010.
[50] V. H. Méndez Quezada, J. Rivier Abbad, and T. Gómez San Román, "Assessment of energy distribution losses for increasing penetration of distributed generation," *IEEE Trans. Power Syst.*, 2006.
[51] Z. Liu, C. Su, H. K. Hoidalen, and Z. Chen, "A Multiagent System-Based Protection and Control Scheme for Distribution System with Distributed-Generation Integration," *IEEE Trans. Power Deliv.*, vol. 32, no. 1, pp. 536–545, 2017.
[52] A. H. Osman, M. S. Hassan, and M. Sulaiman, "Communication-based adaptive protection for distribution systems penetrated with distributed generators," *Electr. Power Components Syst.*, vol. 43, no. 5, pp. 556–565, 2015.
[53] W. Wang, S. Jazebi, F. De León, and Z. Li, "Looping Radial Distribution Systems Using Superconducting Fault Current Limiters: Feasibility and Economic Analysis," *IEEE Trans. Power Syst.*, vol. 33, no. 3, pp. 2486–2495, 2017.
[54] G. Celli, F. Pilo, G. Pisano, R. Cicoria, and A. Iaria, "Meshed vs. radial MV distribution network in presence of large amount of DG," in *IEEE PES Power Systems Conference and Exposition.*, 2004, pp. 1357–1362.
[55] J. C. Kim, S. M. Cho, and H. S. Shin, "Advanced power distribution system configuration for smart grid," *IEEE Trans. Smart Grid*, vol. 4, no. 1, pp. 353–358, 2013.
[56] T. H. Chen, W. T. Huang, J. C. Gu, G. C. Pu, Y. F. Hsu, and T. Y. Guo, "Feasibility study of upgrading primary feeders from radial and open-loop to normally closed-loop arrangement," *IEEE Trans. Power Syst.*, vol. 19, no. 3, pp. 1308–1316, 2004.
[57] S. Lauria, A. Codino, and R. Calone, "Protection system studies for ENEL Distribuzione's MV loop lines," *2015 IEEE Eindhoven PowerTech, PowerTech 2015*, 2015.
[58] E. Sortomme, S. S. Venkata, and J. Mitra, "Microgrid protection using communication-assisted digital relays," *IEEE Trans. Power Deliv.*, 2010.
[59] F. R. Islam, K. Prakash, K. A. Mamun, A. Lallu, and H. R. Pota, "Aromatic network: A novel structure for power distribution system," *IEEE Access*, 2017.
[60] R. Moxley and K. Fodero, "High-speed distribution protection made easy: Communications-assisted protection schemes for distribution applications," in *58th Annual Conference for Protective Relay Engineers*, College Station, TX, USA, USA, 2005.
[61] M. Oldak and B. Kilbourne, "NBP RFI: Communications Requirements - Comments of Utilities Telecom Council," 2010. .
[62] J. C. Tobias, R. P. Leeuwerke, A. L. Brayford, and A. Robinson, "Use of sectionalising circuit breakers in urban MV distribution networks," in *Fifth International Conference on Trends in Distribution Switchgear: 400V-145kV for Utilities and Private Networks*, 1998.
[63] M. J. Thompson and A. Somani, "A tutorial on calculating source impedance ratios for determining line length," in *68th Annual Conference for Protective Relay Engineers*, College Station, TX, USA, 2015, pp. 833–841.
[64] "IEEE Std 2030-2011 - Guide for Smart Grid Interoperability of Energy Technology and Information Technology Operation with the Electric Power System (EPS), End-Use Applications , and Loads," 2011.
[65] R. H. Khan and J. Y. Khan, "A comprehensive review of the application characteristics and traffic requirements of a smart grid communications network," *Comput. Networks*, vol. 57, no. 3, pp. 825–845, 2013.
[66] ETSI, "Draft TR 102 935, Version: 0.1.3. Machine to Machine (M2M); Applicability of M2M architecture to Smart Grid Networks ; Impact of Smart Grids on M2M platform," 2010.
[67] Prashant Kansal and A. Bose, "Bandwidth and Latency Requirements for Smart Transmission Grid Applications," *IEEE Trans. Smart Grid*, vol. 3, no. 3, pp. 1344–1352, 2012.
[68] Western Electricity Coordinating Council (WECC) - Telecommunications and Relay Work Groups, "Communications Systems Performance Guide for Electric Protection Systems," 2013. [Online]. Available: https://www.wecc.org/Reliability/Communication System Performance Guide for Electric Protection Systems.pdf.

[69] S. V Achanta, B. Macleod, E. Sagen, H. Loehner, and S. E. Laboratories, “Apply Radios to Improve the Operation of Electrical Protection,” *SEL J. Reliab. Power*, vol. 1, no. 2, 2010.
[70] E. O. Schweitzer, D. Finney, and M. V. Mynam, “Applying radio communication in distribution generation teleprotection schemes,” in *65th Annual Conference for Protective Relay Engineers*, College Station, TX, USA, 2012, pp. 310–320.
[71] R. Bottura, D. Babazadeh, K. Zhu, A. Borghetti, L. Nordstrom, and C. A. Nucci, “SITL and HLA co-simulation platforms: Tools for analysis of the integrated ICT and electric power system,” in *EuroCon*, Zagreb, Croatia, 2013, pp. 918–925.
[72] S. Ciraci, J. Daily, K. Agarwal, J. Fuller, L. Marinovici, and A. Fisher, “Synchronization Algorithms for Co-Simulation of Power Grid and Communication Networks,” in *22nd International Symposium on Modelling, Analysis & Simulation of Computer and Telecommunication System*, 2014, pp. 355–364.
[73] K. Hopkinson, X. Wang, R. Giovanini, J. Thorp, K. Birman, and D. Coury, “EPOCHS: A platform for agent-based electric power and communication simulation built from commercial off-the-shelf components,” *IEEE Trans. Power Syst.*, 2006.
[74] K. Mets, J. A. Ojea, and C. Develder, “Combining Power and Communication Network Simulation for Cost-Effective Smart Grid Analysis,” *IEEE Commun. Surv. Tutorials*, pp. 1–26, 2014.
[75] Enel Distribuzione SpA, *Distanza di prima approssimazione (DPA) da linee e cabine elettriche*. 2008.
[76] H. W. Dommel, *Electromagnetic Transients Program Theory Book*. Bonneville Power Administration, 1986.
[77] M. O. Faruque, T. Strasser, G. Lauss, V. Jalili-Marandi, P. Forsyth, C. Dufour, V. Dinavahi, A. Monti, P. Kotsampopoulos, J. A. Martinez, K. Strunz, M. Saeedifard, X. Wang, D. Shearer, M. Paolone, R. Brandl, M. Matar, A. Davoudi, and R. Iravani, “Real-Time Simulation Technologies for Power Systems Design, Testing, and Analysis,” *IEEE Power Energy Technol. Syst. J.*, 2015.
[78] Opal-RT Technologies Inc., “Artemis User Guide,” Canada, 2017.
[79] The Mathworks Inc., *Simscape User’s Guide*. Natick, MA: The Mathworks Inc., 2020.
[80] T. Funabashi, *Integration of Distributed Energy Resources in Power Systems: Implementation, Operation and Control*. Academic Press, 2016.
[81] J. A. P. Lopes, N. Hatziargyriou, J. Mutale, P. Djapic, and N. Jenkins, “Integrating distributed generation into electric power systems: A review of drivers, challenges and opportunities,” *Electr. Power Syst. Res.*, 2007.
[82] S. Chowdhury, S. P. Chowdhury, and P. Crossley, *Microgrids and active distribution networks*. 2009.
[83] CIGRE Working Group C6.11, “Development and operation of active distribution networks,” 2011.
[84] R. A. Walling, R. Saint, R. C. Dugan, J. Burke, and L. A. Kojovic, “Summary of distributed resources impact on power delivery systems,” *IEEE Trans. Power Deliv.*, 2008.
[85] C. C. L. Moreira, “Identification and Development of Microgrids Emergency Control Procedures,” University of Porto, 2008.
[86] J. A. P. Lopes, A. G. Madureira, and C. C. L. M. Moreira, “A view of microgrids,” *Wiley Interdisciplinary Reviews: Energy and Environment*. 2013.
[87] R. Lasseter, A. Akhil, C. Marnay, J. Stephens, J. Dagle, R. Guttromson, A. S. Meliopoulous, R. Yinger, and J. Eto, “Consortium for Electric Reliability Technology Solutions White Paper on Integration of Distributed Energy Resources The CERTS MicroGrid Concept,” *Program, Transm. Reliab. Syst. Energy Program, Integr. Interes. Public Comm. Calif. Energy*, 2002.
[88] *IEEE Standard for the Specification of Microgrid Controllers*. 2018.
[89] N. Hatziargyriou, H. Asano, R. Iravani, and C. Marnay, “Microgrids,” *IEEE Power and Energy Magazine*. 2007.
[90] J. A. Pecas Lopes, A. Madureira, N. Gil, and F. Resende, “Operation of Multi-Microgrids,” in *Microgrids: Architectures and Control, Chapter 5*, 2014.
[91] A. Dimeas, A. Tsikalakis, G. Kariniotakis, and G. Korres, “Microgrids control issues,” in *Microgrids: Architectures and Control*, 2013.
[92] IEEE PES Task Force on Microgrid Stability Analysis and Modeling, “Microgrid Stability

Definitions, Analysis, and Examples," *IEEE Trans. Power Syst. (Early Access)*, 2019.
[93] F. Gao and M. R. Iravani, "A control strategy for a distributed generation unit in grid-connected and autonomous modes of operation," *IEEE Trans. Power Deliv.*, vol. 23, no. 2, pp. 850–859, 2008.
[94] H. Bevrani, B. Francois, and T. Ise, *Microgrid Dynamics and Control*. Chennai, India: JohnWiley & Sons, Inc., 2017.
[95] J. A. P. Lopes, C. L. Moreira, and A. G. Madureira, "Defining Control Strategies for MicroGrids Islanded Operation," *IEEE Trans. Power Syst.*, vol. 21, no. 2, pp. 916–924, 2006.
[96] K. P. Schneider, N. Radhakrishnan, Y. Tang, F. K. Tuffner, C. C. Liu, J. Xie, and D. Ton, "Improving Primary Frequency Response to Support Networked Microgrid Operations," *IEEE Trans. Power Syst.*, 2019.
[97] J. H. Eto, J. Undrill, C. Roberts, P. Mackin, and J. Ellis, "Frequency Control Requirements for Reliable Interconnection Frequency Response," Berkley, CA, USA, 2018.
[98] D. Wu, F. Tang, J. C. Vasquez, and J. M. Guerrero, "Control and analysis of droop and reverse droop controllers for distributed generations," in *2014 IEEE 11th International Multi-Conference on Systems, Signals and Devices, SSD 2014*, 2014.
[99] J. Rocabert, A. Luna, F. Blaabjerg, and P. Rodríguez, "Control of power converters in AC microgrids," *IEEE Trans. Power Electron.*, 2012.
[100] J. M. Guerrero, J. Matas, L. G. De Vicuña, M. Castilla, and J. Miret, "Wireless-control strategy for parallel operation of distributed-generation inverters," *IEEE Trans. Ind. Electron.*, 2006.
[101] E. Rokrok, M. Shafie-khah, and J. P. S. Catalão, "Review of primary voltage and frequency control methods for inverter-based islanded microgrids with distributed generation," *Renew. Sustain. Energy Rev.*, vol. 1, no. 82, pp. 3225–3235, 2018.
[102] T. Degner, N. Soultanis, A. Engler, and A. G. de Muro, "Intelligent local controllers," in *Microgrids: Architectures and Control*, 2013, pp. 81–116.
[103] H. Han, X. Hou, J. Yang, J. Wu, M. Su, and J. M. Guerrero, "Review of power sharing control strategies for islanding operation of AC microgrids," *IEEE Trans. Smart Grid*, 2016.
[104] U. Tamrakar, D. Shrestha, M. Maharjan, B. Bhattarai, T. Hansen, and R. Tonkoski, "Virtual Inertia: Current Trends and Future Directions," *Appl. Sci.*, 2017.
[105] S. D'Arco and J. A. Suul, "Virtual synchronous machines - Classification of implementations and analysis of equivalence to droop controllers for microgrids," in *2013 IEEE Grenoble Conference PowerTech, POWERTECH 2013*, 2013.
[106] J. Liu, Y. Miura, and T. Ise, "Comparison of Dynamic Characteristics between Virtual Synchronous Generator and Droop Control in Inverter-Based Distributed Generators," in *IEEE Transactions on Power Electronics*, 2016.
[107] S. D. Arco and J. A. Suul, "Equivalence of Virtual Synchronous Machines and Frequency-Droops for Converter-Based MicroGrids," *IEEE Trans. Smart Grid*, vol. 5, no. 1, pp. 394–395, 2014.
[108] D. Duckwitz, A. Knobloch, F. Welck, T. Becker, C. Glöckler, and T. Bülo, "Experimental short-circuit testing of grid-forming inverters in microgrid and interconnected mode," in *NEIS 2018 - Conference on Sustainable Energy Supply and Energy Storage Systems*, 2020.
[109] J. Rodrigues, A. Lopes, L. Miranda, C. Gouveia, C. Moreira, and J. P. Lopes, "The role of low-voltage-ride-through capability of distributed energy resources for the mitigation of voltage sags in low voltage distribution grids," in *20th Power Systems Computation Conference, PSCC 2018*, 2018.
[110] P. Beires, M. H. Vasconcelos, C. L. Moreira, and J. A. Peças Lopes, "Stability of autonomous power systems with reversible hydro power plants: A study case for large scale renewables integration," *Electr. Power Syst. Res.*, 2018.
[111] X. Lu, J. Wang, J. M. Guerrero, and D. Zhao, "Virtual-impedance-based fault current limiters for inverter dominated AC microgrids," *IEEE Trans. Smart Grid*, 2018.
[112] Cigré Working Group C4.605, "Modelling and Aggregation of Loads in Flexible Power Networks," CIGRE, Paris, France, Tech. Brochure 566, 2014.
[113] J. V. Milanović, K. Yamashita, S. Martínez Villanueva, S. Ž. Djokić, and L. M. Korunović, "International industry practice on power system load modeling," *IEEE Trans. Power Syst.*, vol. 28, no. 3, pp. 3038–3046, 2013.

[114] M. Farrokhabadi, C. A. Canizares, J. W. Simpson-Porco, E. Nasr, L. Fan, P. A. Mendoza-Araya, R. Tonkoski, U. Tamrakar, N. Hatziargyriou, D. Lagos, R. W. Wies, M. Paolone, M. Liserre, L. Meegahapola, M. Kabalan, A. H. Hajimiragha, D. Peralta, M. A. Elizondo, K. P. Schneider, F. K. Tuffner, and J. Reilly, "Microgrid Stability Definitions, Analysis, and Examples," *IEEE Trans. Power Syst.*, 2020.
[115] IEEE PES Task Force on Microgrid Stability Analysis and Modeling, "Microgrid Stability Definitions, Analysis, and Modeling," IEEE PES, Technical Report PES-TR66, 2018.
[116] M. Farrokhabadi, C. A. Cañizares, and K. Bhattacharya, "Frequency control in isolated/islanded microgrids through voltage regulation," *IEEE Trans. Smart Grid*, vol. 8, no. 3, pp. 1185–1194, 2017.
[117] G. Delille, L. Capely, D. Souque, and C. Ferrouillat, "Experimental validation of a novel approach to stabilize power system frequency by taking advantage of Load Voltage Sensitivity," in *2015 IEEE Eindhoven PowerTech, PowerTech 2015*, 2015.
[118] Comitato Elettrotecnico Italiano (CEI), "CEI 0-16:2019-04 Regola tecnica di riferimento per la connessione di Utenti attivi e passivi alle reti AT ed MT delle imprese distributrici di energia elettrica." 2019.
[119] A. A. Salem, A. A. Abdelsalam, A. H. K. Alaboudy, and H. E. A. Talaat, "Dynamic performance of microgrid after fault provoked-islanding considering Induction Motor loads," in *2016 18th International Middle-East Power Systems Conference, MEPCON 2016 - Proceedings*, 2017.
[120] A. H. Kasem Alaboudy, H. H. Zeineldin, and J. Kirtley, "Microgrid stability characterization subsequent to fault-triggered islanding incidents," *IEEE Trans. Power Deliv.*, 2012.
[121] N. Afrin, F. Yang, J. Lu, and M. Islam, "Impact of induction motor load on the dynamic voltage stability of microgrid," in *ANZCC 2018 - 2018 Australian and New Zealand Control Conference*, 2019.
[122] J. D. Rios Penaloza, J. A. Adu, A. Borghetti, F. Napolitano, F. Tossani, and C. A. Nucci, "A Power Control Scheme for the Islanding Transition of a Microgrid with Battery Energy Storage Systems," in *19th EEEIC Environment and Electrical Engineering International Conference*, 2019.
[123] J. D. Rios Penaloza, J. A. Adu, A. Borghetti, F. Napolitano, F. Tossani, and C. A. Nucci, "Influence of load dynamic response on the stability of microgrids during islanding transition," *Electr. Power Syst. Res.*, vol. 190, no. 106607, 2021.
[124] C. Li, C. Cao, Y. Cao, Y. Kuang, L. Zeng, and B. Fang, "A review of islanding detection methods for microgrid," *Renew. Sustain. Energy Rev.*, vol. 35, pp. 211–220, 2014.
[125] I. J. Balaguer, Q. Lei, S. Yang, U. Supatti, and F. Z. Peng, "Control for Grid-Connected and Intentional Islanding Operations of Distributed Power Generation," *IEEE Trans. Ind. Electron.*, vol. 58, no. 1, pp. 147–157, 2011.
[126] R. Caldon, M. Coppo, A. Raciti, and R. Turri, "Dynamic control of inverter-connected generators for intentionally islanded MV distribution networks," in *Proceedings of the Universities Power Engineering Conference*, 2013.
[127] R. Caldon, A. Stocco, and R. Turri, "Feasibility of adaptive intentional islanding operation of electric utility systems with distributed generation," *Electr. Power Syst. Res.*, vol. 78, no. 2008, pp. 2017–2023, 2017.
[128] A. Cagnano, E. De Tuglie, and L. Cicognani, "Prince — Electrical Energy Systems Lab: A pilot project for smart microgrids," *Electr. Power Syst. Res.*, vol. 148, pp. 10–17, 2017.
[129] J. Kim, J. Jeon, S. Kim, C. Cho, J. H. Park, H. Kim, and K. Nam, "Cooperative Control Strategy of Energy Storage System and Microsources for Stabilizing the Microgrid during Islanded Operation," *IEEE Trans. Power Electron.*, vol. 25, no. 12, pp. 3037–3048, 2010.
[130] J. Wang, N. C. P. Chang, X. Feng, and A. Monti, "Design of a Generalized Control Algorithm for Parallel Inverters for Smooth Microgrid Transition Operation," *IEEE Trans. Ind. Electron.*, vol. 62, no. 8, pp. 4900–4914, 2015.
[131] A. Cagnano, E. De Tuglie, M. Trovato, L. Cicognani, and V. Vona, "A simple circuit model for the islanding transition of microgrids," in *IEEE 2nd International Forum on Research and Technologies for Society and Industry Leveraging a Better Tomorrow, RTSI*, Bologna, Italy, 2016.
[132] F. Katiraei, M. R. Iravani, and P. W. Lehn, "Micro-Grid Autonomous Operation During and

Subsequent to Islanding Process," *IEEE Trans. Power Deliv.*, vol. 20, no. 1, pp. 248–257, 2005.
[133] W. El-Khattam, T. S. Sidhu, and R. Seethapathy, "Evaluation of two anti-islanding schemes for a radial distribution system equipped with self-excited induction generator wind turbines," *IEEE Trans. Energy Convers.*, vol. 25, no. 1, pp. 107–117, 2010.
[134] N. Pogaku, M. Prodanović, and T. C. Green, "Modeling, analysis and testing of autonomous operation of an inverter-based microgrid," *IEEE Trans. Power Electron.*, vol. 22, no. 2, pp. 613–625, 2007.
[135] F. Sossan, E. Namor, R. Cherkaoui, and M. Paolone, "Achieving the Dispatchability of Distribution Feeders Through Prosumers Data Driven Forecasting and Model Predictive Control of Electrochemical Storage," *IEEE Trans. Sustain. Energy*, vol. 7, no. 4, pp. 1762–1777, 2016.
[136] U. Datta, A. Kalam, and J. Shi, "Battery Energy Storage System to Stabilize Transient Voltage and Frequency and Enhance Power Export Capability," *IEEE Trans. Power Syst.*, vol. 34, no. 3, pp. 1845–1857, 2018.
[137] H. Saad, J. Mahseredjian, and S. Dennetière, "VSC-MMC Station Models Modular Multi-Level Converter in EMTP-RV," 2014. [Online]. Available: https://www.emtp-software.com/dl?fichier=MicroGridLib.zip. [Accessed: 16-Nov-2020].
[138] S. Golestan, J. M. Guerrero, and J. C. Vasquez, "Three-Phase PLLs: A Review of Recent Advances," *IEEE Transactions on Power Electronics*. 2017.
[139] H. Jin, "Behavior-mode simulation of power electronic circuits," *IEEE Trans. Power Electron.*, vol. 12, no. 3, pp. 443–452, 1997.
[140] Itron Inc, "California commercial end-use survey," Consultant Report, CEC-400-2006-005, 2006.
[141] California Energy Commission, "Attachment 13. References for Energy End-Use, Electricity Demand and GHG Emissions Reference and Calculations. March 1042014. PON-13-301. EPIC Grant program.," Sacramento, 2014.
[142] K. Morison, H. Hamadani, and L. Wang, "Load modeling for voltage stability studies," in *2006 IEEE PES Power Systems Conference and Exposition, PSCE 2006 - Proceedings*, 2006.
[143] "Comprehensive Load Modeling for System Planning Studies," EPRI, Palo Alto, CA, 2009.
[144] C. W. Taylor, *Power System Voltage Stability*. Palo Alto: EPRI Editors, 1994.
[145] J. R. Ribeiro and F. J. Lange, "A new aggregation method for determining composite load characteristics," *IEEE Trans. Power Appar. Syst.*, vol. PAS-101, no. 8, pp. 2869–2875, 1982.
[146] P. Kundur, *Power System Stability and Control*. McGraw-Hill Education, 1994.
[147] L. M. Hajagos, "Laboratory measurements and models of modern loads and their effect on voltage stability studies," *IEEE Trans. Power Syst.*, vol. 13, no. 2, pp. 584–592, 1998.
[148] L. Korunović and D. Stojanović, "Load Model Parameters on Low and Medium Voltage in Distribution Networks," *Elektroprivreda*, vol. 55, no. 2, pp. 46–56, 2002.
[149] A. Bokhari, A. Alkan, R. Dogan, M. Diaz-Aguilo, F. De Leon, D. Czarkowski, Z. Zabar, L. Birenbaum, A. Noel, and R. E. Uosef, "Experimental determination of the ZIP coefficients for modern residential, commercial, and industrial loads," *IEEE Trans. Power Deliv.*, vol. 29, no. 3, pp. 1372–1381, 2014.
[150] "Advanced Load Modeling," EPRI, Palo Alto, CA, and Public Service Company of New Mexico, Albuquerque, 2002.
[151] P. Tielens and D. Van Hertem, "The relevance of inertia in power systems," *Renew. Sustain. Energy Rev.*, no. 55, pp. 999–1009, 2016.
[152] M. T. Muhssin, L. M. Cipcigan, N. Jenkins, S. Slater, M. Cheng, and Z. A. Obaid, "Dynamic Frequency Response from Controlled Domestic Heat Pumps," *IEEE Trans. Power Syst.*, 2018.
[153] J. A. P. Lopes, F. J. Soares, and P. M. R. Almeida, "Integration of electric vehicles in the electric power system," *Proc. IEEE*, 2011.
[154] J. D. Rios Penaloza, F. Napolitano, and F. Tossani, "Computational Aspects of the Dynamic Response of a Microgrid: A Comparative Analysis," in *Proceedings - 2020 IEEE International Conference on Environment and Electrical Engineering and 2020 IEEE Industrial and Commercial Power Systems Europe, EEEIC / I and CPS Europe 2020*, 2020.
[155] M. Karimi Ghartemani, S. A. Khajehoddin, P. K. Jain, and A. Bakhshai, "Problems of startup and phase jumps in PLL systems," *IEEE Trans. Power Electron.*, 2012.
[156] L. Zhang, "Modeling and Control of VSC-HVDC Links Connected to Weak AC Systems," KTH

Royal Institute of Technology, 2010.
[157] F. Gothner, O. M. Midtgard, R. Torres-Olguin, and S. D. Arco, “Effect of Including Transient Virtual Impedance in Droop-Controlled Microgrids,” in *Proceedings - 2018 IEEE International Conference on Environment and Electrical Engineering and 2018 IEEE Industrial and Commercial Power Systems Europe, EEEIC/I and CPS Europe 2018*, 2018.
[158] A. Madureira, C. Moreira, and J. Peças Lopes, “Secondary load-frequency control for microgrids in islanded operation,” *Renew. Energy Power Qual. J.*, 2005.
[159] J. Gouveia, C. L. Moreira, and J. A. P. Lopes, “Grid-Forming Inverters Sizing in Islanded Power Systems- A stability perspective,” in *SEST 2019 - 2nd International Conference on Smart Energy Systems and Technologies*, 2019.
[160] Mathworks, “MatLab & Simulink: Simulink Reference R2018b.” 2018.
[161] M. EL-Shimy, *Dynamic Security of Interconnected Electric Power Systems – Volume 2*. Saarbrücken, Germany: LAP LAMBERT Academic Publishing, 2015.
[162] J. A. P. Lopes, P. M. R. Almeida, F. J. Soares, and C. L. Moreira, “Electric vehicles in isolated power systems: Conceptual framework and contributions to improve the grid resilience,” in *IFAC Proceedings Volumes (IFAC-PapersOnline)*, 2010.
[163] Y. Ota, H. Taniguchi, T. Nakajima, K. M. Liyanage, J. Baba, and A. Yokoyama, “Autonomous distributed V2G (vehicle-to-grid) satisfying scheduled charging,” *IEEE Trans. Smart Grid*, 2012.
[164] J. L. Kirtley, *Electric Power Principles*. 2010.
[165] I. Ibrahim, C. O’Loughlin, and T. O’Donnell, “Virtual inertia control of variable speed heat pumps for the provision of frequency support,” *Energies*, 2020.
[166] Y. J. Kim, L. K. Norford, and J. L. Kirtley, “Modeling and analysis of a variable speed heat pump for frequency regulation through direct load control,” *IEEE Trans. Power Syst.*, 2015.
[167] J. D. Rios Penaloza, J. A. Adu, A. Borghetti, F. Napolitano, F. Tossani, and C. A. Nucci, “Influence of Load Dynamic Response on the Stability of Microgrids During Islanding Transition,” in *Power Systems Computation Conference (PSCC) 2020*, 2020.
[168] H. Sekhavatmanesh, J. Rodrigues, C. C. L. M. Moreira, J. A. Peças Lopes, and R. Cherkaoui, “A convex model for induction motor starting transients imbedded in an OPF-based optimization problem,” in *Power Systems Computation Conference (PSCC) 2020*, 2020.
[169] V. Aravinthan, T. Balachandran, M. Ben-Idris, W. Fei, M. Heidari-Kapourchali, A. Hcttiarachchigc-Don, J. N. Jiang, H. Lei, C. C. Liu, J. Mitra, M. Ni, M. Papic, M. Parvania, M. Sephary, C. Singh, A. Srivastava, A. Stefanov, H. Sun, and S. Tindemans, “Reliability modeling considerations for emerging cyber-physical power systems: Prepared by task force on reliability consideration for emerging cyber-physical energy systems under IEEE PES reliability, risk and probability applications subcommittee,” in *2018 International Conference on Probabilistic Methods Applied to Power Systems, PMAPS 2018 - Proceedings*, 2018.
[170] J. R. Marti, “Accurate modelling of frequency-dependent transmission lines in electromagnetic transient simulations,” *IEEE Trans. Power Appar. Syst.*, 1982.
[171] L. Marti, “Simulation of Transients in Underground Cables with Frequency-Dependent Modal Transformation Matrices,” *IEEE Trans. Power Deliv.*, 1988.
[172] J. Peralta, H. Saad, S. Dennetière, J. Mahseredjian, and S. Nguefeu, “Detailed and averaged models for a 401-level MMC-HVDC system,” *IEEE Trans. Power Deliv.*, vol. 27, no. 3, pp. 1501–1508, 2012.
[173] H. Saad, S. Dennetiere, J. Mahseredjian, P. Delarue, X. Guillaud, J. Peralta, and S. Nguefeu, “Modular multilevel converter models for electromagnetic transients,” *IEEE Trans. Power Deliv.*, 2014.
[174] A. Yazdani and R. Iravani, *Voltage-Sourced Converters in Power Systems*. 2010.
[175] H. Ouquelle, L. A. Dessaint, and S. Casoria, “An average value model-based design of a deadbeat controller for VSC-HVDC transmission link,” in *2009 IEEE Power and Energy Society General Meeting, PES ’09*, 2009.
[176] Y. Che, W. Li, X. Li, J. Zhou, S. Li, and X. Xi, “An improved coordinated control strategy for PV system integration with VSC-MVDC technology,” *Energies, MDPI*, vol. 10, no. 1670, pp. 1–14, 2017.
[177] A. K. Saha, S. Chowdhury, S. P. Chowdhury, and P. A. Crossley, “Modeling and performance

analysis of a microturbine as a distributed energy resource," *IEEE Trans. Energy Convers.*, 2009.
[178] A. Bertani, C. Bossi, F. Fornari, S. Massucco, S. Spelta, and F. Tivegna, "A microturbine generation system for grid connected and islanding operation," in *2004 IEEE PES Power Systems Conference and Exposition*, 2004.
[179] Y. Zhu and K. Tomsovic, "Development of models for analyzing the load-following performance of microturbines and fuel cells," *Electr. Power Syst. Res.*, 2002.
[180] M. G. Villalva, J. R. Gazoli, and E. R. Filho, "Comprehensive approach to modeling and simulation of photovoltaic arrays," *IEEE Trans. Power Electron.*, vol. 24, no. 5, pp. 1198–1208, 2009.
[181] R. Cardenas, R. Pena, S. Alepuz, and G. Asher, "Overview of control systems for the operation of DFIGs in wind energy applications," *IEEE Trans. Ind. Electron.*, 2013.
[182] L. Mihet-Popa, F. Blaabjerg, and I. Boldea, "Wind Turbine Generator Modeling and Simulation Where Rotational Speed is the Controlled Variable," *IEEE Trans. Ind. Appl.*, 2004.
[183] G. Abad, J. López, M. A. Rodríguez, L. Marroyo, and G. Iwanski, *Doubly Fed Induction Machine*. 2011.
[184] T. Ackermann, *Wind Power in Power Systems*. 2005.
[185] M. Bollen and F. Hassan, *Integration of Distributed Generation in the Power System*. 2011.
[186] International Renewable Energy Agency (IRENA), "Battery Storage for Renewables: Market Status and Technology Outlook," 2015.
[187] M. Chen and G. A. Rincón-Mora, "Accurate electrical battery model capable of predicting runtime and I-V performance," *IEEE Trans. Energy Convers.*, vol. 21, no. 2, 2006.
[188] E. Namor, F. Sossan, E. Scolari, R. Cherkaoui, and M. Paolone, "Experimental Assessment of the Prediction Performance of Dynamic Equivalent Circuit Models of Grid-connected Battery Energy Storage Systems," in *8th IEEE PES Innovative Smart Grid Technologies*, Sarajevo - Bosnia and Herzgovina, 2018, no. October.
[189] M. Bahramipanah, D. Torregrossa, R. Cherkaoui, and M. Paolone, "Enhanced electrical model of Lithium-based batteries accounting the charge redistribution effect," in *Proceedings - 2014 Power Systems Computation Conference, PSCC 2014*, 2014.
[190] E. M. G. Rodrigues, R. Godina, G. J. Osorio, J. M. Lujano-Rojas, J. C. O. Matias, and J. P. S. Catalao, "Comparison of battery models for energy storage applications on insular grids," in *2015 Australasian Universities Power Engineering Conference: Challenges for Future Grids, AUPEC 2015*, 2015.
[191] S. M. Mousavi G. and M. Nikdel, "Various battery models for various simulation studies and applications," *Renewable and Sustainable Energy Reviews*. 2014.
[192] L. E. Helseth, "Modelling supercapacitors using a dynamic equivalent circuit with a distribution of relaxation times," *J. Energy Storage*, 2019.
[193] L. Zhang, X. Hu, Z. Wang, F. Sun, and D. G. Dorrell, "A review of supercapacitor modeling, estimation, and applications: A control/management perspective," *Renewable and Sustainable Energy Reviews*. 2018.
[194] H. Chen, T. N. Cong, W. Yang, C. Tan, Y. Li, and Y. Ding, "Progress in electrical energy storage system: A critical review," *Progress in Natural Science*. 2009.
[195] P. Du and N. Lu, *Energy Storage for Smart Grids: Planning and Operation for Renewable and Variable Energy Resources (VERs)*. 2014.
[196] P. Thounthong, S. Raël, and B. Davat, "Energy management of fuel cell/battery/supercapacitor hybrid power source for vehicle applications," *J. Power Sources*, 2009.
[197] E. Clarke, *Circuit Analysis of A-C Power Systems. Vol. I: Symmetrical and Related Components*. JohnWiley & Sons, Inc., 1943.
[198] R. Teodorescu, M. Liserre, and P. Rodríguez, *Grid Converters for Photovoltaic and Wind Power Systems*. 2010.
[199] K. R. Padiyar and A. M. Kulkarni, *Dynamics and Control of Electric Transmission and Microgrids*. 2019.
[200] H. Akagi, E. H. Watanabe, and M. Aredes, *Instantaneous Power Theory and Applications to Power Conditioning*. John Wiley & Sons Inc, 2017.